SECU

AD-A247 869

(2)

IT DOCUMENTATION PAGE

DTIC ELECTE MAR 18 1992 S D

1a. REPORT SECURITY CLASSIFICATION: Unclassified	1b. RESTRICTIVE MARKINGS
2a. SECURITY CLASSIFICATION AUTHORITY	3. DISTRIBUTION / AVAILABILITY OF REPORT: Distribution Unlimited Approved for Public Release
2b. DECLASSIFICATION / DOWNGRADING SCHEDULE	
4. PERFORMING ORGANIZATION REPORT NUMBER(S)	5. MONITORING ORGANIZATION REPORT NUMBER(S): AFOSR-TR- 92 0221
6a. NAME OF PERFORMING ORGANIZATION: Tufts University; 6b. OFFICE SYMBOL (If applicable)	7a. NAME OF MONITORING ORGANIZATION: AFOSR/NP NL
6c. ADDRESS (City, State, and ZIP Code): Dept. of Physics and Astronomy, Medford, MA 02155	7b. ADDRESS (City, State, and ZIP Code): Bolling Air Force Base, Washington, DC 20332
8a. NAME OF FUNDING / SPONSORING ORGANIZATION: AFOSR/NP; 8b. OFFICE SYMBOL (If applicable): NL	9. PROCUREMENT INSTRUMENT IDENTIFICATION NUMBER: AFOSR-89-0147
8c. ADDRESS (City, State, and ZIP Code): Bolling Air Force Base, Washington, DC 20332	10. SOURCE OF FUNDING NUMBERS: PROGRAM ELEMENT NO. 61102F; PROJECT NO. 2311; TASK NO. A1; WORK UNIT ACCESSION NO. NA

11. TITLE (Include Security Classification)
HIGH-RESOLUTION MICROWAVE OBSERVATIONS OF THE SUN (unclassified)

12. PERSONAL AUTHOR(S)
Kenneth R. Lang

13a. TYPE OF REPORT	13b. TIME COVERED	14. DATE OF REPORT (Year, Month, Day)	15. PAGE COUNT
Final Technical	FROM 11/1/88 TO 4/30/92	1992, February 28	198

16. SUPPLEMENTARY NOTATION
Solar activity; Very Large Array; Sun: eruptions, flares, origin and prediction of solar activity; Radio emission from coronal loops and filaments; Resolution of the pre-flare, impulsive and decay phases of solar flares; X-ray emission from coronal loops and flares; Solar Maximum Mission satellite; NASA balloon flights of high-energy solar detectors; Yohkoh solar satellite; Max 91 VLA campaign; Future research and data analysis.

17. COSATI CODES		
FIELD	GROUP	SUB-GROUP

19. ABSTRACT (Continue on reverse if necessary and identify by block number)

This is the final technical report for grant AFOSR-89-0147 entitled HIGH-RESOLUTION MICROWAVE OBSERVATIONS OF SOLAR ACTIVITY. This report covers the period from 01 November 1988 to 30 April 1992. It contains the abstracts for twenty four (24) presentations at professional meetings (Section II); the abstracts for twenty one (21) successful proposals to use the Very Large Array (VLA) or the Arecibo Observatory for studies of flares, or eruptions, on the Sun or other nearby stars (Section III); and reprints of seventeen (17) papers (Section IV).

The twenty four (24) professional presentations included meetings of the American Astronomical Society (AAS), the American Geophysical Union (AGU), the Committee on Space Research (COSPAR), the International Astronomical Union (IAU), and the Union Radio Scientifique International (URSI). The Very Large Array (VLA) and the Arecibo Observatory are the world's largest radio telescopes, each operated at enormous expense by the National Science Foundation (NSF); the twenty one (21) successful proposals with these facilities, totalling fifty one (51) days, therefore represent an extremely efficient method of carrying out research by the Air Force Office

20. DISTRIBUTION / AVAILABILITY OF ABSTRACT: ☑ UNCLASSIFIED/UNLIMITED ☐ SAME AS RPT. ☐ DTIC USERS	21. ABSTRACT SECURITY CLASSIFICATION
22a. NAME OF RESPONSIBLE INDIVIDUAL: Dr. Henry R. Radoski	22b. TELEPHONE (Include Area Code): (202) 767-5021; 22c. OFFICE SYMBOL: NL

DD FORM 1473, 84 MAR — 83 APR edition may be used until exhausted. All other editions are obsolete. — SECURITY CLASSIFICATION OF THIS PAGE

9 MAR 1992

of Scientific Research (AFOSR) that essentially funds salaries for Tufts scientists who use these facilities, analyze the data, and publish the results.

The seventeen (17) papers have been published in the *Astrophysical Journal, the Astrophysical Journal (Letters), Astronomy and Astrophysics, Proceedings of Colloquia and Symposia of the International Astronomical Union (IAU), and Advances in Space Research - Proceedings of the Committee on Space Research (COSPAR).* This has therefore been an extraordinarily productive program, with a publication in the most reputable journals every two months for more than three years.

We have obtained fundamental new insights to the origin and prediction of explosive bursts, or flares, on the Sun that can directly interfere with high-flying aircraft or disrupt communications with them; the wide-ranging implications of these results warrent continued funding for further investigations using the VLA and solar satellites. The VLA results given here indicate, for example, that the magnetic interaction of coronal loops triggers solar flares, and that the preflare, impulsive and decay phases of flares occur in spatially separate, but nearby, coronal loops. They therefore indicate that patrol observations of the underlying photosphere and chromosphere may not lead to reliable flare prediction alone, and that they also discount theoretical flare models involving single coronal loops.

Our research plan has maximized scientific return by combining Very Large Array (VLA) observations with simultaneous observations from the ground (radio spectra or high time resolution) or space (X-ray or γ-ray satellites). This has further extended the advanced, cost-effective manner of carrying out research at the very forefront of current solar physics.

The seventeen (17) published papers include the following key findings:

1. The first detection of quiescent filaments in emission at radio wavelengths, demonstrating the existence of a transition sheath that acts as an interface between the cool Hα filaments and the hot surrounding corona.
2. The discovery of narrow-band radio emission from flare stars, indicating the need for a coherent radiation mechanism.
3. The observation of large-scale, previously-invisible magnetic loops that connect widely-separated active regions and act as magnetic conduits for the triggering of flares, or eruptions, at remote regions on the Sun.
4. The first observations of coronal loops at radio wavelengths; these ubiquitous features, that dominate the structure of the solar corona, had previously only been detected using X-ray observations from space.
5. Noise storms have been resolved for the first time; they originate in large-scale magnetic loops that connect active regions to more distant regions on the Sun.
6. Impulsive stellar flares exhibit rapid variations, lasting 100 milliseconds or less, that require radio sources that are smaller than the star in size and high brightness temperatures $T_B \geq 10^{15}$ K that require coherent plasma radiation or coherent electron-cyclotron masers.
7. Solar flares, or eruptions, appear to be triggered by the magnetic interaction of coronal loops; the preflare, impulsive and decay phases of flares occur in spatially separate, but nearby, coronal loops.
8. Feedback mechanisms between high-lying coronal loops and lower ones may relate noise storms, solar flares, and coronal mass ejections. Coronal loops may also interact magnetically over large scales comparable to a solar radius in size.
9. The three-dimensional structures of solar active regions can be determined from multiple-wavelength observations at radio and X-ray wavelengths and magnetic extrapolations from magnetograms; such investigations of the global structure of solar active regions will provide the evolutionary signatures needed to fully understand solar flares.

The last Section V notes that we have expended all of the funds for the three-year grant AFOSR-89-0147 to complete all of the proposed research. Here we also mention an unsolicited three-year proposal for AFOSR support beginning in Fiscal Year (FY) 1993; the proposed research will build upon our fundamental results and existing unanalyzed data as well as future investigations with the world's best telescopes and satellites at a cost-effective funding level of $100,000 per year.

FINAL TECHNICAL REPORT

FOR

GRANT AFOSR-89-0147

HIGH RESOLUTION MICROWAVE OBSERVATIONS OF SOLAR ACTIVITY

during the period

01 November 1989 to 30 April 1992

Date of Submission: 28 February 1992

Kenneth R. Lang
Principal Investigator
Grant AFOSR-89-0147
Professor of Astronomy
Department of Physics of Astronomy
Robinson Hall
Tufts University
Medford, MA 02155

TABLE OF CONTENTS

PAGE

III. SUCCESSFUL PROPOSALS FOR SOLAR OBSERVATIONS WITH THE VERY LARGE ARRAY (VLA) FROM 1988 to 1991 INCLUSIVE

IV. PUBLISHED PAPERS FROM 1988 to 1991 INCLUSIVE

PAGE

PAGE

I. INTRODUCTION

This final technical report for grant AFOSR-89-0147 covers the period from 01 November 1988 to 30 April 1992. Section II contains the abstracts for twenty four (24) presentations at professional meetings, including those of the American Astronomical Society (AAS), the American Geophysical Union (AGU), the Committee on Space Research (COSPAR), the International Astronomical Union (IAU), and the Union Radio Scientifique International (URSI). These presentations, as well as the subsequent publications (Section IV), have provided new insights to the origin and prediction of explosive bursts, or flares, that can directly interfere with high-flying aircraft or disrupt communications with them. Our Very Large Array (VLA) results at 20 cm wavelength indicate, for example, that preflare heating in coronal loops and the magnetic interaction of coronal loops can trigger the explosive release of stored magnetic energy near the apex of coronal loops, and that the preflare, impulsive and decay phases of solar flares occur in spatially separate, but nearby, coronal loops. They therefore show that previous observations of the underlying solar chromosphere or photosphere will not provide the key predictive element for solar flares; although magnetic shear in the photosphere may be a necessary ingredient for solar flares, most sheared regions do not flare and a change in the photospheric configuration has never been detected during a solar flare. Our results also discount a major theoretical effort that attempted to explain solar flares in terms of instabilities within isolated coronal loops that do not interact with neighboring ones.

Section III contains the abstracts for twenty one (21) successful proposals to use the Very Large Array (VLA) or the Arecibo Observatory for studies of flares, or eruptions, on the Sun or nearby flare stars. Our general approach has been to utilize the unique high-angular-resolution capability of the VLA while enhancing its scientific return with simultaneous observations at other electromagnetic regions from both the ground and space. Our successful proposals therefore include collaborative observations with the French Nancay radio telescope for high time resolution; with the Swiss PHOENIX radio telescope for simultaneous spectra and motions of flares; with the Solar Maximum Mission (SMM) and Yohkoh satellites for flare diagnostics and images at X-ray wavelengths; and with the Gamma Ray Observatory (GRO) satellite for simultaneous gamma-ray observations of solar flares. This has therefore been one of the most advanced and cost-effective programs of solar research ever sponsored by the Air Force Office of Scientific Research (AFOSR). The world's largest radio telescope, the VLA, has been operated at enormous expense by the National Science Foundation (NSF) to carry out AFOSR investigations of solar flares, as have three billion-dollar satellites funded by NASA.

The important scientific results of research carried out under grant AFOSR-89-0147 can be found in Section IV that contains reprints of seventeen (17) papers published in the most reputable journals including the *Astrophysical Journal, the Astrophysical Journal (Letters), Astronomy and Astrophysics, Proceedings of Colloquia and Symposia of the International Astronomical Union (IAU), and Advances in Space Research - Proceedings of the Committee on Space Research (COSPAR).* The key published findings, in the order reproduced here, are:

1. The first detection of quiescent filaments in emission at radio wavelengths, demon-

strating the existence of a transition sheath that acts as an interface between the cool Hα filaments and hot surrounding corona.

2. The discovery of narrow-band radio emission from flare stars, indicating the need for a coherent radiation mechanism.

3. The observation of large-scale, previously-invisible magnetic loops that connect widely-separated active regions and act as magnetic conduits for the triggering of flares, or eruptions, at remote regions on the Sun.

4. The first observations of coronal loops at radio wavelengths; these ubiquitous features that dominate the structure of the the solar corona had previously only been detected using X-ray observations from space.

5. Noise storms have been resolved for the first time; they originate in large-scale magnetic loops that connect active regions to more distant regions on the Sun.

6. Impulsive stellar flares exhibit rapid variations, lasting 100 milliseconds or less, that require radio sources that are smaller than the star in size and high brightness temperatures of $T_B \geq 10^{15}$ K that require coherent plasma radiation or coherent electron masers.

7. Solar flares, or eruptions, appear to be triggered by the magnetic interaction of coronal loops; the preflare, impulsive and decay phases of flares occur in spatially separate, but nearby, coronal loops.

8. Feedback mechanisms between high-lying coronal loops and lower ones may relate noise storms, solar flares, and coronal mass ejections. Coronal loops may also interact magnetically over large scales comparable to a solar radius in size.

9. The three-dimensional structures of solar active regions can be determined from multiple-wavelength observations at radio and X-ray wavelengths and magnetic extrapolations from magnetograms. Such investigations of the global *structure* of solar active regions provide the evolutionary signatures needed to fully understand solar flares.

The last Section V notes that we have expended all of the funds for the three-year grant AFOSR-89-0147 to complete all of the proposed research. Here we also mention our future research plans to continue studies of solar flares, or eruptions, using existing and future observations with the Very Large Array (VLA), as well as the Yohkoh and Gamma Ray Observatory (GRO) satellites. An unsolicited proposal for a three-year program beginning in Fiscal Year (FY) 1993 will soon be submitted to the Air Force Office of Scientific Research (AFOSR). The fundamental new results given in this final technical report, combined with a full realization of their wide-ranging implications and the cost-effective use of the world's best solar telescopes and satellites should encourage future AFOSR funding at the $100,000 yearly level.

II. PAPERS PRESENTED AT PROFESSIONAL MEETINGS FROM 1988 to 1991 INCLUSIVE

A. Workshop on the Solar Interior and Atmosphere
Held in Tucson, Arizona on 15 to 18 November, 1988

VLA NANCAY OBSERVATIONS OF THE SOLAR CORONA

Kenneth R. Lang

ABSTRACT:

The temperature and magnetic structures of coronal loops are determined by Very Large Array (VLA) observations at 20 cm wavelength. Comparisons of VLA 20 cm images with soft X-ray data taken with the Solar Maximum Mission (SMM) satellite indicate that coronal loops have different temperatures and radiation mechanisms that can only be detected by observations in both spectral domains. The 20 cm data show evidence for preflare heating and magnetic interaction that apparently trigger the explosive release of energy near the tops of coronal loops. Large-scale magnetic structures are detected with new 90 cm instrumentation. The extended 90 cm emission is sometimes associated with filaments; other elongated structures have no well-defined optical counterpart. Equatorial and polar holes are also detected. The Nancay radiohelioograph is used as a time filter (temporal resolution up to 20 milliseconds) for the VLA 90 cm data, enabling us to distinguish explosive bursts, groups of bursts, and the the background continuum. Noise storms have been resolved for the first time; they originate in large magnetic loops that connect active regions with more distant regions on the Sun. Successive polarized noise storm bursts (Type I) are emitted by the same source, but they are occasionally interspersed with unpolarized bursts that originate in a different nearby source. The combined data will permit the spatial (VLA) and temporal (Nancay) resolution of a wide variety of explosive phenomena in the corona, including Type I, II and III bursts as well as the presently-unknown initiating source of coronal mass ejections.

B. National Research Council, Union Radio Scientifique International (URSI)
Meeting
Held in Boulder, Colorado on 4 to 6 January 1989
Commission J. Solar and Stellar Radio Bursts.

VLA OBSERVATIONS OF SOLAR AND STELLAR RADIO BURSTS

Kenneth R. Lang and Robert F. Willson

ABSTRACT:

Very Large Array (VLA) observations at 20 cm wavelength specify the temperature and magnetic structure of coronal loops within solar active regions. Snapshot maps at intervals as short as 3 seconds indicate that explosive radio bursts originate at the apex of these loops, and that the bursts may be triggered by preburst heating within coronal loops or magnetic interaction between the loops.

VLA observations at 90 cm wavelength specify closed and open magnetic structures in the low solar corona. Large-scale magnetic loops are often associated with filaments or coronal streamers rather than active regions. Type I radio bursts, that occur during solar noise storms, originate near the apex of large-scale magnetic loops that connect active regions with more distant regions on the solar surface. Successive Type I bursts can originate in the widely-spaced legs of magnetic loops. The large-scale 90 cm loops may interact with the smaller-scale 20 cm ones, giving rise to solar bursts within an underlying active region. similar VLA observations will provide new insights to the unknown initiating source of coronal mass ejections observed by satellite coronagraphs.

VLA observations of dwarf M flare stars indicate narrow-band emission (for YZ CMi), while Arecibo observations indicate rapid variations, small source sizes and high brightness temperatures ($T_B \geq 10^{12}$ K for AD Leo and EQ Peg). Coherent radiation mechanisms are required, placing constraints on the stellar magnetic fields and coronal electron densities. We have not detected evidence

for frequency drifts during radio bursts on stars other than the Sun, suggesting that electron beams and shock waves may not play a dominant role in the radio bursts from dwarf M flare stars.

C. The 173rd Meeting of the American Astronomical Society (AAS)
Held in Boston, Massachusetts on 9 to 13 January 1989

VLA OBSERVATIONS OF CORONAL LOOPS, FILAMENTS AND STREAMERS

Kenneth R. Lang and Robert F. Willson

ABSTRACT:

Very Large Array (VLA) observations at 20 cm wavelength specify the temperature and magnetic structure of small-scale coronal loops within solar active regions. VLA observations at 90 cm wavelength specify large-scale closed and open magnetic structures. Large-scale magnetic loops are often associated with filaments or coronal streamers rather than active regions. The large-scale 90 cm loops may interact with the smaller-scale 20 cm ones, giving rise to solar bursts within an underlying active region.

D. The 173rd Meeting of the American Astronomical Society (AAS)

VLA OBSERVATIONS OF SOLAR RADIO BURSTS

Robert F. Willson and Kenneth R. Lang

ABSTRACT:

Very Large Array (VLA) snapshot maps at intervals as short as 3 seconds indicate that explosive radio bursts originate at the apex of coronal loops (20 cm), and that the bursts may be triggered by preburst heating within coronal loops or magnetic interaction between the loops. Type I radio bursts that occur during solar noise storms, originate near the apex of large-scale magnetic loops (90 cm) that connect active regions with more distant regions on the solar surface. Successive components of other 90 cm bursts originate in the widely separated legs of magnetic loops.

E. American Geophysical Union (AGU) Meeting
Held in Baltimore, Maryland on 7 to 12 May 1989
Solar-Planetary Relations: Solar and Heliospheric Physics.

VLA OBSERVATIONS OF FLARING CORONAL LOOPS.

Kenneth R. Lang, Robert F. Willson and Spiro K. Antiochos

ABSTRACT:

Very Large Array studies of flaring coronal loops indicate that different loops are responsible for preflare, impulsive and postflare activity. Preflare activity in the low solar corona is indicated by the enhancement of 90 cm continuum emission before an impulsive 20 cm burst and a 90 cm noise storm. For this 20 cm burst, the impulsive and decay phases also appear to be located in different sets of loops. Our observations indicate that the size of the impulsive emission rapidly increases with wavelength even though the radio wavelength profiles correlate with hard X-rays. Global studies of large-scale magnetic fields using full-disk 90 cm observations show that primary bursts can trigger secondary ones through otherwise invisible magnetic loops.

F. Nineteenth Meeting of the American Astronomical Society (AAS)
Solar Physics Division
Held in Laurel, Maryland, Johns Hopkins University, Applied Physics Laboratory on 5 to 8 June 1989.
Max 91 Workshop No. 2.

VLA - MAX 91 TESTS OF HIGH ENERGY FLARE PHYSICS

ABSTRACT:

The potential for VLA contributions during the coming maximum in solar activity is illustrated by observations of solar flares on 15 May, 28 May, 8 June, 24 June and 30 September 1988. Here we focus on the high spatial resolution and multiple-wavelength capabilities of the VLA, while also discussing its limitations that can be overcome with simultaneous observations in other spectral domains. The five sets of observations provide evidence for: correlated bursts from widely-separated active regions connected by large-scale coronal loops; spatially separated radio sources during the precursor, impulsive and post-burst phases suggesting successive activation of different coronal loops; and tests of theoretical models of microwave burst emission.

G. Nineteenth Meeting of the American Astronomical Society (AAS) Meeting
Solar Physics Division
Held in Laurel, Maryland, Johns Hopkins University, Applied Physics Laboratory, on 5 to 8 June 1989

MULTIPLE-WAVELENGTH SMM-VLA OBSERVATIONS OF AN M2 CLASS X-RAY FLARE
Robert F. Willson, Kenneth R. Lang and Joan T. Schmelz.

ABSTRACT:

Light curves and spectra of Ca XIX and Fe XXV from the Bent Crystal Spectrometer are compared with simultaneous VLA images at 2, 3.6 and 6 cm wavelength during an M2-class X-ray flare. These observations were part of the International Solar Month in September 1988. These data are also compared with hard X-ray observations from HXRBS, microwave spectra from the Air Force Solar Radio Patrol stations, and Hα images and magnetograms obtained by the SOON and Kitt Peak Observatories. The sizes and brightness temperatures of the microwave sources are compared with those predicted by multithermal and nonthermal models in which the magnetic field strength and temperature are allowed to vary throughout the source. The preburst and postburst structure of the X-ray and microwave emitting plasma are also discussed.

H. International Astronomical Union (IAU)
Colloquium No. 117, Dynamics of Prominences
Held in Hvar, Yugoslavia on 25 to 29 September 1989

RADIO EMISSION FROM QUIESCENT FILAMENTS

Kenneth R. Lang

ABSTRACT:

Full-disk VLA synthesis maps of the quiet Sun indicate that filaments can be seen in emission at 91.6 cm wavelength; they are detected in absorption at shorter microwave wavelengths. The 91.6 cm emission has a brightness temperature of $T_B = 3 \times 10^5$ K. It is hotter, wider and longer than the underlying filament detected at Hα wavelengths, but the similarity between the shape, position, elongation and orientation of the radio and optical features suggests their close association. The 91.6 cm emission is attributed to the thermal bremsstrahlung of a hot transition sheath that envelops the Hα filament and acts as an interface between the cool, dense Hα filament and the hotter, rarefied corona. The transition sheath is seen in emission because of the lower optical depth of the corona at 90 cm, and the width of this sheath is $\approx 10^4$ km. A power law gradient in pressure provides a better match to the observations than a constant pressure model; definitive tests of theoretical models await simultaneous multi-wavelength studies of filaments at different observing angles. When the thermal bremsstrahlung is optically thin, the magnetic field strength in the transition sheath can be inferred from the observed circular polarization. Variable physical parameters of the sheath, such as width, electron density, and electron temperature, can explain controversial reports of the detection of, or the failure to detect, the meter-wavelength counterpart of Hα filaments.

I. International Astronomical Union (IAU)
Symposium No. 137, Flare Stars
Held in Byurakan, Armenia on 23 to 27 October 1989

FLARE STARS AT RADIO WAVELENGTHS

Kenneth R. Lang

ABSTRACT:

The radio emission from dMe flare stars is discussed using Very Large Array and Arecibo observations as examples. Active flare stars emit weak, unpolarized, quiescent radio radiation that may be always present. Although thermal bremsstrahlung and/or gyroresonance radiation account for the slowly-varying, quiescent radio radiation of solar active regions, these processes cannot account for the long-wavelength quiescent radiation observed from nearby dMe flare stars. It has been attributed to nonthermal gyrosynchrotron radiation, but some as yet unexplained mechanism must be continually producing the energetic electrons. Long-duration (hours), narrow-band ($\Delta\nu \leq 0.1$) radiation is also emitted from some nearby dMe stars at 20 cm wavelength. Such radiation may be attributed to coherent plasma radiation or to coherent electron-cyclotron masers. Impulsive stellar flares exhibit rapid variations ($\leq$100 msec) that require radio sources that are smaller than the star in size, and high brightness temperatures $T_B \geq 10^{15}$ K that are also explained by coherent radiation processes. Quasi-periodic temporal fluctuations suggest pulsations during some radio flares. Evidence for frequency structure and positive or negative frequency drifts during radio flares from dMe stars is also presented.

J. International Astronomical Union (IAU)
Symposium No. 142. Basic Plasma Processes on the Sun
Held in Bangalore, India on 1 to 5 December 1989

VLA OBSERVATIONS OF THE CORONAL PLASMA

Kenneth R. Lang

ABSTRACT:

VLA observations at 20 cm wavelength specify the brightness temperature and magnetic field structure of plasma constrained within coronal loops in solar active regions. Comparisons with simultaneous SMM observations at soft X-ray wavelengths lead to measurements of physical parameters like electron density, electron temperature and magnetic field strength. Such comparisons also indicate coronal loops can be detected at either radio or X-ray wavelengths while remaining invisible in the other spectral domain, and that the dominant radiation mechanisms can be thermal bremsstrahlung or thermal gyroresonance radiation. VLA observations at the longer 90 cm wavelength reveal the thermal emission of a hot transition sheath enveloping a cooler, underlying Hα filament seen in absorption. The 20 cm VLA observations indicate that the precursor, impulsive and post-flare components of solar flares originate in spatially separated and resolved sources. The 90 cm VLA data indicate that time-correlated radio bursts can occur in active regions on opposite sides of the solar equator. These regions are apparently linked by large-scale, trans-equatorial magnetic loops at least 2.6×10^5 km (or 6') long; these loops act as magnetic conduits for relativistic electrons moving at one-third the velocity of light.

K. Twentieth Meeting of the American Astronomical Society (AAS) Solar Physics Division
Held in Albuquerque, New Mexico on 10 to 14 June 1990

VLA OBSERVATIONS OF MULTIPLY-IMPULSIVE SOLAR BURSTS AT 20 AND 90 cm WAVELENGTH

Robert F. Willson

ABSTRACT:

The VLA has been used to map the structure of two multiply-impulsive bursts simultaneously at 20 and 90 cm wavelength. For one of these bursts, the 20 cm emission was well-correlated with that at hard X-ray wavelengths; we have spatially resolved the different components of its radio time profile, including a weak precursor and several subsequent impulsive peaks. The 90 cm burst emission occurred both before and during the 20 cm burst and was located above it at $\approx 1.2 R_\odot$. The other 20 cm burst was resolved into an extended ($\theta \approx 40$") and an unresolved ($\theta \leq 10$") source. There was no hard or soft X-ray emission detected during this event. The associated 90 cm emission occurred about 40 seconds later, apparently in a large-scale ($\theta \approx$ 5') loop joining the 20 cm active region to another one. Spectral data have been analyzed for both bursts in order to determine the relevant emission mechanisms.

L. The XXVIII Meeting of the Committee on Space Research (COSPAR).
Symposium S.9 Space Observations of the Solar Corona and the Origin of the Solar Wind.
Held at the Hague, Netherlands on 27 to 29 June 1990.

VLA OBSERVATIONS OF THE INNER CORONA

Kenneth R. Lang

ABSTRACT:

We discuss simultaneous Very Large Array (VLA) and Solar Maximum Mission (SMM) observations which have been used to provide estimates of the electron density, electron temperature and magnetic field strength in coronal loops above active regions. These data indicate that coronal loops can be detected at either radio or X-ray wavelengths while remaining invisible in the other spectral domain. We also discuss VLA observations at the longer 90 cm wavelength that reveal the thermal emission from a hot transition sheath enveloping a cooler, underlying Hα filament seen in absorption. The 90 cm VLA data also indicate that time-correlated radio bursts can occur in widely-separated active regions. These regions appear to be connected by large-scale magnetic loops that act as magnetic conduits for relativistic electrons moving at one-third the velocity of light.

M. The XXVIII Meeting of the Committee on Space Research (COSPAR). Solar- Terrestrial Physics (STP) Session I.2. The Sun-Transient Phenomena
Held at the Hague, Netherlands on 25 June to 30 June 1990.

VLA RESOLUTION OF THE PREFLARE, IMPULSIVE AND POSTFLARE STATES

Kenneth R. Lang

ABSTRACT:

VLA snapshot maps at 3-second intervals show that the precursor, impulsive and decay phases of 20.7 cm flares originate in spatially-separated sources, suggesting successive activation in different coronal loops. Interacting coronal loops apparently trigger the impulsive release of stored magnetic energy and the coronal magnetic configuration then relaxes to a new stable state during the decay phase. The 20.7 cm precursor source is ascribed to thermal gyroresonance emission from coronal loops with typical magnetic field strengths of up to 270 G; this emission is associated with heating and exhibits no detectable hard X-ray emission above 30 keV. The impulsive 20.7 cm source and the hard X-ray emission are attributed to nonthermal electrons in the coronal and chromospheric

portions of a magnetic loop.

N. International Astronomical Union (IAU) Symposium No. 142.
Basic Plasma Processes on the Sun
Held in Bangalore, India on 1 to 5 December 1990

VLA-PHOENIX OBSERVATIONS OF A NARROW-BAND DECIMETRIC BURST

Robert F. Willson and Arnold O. Benz

ABSTRACT:

We discuss observations of a highly-circularly polarized multiply-impulsive microwave burst detected by the Very Large Array and the Phoenix Digital Radio Spectrometer. The VLA was used to resolve the burst in two dimensions, while Phoenix provided high time resolution information about its spectral properties. During part of the burst, positive frequency drifts were detected, suggesting inwardly-propagating beams of electrons emitting Type III-like radiation.

O. The XXVIII Meeting of the Committee on Space Research (COSPAR). Symposium S.9. Space Observations of the Solar Corona and the Origin of the Solar Wind.
Held at the Hague, Netherlands on 27 to 29 June, 1990

MULTIPLE WAVELENGTH RADIO OBSERVATIONS OF MASS EJECTIONS IN THE SOLAR CORONA

J.P. Raulin, A. Kerdraon, K.L. Klein, G. Trottet, Robert F. Willson and Kenneth R. Lang

ABSTRACT:

1988 June 8: Noise storm enhancement
(No associated Hα or microwave burst)

The radio emission (dm-to-m-λ) shows the brightening of a single source (at a site remote from a pre-existing noise storm). This emission is due to nonthermal electrons (brightness temperature $\geq 10^8$ K, circular polarization $\geq$50%). At λ=21 cm and in soft X-rays the evolution of the thermal plasma in the low corona is observed.

The nonthermal emission in the middle corona is preceded by the appearance of a new source in the low corona (heating or density increase).
The time delay between the appearance of this source and the onset of the dm-to-m-λ emission, together with the observed source motion at dm-to-m-λ, suggesting triggering of the noise storm enhancement by an outwardly propagating disturbance ($v = 200$ km sec$^{-1} \approx c_s$).

The similar evolution of the noise storm enhancement at different wavelengths shows that energy is fed continually to the nonthermal electron population during the event. Provided the soft X-ray emission comes from the same active region, its similar duration to the noise storm enhancement suggests a close link between the heating of the soft X-ray source and particle acceleration.

1989 June 20: Moving Type IV Burst
(associated with 3B and SF flares and expanding loops in Hα).

The radio sources in the corona overly a complex of intense activity in Hα, showing a large loop expanding into the corona after a filament eruption. Outward moving cold material is also seen in millimeter waves. The whole event is accompanied by a soft X-ray burst (X1.6). The long duration of the moving Type IV emission and its association with energetic processes in the low atmosphere indicate the continual input of energy into supra-thermal electrons during the whole event. The observations appear to be inconsistent with a model where the electrons are accelerated by a shock wave (resulting from the impulsive flare) during its outward motion through the corona.

P. Twentieth Meeting of the American Astronomical Society (AAS) Solar Physics Division
Held in Albuquerque, New Mexico on 10 to 14 June 1990

A SEARCH FOR THE 154-DAY PERIODICITY IN THE OCCURRENCE RATE OF SOLAR FLARES IN THE EARLY YEARS OF CYCLE 22.

James N. Kile and Edward W. Cliver

We have examined Ottawa 2.8 GHz burst data ($\geq$ 50 sfu) and GOES 1-8 A soft X-ray burst data ($\geq$ M2.5) for evidence of the 154-day periodicity in flare activity during the early years (September, 1986 - February 1990) of cycle 22. Evidence for the 154-day periodicity, significant at the $\leq$ 1% level, was found in both of these data sets for the cycle 21 interval from February, 1980 - September, 1983 in which the periodicity was first detected. Using the Scargle periodogram technique with the significance test of Horne and Baliunias, we find no evidence, as of yet, for a recurrence of the 154-day periodicity during the current 22^{nd} solar cycle.

Q. Twentieth Meeting of the American Astronomical Society (AAS) Solar Physics Division.
Held in Albuquerque, New Mexico on 10 to 14 June 1990

COMSTOC IV. INTERPRETATION OF MULTIWAVELENGTH OBSERVATIONS OF A SUNSPOT AND PLAGE

Jeffrey W. Brosius, Gordon D. Holman, Robert F. Willson, and Joan T. Schmelz

Simultaneous observations of an active region located near disk center were obtained with the Very Large Array (VLA), the Solar Maximum Mission X-Ray Polychromator (SMM/XRP), and the Beijing magnetograph on 18 December 1987, during the Coronal Magnetic Structures Observing Campaign (CoMStOC). The active region contained a sunspot with longitudinal photospheric fields up to 2500 G, and a nearby area of plage. The microwave observations were made at a series of four closely-spaced frequencies within each of the 6 and 20 cm wavebands. The 6 cm emission is closely associated with the sunspot, with loops connecting the sunspot and nearby regions of opposite polarity, and with the plage. Using the systematic shift in the location of the intensity peak in each of the wavelengths in the 20 cm waveband, we calculate magnetic field strength as a function of height in the loops near the sunspot. In the plage, where the X-ray fluxes are sufficiently high that line flux ratios can be used to determine the plasma temperature and column emission measure, we calculate theoretical 20 cm radio maps based on the assumption that thermal bremsstrahlung is the only contributing emission mechanism. A comparison of these theoretical maps with the observed maps enables us to determine the contribution from thermal gyroemission, and hence to determine the magnetic field in the plage. These results are compared with potential field extrapolations of the Beijing magnetogram using a code developed by T. Sakurai.

R. Twentieth Meeting of the American Astronomical Society (AAS)
Held in Albuquerque, New Mexico on 10 - 14 June, 1990

VLA OBSERVATIONS OF MULTIPLY-IMPULSIVE SOLAR BURSTS AT 20 AND 91 cm WAVELENGTH

Robert F. Willson

The VLA has been used to map the structure of two multiply impulsive bursts simultaneously at 20 and 90 cm wavelength. For one of these bursts, the 20 cm emission was well-correlated with that at hard X-ray wavelengths; we have spatially resolved the different components of its radio time profile, including a weak precursor and several subsequent impulsive peaks. The 90 cm burst emission occurred both before and during the 20 cm burst and was located above it at $\approx 1 R_{\odot}$. The other 20 cm burst was resolved into an extended and an unresolved source. There was no hard or soft X-ray emission during this event. The associated 90 cm emission occurred about 40 seconds later, apparently in a large-scale ($\theta \approx 5'$) loop joining the 20 cm active region to another one. In both cases the gradual 20 cm burst emission was spatially separated ($\theta \approx 1'$-$4'$) from the impulsive source, suggesting magnetic interaction of coronal loops over large ($L \approx 4.3$-17.5×10^9 cm) distances.

Microwave spectral data have also been analyzed for both bursts in order to determine the relevant emission mechanisms.

S. International Scientific Working Group Meeting for the Solar A Satellite
Held in Tokyo, Japan on 21 to 27 October, 1990

VLA SUPPORTING OBSERVATIONS FOR SOLAR A

Kenneth R. Lang

High resolution, three second VLA snapshot maps at 20 cm wavelength can be used to resolve coronal loops within individual active regions and thereby reveal the coronal magnetic interaction that can trigger solar flares. These VLA maps can complement simultaneous SXT SOLAR A observations. Simultaneous VLA and Solar A observations can extend and amplify VLA results that resolve the preflare, impulsive and postflare stages of solar flares into nearby, but spatially-separated, sources. If this result is confirmed and found to be usually applicable, it will rule out extensive previous theoretical work that confines all aspects of flare activity to a single coronal loop or arcade of loops. VLA synthesis maps at 91.6 cm wavelength indicate that widely-separated active regions are apparently linked by large-scale, transequatorial loops 100 thousand to a million kilometers long. Three second VLA snapshot maps at this wavelength suggest that energetic electrons accelerated during a radio burst in one active region can move within these global magnetic conduits at nearly the velocity of light, thereby triggering bursts along the large-scale loops in other distant active regions. The SXT aboard SOLAR-A should routinely observe the entire Sun to sample these global magnetic structures. SXT or HXT SOLAR-A observation with limited field of view within an individual active region should be compared with simultaneous, global three-second VLA snapshot maps. Such VLA observations can connect the localized satellite observations with related activity in widely-separated active regions that are outside the satellite's field of view.

T. The 177th Meeting of the American Astronomical Society (AAS)
Held in Philadelphia, Pennsylvania on 14 - 19 January, 1991

VLA-PHOENIX OBSERVATIONS OF CORONAL ACTIVITY

Robert F. Willson, Kenneth R. Lang and Arnold O. Benz

The Very Large Array and the PHOENIX Digital Radio Spectrometer were used to observe solar active regions at 20 and 91 cm wavelength on three consecutive days in July 1990. The high spatial resolution of the VLA was used to resolve different components of solar noise storms, decimetric bursts and Type III bursts, while the high temporal and spectral resolution of the PHOENIX provided measurements of the drift rate and bandwidth of these events. The structure of one intense burst, associated with an M3-class soft X-ray event, showed striking variations in time, frequency and space, suggesting complex motions and interactions of coronal structures at different locations above the flaring active region. The results of correlative studies with other flare-related and slowly-varying phenomena, such as Hα brightenings, filament eruptions and magnetic field changes are also discussed.

U. Twenty-first Meeting of the American Astronomical Society (AAS)
Solar Physics Division
Held in Huntsville, Alabama on April 12, 1991

VLA OBSERVATIONS DURING THE ESP MAX 91 CAMPAIGN

By Robert F. Willson and Kenneth R. Lang

We discuss preliminary results of VLA observations made during the Max 91 Campaign in January 1991. On January 4, active region AR 6432 was observed during an eight hour period at 2, 3.5 and 6.1 cm wavelength. No significant burst activity was detected, but high resolution maps of total intensity and circular polarization were obtained at all three wavelengths. Snapshot maps reveal slowly-varying emission that may be attributed to evolution of magnetic fields in the underlying active region.

On January 11, full-disk 3.3 second images at 20.7 and 91.6 cm were obtained over a six hour period. Several 20.7 cm bursts were detected in association with soft X-ray and Hα flares. Other impulsive, possibly decimetric Type III-like events were observed without obvious X-ray counterparts. Type I noise storm activity at 91.6 cm was observed in association with the most intense 20 cm burst, while groups of isolated bursts were observed at other times from different active regions. Comparisons with simultaneous high time resolution Hα images and OVRO multiwavelength radio data will also be discussed.

V. Paper Presented at the 2nd Gamma Ray Observatory Science Workshop
Held in Annapolis, Maryland on 23-25 September 1991

VLA, PHOENIX AND BATSE OBSERVATIONS OF AN X1 FLARE

By Robert F. Willson, Markus J. Aschwanden and Arnold O. Benz

We present observations of an X1 flare detected simultaneous with the Very Large Array, the PHOENIX Digital Radio Spectrometer and the Burst and Transient Source Experiment (BATSE) aboard the Gamma Ray Observatory (GRO). The VLA was used to produce snapshot maps of the impulsive burst emission on timescales of 1.7 seconds at both 20 and 91 cm. Our results indicate electron acceleration in the higher corona several minutes before the onset of the hard X-ray burst detected by BATSE. Comparisons with high spectral ($\Delta\nu$ = 3 MHz) and temporal (Δt = 40 ms) observations by PHOENIX reveal a variety of radio bursts at 20 cm, such as type III bursts, intermediate drift bursts, and quasi-periodic pulsations during different stages of the X1 flare. From the drift rates of these radio bursts we derive information on local density scale heights, the speed of the radio exciters, and the local magnetic field. Radio emission at 90 cm shows a type IV burst moving outward with a constant velocity of 240 km/sec.

W. Paper Presented at the Tata Institute of Fundamental Research
Poone, India on 5 December 1991

RADIO EMISSION FROM SINGLE STARS - THE SUN

By Kenneth R. Lang

Recent Very Large Array (VLA) observations of the Sun are reviewed. suggesting several potential research topics with the Giant Metre-Wave radio Telescope (GMRT). Quiescent solar radio emission has been fully resolved with the VLA, and related to coronal loops (21 cm), filaments (91 cm) and macrospicules (6 cm). Solar flares are also resolved at 21 cm, showing that the precursor, impulsive and decay phases originate in nearby but spatially separate sources. Large-scale, transequatorial loops (91 cm) act as a magnetic conduit for triggering flares in widely separated active regions. Manned missions to Mars require advance warning of potentially-lethal energetic particles from the Sun; solar flare precursors at radio wavelengths are discussed in this context.

X. Paper Presented at the Tata Institute of Fundamental Research
Poone, India on 6 December 1992

RADIO EMISSION FROM SINGLE STARS - FLARE STARS

Kenneth R. Lang

Perhaps one fourth of the stars in our Galaxy are dMe flare stars that produce energetic outbursts *far more powerful than those on the Sun.* Long-duration, narrow-band radio emission from flare stars is unlike anything observed on the Sun, and requires a coherent radiation mechanism. Rapid temporal variations in the radio emission indicate emitting sizes much smaller than the stars, and brightness temperatures in excess of a million billion (10^{15} K) degrees. Narrow-band and broad band frequency structure is discussed, as are positive and negative frequency drifts of the radio emission from flare stars. We also review recent VLBI observations of these ubiquitous stars.

Y. Paper presented at the Tata Institute of Fundamental Research
Poone, India on 12 December, 1991

RADIO EMISSION FROM INTERACTING BINARY STAR SYSTEMS

Kenneth R. Lang

We review the properties of interacting binary stars such as the RS Canum Venaticorum (RS CVn) stars, cataclysmic binaries, and compact X-ray sources. Rapid rotation of tidally-locked RS CVn stars probably results in enhanced activity at optical, radio and X-ray wavelengths. The two radio stars can be resolved. Radio emission from classical novae is briefly reviewed, while that of galactic powerhouses such as Cygnus X-3 and SS 433 is discussed in greater detail.

III. SUCCESSFUL PROPOSALS FOR SOLAR OBSERVATIONS WITH THE VERY LARGE ARRAY FROM 1988 To 1991 INCLUSIVE

Z. VLA Proposal 7 October 1988

VLA OBSERVATIONS OF CORONAL LOOPS AT 20 cm AND 90 cm WAVELENGTH

Kenneth R. Lang and Robert F. Willson

ABSTRACT:

VLA observations of coronal loops within active regions will be used to specify their temperature and magnetic structure, as well as magnetic reconnection processes that release explosive bursts near the tops of these coronal loops. The physical properties of quiescent active region loops may be inferred from comparisons with simultaneous observations of soft X-ray spectral lines. Simultaneous 90 cm observations will specify large-scale magnetic structures, providing unique information about the initiation mechanisms of coronal mass ejections, solar noise storms and decimetric bursts. The proposed observations may also lead to new insights about coronal holes.

A1. VLA Proposal 7 October 1988

SIMULTANEOUS VLA-NANCAY OBSERVATIONS OF SOLAR RADIO BURSTS

Kenneth R. Lang, Robert F. Willson, Gerard Trottet and Alain Kerdraon

ABSTRACT:

We propose simultaneous observations of solar radio bursts at 90 cm wavelength with the VLA and the Nancay Radioheliograph for the 3 hours of common visibility every 3 days (total of 30 hours). The combined data will provide observations with hitherto-unavailable resolution in space (VLA) and time (NANCAY). Dynamic spectra will also be obtained over a broad frequency range (Nancay) and a relatively narrow one (VLA). We will study the spatial, temporal and spectral properties of Type I and Type III bursts during a period of increased activity in the 11- year solar cycle.

A2. VLA Proposal 20 January 1989

HIGH RESOLUTION VLA-NANCAY OBSERVATIONS OF SOLAR ACTIVITY

Kenneth R. Lang, Robert F. Willson, Gerard Trottet and Alain Kerdraon

ABSTRACT:

We propose simultaneous observations of the Sun at 90 cm wavelength with the VLA and the Nancay radio heliograph during the three hours of common visibility every three days during a three week period in June or July. Solar noise storms and solar radio bursts will be resolved with good angular resolution and high time resolution with the same bandwidth and center frequency. Additional spectral information will be obtained at 20 cm (VLA) and 180 cm (Nancay), and simultaneous $H\alpha$ observations and photospheric magnetograms will be arranged (Meudon and Big Bear). This will continue a study of the spatial, temporal and spectral properties of noise storm continua, Type I bursts and Type III bursts during a period of increasing solar activity.

A3. VLA Proposal 20 January 1989

THE FINAL SMM-VLA COLLABORATION

Kenneth R. Lang and Robert F. Willson

ABSTRACT:

We propose simultaneous VLA and SMM observations of flaring coronal loops during a time of increased solar activity. Coronal loops will be studied on the small scale within individual active regions (VLA: 20 cm; SMM soft and hard X-rays) during the preflare, impulsive and postflare stages, thereby obtaining physical parameters, determining radiation mechanisms and testing theoretical models. VLA observations at 90 cm may detect coronal disturbances related to coronal mass ejections and impulsive flares.

A4. VLA Proposal 30 May 1989

MULTIPLE WAVELENGTH OBSERVATIONS OF THE SOLAR TRANSITION REGION

Kenneth R. Lang and Robert F. Willson

ABSTRACT:

Recent VLA observations of the Sun have shown the presence of compact variable often highly circularly polarized 2 cm sources in regions of weak photospheric fields. The brightness temperatures of $T_B = 10^5$ K suggest that they occur in the transition region or low solar corona. Here we propose multiple wavelength (λ = 1.2, 2 3.5 and 6 cm) observations in order to measure their spectra and to determine their radiation mechanism. Comparisons with simultaneous magnetograms and other optical wavelength images may provide a connection with underlying photospheric structures and allow a test of theoretical models of the transition region and corona.

A5. VLA Proposal 10 October 1989

INTERNATIONAL OBSERVATIONS OF SOLAR ACTIVITY

Kenneth R. Lang, Robert F. Willson, Gerard Trottet, Alain Kerdraon and Arnold O. Benz

We propose simultaneous observations of solar bursts at 20 and 90 cm wavelength with the VLA, the Nancay radioheliograph and the Swiss Digital radio spectrometers PHOENIX and DAEDALUS during the 5 hours of common visibility for a total of 5 days in late April or May. The VLA will provide images with high spatial resolution at 20 and 90 cm, while the Nancay Radioheliograph and PHOENIX will provide high resolution information in both time and frequency at these and other wavelengths, thereby identifying the type of burst the VLA observes. These observations will be compared with ground based optical data to study the spatial and frequency structure of Type I bursts, Type III bursts, noise storms and decimetric bursts and their relationship to other flare related activity such as filament eruptions and coronal mass ejections.

A6. VLA Proposal 10 October 1989

MULTIPLE-WAVELENGTH OBSERVATIONS OF THE X-RAY BINARY STAR LSI + 60°303

Robert F. Willson and Kenneth R. Lang

ABSTRACT:

We propose VLA observations of the X-ray binary star LSI + 61°303 at 3.6, 6.1, 20.7 and 91.6 cm wavelength during a six hour period. These observations are designed to measure short lifetimes (tens of seconds) bursts that can place limits to the burst size and brightness temperature. we will also obtain spectral information which can lead to estimates of the magnetic field strength and lifetime of the energetic particles. These data will be used to constrain models that have been proposed to explain the X-ray and microwave variability of this unusual object.

A7. VLA Proposal 21 November 1989

SURVEY OF NEARBY FLARE STARS AT 2.0, 3.6 AND 6.0 CM WAVELENGTH

Kenneth R. Lang and Robert F. Willson

ABSTRACT:

Nearby dwarf M flare stars have been detected at soft X-ray wavelengths and at long microwave wavelengths (6 cm and 20 cm). One observation with the VLA at 2 cm has been used to develop a model in which the short-wavelength radiation is due to thermal cyclotron radiation of the X-ray emitting plasma, but the longer-wavelength VLA data suggest a different coherent maser radiation mechanism. We propose a VLA survey of bright nearby flare stars at 2.0, 3.6 and 6.0 cm wavelength, in order to test these radiation models. If the thermal cyclotron model is correct, for example, the emission will be more intense at the shorter wavelengths and it should be correlated with the X-ray luminosity.

A8. VLA Proposal 25 January 1990

A VLA SURVEY OF ISOLATED WHITE DWARF STARS WITH MEGA-GAUSS MAGNETIC FIELD STRENGTHS

Kenneth R. Lang, William Leeson and Robert F. Willson

ABSTRACT:

Certain isolated white dwarf stars have intense magnetic fields of up to 10^9 Gauss and hot photospheres of $\geq 10^4$ K. Such stars have detectable radio radiation in spite of their small size, thereby bridging the gap between dwarf M flare stars and pulsars. Detection of this emission could confirm their intense magnetic fields and lead to measurements of their rotation periods. We ask only 10 hours for a preliminary survey of these objects.

A9. VLA PROPOSAL 5 February 1990

LONG-WAVELENGTH, HIGH RESOLUTION OBSERVATIONS OF SOLAR BURSTS IN SPACE, TIME AND FREQUENCY

Kenneth R. Lang, Robert F. Willson, Gerard Trottet, Alain Kerdraon and Arnold Benz

ABSTRACT:

We propose simultaneous observations of the Sun with the VLA, the French Nancay radioheliograph, and the Swiss digital radio spectrometer, PHOENIX, for five days from 13h to 16h UT in June or July. The scientific potential of the proposed observations is demonstrated by past investigations that have spatially resolved various components of solar noise storms and impulsive microwave bursts, while also measuring their outward or inward motions and specifying their spectral characteristics. The B configuration is requested to provide good U-V coverage for the relevant spatial scales at 20 cm and 90 cm. New insights will be obtained for a variety of decimetric bursts that have not yet been spatially resolved.

B1. VLA Proposal 5 February 1990

VLA-RATAN 600 SOLAR MAPS AT THE TIME OF THE JULY 22 SOLAR ECLIPSE

Kenneth R. Lang, Robert F. Willson, George Gelfreikh and Vladimir Bogod

ABSTRACT:

Spectral data with the RATAN 600 at eleven wavelengths between 0.8 and 20.0 cm and during the July 22 solar eclipse will be combined with VLA observations of high angular resolution at 2, 3.6, 6.0 and 20.7 cm to determine radiation mechanisms and coronal magnetic field strengths for the various sources of intense, quiescent solar radiation.

B2. VLA Proposal 5 February 1990

SHORT-WAVELENGTH SURVEY OF NEARBY FLARE STARS

Kenneth R. Lang and Robert F. Willson

ABSTRACT:

Nearby dwarf M flare stars have been detected at soft X-ray wavelengths and at long microwave wavelengths (6 cm and 20 cm). One observation with the VLA at 2 cm has been used to develop a model in which the short-wavelength radiation is due to thermal cyclotron radiation of the X-ray emitting plasma, but the longer-wavelength VLA data suggest a different coherent maser radiation emission mechanism. We propose a VLA survey of 21 bright nearby flare stars at 2.0, 3.6 and 6.0 cm wavelength in order to test these radiation models. If the thermal cyclotron model is correct, for example, the emission will be more intense at shorter wavelengths and it should be correlated with the X-ray luminosity.

B3. VLA Proposal 5 February 1990

VLA INVESTIGATIONS OF NARROW-BAND FEATURES IN SOLAR ACTIVE REGIONS

Kenneth R. Lang and Robert F. Willson

ABSTRACT:

We propose VLA observations of thermal cyclotron lines from the hot, dense plasma trapped within coronal loops, thereby extending our previous VLA result and measuring the geometry and strength of the coronal magnetic field. Angular effects can be determined by observing during two eight-hour periods separated by a few days.

B4. VLA Proposal 28 September 1990

A VLA STUDY OF SOLAR FILAMENTS

Kenneth R. Lang and Robert F. Willson

ABSTRACT:

We propose VLA observations of the Sun at 6, 20 and 90 cm in order to study the quiescent emission from dark Hα filaments. These multi-wavelength data will be used to test theoretical models which specify the temperature and density structure of the transition sheath between the filament and the surrounding corona. Full disk maps at 20 and 90 cm will also allow us to study the global structure and evolution of coronal loops at two different heights, and they may reveal the reorganization or emergence of coronal loops which can trigger flares.

B5. Arecibo Observing Proposal 16 October 1990

DYNAMIC SPECTRA OF MICROWAVE BURSTS FROM ACTIVE STARS

Robert F. Willson, Kenneth R. Lang and John Noto

We propose to use the mini-Gregorian feed at 6 cm and the dual circular polarization feeds at 21 cm with the autocorrelator to detect frequency structure in the burst radiation from six active stars. Detection of such structure will provide important constraints to theoretical models, while also establishing physical parameters such as electron density and magnetic field strengths. Motions of the emitting plasma may be detected as a frequency drift in the emission.

B6. VLA Observing Proposals in November 1990

MAX 91 VLA OBSERVING CAMPAIGN- ENERGETIC SOLAR PHENOMENA

Campaign Leaders: Robert F. Willson and Kenneth R. Lang

This campaign will focus upon Energetic Solar Phenomena (ESP) by providing an outstanding opportunity to explore the realm of high energy X-ray properties of flares with an Antarctic long

duration balloon flight. This MAX '91 campaign shares support of the worldwide FLARES 22 program to observe solar flares.

In 1981, Dr. Robert Lin (Caltech) flew a cooled germanium X-ray spectrometer on a high altitude balloon which returned definitive new information on hard X-ray spectral characteristics of a large flare as well as providing fundamental information on microflares. The flight observing time was less than three hours. Returns of this type of data have not been obtained in the past nine years. The second Max '91 Campaign will be centered upon an improved version of that payload which, under perfect circumstances, could return up to 20 days of uninterrupted X-ray data.

PRIMARY OBJECTIVES:

-To quantify impulsive phase particle energization

-To study relationships between the dynamic evolution of magnetic fields and activity

BASIC OBSERVATIONAL STRATEGY:

Although the balloon spectrometer will record events anywhere on the disk on a continuous basis, the VLA and most other collaborative instruments must be pointed to targeted regions. An ability to respond to changing solar conditions on a daily basis, coupled with strong motivations to provide continuity to the observations of active regions, drives the basic observing philosophy for this campaign. The overall philosophy is to select the most promising of active region (hopefully at Eastern longitudes) at a given time and to stay with that region for a few days so as to provide a continuous coverage of the region's development, activity and evolution. The campaign will follow the target region until a region of obviously greater flare potential or productivity becomes evident. Thus, there will be a tendency to avoid rapid changes of targets in efforts to "chase flares". Rapid changes of targets greatly degrades the continuity of the observations as well as the comprehensive nature of the flare observations that are being pursued.

On a daily basis, target selection and other information will be distributed electronically through the Campaign Action Notices. The Action Notices will be dispatched by electronic means at approximately 2000 UT on any given day and will contain target and other information that will be valid for 24 hours beginning at 1200 UT the following day. These Action Notices will also be distributed via the GEOALERTS (issued at 0330 UT each day and valid beginning at 1200 UT the same day).

Since magnetic coverage is so important in understanding particle transport and in the evolution of regions, regions near the limb will be generally avoided unless a specific objective or active region requires such observations. Measurements of vector and longitudinal magnetic fields from a worldwide complement of instruments are invaluable since they can provide continuity in measuring the magnetic evolution of regions. Such measurements are of fundamental importance to all objectives of the campaign. Note also that it is desirable for magnetic observations to focus on the target region as well as on one, or possibly two, other region(s) of developing interest. Consequently, the Campaign Action Notices may specify secondary targets for instrumentation capable of targeting more than one region.

SCHEDULE:

The launch of the balloon-born spectrometer is a driving factor in determining the dates of this campaign. The intent is to start the campaign with the launch of the balloon. The earliest that the balloon could launch is December 7, but it must launch before late January to assure recovery of the payload. The philosophy of launching balloons in Antarctica is to launch the balloon as soon as conditions allow – not to wait for optimum solar conditions and risk having no launch at all.

Thus the exact launch date and the duration of the campaign will remain uncertain.

An important second factor in scheduling is that several, independent solar radio teams have received a total of 15 days of observing time with the VLA in C and CD configurations over the balloon flight time window. There has been an intentional concentration of VLA days scheduled over the period of time most likely for the balloon to be in the air (Dec. 21 -Jan. 13).

General Schedule: The campaign will begin with the launch of the balloon and will continue for a minimum of 7-10 days. The duration of the campaign will depend upon balloon operations, VLA observing dates, solar activity conditions and inputs from other observatories. The balloon can possibly fly for as long as 20 days; hence, the campaign could last that long but not longer. Scheduled VLA dates that precede or follow the campaign will generally be announced with Max '91 Advisory Notices. Thus VLA target regions will be broadcast to encourage collaborative observations.

THE LONG DURATION ANTARCTIC BALLOON PAYLOAD

The hard x-ray spectrometer (P.I. R. Lin, Caltech) to be flown is a cooled coaxial germanium spectrometer (effective area 50 square centimeters). (Note this is not the Max '91 payload known as HIREGS, but a smaller forerunner of HIREGS which shares some of the same technology.) Flying from Antarctica near the time of solstice, it will observe the sun 24-hours per day. The instrument features a narrow 1 keV energy resolution over its range of 20 keV to 2.5 MeV. This high energy resolution allows accurate measurements of hot "thermal" components as well as high energy non-thermal components of flares. All detected X-ray photons are timed to an accuracy of 50 micro-seconds but the effective time resolution is lower since it depends upon photon statistics. If an observed flare is sufficiently intense, the instrument is capable of returning spectral line information at 511 keV as well as the 2.2 MeV gamma-ray line.

B7. VLA Proposal on 12 February 1991

VLA-PHOENIX-GRO STUDIES OF SOLAR BURSTS

Kenneth R. Lang, Robert F. Willson, Markus J. Aschwanden and Arnold O. Benz

We propose simultaneous observations of solar bursts with the VLA, the PHOENIX Digital Radio Spectrometer and the Gamma Ray Observatory. The Burst and Transient Source Experiment (BATSE) aboard the GRO will provide high time resolution hard X-ray and γ-ray spectra that can be used to study the acceleration of electrons and protons during intense solar flares. VLA observations will yield high spatial resolution images of microwave bursts at 20 and 90 cm, while PHOENIX will provide complementary spectral information that can specify the bandwidth and drift rate. The combined microwave and γ-ray data, together with supporting Hα observations, may help to resolve ongoing controversies over the sites of energetic particle acceleration and the exact acceleration and radiation mechanisms for energetic γ-ray producing electrons.

B8. VLA Proposal on 12 February 1991

VLA-RATAN 600 OBSERVATIONS OF NOISE STORM-PRODUCING ACTIVE REGIONS

Kenneth R. Lang, Robert F. Willson, George Gelfreikh and Vladimir Bogod

We propose collaborative VLA-RATAN 600 observations of the Sun which will be used to explore the relationship between Type I noise storm activity and the evolution of underlying coronal magnetic fields. The VLA will provide high spatial resolution observations of Type I noise storms at 91 cm, while the RATAN will provide wide-band spectral observations of slowly-varying sources at shorter wavelengths. These observations will provide new insights to the three-dimensional structure of coronal magnetic fields and to the mechanisms which transfer energy from active regions to higher-lying noise storm centers.

B9. VLA Proposal 24 May, 1991

VLA-SOLAR A STUDIES OF THE SOLAR CORONA

Robert F. Willson, Kenneth R. Lang and James N. Kile

VLA observations of the Sun at 20 and 91 cm will be compared with simultaneous soft and hard X-ray images obtained by the Japanese Yohkoh satellite. The VLA data will provide information about decimetric bursts produced by energetic electrons in the middle corona, while Yohkoh images will be used to track changes in the morphology and brightness of lower-lying magnetic loops. The combined data will be used to study the morphology, temporal development and physical parameters of flaring loops in both the radio and X-ray domains. They will also be used to investigate the structure of coronal magnetic fields as well as mechanisms which transfer energy from active regions to higher-lying noise storm and Type III burst centers.

C1. VLA Proposal 3 October 1991

HIGH RESOLUTION STUDIES OF SOLAR FLARES WITH THE VLA, THE GRO AND THE SOLAR A SATELLITE

Kenneth R. Lang, Robert F. Willson and James N. Kile.

We propose simultaneous observations of solar flares with the VLA, the Gamma Ray Observatory (GRO) and the Solar A satellite. The instruments aboard the GRO will provide high time resolution hard X-ray and γ-ray spectra that can be used to study the acceleration of electrons and protons during intense solar flares. The soft X-ray telescope on board Solar A will provide high resolution images of active regions during all stages of solar bursts, thereby providing information about energy buildup and release in coronal loops. Our VLA data will complement these observations by providing constraints on source size, location, brightness temperature and polarization at different heights and the combined data will provide new information on particle acceleration and emission mechanisms.

C2. VLA Proposal 3 October 1991

VLA OBSERVATIONS DURING THE COMSTOC '92 CAMPAIGN

Robert F. Willson, Kenneth R. Lang and James N. Kile

We request VLA observations of the Sun during the next Coronal Magnetic Structures Observing Campaign (COMSTOC '92) to be held in May, 1992. VLA observations at 2, 3.5 6 and 20 cm will be compared with soft X-ray images taken by the Solar A satellite, microwave data from the RATAN 600 radiotelescope and photospheric magnetigrams from ground based observatories. These data will be combined with theoretical models to study the thermal and magnetic environment of coronal loops where solar flares occur.

Astron. Astrophys. 199, 325–328 (1988)

ASTRONOMY AND ASTROPHYSICS

C3. High-resolution VLA maps of the quiescent corona at 90 cm wavelength

K.R. Lang [2,*], R.F. Willson [1], and G. Trottet [2]

[1] Department of Physics and Astronomy, Tufts University, Medford, MA 02155, USA
[2] Observatoire de Paris, Section d'Astrophysique de Meudon UA 324, F-92195 Meudon Principal Cedex, France

Received June 15, 1987; accepted February 25, 1988

Summary. We present the first Very Large Array (VLA) synthesis maps of the quiescent corona at 90 cm wavelength and compare them with optical solar features. When the quiet Sun is observed at 90 cm with moderate angular resolution of 100″ to 200″, structures are observed with angular extents, θ, of $\theta = 3'$ to $10'$ and brightness temperatures, T_B, of $T_B \approx 0.5$ to $5.7\ 10^5$ K. Some of these structures are relatively stable over a two-day interval, with positions shifted westward by the amount expected from solar rotation; while others disappear or evolve during this interval. These intense, quiescent 90 cm sources are not associated with active regions; in contrast, simultaneous 20 cm observations reveal coronal loops that are associated with active regions. When the quiet Sun is observed with the VLA at 90 cm wavelength at high angular resolution of 15″ to 30″, compact components are detected with $\theta = 50''$ to 200″ and $T_B = 2.1$ to $4.0\ 10^5$ K. There is no systematic association of any of the 90 cm sources with any optical counterpart, including active regions, filaments, sunspots and the magnetic neutral line in the underlying photosphere. There is no intense 90 cm radiation in the polar regions where $T_B \leqq 0.5\ 10^5$ K, and this apparent depression is at least partly due to coronal holes. We confirm previous meter-wavelength results that indicate that noise storms are the only sources, other than flares, associated with active regions.

Key words: Sun: atmosphere – Sun: corona – Sun: coronal holes – Sun: coronal loops – Sun: magnetic field – Sun: noise storms – Sun: radio radiation

1. Introduction

The radio emission of the quiescent, or non-flaring, corona is dominated by different structures at different wavelengths. The most intense quiescent radiation at 20 cm wavelength is due to a hot, dense plasma trapped within relatively compact coronal loops associated with individual active regions (Kundu and Lang, 1985; Lang et al., 1987a, b). In contrast, the most intense emission of the quiescent corona at meter wavelengths (80 and 160 MHz) is not associated with active regions or with bright regions in the centimeter maps (Sheridan and McLean, 1985). This emission might be associated with relatively large coronal loops or with extended magnetic structures such as coronal streamers.

This paper presents the first VLA images of the quiescent corona at 90 cm wavelength. It therefore refers to a spectral region located between the shorter 20 cm region and the longer meter wavelength one. Our 90 cm observations are presented in Sect. 2, where they are also compared with optical features. Our conclusions are summarized in Sect. 3.

2. Observations

The half-power beamwidth of the VLA's 25-meter telescopes is 32′ at 20 cm wavelength, and this is just equal to the angular extent of the Sun at mean Earth distance. So, the entire solar disk can be imaged at either 20 cm or 90 cm, but with a varying degree of completeness that depends on the array configuration. That is, the 27 individual telescopes can be moved in and out along the Y-shaped arms of the array, creating a radio zoom lens that provides higher angular resolution at the expense of more incomplete information on larger angular structures. For example, the synthesized half-power beamwidth, θ, at 20 cm is $\theta \approx 1''$, 4″, 13″ and 44″ for the A, B, C and D configurations, respectively, while the corresponding values at 90 cm are $\theta \approx 5''$, 18″, 60″ and 200″.

The VLA was used to observe the Sun in the C–D hybrid configuration between 2013 UT on 20 February 1987 and 0015 UT on 21 February 1987 and between 1905 UT on 22 February 1987 and 0020 UT on 23 February 1987. The array was divided into two subarrays with 15 antennas operating at 90 cm wavelength (333 MHz) with 3.125 MHz bandwidth and 12 antennas operating at 20.7 cm wavelength (1446 MHz) with 12.5 MHz bandwidth. The beamwidth of the individual antennae was 138′ at 90 cm and 32′ at 20.7 cm.

All four Stokes parameters were sampled every 6.67 s, and the data were calibrated by observing 3C 48 for five minutes every 70 min. The flux density of 3C 48 was assumed to be 47.0 Jy and 14.6 Jy at 90 cm and 20.7 cm respectively.

In order to construct reliable 90 cm synthesis maps, we had to delete data from the shortest baselines at the end of the day. These data, which corresponded to fringe spacings of 36′ and 48′, were omitted because the large correlated flux exceeded the dynamic range of the correlators. There were no such problems at the beginning of our observations because the projected baselines were longer with correspondingly smaller fringe spacings and correlated fluxes. Shadowing of the antennae at the end of the day

Send offprint requests to: K.R. Lang

* Currently on sabbatical leave at the Observatoire de Paris, Meudon

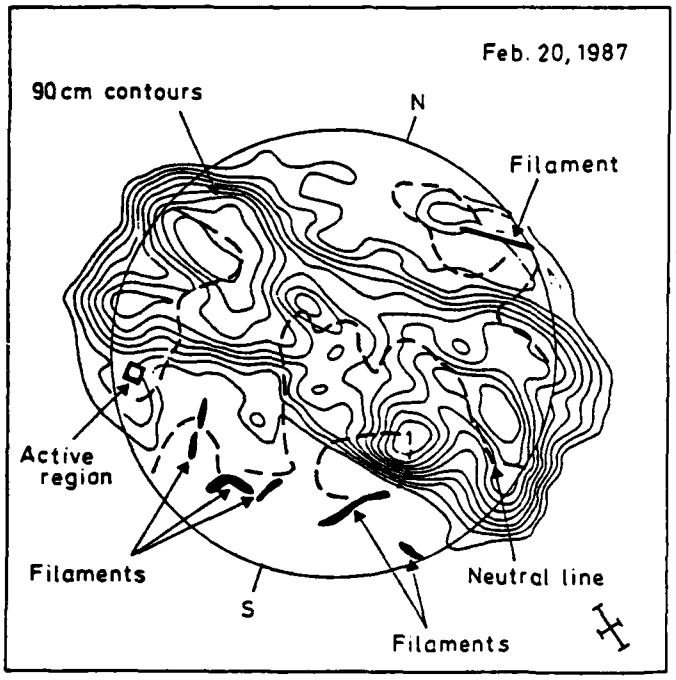

Fig. 1. Four-hour VLA synthesis map of the Sun at 90 cm wavelength on 20 February 1987 is compared with optical solar features including active regions (squares), filaments (solid lines) and the magnetic neutral line (dashed line). The most intense 90 cm emission is not systematically associated with any optical counterpart. There is no intense 90 cm radiation in the polar regions, and this is at least partly due to polar coronal holes. The array was in the C-D hybrid configuration with a synthesized beamwidth denoted by the crosses. The contours mark levels of equal brightness temperature, T_B with an outermost contour of $T_B = 5.5\ 10^4$ K, a contour interval of $5.5\ 10^4$ K, and a peak brightness temperature of $T_B = 5.7\ 10^5$ K. All of the sources are positive and all of the optical data have been extracted from Solar Geophysical Data (1987)

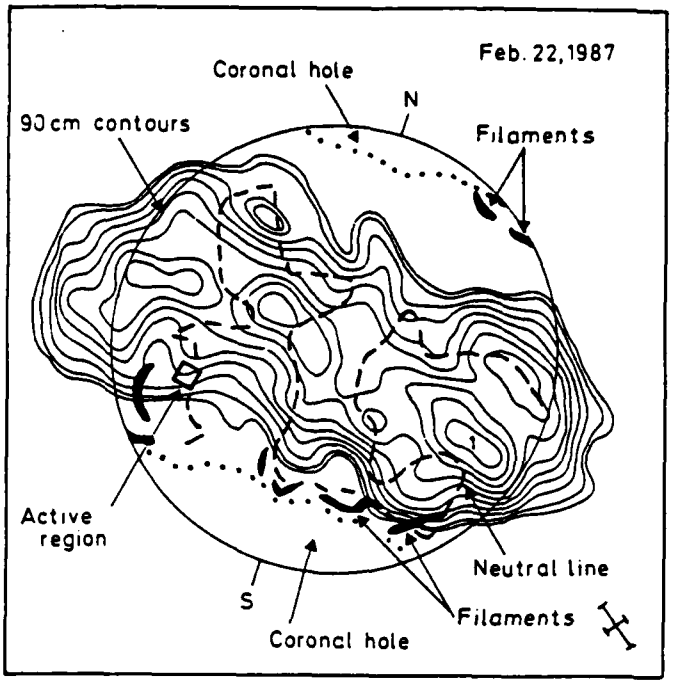

Fig. 2. Four-hour VLA synthesis map of the Sun at 90 cm wavelength on 22 February 1987 is compared with optical solar features including active regions (squares), coronal hole boundaries (dotted lines), filaments (solid lines) and the magnetic neutral line (dashed line). The most intense 90 cm emission is not systematically associated with any optical counterpart. There is no intense 90 cm radiation in the polar regions, and this is at least partly due to polar coronal holes. The array was in the C-D hybrid configuration with a synthesized beamwidth denoted by the crosses. The contours mark levels of equal brightness temperatures, T_B, with an outermost contour of $T_B = 5.5\ 10^4$ K, a contour interval of $5.5\ 10^4$ K, and a peak brightness temperature of $T_B = 5.5\ 10^5$ K. All of the sources are positive, all of the optical data have been extracted from Solar Geophysical Data (1987) and the coronal hole boundaries have been inferred from the He 10830 map supplied by Jack Harvey

can also produce erroneous fringe amplitude changes and incorrect images.

The calibrated and edited data were used together with the standard CLEAN procedure to produce the synthesis maps shown in Figs. 1 and 2. Each map refers to 4 h of observation with a synthesized beamwidth of 113″ × 237″. All of the sources shown in each cleaned map were also present in the dirty map, so the cleaning procedure did not introduce any artifacts. The level of negative residuals was 15 to 20% of the dirty map maximum.

The most intense 20 cm emission on both days was associated with an active region with strong photospheric magnetic fields. We attribute this emission to the coronal loops that have been previously detected in the low corona at 20 cm and soft X-ray wavelengths. The association of intense 20 cm emission with coronal loops in active regions has now been documented by numerous VLA observations (see Lang et al., 1987a, b and references within it), so we do not give our 20 cm maps here.

In contrast to the 20 cm coronal loops, the most intense 90 cm radiation of the quiescent, or non-flaring, corona (see Figs. 1 and 2) is not related to active regions. The 90 cm sources are concentrated near the equatorial regions and provide a distinctly inhomogeneous component to the quiescent corona. The 90 cm structures have brightness temperatures, T_B, of $T_B = 0.5$ to $5.7\ 10^5$ K, which are slightly less than those of the 20 cm coronal loops, but that are comparable to the brightness temperature $T_B \approx 6\ 10^5$ K of the entire quiet Sun (Sheridan and McLean, 1985).

In several cases, the 90 cm sources shown in Figs. 1 and 2 remain, within the uncertainty of measurements, at the longitudes expected from solar rotation (see source 1), but some of the latitudes also apparently change and some sources have disappeared, changed shape or emerged during the two-day interval. These results suggest that the large-scale structures detected at 90 cm wavelength are both inhomogeneous and variable on time scales of a few days.

Assuming an angular radius $\theta \approx 4'$ and a brightness temperature of $T_B \approx 5\ 10^5$ K, we can use the Rayleigh-Jeans law to show that the flux density, S, in a typical intense 90 cm source is $S \approx 1$ s.f.u., where 1 s.f.u. $= 10^4$ Jy (see Lang, 1980). But there are at least five such sources, so their combined flux density is 5 s.f.u., or roughly half the 10 s.f.u. flux density of the quiet Sun at this wavelength (Sheridan and McLean, 1985). Thus, as much as half the total flux density of the quiescent corona at 90 cm wavelength may be emitted from undetected structures. This essentially follows from the fact that the intense 90 cm sources have a brightness temperature comparable to the entire quiet Sun at this wavelength, so if they occupy roughly half the surface area of the Sun they account for roughly half the total flux density.

A comparison of the 90 cm sources with optical features (Figs. 1, 2) indicates that the intense, quiescent 90 cm emission is not systematically associated with any optical counterpart, at least for our observations. Although the north-west filament on 20 February 1987 is apparently associated with an extended 90 cm source, the other filaments on this day and on 22 February are not associated with detectable 90 cm emission. All of the 90 cm sources on these days are concentrated within equatorial regions away from active regions and sunspots. There is a noticeable depression, or lack of intense 90 cm emission, at the poles, and this is at least partly due to polar coronal holes.

Some of the extended 90 cm sources lie on or near the neutral line, but other sources do not. Moreover, some minima in brightness temperature also lie on or near that line, and the 90 cm emission certainly does not trace out all of the neutral line. So, relations with that line may be due to chance, and there is no systematic association with it.

When the VLA zeroes in for a closer look, the 90 cm structures are resolved into compact components. For example, the VLA was used to observe the Sun in the B configuration between 1545 UT and 2230 UT on 23 August 1986. An array of 13 antennas operating at 90 cm wavelength with a bandwidth of 3.125 MHz was used to produce the synthesis map shown in Fig. 3. In this case, the data were calibrated by observing 3C 286 (90 cm flux 29.0 Jy) for 5 min every 40 min, and the synthesized beamwidth was 16″ × 29″.

Components with angular dimensions, θ, of $\theta = 50''$ to $200''$ and brightness temperatures, T_B, of $T_B = 2.1$ to $4.0\ 10^5$ K were detected. As indicated in Fig. 3, these sources are not directly related to the active regions that would have been detected if we had simultaneous VLA observations at 20 cm wavelength.

The only possible optical counterpart of the intense compact 90 cm sources is the inversion line (magnetic neutral line) of the photospheric magnetic field, but these sources do not trace out the full magnetic neutral line. If the quiescent 90 cm sources are related to the magnetic neutral line, some additional factor is causing them to be concentrated over only small parts of it. This factor is apparently unrelated to Hα filaments: an examination of Meudon data (DASOP) indicated no detectable Hα filament or plage at the latitudes of the enhanced 90 cm emission, either on the day of observation or on three rotations before or after that day.

There is, however, one source of 90 cm radiation that is associated with active regions; it is the ubiquitous noise storms. This nonthermal radiation is the most common type of activity observed on the Sun at decimetric and metric wavelengths. The noise storms might be confused with quiescent radiation because of their long durations (hours to days); but they are actually sources of continued activity, apparently located in large magnetic arches that connect active regions with their surroundings (Mercier et al., 1984). Metric wavelength observations of noise storms provided some of the first evidence for stable magnetic connections between solar active regions and more distant areas on the Sun (Lantos-Jarry, 1970; Daigne et al., 1971).

When the VLA is used to resolve a noise storm at 90 cm wavelength, it is indeed found near the apex of large-scale magnetic loops that apparently connect two active regions (Lang and Willson, 1987). Intense radiation at 183 cm wavelength is also associated with this loop system (see Fig. 4). This radiation could be due to low-level noise storm activity, for such noise storm continua are an important source of slowly varying radiation at 183 cm wavelength (Alissandrakis et al., 1985; Lantos et al., 1987). Other extended quiescent coronal features at 183 cm, such as the one near the center of the map shown in Fig. 4, resemble those

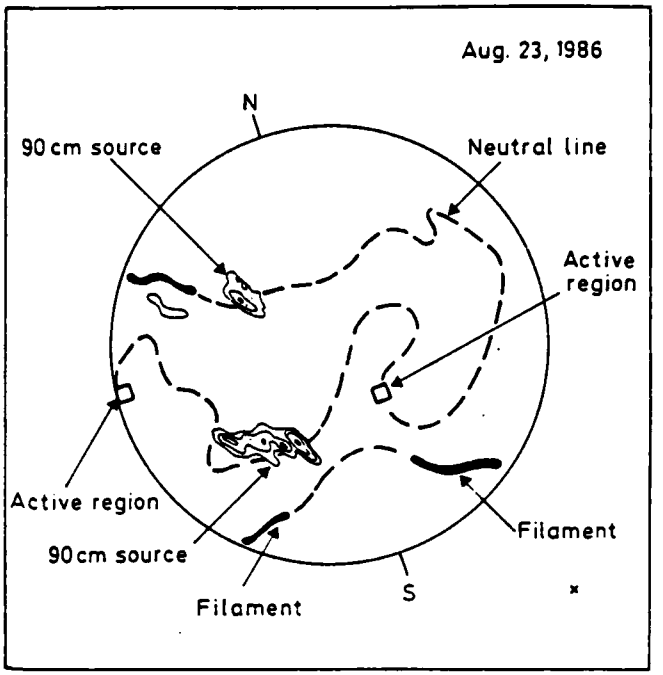

Fig. 3. A VLA synthesis map at 90 cm wavelength during a 6h45 min period on 23 August 1986 is compared with optical solar features including active regions (squares), filaments (solid lines) and the probable magnetic neutral line (dashed line). At least three compact 90 cm sources have been detected with angular dimensions of 50″ × 200″. Here the 90 cm contours mark levels of equal brightness temperature, T_B, with an outermost contour of $T_B = 2.1\ 10^5$ K, a contour interval of $4.1\ 10^4$ K and a peak brightness temperature of $T_B = 4.0\ 10^5$ K. The VLA was in the B configuration with a 16″ × 29″ synthesized beamwidth denoted by the small solid cross in the lower right corner. All of the optical data have been extracted from Solar Geophysical Data (1986)

found at 90 cm with the VLA, with no apparent correlation with any optical counterpart and comparable brightness temperatures.

Our results are in accord with previous observations which showed that intense quiescent emission at meter wavelengths (80 and 169 MHz) is not associated with active regions (Axisa et al., 1971; Sheridan and McLean, 1985). A statistical study of numerous one-dimensional Nançay scans at 169 MHz indicated, however, that the longitudes of many quiescent sources are associated with filament corridors as seen on Hα synoptic maps and not on daily maps (Axisa et al., 1971). In contrast, fewer two-dimensional maps at the same frequency show a poor apparent association with filaments and a possible association with the magnetic neutral line in the underlying photosphere (Alissandrakis et al., 1985; Lantos et al., 1987). Our observations do not confirm either result, indicating no systematic association with any optical counterpart; but we can not rule out such associations, particularly during different parts of the solar cycle.

Correlations of radio sources with optical counterparts are confused by nonradial divergence, refraction effects and solar tilt. There are additional uncertainties due to random correlations with the long magnetic neutral line; its placement on the solar surface differs by several degrees depending on the technique used. A deeper understanding of the quiescent coronal sources is likely to come from multiple-wavelength observations in the radio part of the electromagnetic spectrum.

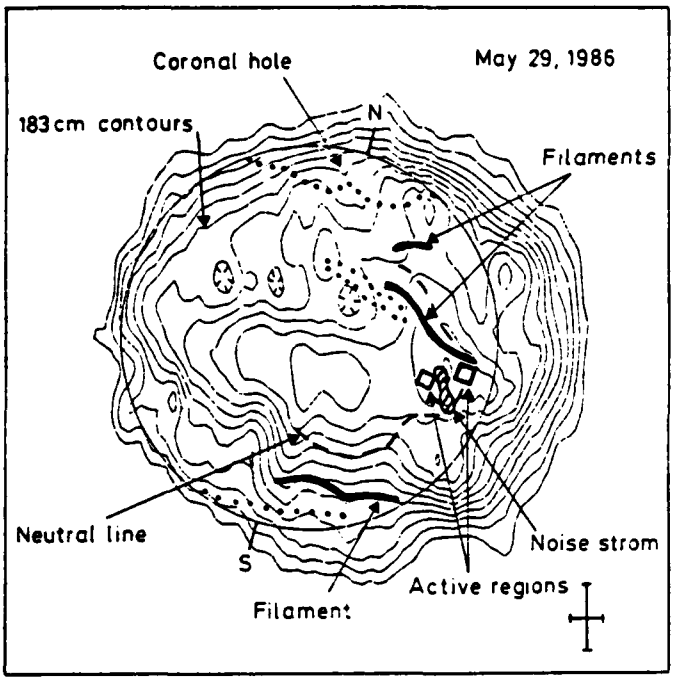

Fig. 4. A Nançay Radioheliograph synthesis map at 183 cm wavelength during an 8 h period is compared with a 90 cm noise storm (VLA-hatched area) and various optical solar features including active regions (squares), coronal hole boundaries (dotted lines), filaments (solid lines) and the magnetic neutral line (dashed line). The 90 cm noise storm emission apparently comes from large-scale magnetic loops that connect active regions, and the apex of these loops is probably associated with a maximum in the intensity of the 183 cm radiation. Here the 183 cm contours mark levels of equal brightness temperature, T_B, with an outermost contour of $T_B = 2.0\ 10^5$ K, a contour interval of $5.0\ 10^4$ K and a peak brightness temperature of $7.5\ 10^5$ K. A detailed understanding of these sources will require greater angular resolution and spectral information. The 1'.2 × 4'.5 synthesized beamwidth is denoted by crosses in the lower right corner, and all of the optical data have been extracted from Solar Geophysical Data (1986)

3. Conclusions

The quiescent corona at 90 cm wavelength is very inhomogeneous and variable, with the most intense emission concentrated within structures near the equatorial regions. This emission may be the thermal bremsstrahlung of a coronal plasma that might be confined in large-scale magnetic structures. The 90 cm sources are not systematically associated with any optical counterpart including active regions, filaments, sunspots and the magnetic neutral line, at least for the observations presented here. There is no intense 90 cm radiation in the polar regions, and this is at least partly due to coronal holes. More compact 90 cm sources in the quiescent corona also show no systematic correlation with optical counterparts. Associations with the magnetic neutral line are uncertain, and future multiple-wavelength radio observations might provide new insights to the paradoxical quiscent coronal structures.

Acknowledgements. Radio astronomical studies of the Sun at Tufts University are supported under grant AFOSR-83-0019 with the Air Force Office of Scientific Research and contract N 00014-86-K-0068 with the Office of Naval Research. Collaborative long-wavelength solar observations by Tufts University and the Observatoire de Paris are supported by National Science Foundation grant INT-8602285 and Centre National de la Recherche Scientifique grant 920038. The Very Large Array is operated by Associated Universities Inc., under contract with the National Science Foundation. We thank C.E. Alissandrakis, K.-L. Klein, P. Lantos, C. Mercier and M. Pick for useful discussions.

References

Alissandrakis, C.E., Lantos, P., Nicolaidis, E.: 1985, *Solar Phys.* **97**, 267
Axisa, F., Avignon, Y., Martres, M.J., Pick, M., Simon, P.: 1971, *Solar Phys.* **19**, 110
Daigne, G., Lantos-Jarry, M.F., Pick, M.: 1971, in *Solar Magnetic Fields*, ed. Howard, p. 609
Kundu, M.R., Lang, K.R.: 1985, *Science* **228**, 9
Lang, K.R.: 1980, in *Astrophysical Formulae*, 2nd ed., New York, Springer-Verlag, p. 23
Lang, K.R., Willson, R.F.: 1987, *Astrophys. J.* **319**, 514
Lang, K.R., Willson, R.F., Smith, K.L., Strong, K.T.: 1987a, b, *Astrophys. J.* **322**, 1035, 1044
Lantos, P., Alissandrakis, C.E., Gergely, T., Kundu, M.R.: 1987, *Solar Phys.* **112**, 325
Lantos-Jarry, M.F.: 1970, *Solar Phys.* **15**, 40
Mercier, C., Elgaroy, O., Tlamicha, A., Zlobek, P.: 1984, *Solar Phys.* **92**, 375
Saito, K.: 1970, *Ann. Tokyo Astron. Obs. Ser. 2*, **12**, 53
Sheridan, K.V., Labrum, N.R., Payten, W.J., Nelson, G.J., Hill, E.R.: 1983, *Solar Phys.* **83**, 167
Sheridan, K.V., McLean, D.J.: 1985, in *The Quiet Sun at Metre Wavelengths, Solar Radiophysics*, eds. D.J. McLean, N.R. Labrum, New York, Cambridge University Press, p. 443
Solar Geophysical Data: 1986, 1987, Part 1, No 503, p. 53, No 506, p. 47, No 512, p. 50, 52

THE ASTROPHYSICAL JOURNAL, 326:300–304, 1988 March 1

C4. NARROW-BAND, SLOWLY VARYING DECIMETRIC RADIATION FROM THE DWARF M FLARE STAR YZ CANIS MINORIS. II.

KENNETH R. LANG AND ROBERT F. WILLSON
Department of Physics and Astronomy, Tufts University
Received 1987 May 29; accepted 1987 August 21

ABSTRACT

The Very Large Array has been used in the spectral-line mode to obtain the frequency spectra of the radiation from the dwarf M star YZ Canis Minoris at frequencies, ν, near 1465 MHz. The slowly varying (minutes) radiation was, within the observational uncertainties, 100% left-hand circularly polarized. The radiation during several 10 minute intervals exhibited evidence for narrow-band structure with a bandwidth $\Delta\nu \approx 30$ MHz and a fractional bandwidth of $\Delta\nu/\nu \approx 0.02$. Broad-band radiation with $\Delta\nu \geq 50$ MHz and $\Delta\nu/\nu \geq 0.03$ was observed during other 10 minute intervals. The highly polarized, slowly varying, narrow-band emission is attributed to coherent radiation from an electron-cyclotron maser in a magnetic field of strength $H \approx 260$ G. If this radiation is from coronal loops similar to those observed on the Sun, then a source size of $L_s \approx 2 \times 10^7$ cm and brightness temperature $T_B \approx 0.5 \times 10^{17}$ K are inferred for the narrow-band source. The observed broad-band radiation may be due to the superposition of many rapid, narrow-band bursts with different central frequencies. The fact that the observed narrow-band radiation persists for 10 minutes indicates that there was no substantial change in the source height, size, magnetic field strength, or electron density during this time. The "quiescent" microwave radiation of some dwarf M stars might be due to the superposition of nearly continuous, low-level coherent bursts; this activity might play a role in the heating of stellar coronae.

Subject headings: radiation mechanisms — stars: flare — stars: individual (YZ CMi) — stars radio radiation

I. INTRODUCTION

Radio and microwave bursts from dwarf M stars have been attributed to coherent radiation mechanisms. High brightness temperatures of $T_B \geq 10^{12}$–10^{15} K were, for example, inferred from the flux densities of rare, powerful bursts under the assumption that the radio emitter was smaller than the stellar disk; coherent processes are required to explain these high brightness temperatures (see Lang and Willson 1986*a* for a review). Observations with high time resolution indicated that the 20 cm bursts from one dwarf M star, AD Leonis, had rise times of milliseconds, relatively small sizes $L \leq 10^8$ cm, and high brightness temperatures $T_B \geq 10^{16}$ K (Lang *et al.* 1983; Lang and Willson 1986*a*). These bursts were up to 100% circularly polarized, suggesting an intimate connection with the star's magnetic fields.

Lang and Willson (1986*b*) first provided evidence for the narrow-band frequency structure expected from a coherent radiation process. They showed that the variation in the radiation from the dwarf M star YZ Canis Minoris had a bandwidth $\Delta\nu \leq 100$ MHz. This was because there was no correlation between the variations detected at 1415 and 1515 MHz.

This two-frequency experiment was repeated with similar results for the dwarf M stars AD Leonis and L726-8A (White, Kundu, and Jackson 1986). A 2 hr variation in the radiation from AD Leonis was observed at 1415 MHz but did not appear at 1515 MHz. The flux and evolution of a flare from L726-8A differed at the two frequencies.

Intensity was plotted as a function of both time and frequency (dynamic spectra) for radiation from the dwarf M star UV Ceti (L726-8B) near 1415 MHz (Bastian and Bookbinder 1987). One left circularly polarized burst showed no variation as a function of frequency across the 41 MHz band, but another right circularly polarized burst exhibited complex frequency structure with narrow-band components whose fractional bandwidths were as small as the frequency resolution (bandwidth $\Delta\nu \leq 3$ MHz and $\Delta\nu/\nu \leq 0.002$). Jackson, Kundu, and White (1987) similarly produced dynamic spectra for UV Ceti by observing four frequencies simultaneously. Although the bandwidths were not measured, the dynamic spectrum of one 10 minute burst suggested complex frequency-time structure with both positive and negative frequency drifts. The features that showed a positive drift were interpreted in terms of disturbances traveling downward in the star's corona where they excite radiation at higher frequencies or shorter wavelengths.

In this paper we report measurements of the frequency spectra of YZ Canis Minoris using 15 continuous 3.125 MHz bands. In § II we present observations of frequency structure with narrow bandwidths $\Delta\nu \approx 30$ MHz that persist over 10 minutes of time without evidence for a drift. The fractional bandwidth $\Delta\nu/\nu \approx 0.02$. Here we also show that radiation over other 10 minute intervals appears to be broad band with $\Delta\nu \geq 50$ MHz, but these spectra could represent the time average of many rapid, narrow-band events. In § III we interpret the narrow-band, 30 MHz structure in terms of electron-cyclotron maser emission. Here we also draw attention to certain solar bursts that may require a similar coherent radiation mechanism. We conclude by mentioning the implications of continued coherent burst activity for the heating of stellar coronae.

II. OBSERVATIONS

The dwarf M star YZ Canis Minoris (GL 285, dM4.5e) was observed with the Very Large Array (VLA) between 08:10 and 12:22 UT on 1987 January 6 in the C-configuration. The VLA

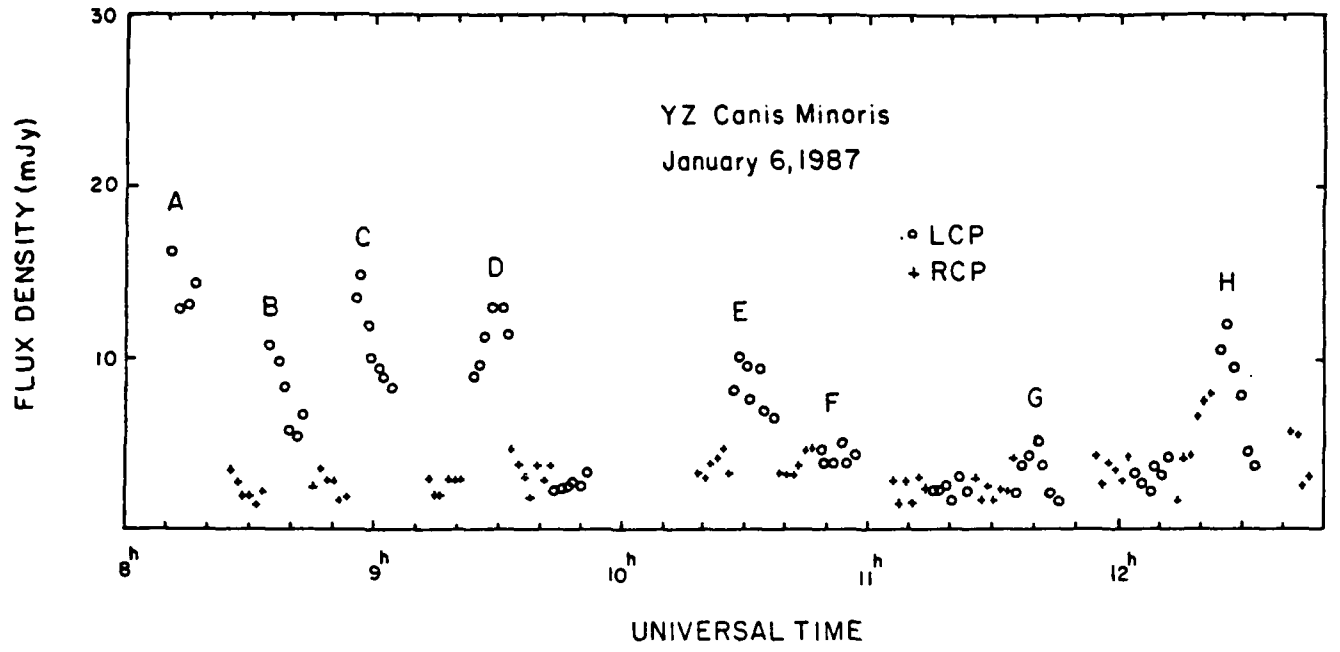

FIG. 1.—The total intensity of the radiation received from the dwarf M flare star YZ Canis Minoris is plotted as a function of time. The left circularly polarized (LCP) and right circularly polarized (RCP) signals were alternately recorded for 10 minute intervals within a 50 Hz bandwidth centered at 1464.9 MHz. Here the visibility data of all baselines from the 15 independent channels has been averaged over a 1.5 minute time interval with a 3 σ noise level of 2.9 mJy. Frequency spectra of the slowly varying LCP radiation marked by the letters A, B, C, ..., H are shown in Figs. 2 and 3.

was used in the 16-channel spectral line mode centered at 1464.9 MHz. At this frequency, the half-power beamwidth of the antennas is $\sim 31'$ and the synthesized beamwidth is $\sim 13'' \times 22''$. The 50 MHz bandwidth was divided into 15 continuous channels of 3.125 MHz width; the 16th channel was used to record the integral flux over the inner 37.5 MHz of the bandwidth. The full array of 26 antennas was used to sample the signal intensity every 10 s, and the left circularly polarized (LCP) and right circularly polarized (RCP) signals were observed for alternate 10 minute intervals. A bandpass calibration for each of the 16 channels was applied to the visibilities during the observations. The phase data were calibrated by observing PKS 0735+178 for a 3 minute interval every 40 minutes, and the flux density calibration was made from observations of 3C 286 whose flux density is 14.7 Jy at 1465 MHz (1 Jy = 10^{-23} ergs cm^{-2} s^{-1} Hz^{-1}).

The raw visibilities were first examined, baseline-by-baseline and channel-by-channel for interference or other corrupted data, and than edited. The calibrated visibility data for the 16 channels were then averaged, baseline-by-baseline, with running means over 1.5 minutes and then vector-averaged. A synthesis map was then made for each 1.5 minute time interval using the standard CLEAN procedure.

The source flux densities were determined from these maps and plotted as a function of time in Figure 1. Here the flux density scale is in mJy, 10^{-3} Jy, and the 3 σ noise level is 2.9 mJy. The observed radiation was 100% left-hand circularly polarized, within an observational uncertainty of about 10%. The highly polarized radiation also exhibited variations on time scales of minutes: these variations are relatively slow when compared with those of more impulsive stellar bursts (milliseconds to seconds).

The 10 s visibility data observed within each 3.125 MHz channel was then averaged, baseline-by-baseline, with running means over 10 minutes and then vector-averaged. A synthesis map was then made for each of the 15 channels using the standard CLEAN procedure. The flux densities determined from these maps are plotted as a function of observing frequency in Figures 2 and 3. Several of these 10 minute spectra provide evidence for narrow-band radiation with a bandwidth $\Delta\nu \approx 30$ MHz near a central frequency $\nu = 1465$ MHz, or $\Delta\nu/\nu \approx 0.02$. Other spectra have broad bandwidths $\Delta\nu \geq 50$ MHz, or $\Delta\nu/\nu \geq 0.03$.

III. DISCUSSION

The highly polarized emission may be attributed to coherent radiation from an electron-cyclotron maser. The maser will radiate at harmonics, n, of the gyrofrequency $\nu_H = 2.8 \times 10^6 H$ Hz, where H is the magnetic field strength. Although the first harmonic may be absorbed in overlying atmospheric layers, the second harmonic can escape with up to 100% circular polarization (Melrose and Dulk 1982). For $n = 2$ and our observing frequency of $\nu = n\nu_H = 1.465 \times 10^9$ Hz, the required magnetic field strength is $H \approx 260$ G.

The electron-cyclotron maser emission is confined to a thin cone at large angles $\theta_0 = 70°$ to $85°$ with respect to the magnetic field. A narrow relative bandwidth of $\Delta\nu/\nu \approx \cos^2 \theta_0 \approx 0.01$ to 0.10 is expected.

The observed bandwidth will depend on the gradient of the magnetic field and the size of the source. A sharper field gradient will produce a wider range of gyrofrequencies and a broader bandwidth, while a smaller source size will limit the magnetic field variation and produce a narrower bandwidth.

If the emission is confined to magnetic loops like those on the Sun, then the magnetic scale height $L_H \approx 10^9$ cm. Such a scale height is plausible for coronal loops on YZ Canis Minoris

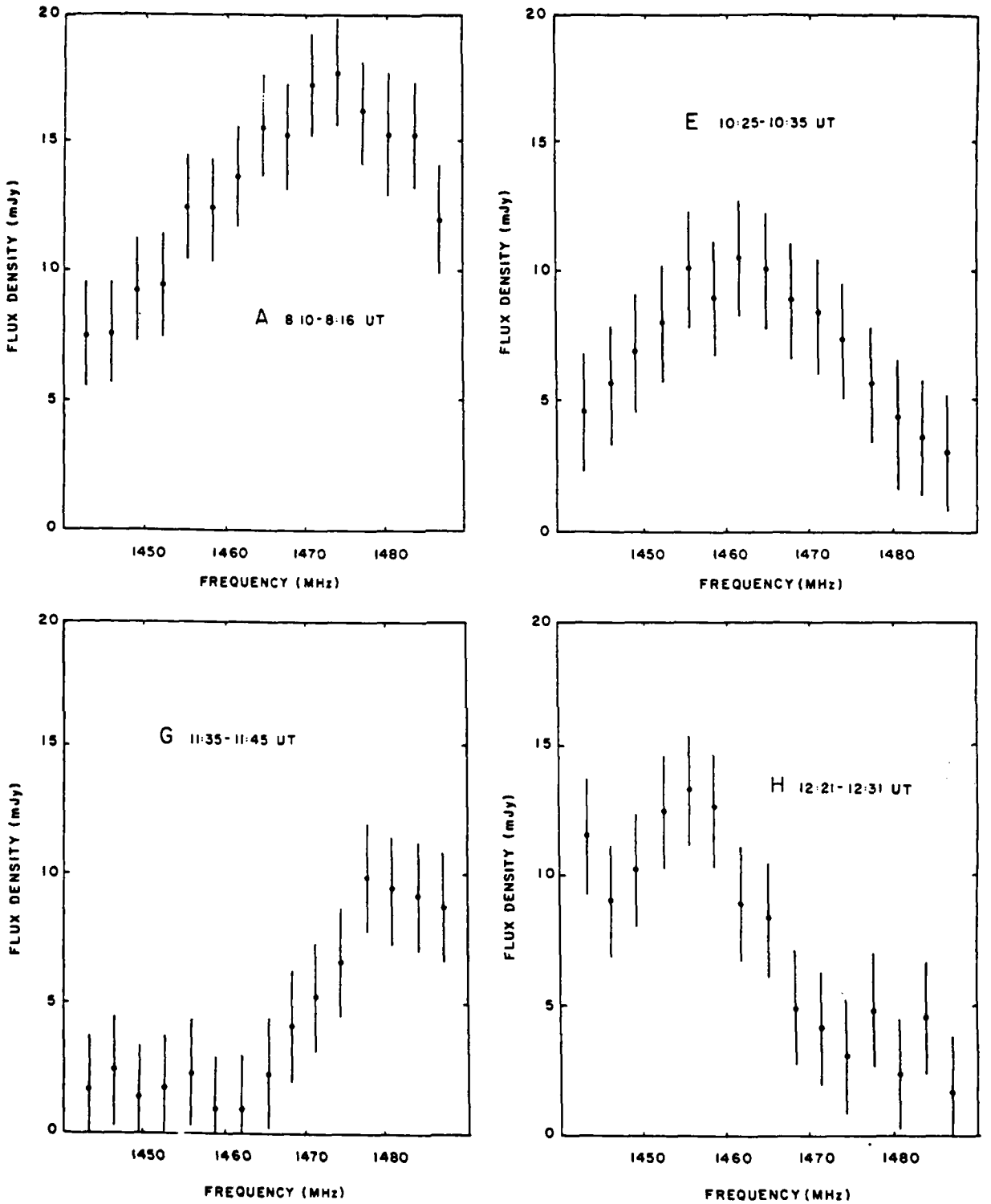

FIG. 2.—Frequency spectra of the left circularly polarized radiation from YZ Canis Minoris for the intervals marked A, E, G, and H in Fig. 1. Here we have plotted the total intensity received in 15 contiguous channels, each 3.125 MHz wide, during the time interval denoted on each plot. The observed value is plotted as a small circle with two vertical bars, each denoting the 3 σ noise level for the relevant time interval and bandwidth. These spectra have been grouped together because they all show evidence for narrow-band radiation with a bandwidth $\Delta\nu \approx 30$ MHz near a central frequency $\nu = 1465$ MHz, or $\Delta\nu/\nu \approx 0.02$.

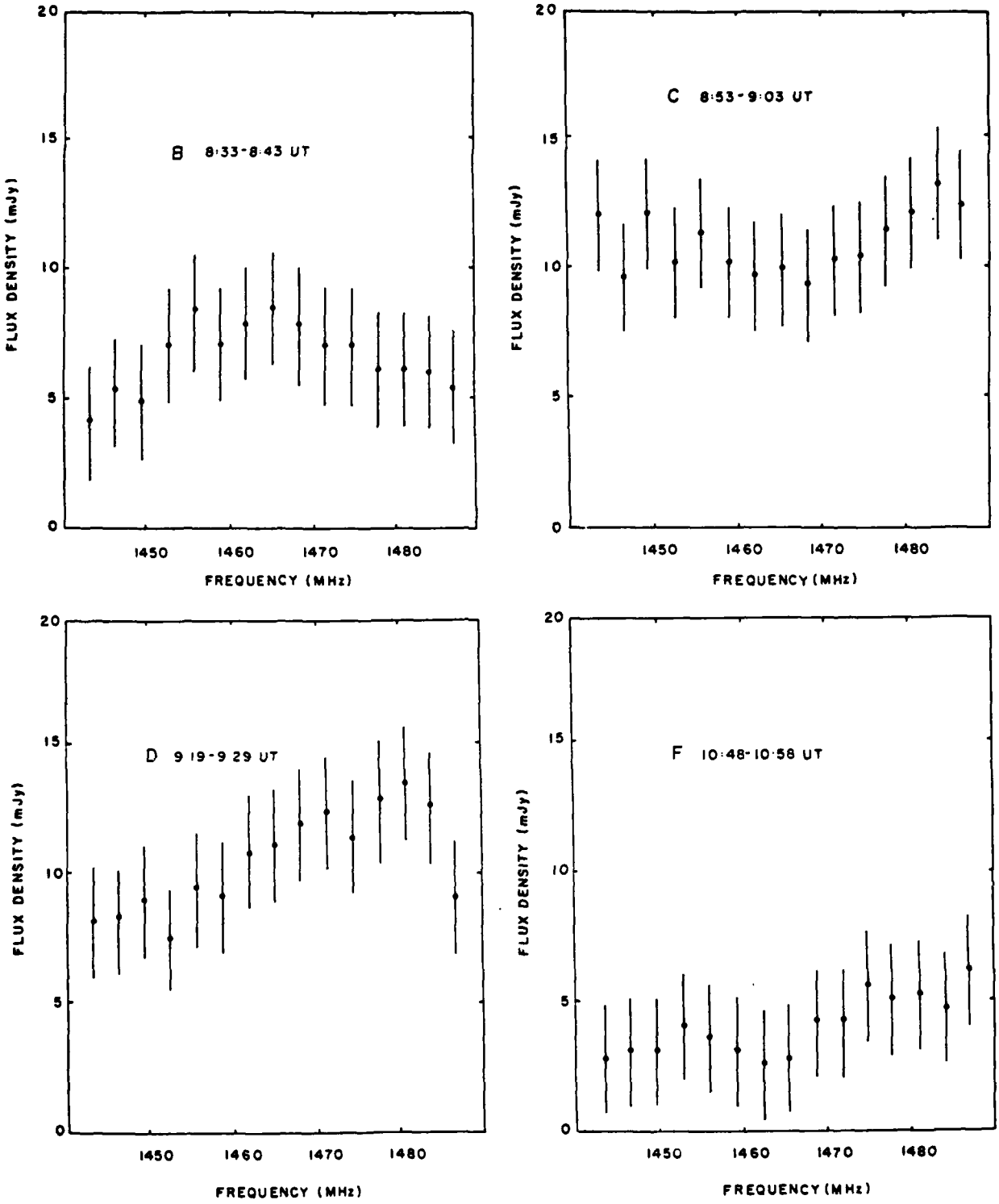

FIG. 3.—Frequency spectra of the left circularly polarized radiation from YZ Canis Minoris for the intervals marked B, C, D, and F in Fig. 1. Here we have plotted the total intensity received in 15 contiguous channels, each 3.125 MHz wide, during the time interval denoted on each plot. The observed value is plotted as a small circle with two vertical bars, each denoting the 3 σ noise level for the relevant time interval and bandwidth. These spectra have been grouped together because they all show evidence for broad-band radiation with a bandwidth $\Delta\nu \geq 50$ MHz near a central frequency $\nu = 1465$ MHz, or $\Delta\nu/\nu \geq 0.03$.

whose radius $R \approx 2.6 \times 10^{10}$ cm (Pettersen 1980). The size, L_s, of the masing source with a 30 MHz bandwidth is then given by

$$L_s = L_H \frac{\Delta\nu}{\nu} \approx 2 \times 10^7 \text{ cm}, \quad (1)$$

and its brightness temperature, T_B, is

$$T_B \approx 10^{13} \frac{SD^2}{\nu^2 L_s^2} \approx 0.5 \times 10^{17} \text{ K}, \quad (2)$$

where the flux density $S = 0.015$ Jy, the star's distance $D = 1.8 \times 10^{19}$ cm, our observing frequency $\nu = 1.465 \times 10^9$ Hz, and $L_s = 2 \times 10^7$ cm. Melrose and Dulk (1982) have shown that an electron-cyclotron maser can produce similar brightness temperatures of $T_B = 10^{16}$ to 10^{17} K.

Of course, the broad-band radiation from YZ Canis Minoris can also be attributed to coherent radiation from an electron-cyclotron maser. The 10 minute spectra may have averaged over several narrow-band bursts of short duration and different central frequencies, thereby producing broad-band spectra. In fact, microwave spikes emitted during solar burst have short durations of $\tau_D \leq 10$ ms, high brightness temperatures of $T_B \geq 10^{12}$ K, and relative bandwidths of $\Delta\nu/\nu \approx 0.015$ (Benz 1985), and these spike bursts have been attributed to electron-cyclotron maser emission (Holman, Eichler, and Kundu 1980). Decimetric bursts from the dwarf M star AD Leonis are also composed of millisecond spikes with rise times of $\tau_R \leq 5$ ms and durations of $\tau_D \leq 10$ ms (Lang and Willson 1986*a*). Such spikes would not be resolved with the 10 s integration time at the VLA.

In fact, the interesting aspect of the narrow-band radiation from YZ Canis Minoris is that is persists for 10 minutes with a well-defined bandwidth and central frequency. If this radiation is composed of bursts with shorter duration, they have to be coming from a region in which there is no substantial change of physical parameters such as height, size, magnetic field strength, and electron density. A substantial change in height, size, or magnetic field strength would produce a drift in the central frequency which is not observed. If there is any drift it has to be slower than 0.05 MHz s^{-1}. A substantial increase in the electron density above $N_e \approx 6 \times 10^9$ cm^{-3} would make the plasma frequency ν_p exceed the gyrofrequency, and plasma radiation would dominate the emission.

As discussed by Lang and Willson (1986*a*, *b*) and by Bastian and Bookbinder (1987), an alternative coherent process might be plasma radiation. Solar type II, III, and IVM bursts as well as weaker narrow-band decimetric bursts or blips with $\Delta\nu/\nu \leq 0.1$ have been attributed to plasma radiation (Furst, Benz, and Hirth 1982; Benz, Bernold, and Dennis 1983). As pointed out by Bastian and Bookbinder (1987) one difficulty with this interpretation is that plasma radiation tends to rapidly drift toward lower frequencies as the disturbance travels outward into the lower density corona. The drift rate, $\Delta\nu/\Delta t \approx 0.5 U_b \nu / H_e$, where U_b is the velocity of the distrubance and H_e is the scale height. For $H_e \approx 10^{10}$ cm, $\nu = 1465$ MHz, and $\Delta\nu/\Delta t < 0.5$ MHz s^{-1}, we require that $U_b < 7$ km s^{-1}, or about 30–200 times slower that the speeds observed in moving type IV bursts (Robinson 1978). For higher speeds, the frequency drift rate is correspondingly higher and would give rise to an apparently broad-band spectrum.

Finally, we also note that YZ Canis Minoris appears to undergo nearly continuous coherent burst activity for periods as long as 4 hr (see Fig. 1). The "quiescent" microwave emission of some dwarf M stars might therefore be due to the superposition of many low-level coherent bursts. Similar continued low-level variability has been reported for the X-ray emission from dwarf M stars (Butler *et al.* 1986; Ambruster, Sciortino, and Golub 1987). The continued variability might well be related to emerging magnetic flux that plays a role in heating the stellar coronae. It is interesting to note that Melrose and Dulk (1982) have shown that cyclotron maser emission at the second harmonic may heat the overlying coronal plasma to $T_e \approx 3 \times 10^7$ K, thereby giving rise to X-ray bursts.

Radio astronomical studies of the Sun and other nearby active stars at Tufts University are supported under grant AFOSR-83-0019 with the Air Force Office of Scientific Research. Related solar observations are supported by contract N00014-86-K-0068 with the Office of Naval Research (ONR). The Very Large Array is operated by Associated Universities, Inc., under contract with the National Science Foundation.

REFERENCES

Ambruster, C. W., Sciortino, S., and Golub, L. 1987, *Ap. J. Suppl.*, **65**, 273.
Bastian, T. S., and Bookbinder, J. A. 1987, *Nature*, **326**, 678.
Benz, A. O. 1985, *Solar Phys.*, **96**, 357.
Benz, A. O., Bernold, T. E. X., and Dennis, B. R. 1983, *Ap. J.*, **271**, 355.
Butler, C. J., Rodono, M., Foing, B. H., and Haisch, B. M., 1986, *Nature*, **321**, 679.
Furst, E., Benz, A. O., and Hirth, W. 1982, *Astr. Ap.*, **107**, 178.
Holman, G. D., Eichler, D., and Kundu, M. R., 1980, in *IAU Symposium 86, Radio Physics of the Sun*, ed. M. Kundu and T. Gergely (Dordrecht: Reidel), p. 457.
Jackson, P. D., Kundu, M. R., and White, S. M., 1987, *Ap. J. (Letters)*, **316**, L85.
Lang, K. R., Bookbinder, J., Golub, L., and Davis, M. M. 1983, *Ap. J. (Letters)*, **272**, L15.
Lang, K. R., and Willson, R. F. 1986*a*, *Ap. J.*, **305**, 363.
———. 1986*b*, *Ap. J. (Letters)*, **302**, L17.
Melrose, D. B., and Dulk, G. A. 1982, *Ap. J.*, **259**, 844.
Pettersen, B. R. 1980, *Astr. Ap.*, **82**, 53.
Robinson, R. D. 1978, *Solar Phys.*, **60**, 383.
White, S. M., Kundu, M. R., and Jackson, P. D. 1986, *Ap. J.*, **311**, 814.

KENNETH R. LANG and ROBERT F. WILLSON: Department of Physics and Astronomy, Robinson Hall, Tufts University, Medford, MA 02155

Adv. Space Res. Vol. 8. No. 11. pp. (11)49–(11)53. 1988
Printed in Great Britain.

0273–1177/88 $0.00 + .50

C5. SIMULTANEOUS VLA–SATELLITE OBSERVATIONS OF THE SUN

Kenneth R. Lang*

**D.A.S.O.P. Observatoire de Paris, Meudon, 92195 Meudon Principal Cedex, France; Department of Physics and Astronomy, Tufts University, Medford, MA 02155, U.S.A.*

ABSTRACT

The Very Large Array (VLA) and satellite-borne telescopes can be used in the 1990s to provide unique observations of the quiescent and active corona with comparable resolution in time and space. Recently available 90-cm VLA data specify closed and open magnetic structures in the low solar corona, providing unique information about the initiating source of coronal mass ejections observed by satellite coronagraphs. The physical properties of quiescent coronal loops can be inferred from combined soft X-ray (electron density and temperature) and 20-cm VLA (magnetic field strength and structure) data. Systems of coronal loops within a single active region have different temperatures and different radiation mechanisms that can only be detected by observations in both spectral domains. The combined VLA-satellite observations will also specify magnetic interaction and particle acceleration before and during flares, including magnetic triggering in the corona (VLA) and preflare heating (VLA-satellite).

INTRODUCTION

The Very Large Array (VLA) can provide unique information about large-scale magnetic structures, coronal holes, and coronal loops. Newly-developed receiving systems at 92-cm wavelength permit observations of quiescent and active emission from filaments and coronal holes, while 20-cm observations provide similar information for coronal loops within active regions.

FILAMENTS AND CORONAL HOLES

The first VLA synthesis maps of the quiescent corona at 92-cm wavelength (327 MHz) revealed intense, elongated structures that were not systematically associated with any optical counterpart, including active regions, filaments, sunspots and magnetic neutral lines /1/. Filaments are sometimes associated with enhanced 92-cm emission, however, and there is a reduction in brightness over polar coronal holes at this wavelength /1/, /2/.

The ubiquitous noise storms are the only source of intense 92-cm radiation associated with solar active regions. These storms are apparently located in large-scale magnetic loops that connect active regions with more distant areas on the Sun /3/. Individual noise storm bursts and the background continuum can be resolved in both space and time by using simultaneous observations with the VLA and the Nancay Radioheliograph /4/. Such information will provide important constraints to our future understanding of noise storms and related activity on the Sun.

Recent VLA synthesis maps indicate that intense, quiescent 92-cm radiation is definitely associated with the large-scale magnetic structures detected as dark filaments in Hα photographs (see Fig. 1, 2). Such an association was first suggested by a statistical study of numerous one-dimensional scans of moderate angular resolution at meter wavelengths (169 MHz) /5/, but subsequent two-dimensional maps at this wavelength suggested that extended quiescent filaments have no radio counterpart /6/, /7/. The results shown in Figures 1 and 2 indicate that this is not always the case at 92-cm.

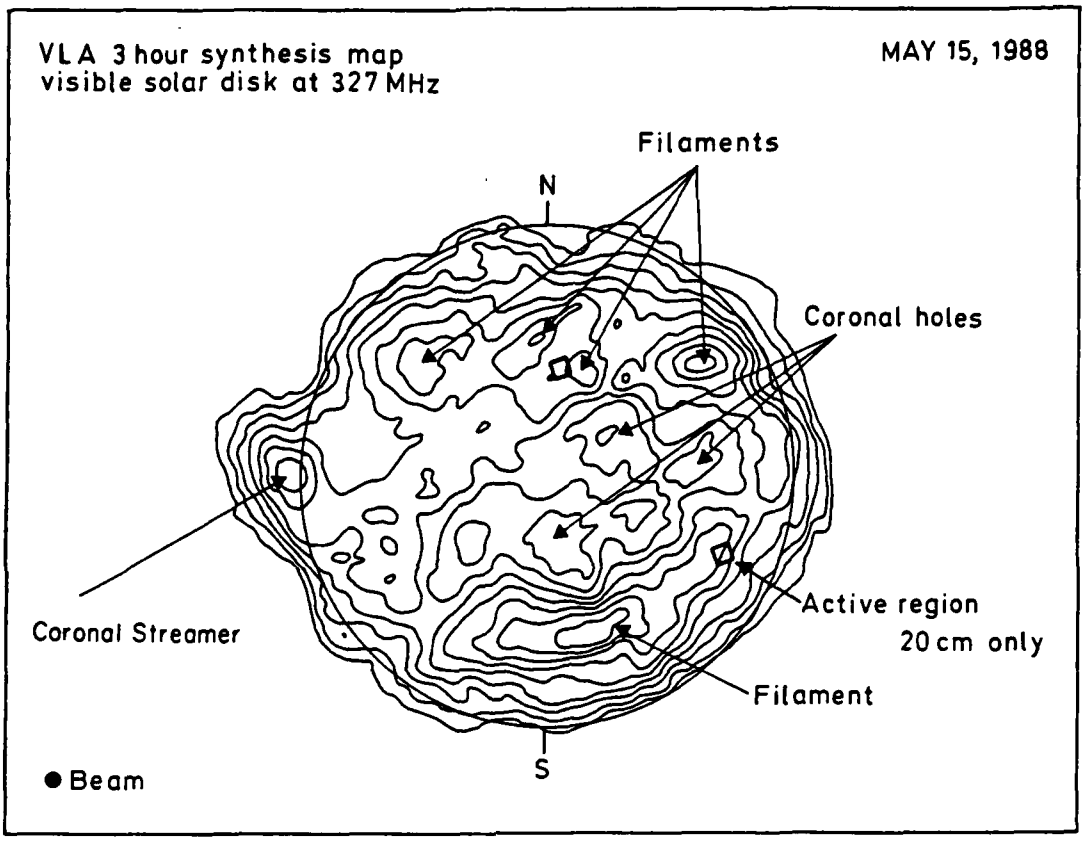

Fig. 1. Three-hour VLA synthesis map at 92-cm wavelength (327.0 MHz) on 15 May, 1988 between 13 h and 16 h U.T. The regions of enhanced 92-cm emission are well correlated with dark filaments shown in a Hα photograph taken on the same day (see Figure 2). The elongated filaments have similar shapes at 92-cm and Hα wavelengths. Active regions (squares) are not associated with enhanced 92-cm radiation; but they dominate the intense radiation at 20-cm wavelength and are observed as bright Hα features. Regions of depressed 92-cm emission are at least partly due to equatorial coronal holes. The contours mark levels of equal brightness temperature, T_B, with an outermost contour of $T_B = 7.8 \times 10^4$ K, a contour interval of 7.8×10^4 K, and a peak brightness temperature of $T_B = 7.8 \times 10^5$ K. The synthesized beamwidth is denoted by the small black spot in the lower left-hand corner; it has angular dimensions of 80" x 55" at a position angle of -20°.

Future VLA observations of large-scale magnetic structures can be used to test models for the origin of coronal mass ejections. These outward-moving magnetic bubbles are currently thought to be initiated by global magnetic changes; associated chromospheric activity, detected as erupting prominences or Hα flares, is thought to be the result, rather than the cause, of these changes /8/. Such models have been derived from observations with satellite-borne coronagraphs whose occulting disks block the visible photosphere and the low corona. VLA observations at 92-cm wavelength can enhance and extend future coronagraph investigations by observing the formation of coronal mass ejections in the low solar corona at both the limb and across the entire solar disk.

Reductions or depressions in the 92-cm radiation are apparently associated with coronal holes in both the polar and equatorial regions (see /1/ and Fig. 1). Future VLA observations can therefore provide new insights to the formation and evolution of coronal holes and the high-speed solar wind that probably originates in them. Comparisons with satellite observations may resolve current uncertainties about the density and temperature of these coronal holes /9/.

Fig. 2. A Hα spectroheliogram taken at 6 h 36 m U.T. on 15 May 1988 at the Observatoire de Paris, Meudon. Five dark filaments are well correlated with regions of enhanced emission at 92-cm wavelength (see Figure 1); the elongated shape of the longer filaments is also detected in the radio data. Areas of bright Hα emission (plage-active regions) are not associated with enhanced 92-cm emission; but they dominate the radiation at 20-cm wavelength.

Although intense, quiescent 92-cm sources are not associated with active regions, the quiescent emission at 20-cm wavelength is dominated by radiation from coronal loops that are often anchored within single active regions. These magnetic loops are smaller than the large-scale magnetic structures detected at the longer wavelength; but the 20-cm loops dominate the coronal structure of active regions and store the magnetic energy that is released during powerful eruptions from them /10/, /11/.

When the 20-cm VLA results are combined with satellite observations of spectral lines at soft X-ray wavelengths, the physical properties and dominant radiation mechanisms can be specified /12/. There are coronal structures that are detected at 20-cm but remain invisble at X-ray wavelengths and vice versa (see Fig. 3). Future VLA data will also uniquely specify the strength and structure of the coronal magnetic fields.

Observations of the 20-cm loops during the coming solar maximum will help establish magnetic changes that probably trigger solar eruptions /13/, /14/. The magnetic interaction of coronal loops apparently involves reconnection processes that release stored magnetic energy and accelerate particles near their tops (see Fig. 4). Simultaneous satellite observations at soft and hard X-ray wavelengths will help unravel the detailed triggering and acceleration mechanisms.

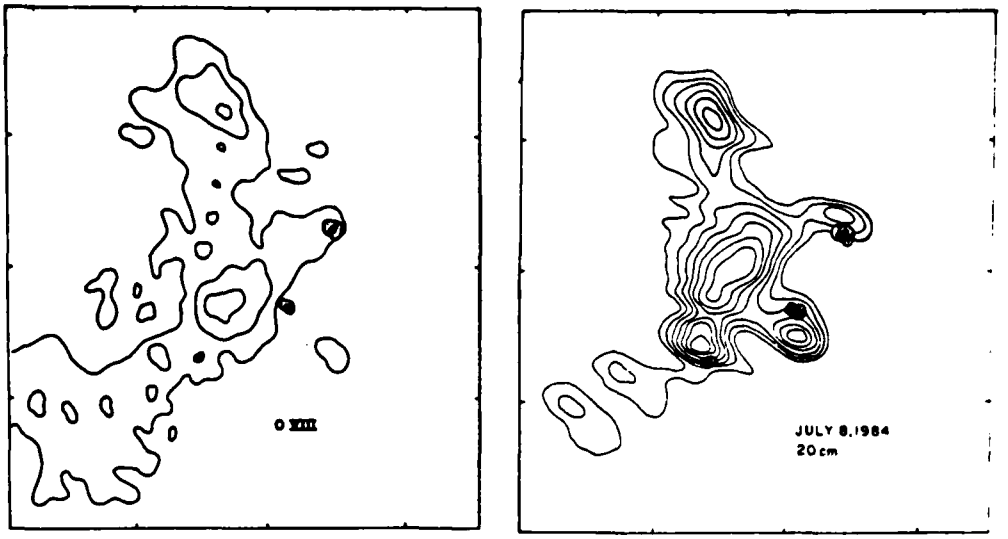

Fig. 3. A comparison of soft X-ray (Solar Maximum Mission Satellite) and 20 cm (Very Large Array) images of AR 4532 on 1984 July 8. The field of view of both images is the same, and the angular scale can be inferred from the 120" spacing between the fiducial marks on the axes. The contours of the 20 cm map mark levels of equal brightness temperature corresponding to 0.4, 0.5, 0.6...1.0 times the maximum brightness temperature of 1.4×10^6 K. The soft X-ray data were taken in the O VIII line (18.9 A) with contours corresponding to 4, 8, and 15 counts s^{-1} above a background level of 10 counts s^{-1} with a maximum signal of 20 counts s^{-1}. Here the sunspots are denoted by small black dots with a circle around them.

Fig. 4. A VLA snapshot map during a 10-second interval at 20 cm wavelength catches a powerful eruption at the site of particle acceleration. The energetic particles originate at the apex of coronal loops; some of them travel to the Earth where they interfere with radio communication and high-flying aircraft. The VLA contours are superposed on an Hα photograph of flare emission at lower levels in the solar atmosphere.

ACKNOWLEDGEMENTS

Radio astronomical studies of the Sun at Tufts University are supported under grant AFOSR-83-0019 with the Air Force Office of Scientific Research and contract N00014-86-K-0068 with the Office of Naval Research. Collaborative long-wavelength solar observations by Tufts University and the Observatoire de Paris are supported by National Science Foundation grant INT-8602285 and Centre National de la Recherche Scientifique grant 920038. Simultaneous SMM and VLA observations of the Sun are supported by NASA grant NAG 5-501. The Very Large Array is operated by Associated Universities Inc., under contract with the National Science Foundation.

REFERENCES

1. K. R. Lang, R. F. Willson, and G. Trottet, High-resolution VLA maps of the quiescent corona at 90-cm wavelength, Astron. Astrophys. 199, 325-328.

2. R. K. Shevgaonkar, M. R. Kundu, and P. D. Jackson, Variability of Metric Emission from the Sun, Astrophys. J., 329, 982-990.

3. K.R. Lang, and R. F. Willson, Astrophys. J. 319, 514-519 (1987). Also see M. F. Lantos-Jarry, Solar Phys., 15, 40 (1970).

4. A. Kerdraon, G. Trottet, K. R. Lang, and R. F. Willson, High-resolution VLA-Nancay observations of the Sun, this issue.

5. F. Axisa, Y. Avignon, M. J. Martres, M. Pick, and P. Simon, Solar Phys. 19, 110-127 (1971).

6. C. E. Alissandrakis, P. Lantos, and E. Nicolaidis, Solar Phys., 97, 267-282 (1985).

7. P. Lantos, C. E. Alissandrakis, T. Gergely, and M. R. Kundu, Solar Phys., 112, 325-340 (1987).

8. A. J. Hundhausen, The origin and propagation of coronal mass ejections, Solar Wind Six, in press (1988).

9. G. A. Dulk, K. V. Sheridan, S. F. Smerd, and G. L. Withbroe, Solar Phys. 52, 349-367 (1977).

10. K. R. Lang, and R. F. Willson, Adv. Space Res., 2, No. 11, 91-100 (1983).

11. K. R. Lang, and R. F. Willson, Adv. Space Res. 4, No. 7, 105-110 (1984).

12. K. R. Lang, R. F. Willson, K. L. Smith, and K. T. Strong, Astrophys. J., 322, 1035-1043, 1044-1051 (1987).

13. M. R. Kundu, and K. R. Lang, Science, 228, 9-15 (1985).

14. K. R. Lang, and R. F. Willson, Adv. Space Res. 6, No. 6, 97-100 (1986).

C6 HIGH RESOLUTION VLA - NANCAY OBSERVATIONS OF THE SUN *

Alain Kerdraon and Gérard Trottet
D.A.S.O.P.
Observatoire de Paris - Meudon; CNRS-UA 324
92195 MEUDON PRINCIPAL CEDEX
FRANCE

Kenneth R. Lang ** and Robert F. Willson
Department of Physics and Astronomy
Robinson Hall
Tufts University
MEDFORD, MA 02155
U.S.A.

* Presented at the XXVII COSPAR (Committee on Space Research) meeting in Helsinki, Finland, during Workshop XV - Scientific Planning for the Next Solar Maximum and Beyond on 26 July 1988.

** On sabbatical leave from Tufts University at the Observatoire de Paris - Meudon.

A B S T R A C T

The Very Large Array (VLA) and the Nançay Radioheliograph (NR) can be used in the 1990s to provide unique observations of the quiescent and active corona. The combined data can specify the evolution and magnetic structure at a variety of heights in the quiescent corona, from compact to extended structures such as loops, streamers and coronal holes. The scientific potential of simultaneous VLA - NR research is illustrated by observations of solar noise storms with hitherto unavailable resolution in space (VLA), time (NR). Unique information will also be provided for other types of solar bursts, leading to an improved understanding of solar activity during the coming maximum.

NOISE STORMS

Noise storms are the most common type of solar activity observed at metric wavelengths. They consist of a slowly-varying, wide-band continuum radiation with superposed short-lived, narrow-band bursts. These bursts have been designated Type I bursts to distinguish them from other types of solar bursts. The background continuum, which is usually observed between 50 and 350 MHz, normally continues for a few hours, while individual bursts have bandwidths between 2 and 10 MHz and durations of 0.1 to 2 seconds /1/.

Both the background continuum and the bursts are usually strongly circularly polarized (up to 100 %), but unpolarized bursts are occasionally observed. The sense of circular polarization is constant throughout the storm; it is attributed to the ordinary mode of plasma radiation in a strong magnetic field /3/.

Noise storms have been extensively studied with the Culgoora and Nançay radioheliographs, whose respective beamwidths are $\theta \sim 2.'0$ and $1.'3$ at 160 MHz. The resolved storm sources have sizes that tend to increase with height, and radiation at lower frequencies originates at higher altitudes

../..

(see Fig. 1 and /4/). These sources appear to be located in large-scale magnetic loops extending high into the corona from one or more active region /5/, /6/; suggesting plasma radiation within the legs of magnetic loops whose field lines diverge with height /7/, /8/. At a given frequency, successive Type I bursts may come from either a fixed or different locations /9/, /10/, and can have a variety of sizes /11/.

Storm sources were nevertheless often unresolved with the Culgoora and Nançay instruments, for they were often operating at the limits of their capability. The Very Large Array (VLA) now provides a substantial improvement in angular resolution, θ with $\theta \approx 5''$ at 92 cm wavelength (327 MHz) in the A configuration. It has been used to fully resolve one noise storm that had an elongated shape (40" x 200"), and contained four compact components, each 40" across, during the onset and early stages /12/. Such complexity may rule out the simple conical model, or at least involve its extension to include magnetic flux tubes or scattering on field-aligned density inhomogenities.

Because the VLA has limited integration times of $\tau \geq 3.3$ sec., simultaneous observations with the Nançay Radioheliograph ($\tau \geq 0.02$ sec.). are required to isolate individual bursts and to discriminate between the bursts and background continuum. We have therefore begun such observations during the period of common solar visibility (13 h to 16 h U.T.). This collaborative program will continue throughout the coming maximum in solar activity, thereby enhancing the scientific return of both ground-based and balloon or satellite-bourne instruments.

Simultaneous observations of a solar noise storm were carried out on 27 June 1987 with the VLA in the A configuration and operating at a signal frequency of 333.0 MHz with a bandwidth of 3.125 MHz; the Nançay Radioheliograph (NR) operated at 327.0 MHz with a 700 kHz bandwidth. The integrated signal from all the VLA interferometer pairs was plotted as a function of time and compared with a similar NR record to determine bursts that were detected by both telescopes.

The VLA was then used to make successive 10-second snapshot maps for intervals of several minutes centered at the common burst time. Two examples are shown in Fig. 2. The unpolarized and polarized bursts both have elongated shapes, but they originate in different sources that are separated by 60". The unpolarized burst (degree of circular polarization $\mathcal{J}_c \lesssim 10$ %) consists of a single elongated source with angular dimensions of 30" x 80", whereas the polarized one ($\mathcal{J}_c \approx 70$ %) contained two components separated by $\approx$20" and embedded within an elongated 40" x 60" structure. Although previous observers have established similar overall source sizes, the VLA has determined the elongated shape, source complexity and separate burst positions for the first time.

The NR has been used to determine the time profiles shown in Fig. 3. The unpolarized burst has a rapid rise and exponential decay; its most intense component is resolved in time with a duration of $\approx$ 2 sec. The time of the VLA snapshot map for one of them is designated by the horizontal bar. Successive 10-second snapshot maps throughout the two-minute interval indicate that the entire chain of bursts came from the same elongated source located at the same position. Subsequent highly-polarized chains of Type I bursts may originate in other sources, however, and the unpolarized burst definitely does.

PHYSICS OF SOLAR BURSTS

These previously-unpublished noise storm results illustrate the scientific potential of simultaneous VLA-NR observations of solar activity. They will be extended during the coming maximum to include other types of solar bursts, thereby providing constraints to theoretical models. The dynamical evolution of the source size is, for example, required as an input to models of the gradual and impulsive phases of solar flares. VLA-NR observations with high resolution in time, space and frequency are also required to provide fresh insights to the physics of burst phenomena such as pulsations /13/.

ACKNOWLEDGEMENTS

ACKNOWLEDGEMENTS

Radio astronomical studies of the Sun at Tufts University are supported under grant AFOSR-83-0019 with the Air Force Office of Scientific Research and contract N00014-86-K-0068 with the Office of Naval Research. Collaborative long-wavelength solar observations by Tufts University and the Observatoire de Paris are supported by National Science Foundation grant INT-8602285 and Centre National de la Recherche Scientifique grant 920038. Simultaneous SMM and VLA observations of the Sun are supported by NASA grant NAG 5-501. The Very Large Array is operated by Associated Universities Inc., under contract with the National Science Foundation. The Nançay Radioheliograph is supported by INSU. (Institut National des Sciences de l'Univers) by CNRS (Centre National de la Recherche Scientifique) and by Paris Observatory.

REFERENCES

1. O. Elgaroy, Solar Noise Storms, (New York : Pergamon Press, 1977).
2. C. Mercier, O. Elgaroy, A. Tlâmicha, and P. Zlobec, Solar Phys., 92 375-381 (1984).
3. K. Kai, P.B. Melrose, and S. Suzuki, Storms, in Solar Radiophysics, ed. D.J. McLean and N.R. Labrum (New York : Cambridge University Press, 1985), pp. 415-442.
4. J.V. Sheridan, N.R. Labrum, W.J. Payten, G.J. Nelson, and E.R. Hill, Solar Phys., 83 167-177(1983).
5. M.F. Lantos-Jarry, Solar Phys. 15, 40-47 (1970).
6. P. Lantos, A. Kerdraon, G.G. Rapley, and R.D. Bentley, Astron. Astrophys. 101, 33-38 (1981).
7. D.J. McLean, Proc. Astron. Soc. Austr. 4, 132-138 (1981).
8. K.V. Sheridan, Storm-Source structure from two-dimensional radio-heliograph observations at meter wavelengths, in Solar Radio Storms, ed. A.O. Benz and P. Zlobec (Osservatorio Astronomico : Trieste, 1982), pp. 12-25.
9. A. Kerdraon, and C. Mercier, New observational results on noise storms, in Solar Radio Storms, ed. A.O. Benz and P. Zlobec (Osservatorio Astronomico : Trieste, 1982), pp. 27-37.
10. R.A. Duncan, Solar Phys. 97, 137-182 (1985).
11. A. Kerdraon, Astron. Astrophys. 71, 266-268 (1979).
12. K.R. Lang, and R.F. Willson, Astrophys. J. 319, 514-519 (1987).
13. G. Trottet, A. Kerdraon, A.O. Benz, and R. Treumann, Astron. Astrophys. 93, 129-132 (1981).

FIGURE LEGENDS

Fig. 1. Multiple-frequency observations of a solar noise storm with the Nançay Radioheliograph on 3 February 1986 at 150 and 164 MHz (small solid circle), 327 MHz (dashed circle) and 408 MHz (dark spot). The square denotes the position of the associated active region in the underlying photosphere. The noise storm is displaced away from a radial projection above the active region. Lower frequencies are emitted in higher regions, and the source size tends to increase with height.

Fig. 2. Very Large Array (VLA) synthesis maps for ten second intervals during a polarized burst ($\sim$50 % - right) and an unpolarized burst (left) on 27 June 1987. The two intervals began at 14h 30m 36.0s and 14h 46m 16s U.T., respectively. The fiducial marks on the axes are separated by 60", and the contours mark levels of equal brightness temperature, T_B , with an outermost contour and contour interval of 4.4×10^7 K. The peak brightness temperatures for the two intervals are 6.2×10^8 K and 3.1×10^8 K, respectively.The synthesized beam is denoted by the black spot in the lower left-hand corner; it has an angular extent of $\theta \approx 6"$. The time profiles for the two bursts are given in Figure 3.

Fig. 3. Intensity plotted as a function of time for an unpolarized burst (top) and a polarized burst (50 % - bottom) with 0.5 second time resolution over two minutes on 27 June 1987. These time profiles were taken with the Nançay Radioheliograph at the same observing frequency as the VLA ($\sim$327 MHz) and included the times of the 10 second VLA maps shown in Figure 2.

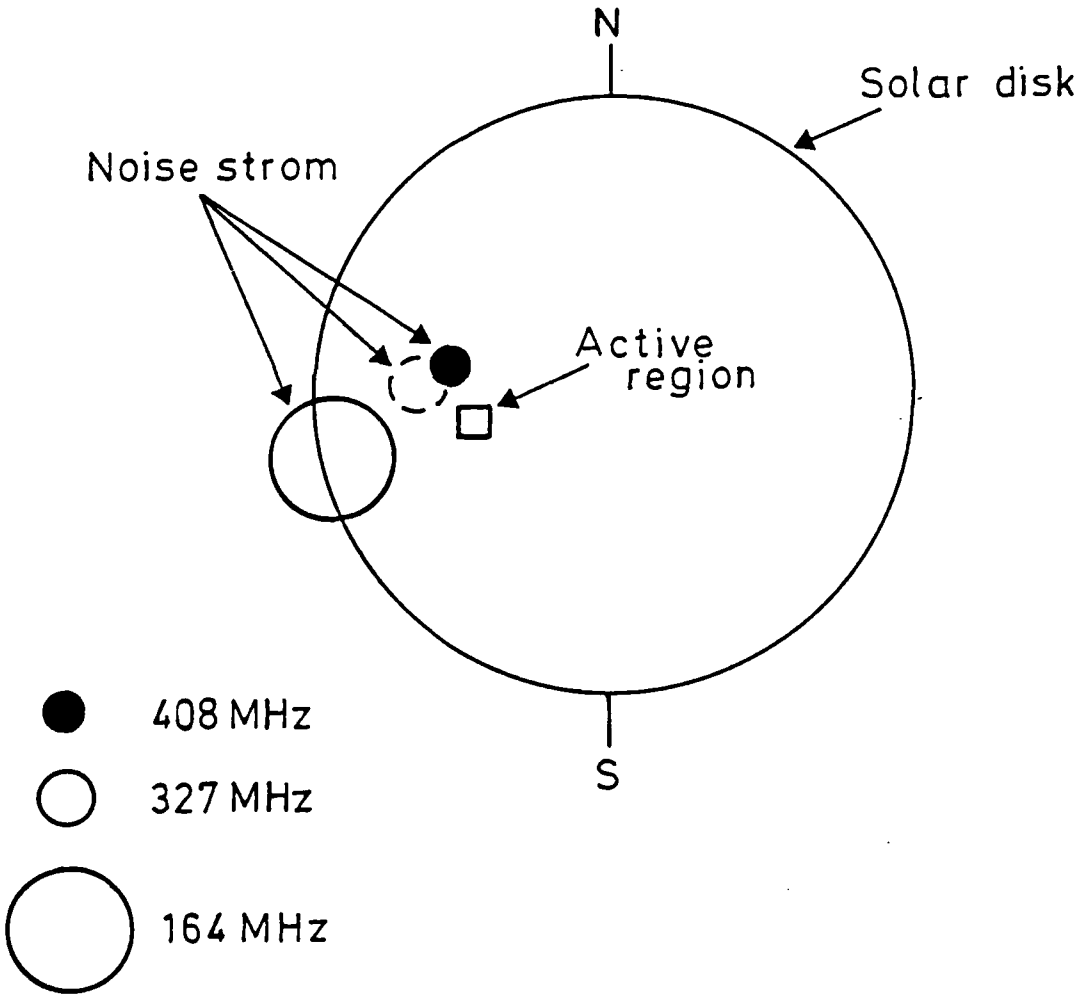
N
Solar disk
Noise strom
Active region
S
408 MHz
327 MHz
164 MHz

Figure 1

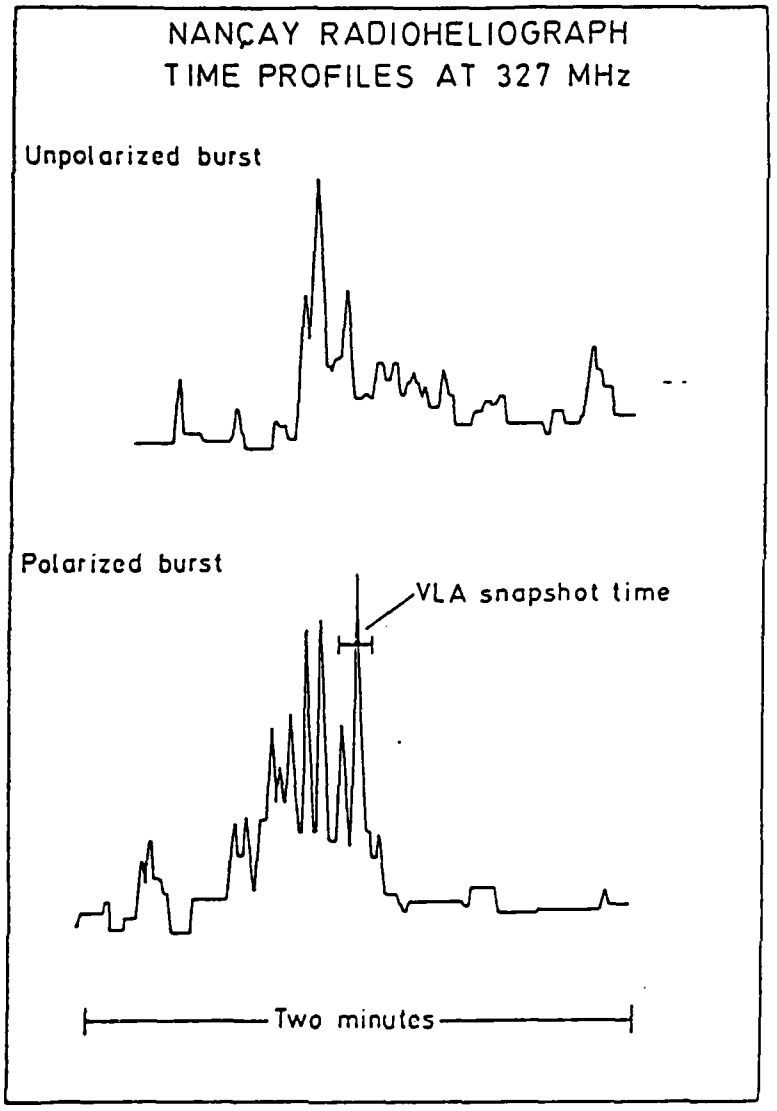

Figure 3

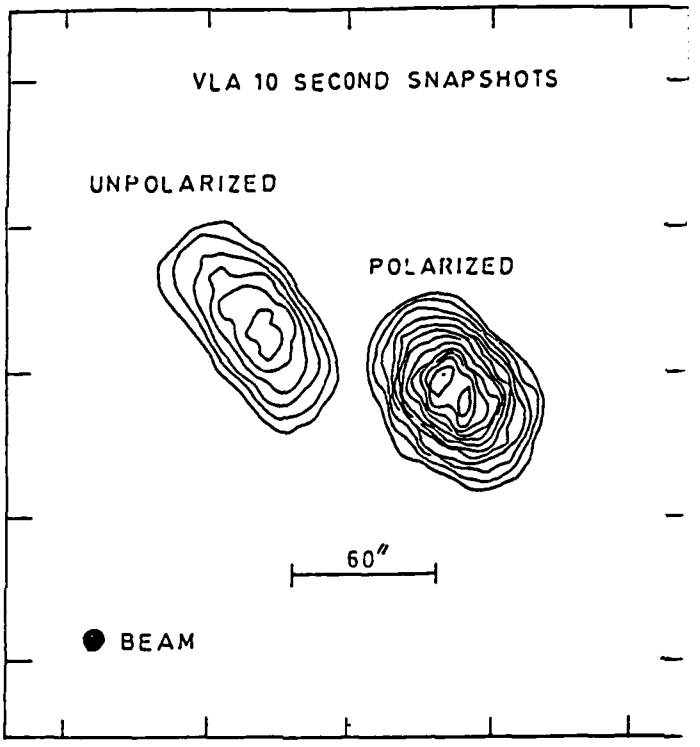

Figure 2

THE ASTROPHYSICAL JOURNAL, 344:L77–L80, 1989 September 15

C7. TIME-CORRELATED BURSTS FROM WIDELY SEPARATED SOLAR ACTIVE REGIONS AT 91.6 CENTIMETER WAVELENGTH

KENNETH R. LANG AND ROBERT F. WILLSON
Department of Physics and Astronomy, Tufts University
Received 1989 March 10; accepted 1989 June 28

ABSTRACT

VLA synthesis maps at 20.7 cm wavelength, VLA snapshot maps at 91.6 cm wavelength, and NSO–Kitt Peak photospheric magnetograms indicate that time-correlated radio bursts can occur in active regions on opposite sides of the solar equator. These regions are apparently linked by large-scale, transequatorial magnetic loops that are at least 2.6×10^5 km (or 6′) long. Energetic electrons accelerated during a radio burst in one active region probably move along this magnetic conduit at velocities of about one-third the velocity of light, thereby triggering radio bursts in the other active region.

Subject headings: Sun: corona — Sun: flares — Sun: magnetic fields — Sun: radio radiation — Sun: X-rays

I. INTRODUCTION

Evidence for correlated radio bursts from widely separated regions on the Sun was presented by Kai (1969) when he showed a type III burst can be followed within 10 s by a reverse-slope type III burst at distances $L > 10^5$ km. This suggested that electron beams are channeled along a large-scale magnetic loop at relativistic speeds $v \sim 0.3c$, first moving upward from the primary acceleration sight and then downward in a remote leg of the loop. Tang and Moore (1982) demonstrated that two large flares produced Hα brightenings in quiet regions more than 10^5 km away from the flaring active region, and that these remote brightenings were accompanied by reverse-slope type III bursts. They suggested that the Hα brightenings were initiated by the nonthermal electrons producing the secondary radio burst.

Rust and Webb (1977) had, in the meantime, shown that active region flares can be associated with sudden X-ray enhancements of large-scale loops or arcades of loops that extend outside the flaring active regions to distances $L > 10^5$ km, but that subsequent Hα brightenings at the remote end of the interconnecting X-ray loop suggested shocklike excitation velocities of 300–1200 km s^{-1}.

Secondary microwave bursts caused by a distant primary one have also been reported by Kundu, Rust, and Bobrowsky (1983) and Nakajima *et al.* (1985); they respectively observed remote unpolarized microwave bursts accompanied by Hα brightening and remote polarized bursts with no Hα counterpart. In both cases, the relativistic velocity required by the measured time delay and the spatial separation indicated that the secondary burst was excited by high-energy electrons produced in the primary burst sight.

Simnett and Dennis (1987) have more recently shown that rapid ($\leqslant 100$ s) soft X-ray bursts can be produced in widely separated active regions connected by extensive coronal magnetic loops. Kundu, Schmahl, and Fu (1989), observing with the VLA at 6 and 21 cm, have inferred the presence of a large-scale ($L > 10^5$ km), transequatorial arch from near-simultaneous changes in the microwave emission of two widely separated active regions. In the latter case, a coronal instability associated with a filament disruption was supposed to produce simultaneous effects in the two active regions.

In this *Letter* we also present evidence for interactive bursts from active regions on opposite sides of the solar equator. Our 91.6 cm VLA observations, presented in § II, provide high-resolution, two-dimensional structural information about these large-scale interactions, while the simultaneous 20.7 cm VLA data and photospheric magnetograms provide information about the underlying active regions. In § III we note that secondary soft X-ray emission was also detected and interpret our observations in terms of energetic electrons that are channeled along large-scale, otherwise invisible magnetic loops connecting active regions on either side of the solar equator.

II. OBSERVATIONS

The Sun was observed with the VLA in the C/D hybrid configuration between 1315 and 1610 UT on 1988 May 15 using 27 antennas at 20.7 cm wavelength (1446 MHz) and 19 antennas at 91.6 cm wavelength (327.5 MHz) with respective bandwidths of 12.5 and 3.125 MHz. The individual antenna beamwidths were 138′ and 32′ at 91.6 and 20.7 cm, respectively; we were therefore able to make full-disk synthesis maps at both wavelengths with respective synthesized beamwidths of 55″ × 80″ and 12″.4 × 18″. The 20%–25% uncertainty in the absolute calibration of the solar brightness temperatures has been discussed by Lang and Willson (1989). Although all four Stokes parameters were sampled every 3.3 s, there was no detectable polarization at either wavelength, so our 3 hr synthesis maps refer to the total intensity, I. Their contours mark levels of equal brightness temperature, T_B.

These maps are shown in Figure 1. The 20.7 cm emission is concentrated within small-scale (angular sizes $\theta \approx 1'$) sources above individual active regions in which bright Hα plage is also found. The outermost contour and contour interval of the 20.7 cm map are equal to $T_B = 2.5 \times 10^5$ K, with a peak brightness temperature of $T_B = 2.5 \times 10^6$ K. The 20.7 cm brightness temperatures are therefore similar to the electron temperatures of the hot plasma trapped within coronal loops above active regions, suggesting that these loops are optically thick to thermal bremsstrahlung (Lang, Willson, and Gaizauskas 1983). Such optically thick loops would account for the lack of detectable circular polarization.

In contrast to the 20.7 cm emission, the most intense 91.6 cm radiation is concentrated within large-scale ($\theta \approx 3'$) structures that are not associated with active regions; the quiet Sun, 91.6

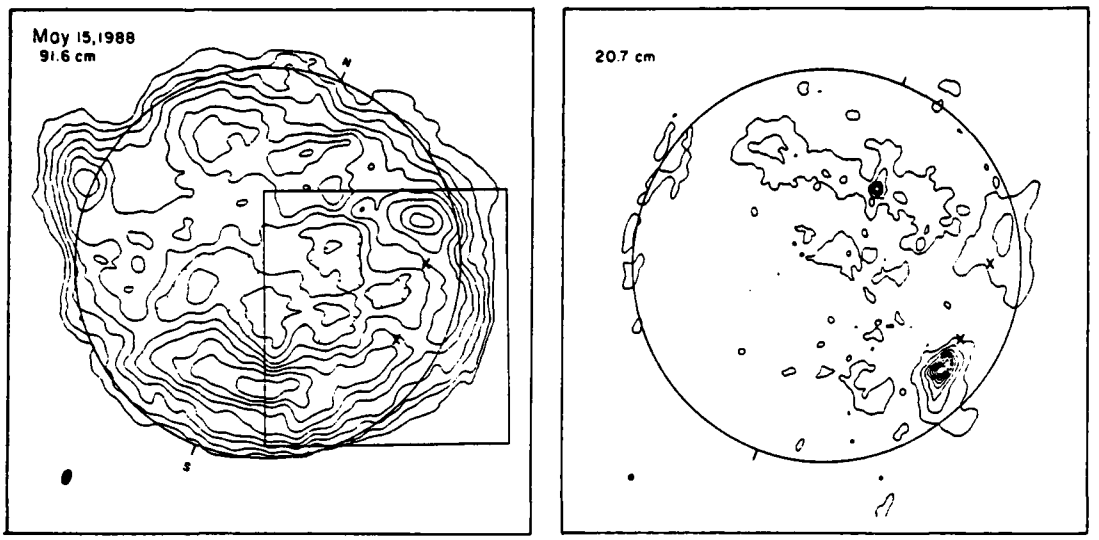

FIG. 1.—Very Large Array (VLA) 3 hr synthesis maps of the total intensity, I, from the visible solar disk at 91.6 cm (*left*) and 20.7 cm (*right*). The circle denotes the visible solar limb, the tick marks denote solar north and south, and the synthesized beamwidths are denoted by the dark spots in the lower left-hand corners. The boxed area of the 91.6 cm map denotes the field of view for the 3.3 s synthesis maps shown in Fig. 3; they illustrate interacting flare emission from the two places marked by X on opposite sides of the solar equator.

cm emission is instead associated with dark, elongated filaments (also see Lang and Willson 1989). The contours of the 91.6 cm map mark levels of equal brightness temperature, T_B, with an outermost contour of $T_B = 7.8 \times 10^4$ K, a contour interval of 7.8×10^4 K, and a peak brightness temperature of $T_B = 7.8 \times 10^5$ K.

The boxed area of the 91.6 cm map denotes the field of view for the snapshot maps shown in Figure 3; it contains two X marks that denote the location of the two groups of bursts whose temporal evolution is shown in Figure 2. The 91.6 cm time profiles indicates these two groups, beginning at ~1537 and ~1540 UT. The second group was associated with a weak soft X-ray flare (*dashed line*, class B1.5). Both groups were also detected at 122 cm wavelength using the Air Force Solar Patrol Telescope at the Sagamore Hill observatory, but with more intense emission than at 91.6 cm, indicating nonthermal radiation with a positive spectral index in both cases. The Sagamore Hill radio data were supplied by Ed Cliver. The only available Hα data (SOON) showed Hα brightening at 1537 UT in AR 5014 (S17 W57 at 00 UT on May 15). The SOON Hα data were supplied by Judy Nelson of the Goddard Space Flight Center. Active region AR 5014 was also active on the days before and after May 15 (see *Solar Geophysical Data* Hα flare reports). There was no detectable circular polarization for

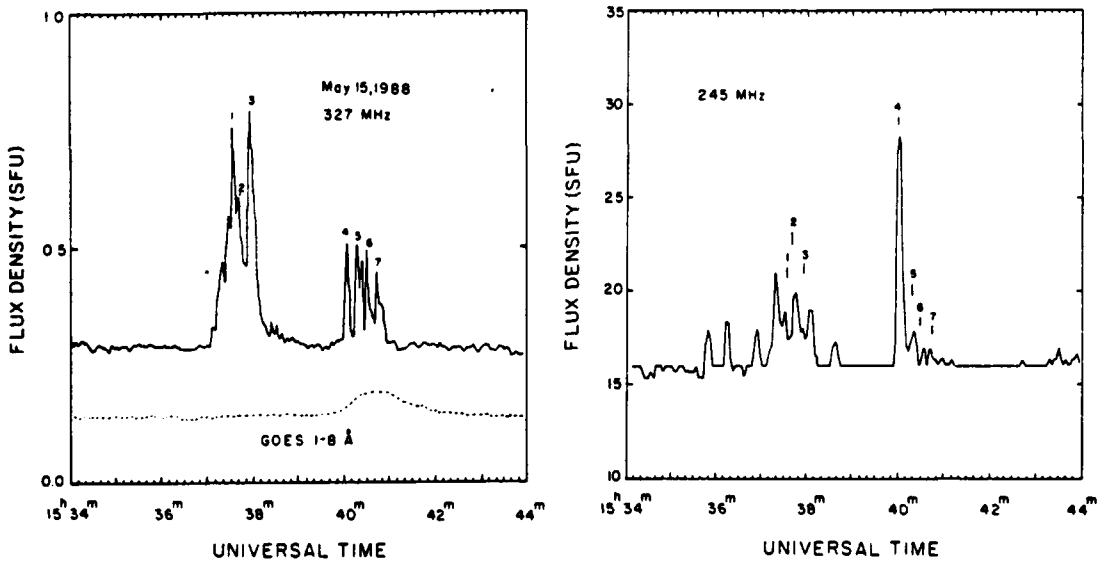

FIG. 2.—The time profile of the 91.6 cm (327 MHz—*left*) emission detected with one of the short VLA baselines (fringe spacing of about 5') is compared with that observed at 122 cm (245 MHz—*right*) over the same time interval on 1988 May 15 with the Air Force Solar Patrol telescope at the Sagamore Hill Radio Observatory. A plot of the *GOES* satellite soft X-ray flux is also shown as a dashed line. The numbers above the individual bursts refer to the times of the VLA 3.3 snapshot maps shown in Fig. 3.

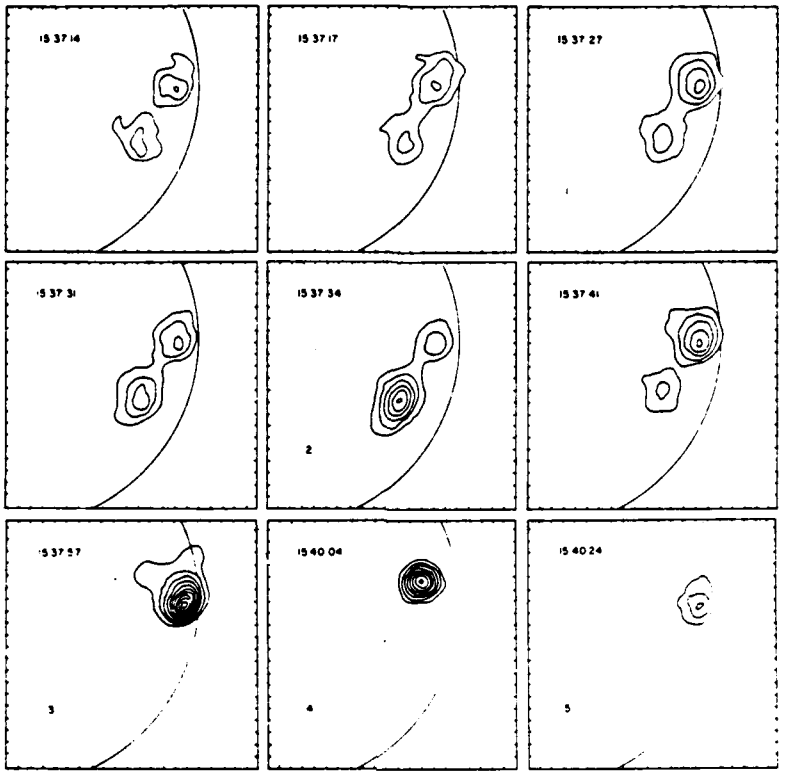

FIG. 3.—Very Large Array 3.3 s snapshot maps at 91.6 cm (327 MHz) for different times during the burst shown in Fig. 2. The locations of the bursts correspond to the crosses on the 90 cm synthesis map shown in Fig. 1. Note how the burst location shifts between the two regions, suggesting activation in the legs of one or more large-scale magnetic loops that cross the solar equator.

the 91.6 cm bursts (degree of circular polarization $\rho_c < 8\%$), suggesting type III bursts rather than type I, and there was no detectable burst emission at 20.7 cm (flux $S < 0.2$ SFU).

In Figure 3 we show 3.3 s snapshot maps of the individual bursts numbered in Figure 2. During the early states of the first group of bursts, emission was found in both northern and southern sources, each about 2'.5 in size with a peak brightness temperature of $T_B \sim 3 \times 10^6$ K and an angular separation of about 5'.5. Here the contour intervals are in units of equal brightness temperature, T_B, with an outermost contour and contour interval of 1×10^6 K. The angular scale may be inferred from the 1' spacing between the fiducial marks on the axes.

The locations of the northern and southern burst sources are denoted by crosses in Figure 1; they are displaced equatorward from two active regions shown in the 20.7 cm map, suggesting emission from the legs of large-scale coronal loops that straddle the equator and join the two active regions.

The presence of a large-scale magnetic conduit that links active regions on two sides of the solar equator is also inferred from subsequent burst emission that was localized first in the northern source, then in the southern one and thereafter in the northern region again. Such hypothetical, and otherwise invisible, transequatorial loops are further suggested by the photospheric magnetogram on 1988 May 15 (Fig. 4 [Pl. L5]); it indicates that large areas of opposite leading magnetic polarity underlie the northern and southern burst sources.

III. DISCUSSION

Our interpretation of correlated burst emission over widely separated areas does not differ substantially from that of Kai (1969), Tang and Moore (1982), Kundu, Rust, and Bobrowsky (1983), and Nakajima *et al.* (1985). Examination of the NSO–Kitt Peak magnetogram for 1988 May 15 indicates that the positions of the two burst sources (designated by two X marks in Fig. 1) are displaced equatorward from two active regions; designated AR 5012 and AR 5014, near the northwest and southwest limb, respectively. We propose that the two active regions are linked by one or more large-scale, otherwise invisible magnetic loops that stretch across the solar equator connecting regions separated by 6', over a distance of at least 2.6×10^5 km. Some triggering agent travels across this distance, producing bursts with time delays of ~3–6 s at velocities up to 10^5 km s^{-1}, or about one-third the velocity of light. Energetic electrons are probably accelerated during a burst in one active region and hurled at these velocities along large-scale magnetic loops to produce bursts in another active region located at the other footpoint of the loop.

Radio astronomical studies of the Sun at Tufts University are supported under grant AFOSR-89-0147 with the Air Force Office of Scientific Research. The Very Large Array is operated by Associated Universities, Inc., under contract with the National Science Foundation. The data presented in this *Letter* were taken during collaborative long-wavelength solar observations by Tufts University and the Observatoire de Paris-Meudon, under the support of National Science Foundation grant INT-8602285 and Centre National de la Recherche Scientifique grant 920038.

REFERENCES

Kai, K. 1969, *Proc. Astr. Soc. Australia*, **1**, 186.
Kundu, M. R., Rust, D. M., and Bobrowsky, M. 1983, *Ap. J.*, **265**, 1084.
Kundu, M. R., Schmahl, E. J., and Fu, Q.-J. 1989, *Ap. J.*, **336**, 1078.
Lang, K. R., and Willson, R. F. 1989, *Ap. J. (Letters)*, **344**, L73.
Lang, K. R., Willson, R. F., and Gaizauskas, V. 1983, *Ap. J.*, **267**, 455.
Nakajima, H., Dennis, B. R., Hoyng, P., Nelson, G., Kosugi, T., and Kai, K. 1985, *Ap. J.*, **288**, 806.
Rust, D. M., and Webb, D. F. 1977, *Solar Phys.*, **54**, 403.
Simnett, G. F., and Dennis, B. R. 1987, in *Rapid Fluctuations in Solar Flares*, ed. B. R. Dennis and L. E. Orwig (NASA Conf. Pub. 2449), p. 123.
Tang, F., and Moore, R. L. 1982, *Solar Phys.*, **77**, 263.

KENNETH R. LANG and ROBERT F. WILLSON: Department of Physics and Astronomy, Robinson Hall, Tufts University, Medford, MA 02155

FIG. 4.—The contours of a 3.3 s VLA snapshot map showing the 91.6 cm burst emission at 153731 UT is overlaid on a National Solar Observatory (NSO)–Kitt Peak magnetogram. This comparison indicates that the hypothetical transequatorial loops connecting 91.6 cm burst locations may also connect underlying photospheric regions of opposite leading magnetic polarity. Magnetogram courtesy of Jack Harvey.

LANG AND WILLSON (*see* 344, L79)

THE ASTROPHYSICAL JOURNAL, 344:L73–L75, 1989 September 15

C8. RADIO EMISSION FROM QUIESCENT SOLAR FILAMENTS AT 91.6 CENTIMETER WAVELENGTH

KENNETH R. LANG AND ROBERT F. WILLSON
Department of Physics and Astronomy, Tufts University
Received 1989 March 10; accepted 1989 June 28

ABSTRACT

Full-disk VLA synthesis maps of the quiet Sun at 91.6 cm wavelength reveal large-scale (angular size $\theta \sim 3'$), hot (brightness temperatures $T_B \sim 3 \times 10^5$ K) structures that overlie dark Hα filaments. The similarity between the shape, position, elongation, and orientation of the radio and optical features suggests their close association. We interpret the 91.6 cm emission in terms of the thermal bremsstrahlung of a hot sheath that envelops the cooler Hα filament. A power-law gradient in pressure provides a better match to the observations than a constant pressure model. Variable physical parameters of the sheath, such as width, electron density, and electron temperature, can explain controversial reports of the detection of, or failure to detect, the meter-wavelength counterpart of Hα filaments.

Subject headings: Sun: corona — Sun: magnetic fields — Sun: prominences — Sun: radio radiation

I. INTRODUCTION

Filaments are cooler than the surrounding corona and therefore appear as depressions in the quiet Sun background at centimeter wavelengths (Gary 1986; Kundu, Melozzi, and Shevgaonkar 1986); the cool filaments can also appear as depressions at millimeter wavelengths (Schmahl, Bobrowksy, and Kundu 1981). Regions that overlie filaments can now be detected using the VLA at the longer 91.6 cm wavelength; the higher temperatures produce regions of increased emission when compared with the surrounding quiet Sun background.

Previous observations have, however, led to an ongoing controversy about the optical counterparts of the quiescent, or nonflaring, solar radiation at meter wavelengths. A statistical study of numerous one-dimensional Nançay scans suggested that many quiescent meter-wavelength sources are associated with filament corridors as seen on Hα synoptic maps (Axisa *et al.* 1971), but subsequent two-dimensional maps indicated that most filaments have no radio counterpart at meter wavelengths (Alissandrakis, Lantos, and Nicolaidis 1985; Lantos *et al.* 1987).

The VLA provides an order-of-magnitude improvement in angular resolution over all previous meter-wavelength investigations of the quiet Sun and might therefore help resolve this controversy. The first VLA observations of the quiescent corona at 92 cm wavelength indicated no systematic association of any of the radio sources with any optical counterpart, including active regions, filaments, sunspots and the magnetic neutral line in the underlying photosphere (Lang, Willson, and Trottet 1987). Full-disk VLA observations by Shevgaonkar, Kundu, and Jackson (1988) indicated that the 90 cm sources may be identified as streamers above Hα filaments. However, our comparison of their data with Hα observations (*Solar Geophysical Data*) indicates that many of the intense 90 cm sources do not overlie Hα filaments.

One probable source of confusion is noise storms, the most common form of solar activity at meter wavelengths. The numerous type I bursts and background continuum of noise storms have been associated with coronal loop structures detected during the *Skylab* mission at soft X-ray wavelengths (Stewart and Vorpahl 1977; Gergely *et al.* 1980) as well as with large-scale EUV loops (Stewart, Brueckner, and Dere 1986). VLA observations at 91.6 cm wavelength confirm the location of noise storms in large-scale magnetic loops that either overlie coronal loops within individual active regions or connect these regions with more distant areas on the Sun (Lang and Willson 1987); such conclusions were also anticipated by metric wavelength observations with the Nançay Radioheliograph (Lantos-Jarry 1970; Mercier *et al.* 1984). Detection of the meter-wavelength counterpart of filaments requires observations when the intense noise storms are not present.

In this *Letter* we present VLA 91.6 cm synthesis maps during quiescent periods without any noise storm activity. In § II we show that there is an excellent association of some 91.6 cm sources with Hα filaments. The radio filaments are enhanced over the surrounding quiescent emission, rather than depressed. Not all Hα filaments, however, exhibit detectable 91.6 cm counterparts. In § III we interpret some quiescent 91.6 cm sources in terms of the thermal radiation of a sheath overlying a Hα filament, and with temperatures intermediate between those of its Hα counterpart and the surrounding corona.

II. OBSERVATIONS

The Sun was observed with the VLA in the C/D hybrid configuration between 1315 and 1610 UT on 1988 May 15 using 27 antennas at 20.7 cm wavelength (1446 MHz) and 19 antennas at 91.6 cm wavelength (327.5 MHz) with respective bandwidths of 12.5 and 3.125 MHz. The full-disk synthesis maps at 20.7 cm are given elsewhere (Lang and Willson 1989), where they are used to identify active regions that interact via large-scale, transequatorial magnetic loops. Here we focus on the full-disk 91.6 cm synthesis map shown in Figure 1 (Plate L4) (*left*). Although all four Stokes parameters were sampled, there was no detectable circular polarization, so our 3 hr synthesis map refers to the total intensity, I. Burst data have been removed prior to making this synthesis map.

All the data were calibrated by observing 3C 48 for 5 minutes every 40 minutes; the flux density of 3C 48 was assumed to be 47.0 and 14.6 Jy at 91.6 and 20.7 cm, respectively.

Because the VLA lacks enough short baselines to adequately

sample the full solar disk at 91.6 cm, the 3 hr dirty, or uncleaned, map exhibited a negative ring surrounding the radio disk. This artifact has been previously discussed by Shevgaonkar, Kundu, and Jackson (1988). It was removed by using the maximum entropy algorithm (MEM) on the dirty map together with an assumed full-disk model that accounted for the missing short-baseline flux. This procedure has been discussed by Cornwell (1986) and Bastian (1988).

The MEM method converged after 15 iterations to indicate a total solar flux of 15–17 SFU, depending on the assumed size of the solar disk at 91.6 cm wavelength (we varied its radius between 1.50 and 1.20 $R_\odot$). This flux is 3–5 SFU lower than the 20 SFU value that is extrapolated from spectral data obtained on 1988 May 15 at the Sagamore Hill Radio Observatory (data courtesy of Ed Cliver).

Uncertainties in the absolute calibration of the VLA solar observations have been discussed by Kundu, Schmahl, and Fu (1989) and by Shevgaonkar, Kundu, and Jackson (1988). One uncertainty results from a software error in the program that applies the system temperatures of solar calibration antennas to other antennas (Ray Gonzalez, private communication). This uncertainty results in an underestimate of brightness temperatures by a factor of 1.8, and our data have been corrected for this error. Another uncertainty is attributed to measurements of the high-temperature noise diodes on the solar calibration antennas; they are not measured regularly enough at the VLA to assure accurate measurements of the system temperature. The lower total solar flux that we derived from the maximum entropy procedure probably reflects this uncertainty in the system temperature, and our inferred brightness temperatures may therefore be in error by 20%–25%. This is reflected in the stated uncertainties of our measurements and the error bars of the plots of them.

The contours of the resulting map (Fig. 1, *left*) mark levels of equal brightness temperature, T_B, with an outermost contour of $T_B = 7.8 \times 10^4$ K, a contour interval of 7.8×10^4 K, and peak brightness temperature of $T_B = 7.8 \times 10^5$ K. The mean brightness temperatures of the elongated sources marked A and B are, for example, estimated to be $T_B \sim 3 \times 10^5$ K above the surrounding quiet Sun level of $T_B \sim 4 \times 10^5$ K, with an uncertainty of 20%.

An Hα photograph taken on the same day (1988 May 15) is also shown in Figure 1 (*right*); it contains several dark, elongated filaments. Two of these have counterparts in the 91.6 cm map with similar shapes, positions, elongations, and orientations; they are designated by the letters A and B in the 91.6 cm map. The smaller filaments seen in the north central regions also seem to have 91.6 cm counterparts, but there is no increased 91.6 cm emission in the vicinity of the dark filaments that lie near the northeast and southeast limbs (marked C and E on the 91.6 cm map).

The intense 91.6 cm emission detected near the equator on the east limb (marked D) may be due to a coronal streamer. Sacramento Peak coronagraph data (*Solar Geophysical Data*) show coronal material in this region, as well as those that have no detectable 91.6 cm radiation. No underlying active regions or filaments were visible as the Sun rotated and the limb region turned into view during the following days.

Depressions in the 91.6 cm radiation are found in the central equatorial regions (*hatched regions*). They may be at least partly due to coronal holes, but the only available He 10830 data, taken on May 14, do not exhibit a detectable equatorial coronal hole. Examination of the 91.6 cm maps for shorter time scales showed no evidence for variable features on time scales of a few tens of minutes, so our data does not confirm reports of such variations by Shevgaonkar, Kundu, and Jackson (1988).

III. DISCUSSION

The similarity in shape, position, elongation, and orientation strongly suggests that the radio emission from sources A and B is associated with the underlying dark filaments detected in the Hα photograph, but the radio emission could also be associated with bright Hα plage and their associated higher magnetic fields. The most intense emission from source A coincides with a dark filament rather than plage, and the most intense part of source B corresponds to the largest part of the underlying filament. Moreover, the weaker emission from both sources has the same shape and orientation as the associated narrow, elongated filaments. We therefore attribute the radio emission to these filaments, while noticing that Hα plage might also play a role in enhanced 91.6 cm emission.

We therefore interpret the regions of increased 91.6 cm emission around filaments (sources A and B) in terms of a hot sheath that envelops the cooler Hα filaments; such a surrounding sheath is suggested by the fact that the radio wavelength features are similar in shape to, but wider, longer and hotter than, their optical counterparts. The mean 91.6 cm brightness temperatures of $T_B \sim 3 \times 10^5$ K, for example, lie between the electron temperatures of the cool Hα filaments and the electron temperature of the surrounding corona.

In order to gain a quantitative view of the transition sheath, we compare our observations with the data and models given by Kundu, Melozzi, and Shevgaonkar (1986). Their VLA observations at the shorter 6 and 20 cm wavelengths indicated radio depressions above Hα filaments, in comparison with the hot surrounding corona, but a transition sheath was indicated by the fact that the radio filaments are larger in size than their optical counterparts and that the brightness temperature, T_B, of the radio filaments increases with wavelength from $T_B \sim 1.5 \times 10^4$ K at 6 cm to $T_B \sim 5 \times 10^4$ K at 20 cm. Our higher brightness temperature of $T_B \sim 3 \times 10^5$ K at the longer 91.6 cm wavelength can be explained by the larger optical depth of thermal bremsstrahlung from the transition sheath at longer wavelengths, and the fact that the 91.6 cm sheath is seen in emission can be explained by the relatively low optical depth of the low-density corona.

To be exact, we have assumed that the variation of temperature with height in the transition sheath is that given by Kundu, Melozzi, and Shevgaonkar (1986); their data resulted from an assumed balance between the thermal energy conducted in from the corona and the energy radiated away. These temperatures, T, were then combined with three pressure models to infer the electron density, N, and the equation of transfer was solved assuming free-free emission with these values of temperature and density. The three models were a constant pressure model $P = NT = 3 \times 10^{14}$ cm^{-3} K, and two power-law models $P = NT = aT^n$, with $a = 2.5 \times 10^{17}$, $n = -0.58$, and $a = 4 \times 10^{17}$, $n = -0.62$. The calculated brightness temperatures of two models are shown in Figure 2 together with our measurements at 91.6 cm and those of other observers at shorter wavelengths. This figure indicates that the brightness temperature of the constant pressure model is too high at both 20 cm and 90 cm, with respective values of $T_B \sim 9 \times 10^4$ K and $T_B \sim 6 \times 10^5$ K. The power-law models are more in accord with the observational data; at 20 cm and 90

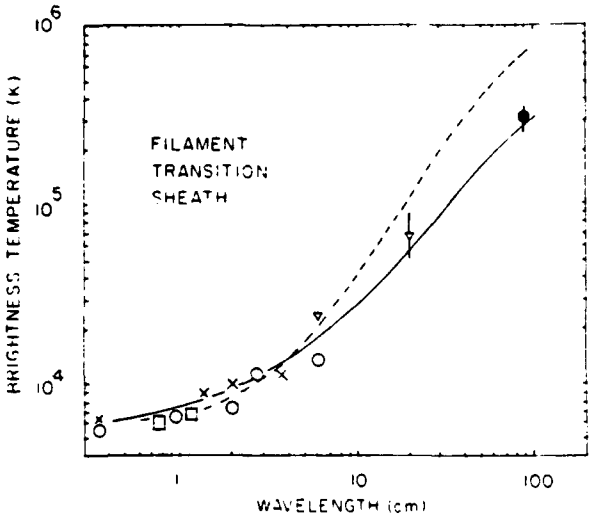

FIG. 2.—Calculated brightness temperatures for a constant pressure $P = 3 \times 10^{14}$ cm^{-3} K (*dashed line*) and a power-law pressure $P = 2.5 \times 10^{17} T^{-0.38}$ with $dT/dh = 0$ at height $h = 0$ (*solid line*). The observed temperature at 91.6 cm (*filled circle*) is from this *Letter*, whereas the other values (*crosses, open circles, open squares,* and *open triangles*) are from Kundu, Melozzi, and Shevgaonkar (1986) with their 6 and 20 cm measurements increased by a factor of 1.7 due to the detection of a software calibration error. The brightness temperatures refer to mean values over the radio source.

cm they both produce respective values of $T_B \sim 5 \times 10^4$ K and $T_B \sim 3 \times 10^5$ K.

So, the observed 91.6 cm structures that are associated with these Hα filaments may be interpreted as the thermal bremsstrahlung of a hot (electron temperature $T_e \approx 3 \times 10^5$ K) sheath that envelops a Hα filament. Such a sheath acts as the boundary between the filament and the surrounding 10^6 K corona. A loop thickness of $L \approx 10^9$ cm, or about 1/50 of the $10' \approx 5 \times 10^{10}$ cm extent of the radio sources A and B, may be assumed; such a thickness is consistent with the models of Kundu, Melozzi, and Shevgaonkar (1986). If the hypothesized sheath were substantially thinner than the assumed thickness of $L \approx 10^9$ cm, then the optical depth for thermal bremsstrahlung would be much smaller, and the optically thin sheath might not be detectable. And if the electron density of the sheath was only slightly higher, then its plasma frequency would exceed our observing frequency, and the sheath radiation could not propagate out to be observed. Variable physical parameters of the sheath might therefore easily explain why the elusive meter-wavelength counterpart of Hα filaments is only sometimes observed; just the right thickness, electron density, and electron temperature are required for detection.

Radio astronomical studies of the Sun at Tufts University are supported under grant AFOSR-89-0147 with the Air Force Office of Scientific Research. The Very Large Array is operated by Associated Universities, Inc., under contract with the National Science Foundation. The data presented in this *Letter* were taken during collaborative long-wavelength solar observations by Tufts University and the Observatoire de Paris-Meudon, under the support of National Science Foundation grant INT-8602285 and Centre National de la Recherche Scientifique grant 920038.

REFERENCES

Alissandrakis, C. E., Lantos, P., and Nicolaidis, E. 1985, *Solar Phys.*, **97**, 267.
Axisa, F., Avignon, Y., Martres, M. J., Pick, M., and Simon, P. 1971, *Solar Phys.*, **19**, 110.
Bastian, T. 1988, Ph.D. thesis, University of Colorado.
Cornwall, T. 1986, in "Synthesis Imaging" (NRAO Summer School Course Notes), p. 117.
Gary, D. E. 1986, in *Coronal and Prominence Plasmas*, ed. A. I. Poland (NASA Conf. Pub. 2442), p. 121.
Gergely, T. E., Kundu, M. R., Golub, L., and Webb, D. 1980, in *IAU Symposium 86, Radio Physics of the Sun*, ed. M. R. Kundu and T. E. Gergely (Dordrecht: Reidel), p. 435.
Kundu, M. R., Melozzi, M., and Shevgaonkar, R. K. 1986, *Astr. Ap.*, **167**, 166.
Kundu, M. R., Schmahl, E. J., and Fu, Q.-J. 1989, *Ap. J.*, **336**, 1078.
Lang, K. R., and Willson, R. F. 1987, *Ap. J.*, **319**, 514.
———. 1989, *Ap. J. (Letters)*, **344**, L77.
Lang, K. R., Willson, R. F., and Trottet, G. 1988, *Astr. Ap.*, **199**, 325.
Lantos, P., Alissandrakis, C. E., Gergely, T., and Kundu, M. R. 1987, *Solar Phys.*, **112**, 325.
Lantos-Jarry, M. F. 1970, *Solar Phys.*, **15**, 40.
Mercier, C., Elgaroy, O., Tiamicha, A., and Zlobec, P. 1984, *Solar Phys.*, **92**, 375.
Schmahl, E. J., Bobrowksy, M., and Kundu, M. R. 1981, *Solar Phys.*, **71**, 311.
Shevgaonkar, R. K., Kundu, M. R., and Jackson, P. D. 1988, *Ap. J.*, **329**, 982.
Stewart, R. T., Brueckner, G. E., and Dere, K. P. 1986, *Solar Phys.*, **106**, 107.
Stewart, R. T., and Vorpahl, J. 1977, *Solar Phys.*, **55**, 111.

KENNETH R. LANG and ROBERT F. WILLSON: Department of Physics and Astronomy, Robinson Hall, Tufts University, Medford, MA 02155

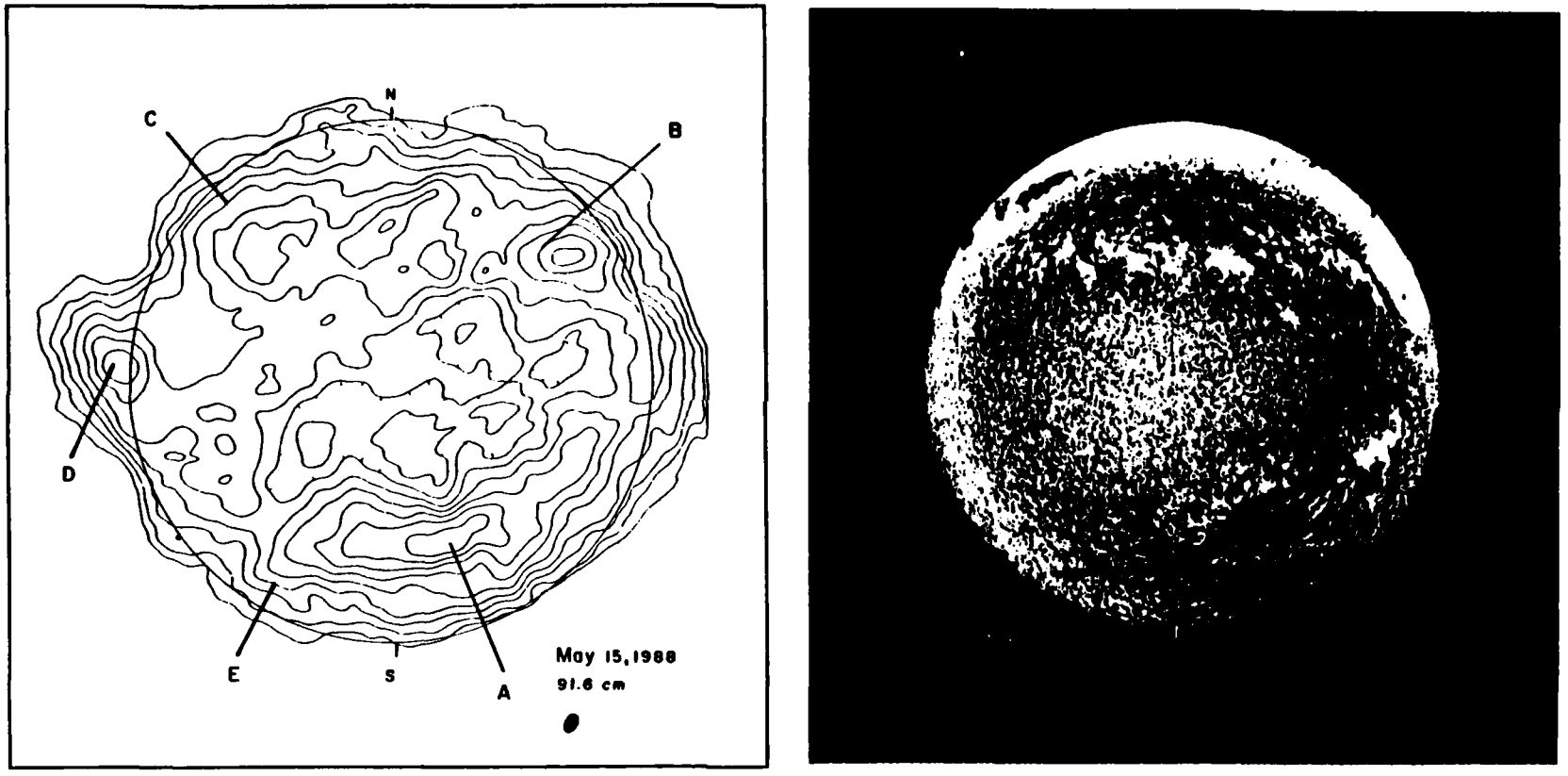

FIG. 1.—A 3 hr Very Large Array (VLA) synthesis map of the total intensity, *I*, from the visible solar disk at 91.6 cm (*left*) is compared with an Hα photograph (*right*) taken at the Boulder Solar Observatory at 1415 UT on the same day (1988 May 15, courtesy of Patrick McIntosh and Helen Coffey). The synthesized beamwidth is denoted by the small black spot in the lower right-hand corner; it has angular dimension of 80″ × 55″ at a position angle of −20°. The circle in the 91.6 cm map denotes the visible solar limb, and the tick marks denote solar north and south. Radio wavelength emission from dark, elongated filaments in the Hα photo are designated by A and B in the 91.6 cm map. Filaments C and E did not correspond to enhanced 91.6 cm emission, while source D probably coincides with a coronal streamer. The hatched regions in the central equatorial regions correspond to depressions in the 91.6 cm emission.

LANG AND WILLSON (*see* 344, L73)

THE ASTROPHYSICAL JOURNAL, 350:856–867, 1990 February 20

C9. IMPULSIVE MICROWAVE BURST AND SOLAR NOISE STORM EMISSION RESOLVED WITH THE VLA

ROBERT F. WILLSON AND KENNETH R. LANG
Department of Physics and Astronomy, Tufts University
AND
MARGARET LIGGETT
Solar Astronomy, California Institute of Technology
Received 1989 April 7; accepted 1989 August 22

ABSTRACT

The Very Large Array (VLA) was used to study the evolution of a microwave burst at 20.7 cm wavelength and a type I noise storm at 91.6 cm wavelength. Snapshot maps of the 20.7 cm emission show that the precursor, impulsive and postburst phases originated in spatially separated sources, suggesting successive activation in different coronal loops. Our observations show that a higher-lying 91.6 cm continuum source began to brighten and change shape ~30 minutes before the onset of the 20.7 cm burst, possibly indicating an interaction between magnetic loops in these two spectral regions. Comparisons with off-band Hα images show that these changes may have been associated with the disappearance of one of the active region filaments. The 91.6 cm level increased again a few minutes after the microwave burst, and this was immediately followed by the onset of a type I noise storm. The sizes (θ = 1'.5–2') and brightness temperatures (T_B = 2–10 × 10^7 K) of the 20.7 cm burst sources were compared with those predicted by multithermal and nonthermal models of microwave burst emission in which the magnetic field strength and temperature are allowed to vary throughout the source. Our results indicate that the multithermal model gives a better fit to the data, with magnetic field strengths of B = 75–120 G at the locations of the bursts. These values are consistent with those inferred from potential magnetic field extrapolations into the corona, using Kitt Peak photospheric magnetograms as boundary conditions.

Subject headings: interferometry — polarization — Sun: corona — Sun: radio radiation

I. INTRODUCTION

During the past decade, high-resolution, VLA observations of the Sun have provided valuable new insights to the physical processes responsible for solar radio bursts. For example, observations at 20 cm wavelength indicate that the regions of energy release are usually located at the apex of coronal loops, while bursts at shorter wavelengths are generally located along the legs or feet of loops (Marsh and Hurford 1980; Alissandrakis and Kundu 1978; Lang and Willson 1984, 1986; Willson 1983; Willson and Lang 1984). In some cases, preburst changes in the active regions are detected as increases in the intensity and polarization of the microwave emission on time scales of a few minutes before the bursts (Kundu *et al.* 1982; Willson 1984; Kundu and Lang 1985). These changes may be related to preburst heating in coronal loops and to the reconfiguration of coronal magnetic field structures which subsequently trigger the impulsive phase. Recently, improvements at the VLA have made it possible to study bursts at 90 cm wavelength with an angular resolution of ~5″ when the array is in the most extended configuration. At this wavelength, solar noise storms are the most common type of solar activity, although other types of bursts, such as type III may also be detected (Willson *et al.* 1989). A typical noise storm consists of a slowly varying, wide-band continuum with superposed impulsive bursts (Elgaroy 1977). The first VLA observations of a solar noise storm showed that it had an elongated shape (~40″ × 200″) and contained four compact sources of ~40″ in size (Lang and Willson 1987). The high-degree and sense of circular polarization ($\rho_c \approx 95\%$) was consistent with previous low-resolution observations which suggested that noise storm emission is fundamental plasma radiation (Elgaroy 1977 and references therein). The noise storm followed a soft X-ray burst by ~20 minutes, suggesting an outwardly moving disturbance or triggering event originating from lower in the corona. Recent VLA observations by Habbal, Ellman, and Gonzalez (1989) did not show any clear correlation between the temporal evolution of the emission at 20 and 90 cm, but in this paper we provide evidence for interaction between magnetic loops detected in the two spectral regions.

There is an uncertainty about which flare-related phenomena are associated with noise storms. Numerous studies (Dodson and Doselman 1951; Das and Sethumadhaven 1953; Davies 1953; Wild and Zirin 1956; McClean 1973) have suggested that noise storms are associated with eruptive prominences while Webb and Kundu (1978) have discussed examples of noise storms that were related to eruptive filaments and long-duration X-ray events outside active regions. Lantos *et al.* (1981) have also presented evidence for an association between a noise storm, a long-duration X-ray event, and a coronal transient. From an analysis of *Skylab* EUV data, Stewart, Brueckner, and Dere (1986) found that the occurrence of major type I metric noise storms is highly correlated with strong changes in the coronal magnetic field structure and with newly emerging flux. They concluded that storms are caused by large-scale rearrangement of coronal fields connecting active regions, rather than by changes of fields within isolated active regions. Theoretical investigations also suggest that emerging flux in regions of strong preexisting coronal magnetic fields may play an important role in the triggering of type I noise storms (McClean 1981; Spicer, Benz, and Huba 1981; Stewart 1985).

Thus, there is evidence that both microwave and decimetric bursts can be triggered by the interactions of magnetic loops. Simultaneous observations at these wavelengths may therefore provide insight to where in a loop or system of loops these interactions actually begin while also providing constraints to models of microwave burst emission and noise storms.

II. OBSERVATIONS

a) Impulsive Microwave Burst at 20.7 cm Wavelength

i) *Time Profiles*

The VLA (C/D hybrid configuration) was used to observe the Sun between 1315 UT and 1622 UT on 1988 June 24. Observations were made using the entire array simultaneously at wavelengths of 20.7 cm (1446 MHz) and 91.6 cm (327.5 MHz) with respective bandwidths of 12.5 MHz and 0.781 MHz. During these observations, all 27 antennas were operating at 20.7 cm wavelength and 22 were operating at 91.6 cm wavelength. At these wavelengths the antenna beamwidths are ~32′ (20.7 cm) and 145′ (91.6 cm) with zero-hour angle synthesized beamwidths of ~12″.5 × 22″ and 55″ × 97″. The data were sampled every 3.3 s and calibrated from observations of 3C 48 every 40 minutes. These data were then used to make CLEANed maps of the total intensity, I, and circular polarization or Stokes parameter V, at both wavelengths on intervals as short as 3.3 s.

On 1988 June 24, the most active region on the Sun was AR 5047, located near the southwest limb (S17 W52 at 1600 UT). This region had produced dozens of Hα flares and soft X-rays burst during the previous few days, including several X-class events (Solar Geophysical Data). At ~1600 UT the region produced one X2.4 burst which we detected at 20.7 cm at the VLA. This event was followed ~40 minutes later by an X5.6-class soft X-ray burst, but our observations had ended by that time. Unfortunately the *Solar Maximum Mission Satellite* (*SMM*) was in the nighttime part of its orbit during the X2.4 burst and thus could not provide complementary soft and hard X-ray data. However, at ~1720 UT, the Coronal Polarimeter (C/P) aboard the *SMM* did detect a coronal mass ejection above the southwest limb. Since there were no other active regions in the vicinity of AR 5047, the CME was almost certainly associated with one of the two X flares (J. Burkpile, private communication, 1988).

In Figure 1 we show time profiles of the visibility amplitudes between 1600 and 1620 UT at 20.7 cm and 91.6 cm wavelengths as observed on one of the shortest VLA baselines (fringe spacing of 250″ at 91.6 cm and 55″ at 20.7 cm.) The 20.7 cm burst profile exhibits two impulsive ($\tau < 10$ s) spikes (160626 and ~160647 UT) two faint precursors which precede the impulsive phase by a few minutes, and finally a secondary peak (~160810 UT) that occurs after the start of the gradual decay phase.

In Figure 2 we show a plot of the *GOES* X-ray emission during this same time interval as well as profiles of total flux at eight wavelengths between 1.94 cm (15400 UT) and 122 cm (245 MHz) as recorded by the San Vito station of the Air Force Solar Radio Patrol (courtesy of Ed Cliver). Note that the duration of the microwave burst is considerably shorter than that of the soft X-ray burst. In fact, the *GOES* data showed that the soft X-ray emission had not yet reached its preburst level before the second X-flare began at ~1645 UT. In this figure the original 1 s time resolution radio data have been averaged over 3 s in order to provide a more direct comparison with the

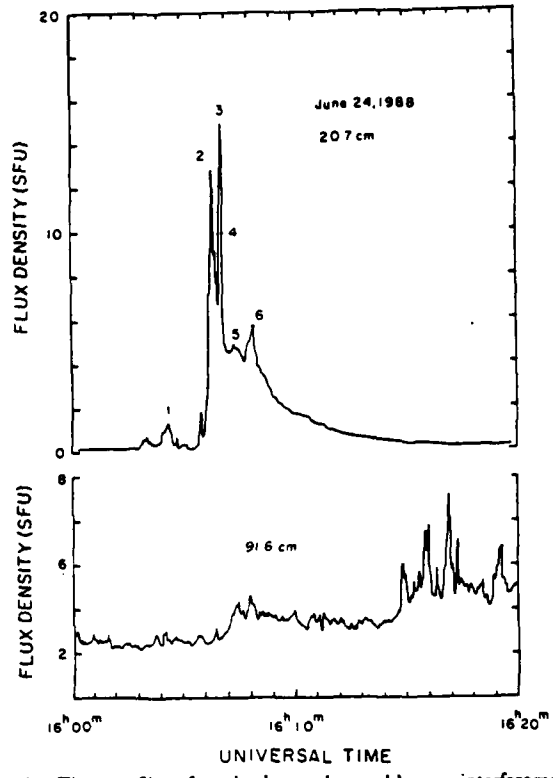

FIG. 1.—Time profiles of a solar burst observed by one interferometer pair of the VLA at 20.7 cm (1446 MHz) and 91.6 cm (327.5 MHz) during a 20 minute interval on 1988 June 24. Snapshot maps of the components (1–6) of the 20.7 cm burst are shown in Fig. 4. VLA maps of the 91.6 cm emission are shown in Figs. 7–9.

3.3 s VLA data. Notice that although the profiles are similar, the peak flux at 21 cm is about a factor of 3 higher than shown on the plot of visibility amplitude in Figure 1. This indicates that the burst emission was larger than the 55″ resolution VLA baseline on which the correlated flux was measured.

Microwave spectra measured at different times during the burst are also shown in Figure 2. They indicate that the flux decreases sharply at the longer wavelengths, with a spectral index of $\alpha \approx 0.8$–0.9 below the spectral peak. In the case of the two impulsive 20.7 cm spikes, the frequency of maximum emission may lie above the highest observed frequency of 15,400 MHz. These data also indicate that the microwave burst emission probably does not extend much below ~1415 MHz. The absence of any obvious counterpart at 606, 410, and 245 MHz may be due to Razin suppression or free-free absorption by thermal plasma, both of which reduce the intensity of microwave bursts at long wavelengths (e.g., Dulk 1985). The gradual increase in intensity at 606 MHz starting at ~1608 UT, and which appears to have a relatively narrow bandwidth, might be attributed to a decimetric type IV continuum burst. Such bursts are, for example, known to begin a few minutes after impulsive microwave bursts (e.g., Kundu 1965; Dulk 1985). The emission at 410 MHz and 245 MHz which exhibits a gradual increase with superposed impulsive bursts may be associated with what we believe to be a type I noise storm detected at 327 MHz with the VLA (see § II*b*). In § III we use the higher frequency data, together with our VLA results, to estimate the magnetic field strength in the burst sources and to test different models of burst emission.

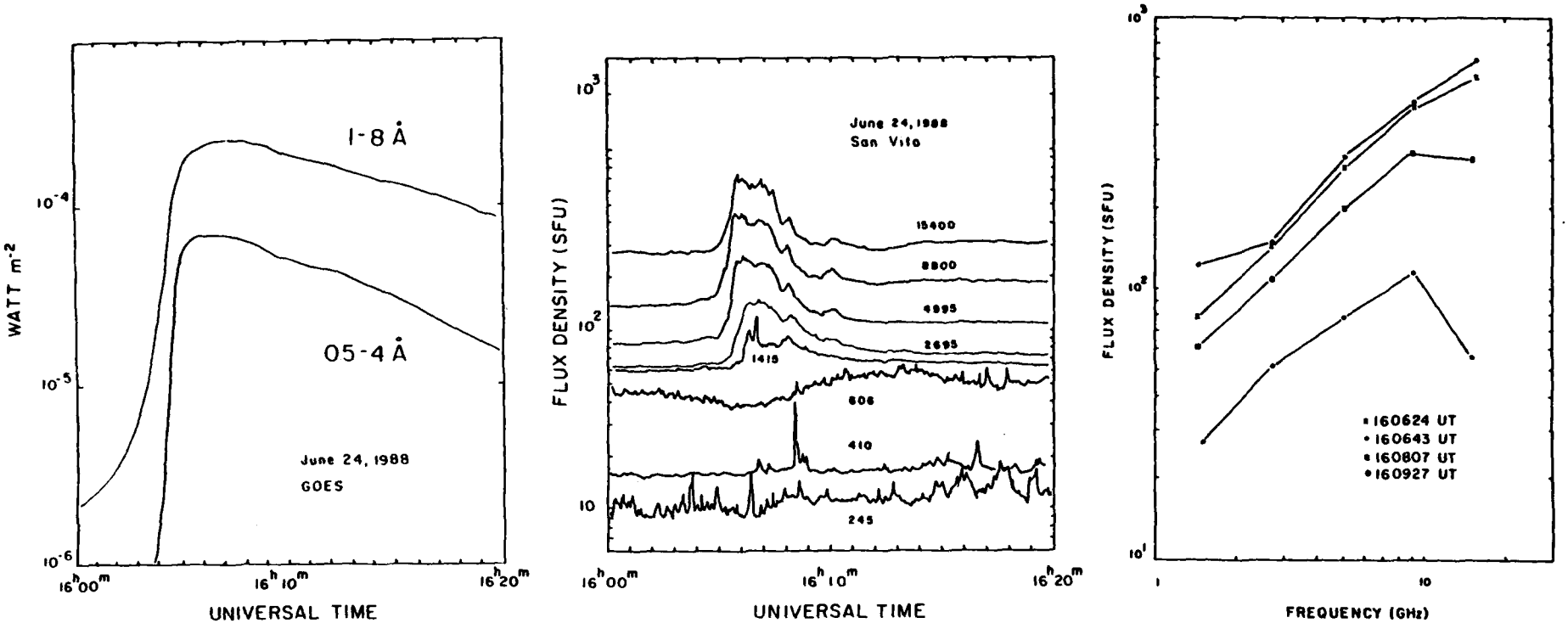

FIG. 2.—Time profiles of the burst observed by the *GOES* X-ray satellite (*left*) and by the San Vito station of the Air Force Solar Radio Patrol (*middle*) together with microwave spectra during the impulsive and decay phases (*right*).

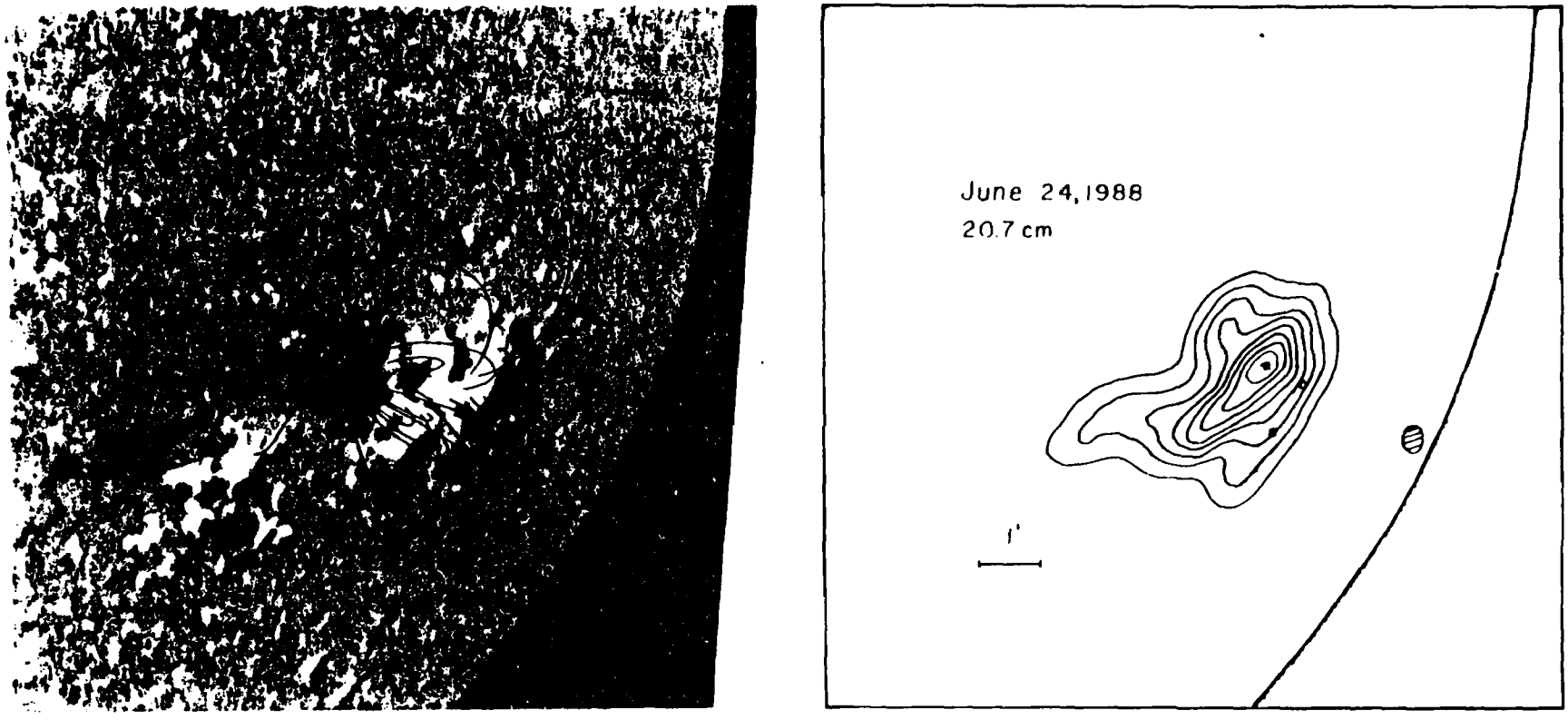

FIG. 3.—A VLA synthesis map of total intensity at 20.7 cm wavelength (*right*) is compared with a Kitt Peak magnetogram (*left*) taken on the same day. Potential magnetic field lines extrapolated into the corona are superposed on the magnetogram. The VLA map was produced using data taken during the 2.5 hour interval prior to the microwave burst shown in Fig. 1. The angular scale may be inferred from the 60" spacing between fiducial marks on the axes. The contour intervals are in units of equal brightness temperature, T_B, with an outermost contour and contour interval of $T_B = 3.6 \times 10^5$ K. The circle, cross, and square mark, respectively, the locations of burst emission during the precursor, impulsive, and postimpulsive phases. Snapshot maps of these different phases are shown in Fig. 4. The hatched eclipse near the solar limb denotes the position of the 91.6 cm source shown in Fig. 7.

ii) *VLA Maps of Quiescent 20.7 cm Emission*

In Figure 3 we compare a 20.7 cm VLA synthesis map of total intensity with a Kitt Peak magnetogram taken on the same day (courtesy of Jack Harvey and Kermit Smith). This map was made using data from 1315–1555 UT, and therefore represents the quiescent emission leading up to the impulsive burst. Here we also show magnetic field lines that have been extrapolated into the corona using a computer code kindly provided by T. Sakurai. This program, described in detail by Sakurai (1981), solves Laplace's equation to calculate potential magnetic field lines using photospheric fields as boundary conditions. Since Kitt Peak magnetograms are known to saturate above ~ 100 G, the strong umbral fields ($B \approx 2400$–2600 G were corrected by using sunspot strengths and sizes obtained from Mount Wilson, in a manner described by Gary and Hurford (1988) who made similar comparisons with VLA data.

As shown in the figure, the most intense 20.7 cm emission is concentrated in a looplike structure ($\theta \approx 2' \times 3'$) that lies along an arcade of magnetic loops connecting the underlying sunspots. Its peak brightness temperature is $T_B \approx 3 \times 10^6$ K, and there was no detectable circular polarization, ($\rho_c < 10\%$), suggesting optically thick thermal emission. Maps made for time intervals ranging from 10 minutes to one hour revealed no significant changes in structure, brightness, or polarization, indicating that the 20.7 cm source was stable during the several hours before the 20.7 cm burst. In this figure, the circle, cross, and square mark, respectively, the locations of burst emission during the precursor, impulsive and post impulsive phases of the 20.7 cm burst shown in Figure 1 (see next section).

iii) *VLA Maps of the 20.7 cm Burst*

Figure 4 shows 3.3 s 20.7 cm wavelength maps of total intensity at the peaks of the faint precursor and impulsive spikes and during the decay phase. In order to more clearly distinguish the burst and quiescent emission, we first subtracted the preburst visibility function at 1602 UT from the subsequent burst data. As shown, the precursor has an elongated shape whose peak lies $\sim 1'$ west of the quiescent 20.7 cm source (denoted by a cross in the figure). Its peak brightness temperature is $T_B \sim 4 \times 10^6$ K, and there was no detectable circular polarization.

Maps depicting the evolution of the main burst show that the peaks of the two impulsive spikes (160626 and 160647 UT) lie at the same position as the quiescent emission. Each burst has a half-power angular size of $\sim 1'.5$ and a peak brightness temperature of $T_B \approx 10^8$ K. There is no indication of circular polarization above an instrumental uncertainty of $\rho_c \approx 15\%$–20%.

Notice that after ~ 1607 UT the emission, including the gradual decay phase and the secondary impulsive burst at 160807 UT, lies $\sim 2'$ south of the first two impulsive peaks. In fact the maps show that this southern component began to emerge within ~ 3 s after the second impulsive spike at 160647 UT, suggesting successive activation in an adjacent set of loops. Although the burst is located near the limb, our maps after 160807 UT showed no evidence for systematic changes in position or size, as would be expected if the postburst source were expanding or moving outward into the corona at any velocity $v \geq 10$ km s^{-1}.

In Figure 5 we show a Big Bear Observatory Hα photograph taken during the decay phase of the 20.7 cm burst. This photograph shows a number of Hα flare ribbons which mark at least two sets of flare loops. Inspection of a time sequence of images shows that the pair of flare kernels, denoted by a_1 and a_2, and located in the eastern half of AR 5047 appeared at ~ 1600 UT, or several minutes before the first 20.7 cm precur-

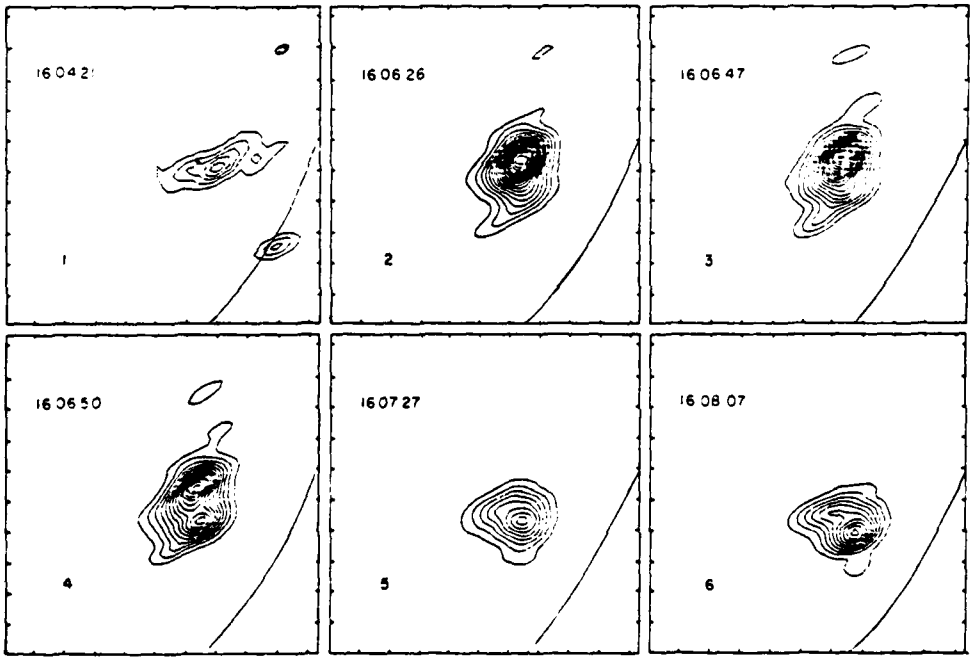

FIG. 4.—VLA snapshot maps of the total intensity, I, at 20.7 wavelength during 3.3 s intervals at the times denoted by 1–6 in Fig. 1. The precursor (1) had no detectable circular polarization and is spatially separated from the subsequent impulsive bursts (2 and 3). The cross denotes the peak of the impulsive burst in (1), and of the peak of the quiescent emission shown in Fig. 3. The sources are resolved with a synthesized beamwidth of 12" × 30"; the angular scale may be inferred from the 60" spacing between the fiducial marks on the axes. The contour intervals are in units of equal brightness temperature, T_B, with an outermost contour and contour interval of $T_B = 4.4 \times 10^5$ K ($T_{B_{max}} = 4.4 \times 10^6$ K) for (1) and an outermost contour and contour interval of $T_B = 5.5 \times 10^6$ K ($T_{B_{max}} = 1.0 \times 10^8$, 1.3×10^8, 7.7×10^7, 4.4×10^7, 5.5×10^7 for 2.3.4.5, and 6, respectively.

sor. It is interesting to note that other observations have shown that Hα emission can precede the impulsive phase by a few minutes to tens of minutes, possibly indicating magnetic triggering in adjacent loops (Martin 1980; Rust *et al.* 1981; Webb 1983). The second pair of kernels, b_1 and b_2, located in the western part of the region, appeared at ~1605 UT, or about the same time as the impulsive emission. A coregistration of the snapshot maps with this image shows that the peak of the impulsive microwave emission is located about midway between b_1 and b_2. If these kernels represent the footprints of a flaring loop, then the location of the 20.7 cm burst peak suggests that the energy release occurred near the loop top.

b) Activity at 91.6 cm *Wavelength*

i) *Time Profile*

Figure 6 shows plots of the correlated flux and circular polarization between 1400 and 1620 UT. There are two groups of type I bursts, one preceding (1448–1507 UT), the other following (1615–1620 UT) the 20.7 cm burst. These bursts are superposed upon a slowly varying background level that is punctuated by hundreds of low-intensity spikes whose durations are almost always less than the 3.3 s VLA integration time. We also draw attention to the gradual increase of the background intensity starting at ~1525 UT, and to the more pronounced jump at ~1607 UT, or ~1 minute after the second impulsive 20.7 cm burst (Fig. 1). Although the bottom half of Figure 6 suggests a steady increase in circular polarization, we believe that this is an instrumental effect which is due to the gradual resolution of large-scale unpolarized structure on this baseline. Longer baselines, for example, show systematically higher and more constant degrees of circular polarization, while synthesis maps (excluding bursts) show no systematic trends in the polarization of the dominant left circularly polarized ($\rho_c \approx 90\%$) source associated with AR 5047 (see next section). We include the plot of ρ_c only in order to illustrate relatively rapid changes in polarization (which could not be due to change in resolution) such as occur during the first group of type I bursts.

ii) *Noise Storm Resolved and Preburst Enhancement*

Figure 7 shows a sequence of maps depicting the evolution of the 91.6 cm emission from 1315–1600 UT, excluding the 20 minute interval between 1448–1507 UT, containing bursts. Figure 7(*a*), for example, represents the slowly varying source before the slow rise in intensity shown in Figure 6. During this time the emission is resolved by the 1′ × 2′ synthesized beam and concentrated in an elliptical source of ~3′ × 5′ in size whose center is shifted limbward by ~3′ with respect to the active region and the 20.7 cm loop. The source has a peak brightness temperature of $T_B \approx 3.5 \times 10^7$ K and is 85% left circularly polarized. Maps made on shorter time intervals showed no significant changes in size or brightness temperature, indicating that the 91.6 cm source was also relatively stable during this period. Figure 7 however shows that between 1545–1600 UT the source began to brighten and extend to the north, reaching a brightness temperature of $T_B \sim 5 \times 10^7$ K at 1600 UT. Since there were no impulsive bursts during this period (Fig. 6) this sequence of maps depicts a gradual evolution of the continuum source, rather than a rapid evolution caused by bursting sources.

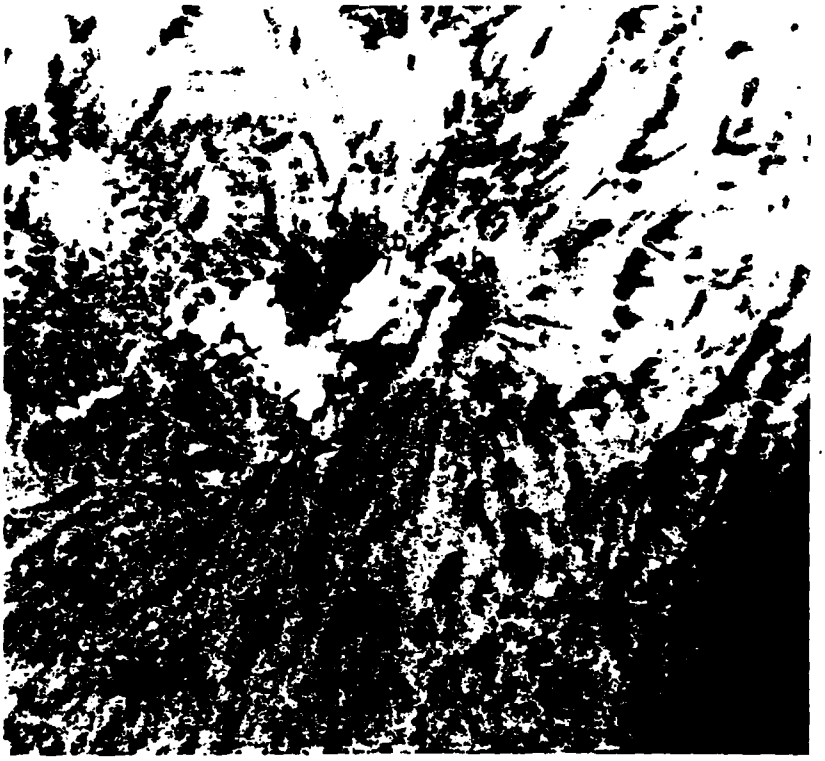

FIG. 5.—A Big Bear Observatory off-band Hα (Hα + 0.6 Å) filtergram taken at 161109 UT showing the location of flare kernels following the microwave burst. The kernels a_1 and a_2 appeared ~5 minutes before the impulsive phase of the burst; b_1 and b_2 were nearby coincident with it. The cross denotes the location of the impulsive source (2), shown in Fig. 4.

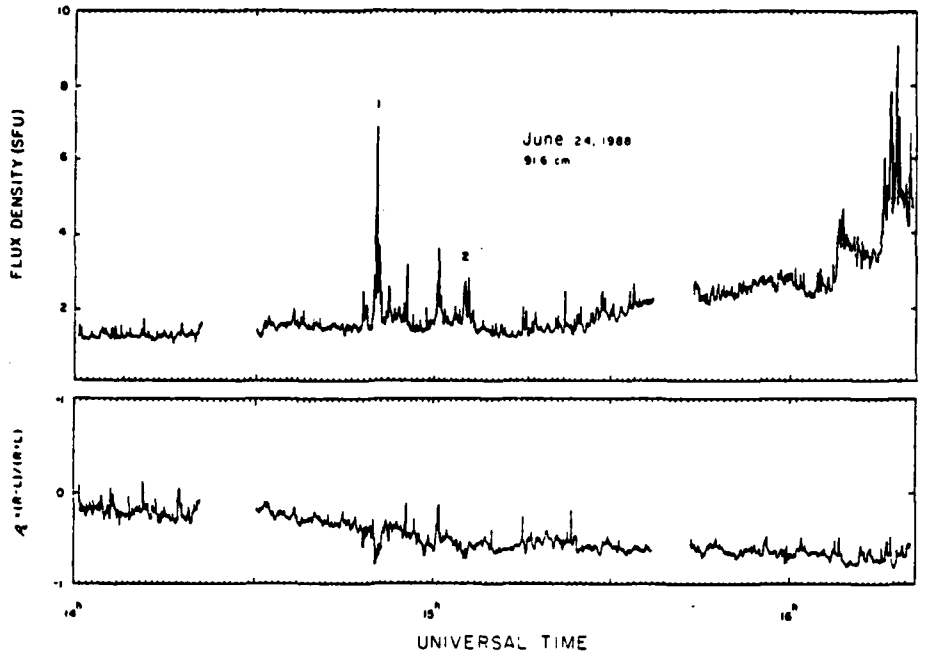

FIG. 6.—Time profile of the total intensity, I (*top*), and circular polarization, ρ_c (*bottom*) observed with one interferometer pair at 91.6 cm wavelength on 1988 June 24. Here the data are plotted with a time resolution of 3.3 s. Spike-like bursts are superposed upon a slowly varying background that begins to increase ~30 minutes before an intense microwave burst.

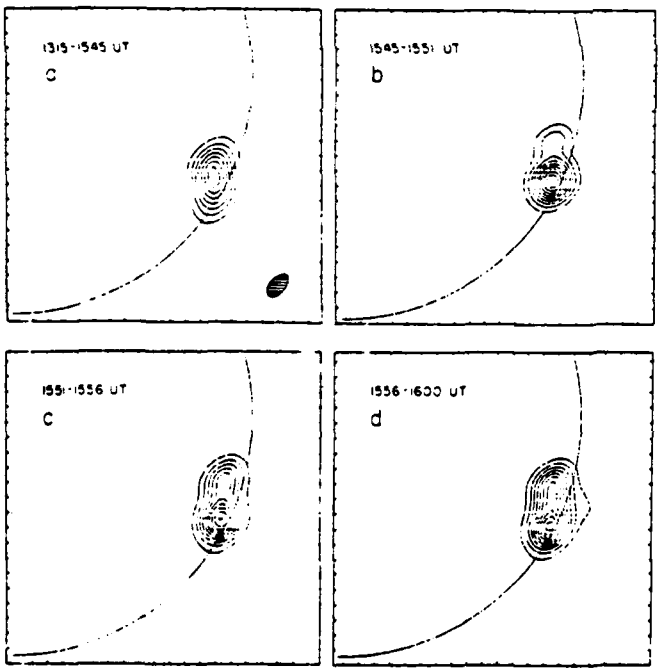

FIG. 7.—VLA synthesis maps of total intensity, I, at 91.6 cm wavelength between the indicated time intervals. The synthesized beam is shown in the upper left hand panel. It has an angular size of 65" × 114". The angular scale may be inferred from the 60" spacing between the fiducial marks on the axes. The 91.6 cm source is seen to begin to change shape and elongate ~15 minutes prior to the impulsive 20 cm burst shown in Fig. 1. The polarization remained nearly constant at $\rho_c \approx 85\%$ (LCP) throughout this time interval. The contour intervals are in units of equal brightness temperature, T_B, with an outermost contour and contour interval of 5×10^6 K.

The high brightness temperatures and degree of circular polarization suggest that the emission is nonthermal and associated with active-region magnetic fields. By way of comparison, VLA observations of the solar corona at 90 cm, reveal large-scale ($\theta \approx 3'$–$5'$) unpolarized structures with brightness temperatures of $T_B = 0.5$–5×10^5 K (Lang, Willson, and Trottet 1988; Shevgaonkar, Kundu, and Jackson 1988; Lang and Willson 1989). These sources are not systematically associated with active regions and may delineate large-scale magnetic loops or filament sheaths whose brightness temperature can be attributed to thermal bremsstrahlung emission.

The 91.6 cm source discussed here may in fact be the continuum emission of a type I noise storm (Elgaroy 1977). In this case, the sense of circular polarization should correspond to the ordinary mode expected of plasma radiation in a unipolar flux tube (Kerdraon and Mercier 1982). We therefore expect the left circularly polarized emission to be associated with the leading spot of positive magnetic polarity shown in Figure 3. In fact, our potential magnetic field extrapolation indicates that the 91.6 cm sources lie within either a large-scale loop extending beyond the field of view or along open magnetic field lines which are anchored to photospheric fields of the leading spot of positive polarity. We may then estimate the height of the 91.6 cm source if it assumed to lie radially above the leading spot. From the position of the spot (S17 W52) and the angular displacement of the source shown in Figure 7(*a*), ($\Delta\theta \approx 3'$) we infer a height of $h = 0.18 \pm 0.03\ R_\odot$. This is in agreement with the height inferred by Lang and Willson (1987) for a noise storm observed at 327 MHz using the VLA. Although it has been reported that noise storm centers are not located radially above the associated active regions (Kerdraon and Mercier 1982) the center of the quiescent source (from 1300–1545 UT) does appear to project nearly radially above the leading spot in the active region. The brightening at its northern end may represent newly accelerated particles radi-

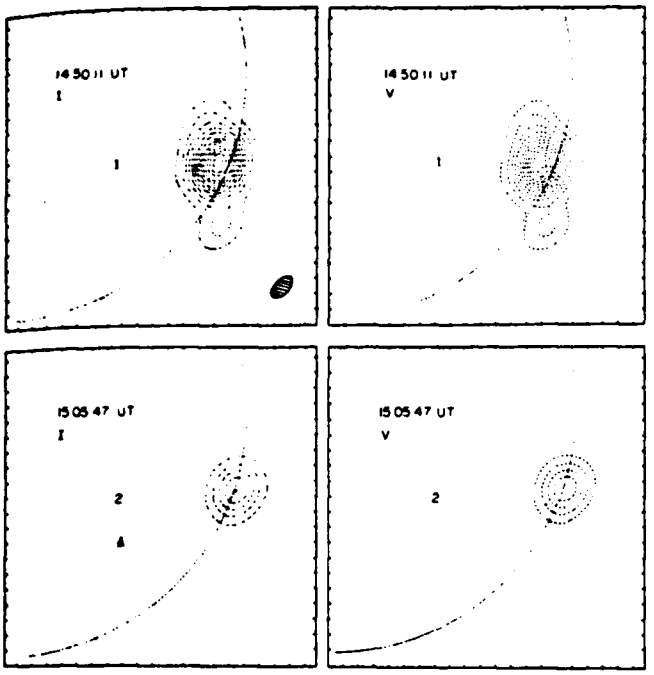

FIG. 8.—VLA 3.3 s snapshot maps at 91.6 cm wavelength of total intensity, I, and stokes parameter, V, at the peaks of two impulsive bursts shown in Fig. 6. The synthesized beamwidth is shown in the upper left hand panel. It has an angular size of 55" × 90". The angular scale may be inferred from the 60" spacing between the fiducial marks on the axes. The countour intervals are in units of equal brightness temperature, T_B, with an outermost contour and contour interval of 5×10^6 K.

ating in this part of a diverging flux tube that bends upward and crosses the equator, possible connecting to a distant active region.

iii) *Impulsive Bursts*

Snapshot maps of the 91.6 cm impulsive emission are shown in Figures 8 and 9. Here, the preburst visibility level has also been subtracted before making these maps. The emission from groups of bursts shown in Figure 6 originates in an elliptical source ($\theta \approx 3'' \times 5''$) whose position is coincident with that of the slowly varying sources shown in Figure 7. In all cases, the emission was 90%–100% left circularly polarized, with peak brightness temperatures of $T_B = 1.5\text{–}5 \times 10^7$ K. These values are characteristic of type I bursts, but the 3.3 s observations may have integrated the emission of several such bursts or chains of bursts which have durations, τ of less than ~ 1 s (Elgaroy 1977). In this case the true brightness temperatures would exceed those observed, by a factor of approximately $(3.3/\tau)^2$.

Although the structure of the 91 cm emission varies from peak to peak, there was no evidence for a systematic shift in position of successive bursts for either group at any velocity $v \geq 150$ km s^{-1}. Van Nieukoop (1986), for example, found that at 243 MHz, some groups of type I bursts showed a systematic angular displacement with time, suggesting disturbances moving with apparent velocities of up to 15,000 km s^{-1}.

The coincidence in position as well as the similarity in the degree of circular polarization of the continuum and type I burst suggests that both are emitted in a region of about the same magnetic field strength and density. Our magnetic field extrapolations indicate a magnetic field strength of $B \approx 10$ G at the position of the 91.6 cm burst. If the type I emission propagates in the ordinary mode at the fundamental of plasma

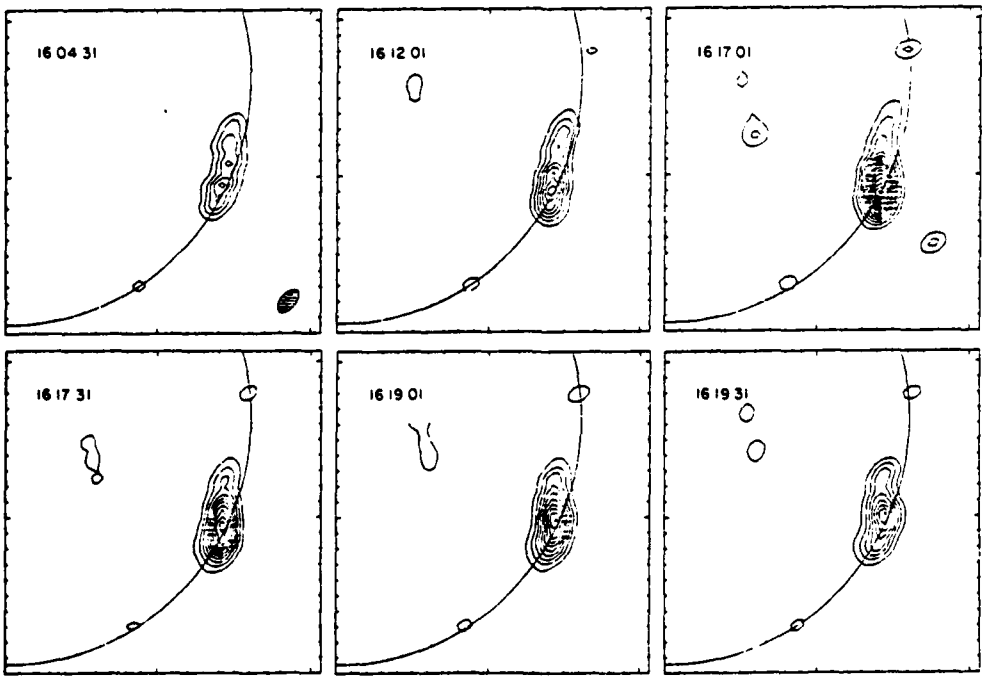

FIG. 9.—VLA snapshot maps of the total intensity, I, at 91.6 cm wavelength during 3.3 s intervals at the times indicated. The 91.6 cm source is shifted with respect to the 20.7 cm one (Fig. 3) by an angle $\theta \approx 3'$ towards the limb. The synthesized beamwidth is shown in the upper left hand panel. It has an angular size of 50" × 95". The angular scale may be inferred from the 60" spacing between the fiducial marks on the axes. The contour intervals are in units of equal brightness temperature, T_B, with an outermost contour and contour interval of 3.2×10^6 K.

frequency, ν_p, (Dulk 1985; Kai, Melrose, and Suzuki 1985; Melrose 1985, 1987) then $\nu_{obs} > \nu_p > \nu_B$, where $\nu_B = 2.8 \times 10^6$ B is the gyrofrequency. At $\nu_{obs} = 327.5$ MHz, this corresponds to an electron density of $N_e = 1.3 \times 10^9$ cm^{-3} and $B < 116$ G, which is consistent with our field extrapolations.

III. DISCUSSION

a) *Correlated Activity at 20.7 cm, 91 cm and Optical Wavelengths*

Our data at 20.7 cm and 91.6 cm wavelength show intriguing correlations between activity at these two wavelengths. For example, our 91.6 cm maps (Fig. 7) indicate that the region emitting the storm continuum began to increase in size and intensity about 30 minutes before the impulsive 20.7 cm burst. Although a group of type I bursts occurred earlier at the same location, they apparently did not initiate this increase. The 91.6 cm continuum level again abruptly increased a few minutes after the 20.7 cm burst, and this was followed ~15 minutes later by another group of type I bursts. These results may suggest a feed-back mechanism in which interactions of large-scale loops trigger burst activity in lower lying loops and vice versa.

The onset of the increase 91.6 cm (Fig. 7) may have also been related to changes in one of the active regions filaments. In Figure 10 we show two Big Bear Solar Observatory off-band Hα (Hα-0.6 Å) filtergrams illustrating that a portion of one end of the filament, marked A, disappeared sometime between 1537 UT and 1543 UT. Later frames (after 1600 UT) show the presence of filament material in that area. The time gap (1537–1543 UT) was due to a gap in the data leaving one not knowing whether there was a true eruption and reappearance of this portion of the filament or, if line of sight motion in the filament was greater than 30 km s^{-1}, it might not have been visible at this wavelength. More subtle changes at the other end of the filament (marked B) can be seen on BBSO filtergrams between 1546–1548 UT. Various small motions and weak brightenings were noted at both ends of this filament from 1505 UT. The filament lies in the vicinity of the two Hα kernels (a_1 and a_2 in Fig. 5) that appeared at 1600 UT, but is displaced from the sunspot that marks the footpoints for the open magnetic field lines that thread the 91.6 cm emission.

Filaments have long been known to exhibit preflare activity, often showing upward motions or reconfiguration tens of minutes before flare onset (Martin and Ramsey 1972; Webb, Krieger, and Rust 1976). These activations are often accompanied by changes in the photosphere or chromosphere which have been taken as evidence for the evolution or emergence of magnetic flux (Rust 1976; Kundu and Woodgate 1986). The newly formed magnetic loops can then interact with existing magnetic fields, thereby providing the triggering mechanism for microwave bursts (Heyvaerts, Priest, and Rust 1977). Filament activity can also apparently result in the production of nonthermal electrons. Webb and Kundu (1978) found a close temporal and spatial association between erupting filaments and noise storm continua, while Webb, Krieger, and Rust (1976) showed that X-ray and microwave gradual rise and fall peaks follow the end of filament disappearances by tens of minutes. Finally, preburst activity at 6 cm wavelength, including an increase in intensity and polarization, has also been associated with motions and changes in a nearby filament (Kundu *et al.* 1985).

At least one theoretical model has been proposed that relates noise storms to changes in magnetic fields, and presumably to filament activity (Spicer, Benz, and Huba 1981). In the model shock waves are generated at the boundary of new emerging flux and the ambient corona, thereby accelerating the particles that produce the type I bursts. Although this model may explain our observations, confirmation may have to wait until VLA images of noise storm sources are correlated with simultaneous high time resolution magnetograms which resolve changes in photospheric magnetic fields.

b) *Estimates of Magnetic Field Strength in the 20.7 cm Burst Sources*

In this section we combine our measurements of the size and brightness temperatures of the 20.7 cm burst components with the solar radio patrol data shown in Figure 2 to estimate the magnetic field strength in these sources. In particular we consider two models of burst emission developed by Dulk and Dennis (1982), called multithermal and nonthermal models which make specific predictions about the size and brightness temperature of a microwave burst source as a function of frequency. These models assume that the impulsive emission at hard X-rays and microwaves comes from the same population of electrons and that the source can be described as a set of loops which confine the highest energy electrons to a compact core. In the multithermal model, the average electron temperature, T, and magnetic field strength, B, both decrease with radius from the center of the core according to the power laws

$$T = T_{max}\left(\frac{r}{r_{min}}\right)^{-\alpha_T}$$

$$B = B_{max}\left(\frac{r}{r_{min}}\right)^{-\alpha_B},$$

where r_{min} is the core radius ($r > r_{min}$). T_{max} and B_{max} are the maximum temperature and magnetic field strength in the core, and α_T and α_B are related to the X-ray photon number index, α_x, and the microwave spectral index, α_m, by

$$\alpha_T = \frac{6}{2\alpha_x - 3}$$

$$\alpha_B = \frac{7\alpha_T\alpha_m - 24\alpha_T - \alpha_m + 22}{18 - 22\alpha_m}.$$

Here, α_m is obtained from the optically thick region of the microwave spectrum (at $\nu < \nu_{max}$) where the flux density increases with frequency as $S \propto \nu^\alpha \propto A\nu^2 T_{eff}$ and where A is the projected area of the source and T_{eff} is the effective brightness temperature.

For the nonthermal model, it is assumed that the energy electron distribution is a power law of index $\delta = \alpha_x - 0.5$ and that only the magnetic field strength varies with distance from the core. In this case the microwave spectral index is related to α_B by

$$\alpha_m = 2.9 - \frac{(0.9\alpha_B + 2)(1.2 + \delta)}{\alpha_B(0.2 + \delta) - 1}.$$

Using the equations for a gyrosynchrotron-emitting source given by Dulk, Melrose, and White (1979) and Dulk and Marsh (1982), Dulk and Dennis (1982) derive expressions for the flux, brightness temperature, size and magnetic field strength as a function of frequency for both the multithermal and nonthermal models. For both models, one must know the

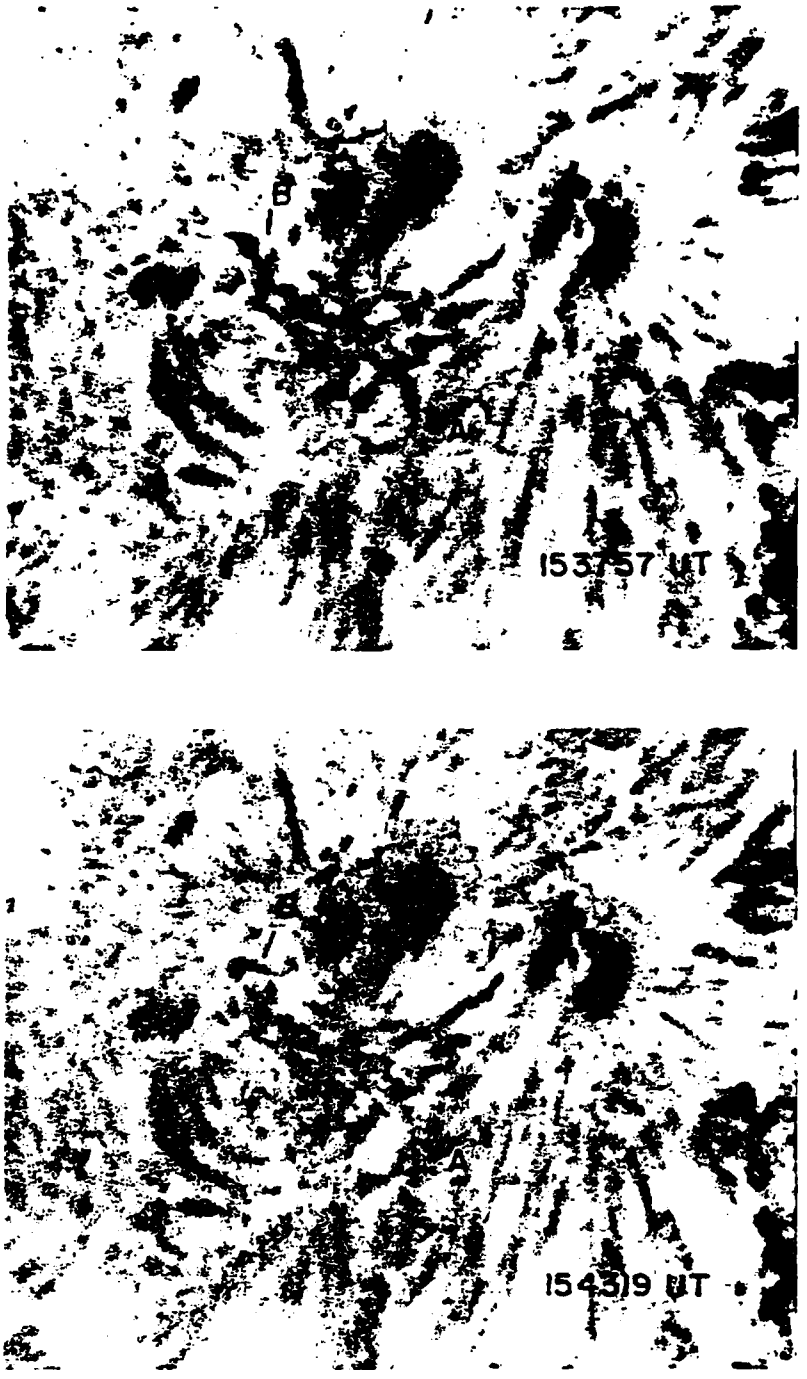

FIG. 10.—Big Bear Observatory off-band Hα (Hα − 0.6 Å) images showing the disappearance of a section of filament (A) between 153757 UT and 154319 UT.

flux, $S_{\nu_{max}}$, at the turnover frequency, ν_{max}, the hard X-ray spectral index, α_x, and the core size, r_{min}. For the multithermal model, one must also know the effective brightness temperature T_{max}, at the peak frequency corresponding to $r = r_{min}$. Since there were no hard X-ray observations during this burst, we have made calculations for a range of values of $\alpha_x = 3.5$–7.0, which are consistent with those inferred from other observations (e.g., Dennis 1989). For the multithermal model, we assumed a core temperature of $T_{max} = 5 \times 10^7$ K, a value that is somewhat higher than the brightness temperature observed during the impulsive phase. For this model the core radius at a given time was derived using this T_{max} and the observed flux density at the peak frequency (see eq. 11 of Dulk and Dennis 1982). Since the nonthermal emission does not depend on T_{max}, we could not calculate the nonthermal core radius in this way. Instead, we followed the procedure outlined by Dulk and Dennis (1982) and assumed a set of values ranging from $r_{min} = 2.15 \times 10^8$ cm, corresponding to core angular sizes of $\theta = 5''$–$40''$. These sizes bracket the range of burst sizes we recently observed at 2 cm and 3.5 cm wavelength using the VLA (Willson *et al.* 1990).

The results of our calculations are given in Table 1. Here we

TABLE 1

OBSERVED AND DERIVED PARAMETERS FOR DIFFERENT TIMES DURING THE 20.7 cm BURST

						Multithermal Model				Nonthermal Model			
UT	T_B (K)	Angular size (')	Spectral Index	S_{max} (SFU)	ν_{max} (GHz)	α_x	B (G)	T_B (K)	Angular size (')	δ	B (G)	T_B (K)	Angular size (')
160626.....	1×10^8	1.0 × 1.5	0.85	600	≥15.4	5	42	1.1×10^8	1.3	6.0	155	1.1×10^8	1.3[a]
160647.....	1.3×10^8	1.0 × 1.5	0.72	705	≥15.4	5.5	35	1.5×10^8	1.3	6.0	130	1.4×10^8	1.4[a]
160807.....	5.5×10^7	1.4 × 1.5	0.92	327	~8.8	3.8	75	5.3×10^7	1.6	6.0	270	5.9×10^7	1.5[b]
160927.....	2.2×10^7	1.5 × 2.0	0.80	117	~8.8	3.5	160	1.8×10^7	1.9	6.0	640	2.5×10^7	1.7[b]

[a] $r_{min} = 1 \times 10^9$ cm.
[b] $r_{min} = 1.5 \times 10^9$ cm.

give the peak brightness temperature, half-power angular size, spectral index, and peak flux and frequency for each of four different 20.7 cm burst components, together with the magnetic field strength, angular size and brightness temperature for the best-fit multithermal and nonthermal models.

Our results show that for a given T_{max} and r_{min}, the multithermal model gives a satisfactory fit for spectral indices of $\alpha_x = 3.5$–5.5 and magnetic field strengths of $B = 35$–160 G. These values of B are consistent with those obtained from our potential field calculations which indicate field strengths of $B = 75$–120 G at the locations of the burst sources. However, the fact that the magnetic field strength in the nearly cospatial sources at 160807 and 160927 UT differ by about a factor of two may suggest that our assumption of a constant core temperature of $T_{max} = 5 \times 10^8$ K is incorrect. With $T_{max} = 1 \times 10^8$ K and $\delta = 5$ at 160927 UT, for example, we derive a magnetic field strength of $B = 115$ G, closer to the value inferred for the secondary impulsive peak at 160807 UT. These models also predict magnetic field strengths of $B = 10$–25 G and angular sizes of $\theta = 4'$–$8'$ at 91.6 cm. However, since the observed emission at this wavelength is probably due to plasma radiation and not to gyrosynchrotron emission (the long wavelength counterpart of the microwave burst is very likely attenuated by thermal plasma, see § II *b*[i]), the brightness temperatures and sizes of the 91.6 cm sources provide no useful constraints on these models.

For the same values of r_{min}, the nonthermal model predicts consistently higher magnetic field strengths and smaller angular sizes than are observed at 20.7 cm. This is because the source size decreases less rapidly with frequency in the nonthermal model, than in the multithermal model. In order to get the observed sizes of 1'.5, we require larger core sizes of $r_{min} = 1$–1.5×10^9 cm (corresponding to angular sizes of 28″–40″). However with these larger values of r_{min}, the nonthermal model predicts magnetic field strengths that are probably too high. At the turnover frequency of 15.4 GHz, for example, the expected core magnetic field strengths are $B_{max} = 2500$ G, or about equal to the field strengths in some of the spots. In contrast, the corresponding core strengths in the multithermal models are $B_{max} \simeq 125$–220 G. In view of this difficulty, we therefore conclude that the multithermal model provides a better explanation for these data.

IV. SUMMARY

We may summarize our main results as follows:

1. The VLA snapshot maps show that the precursor, impulsive, and postimpulsive phases of the 20.7 cm burst are located in spatially separated sources, suggesting activation in different coronal loops or systems of loops. The hot precursor source apparently interacted with an adjacent one, leading to the explosive release of energy during the impulsive phase. The system of coronal loops then seems to have relaxed to a more stable state when yet another nearby source emitted the decay phase. These results are similar to those obtained by Machado *et al.* (1988), who showed that X-ray flaring activity usually involves two or more interacting magnetic dipoles within an active region, with an initiating dipole impacting against an adjacent one.

2. The gradual enhancement of a 91.6 cm noise storm continuum source about 30 minutes before the microwave burst together with subsequent type I bursts suggests that some sort of feed-back mechanism may exist between activity in higher lying loops and lower lying ones. The additional observation of filament activity lends support to this idea, although further observations at radio, X-ray, and optical wavelengths are needed to confirm it.

3. The inhomogeneous source models of Dulk and Dennis (1982) were used to estimate the magnetic field strength in the 20.7 cm burst sources. The brightness temperatures and sizes of these sources, together with microwave data from solar radio patrol instruments are probably more consistent with a multithermal rather than a nonthermal gyrosynchrotron-emitting source. The derived magnetic field strengths at 20.7 cm for the nonthermal models are $B = 35$–160 G, with core field strengths of $B = 125$–220 G. The nonthermal models require core field strengths of $B = 2500$ G, which, though comparable to the strengths in the underlying sunspots, are considerably higher than expected for sources located in the solar corona.

Radio astronomical studies of the Sun at Tufts University are supported under grant AFOSR-89-0147 with the Air Force Office of Scientific Research.

We thank the referee for a number of helpful suggestions. We are grateful to Kermit Smith of Goddard Space Flight Center for providing the Kitt Peak magnetogram. We also thank Edward Cliver of the Air Force Geophysics Laboratory for providing the Air Force Solar Radio Patrol data and T. Sakurai for providing the magnetic field extrapolation program. Our simultaneous VLA and *Solar Maximum Mission* (*SMM*) observations of the Sun are supported by NASA grant NAG 5-501. The Very Large Array is operated by Associated Universities, Inc. under contract with the National Science Foundation.

REFERENCES

Alissandrakis, C. E., and Kundu, M. R. 1978, *Ap. J.*, **222**, 342.
Das, A. K., and Sethumadhaven, K. 1953, *Nature*, **172**, 446.
Davies, R. D. 1953, *Nature*, **172**, 446.
Dennis, B. R. 1989, *Solar Phys.*, **118**, 49.
Dodson, H. W., and Doselman, R. W. 1951, *Ap. J.*, **113**, 519.
Dulk, G. A. 1985, *Ann. Rev. Astr. Ap.*, **23**, 169.
Dulk, G. A., and Dennis, B. R. 1982, *Ap. J.*, **260**, 875.
Dulk, G. A., and Marsh, K. A. 1982, *Ap. J.*, **259**, 350.
Elgaroy, E. O. 1977, Solar Noise Storms (Oxford: Pergamon Press).
Gary, D. E., and Hurford, G. J. 1988, *Ap. J.*, **317**, 522.
Habbal, S. R., Ellman, N. E., and Gonzalez, R. 1989, *Ap. J.*, in press.
Heyvaerts, J., Priest, E. R., and Rust, D. M. 1977, *Ap. J.*, **216**, 123.
Kai, K., Melrose, D. B., and Suzuki, S. 1985, in *Solar Radiophysics*, ed. D. J. McLean and N. R. Labrum (Cambridge: Cambridge University Press), p. 415.
Kerdraon, A., and Mercier, C. 1982, in *Solar Noise Storms, Proceedings of the 4th Workshop on Solar Radio Noise Storms*, ed. A. O. Benz and P. Zlobec (Osservatorio Astronomico di Trieste), Trieste, p. 27.
Kundu, M. R. 1965, *Solar Radio Astronomy* (New York: Interscience Publishing).
Kundu, M., Gaizauskas, V., Woodgate, B., Schmahl, E. J., Jones, H., and Shine, R. A. 1985, *Ap. J. Suppl.*, **57**, 621.
Kundu, M. R., and Lang, K. R. 1985, *Science*, **228**, 9.
Kundu, M. R., Schmahl, E. J., Velusamy, T., and Vlahos, L. 1982, *Astr. Ap.*, **108**, 188.
Kundu, M. R., and Woodgate, B. 1986, *Energetic Phenomena on the Sun*, ed. M. R. Kundu and B. Woodgate (Greenbelt: NASA CP-2439), Chap. 1.
Lang, K. R., and Willson, R. F. 1984, *Adv. Space Res.*, Vol. 2 (11), p. 91.
———. 1986, *Adv. Space Res.*, Vol. 4 (7), p. 105.
———. 1987, *Ap. J.*, **319**, 514.
———. 1989, *Ap. J. (Letters)*, **344**, L73.
Lang, K. R., Willson, R. F., and Trottet, G. 1988, *Astr. Ap.*, **199**, 325.
Lantos, D., Kerdraon, A., Rapley, G. G., and Bentley, 1981, *Astr. Ap.*, **101**, 33.
Machado, M. E., Moore, R. L., Hernandez, A. M., Rovira, M. G., Hagyard, M. J., and Smith, J. B. 1988, *Ap. J.*, **326**, 425.
Marsh, K. A., and Hurford, G. J. 1980, *Ap. J. (Letters)*, **240**, L111.
Martin, S. F. 1980, *Solar Phys.*, **68**, 217.
Martin, S. F., and Ramsey, H. E. 1972, in *Solar Activity Observations and Predictions*, ed. P. McIntosh and M. Dryer (Cambridge: MIT Press), p. 371.
McClean, D. J. 1973, *Proc. Astr. Soc. Austr.*, **2**, 222.
———. 1981, *Proc. Astr. Soc. Aust.*, **4**, 132.
Melrose, D. B. 1985, in *Solar Radiophysics*, ed. D. J. McClean and N. R. Labrum (Cambridge: Cambridge University Press), p. 177.
———. 1987, *Solar Phys.*, **111**, 89.
Mercier, C., Elgaroy, O., Tlamicha, A., and Zlobec, P. 1984, *Solar Phys.*, **92**, 375.
Rust, D. M. 1976, *Phil. Trans. R. Soc. London*, Ser. A., **281**, 427.
Rust, D. M., Benz, A. O., Nelson, G. J., Pick, M., and Ruzdjak, V. 1981, *Ap. J. (Letters)*, **244**, L179.
Sakurai, T. 1981, *Solar Phys.*, **76**, 301.
Shevgaonkar, R. K., Kundu, M. R., and Jackson, P. D. 1988, *Ap. J.*, **329**, 982.
Spicer, P. S., Benz, A. O., and Huba, J. D. 1981, *Astr. Ap.*, **105**, 221.
Stewart, R. T. 1985, *Solar Phys.*, **96**, 381.
Stewart, R. T., Brueckner, G. E., and Dere, K. P. 1986, *Solar Phys.*, **106**, 107.
Van Nieukoop, J. 1986, *Solar Phys.*, **103**, 129.
Webb, D. F. 1983, *A Study of Coronal Precursors of Solar Flares* (Technical Report AFGL-TR-83-0126).
Webb, D. F., and Kundu, M. R. 1978, *Solar Phys.*, **57**, 155.
Webb, D. F., Krieger, A. S., and Rust, D. M. 1976, *Solar Phys.*, **48**, 159.
Wild, J. P., and Zirin, H. 1956, *Australian J. Phys.*, **9**, 315.
Willson, R. F. 1983, *Solar Phys.*, **83**, 285.
———. 1984, *Solar Phys.*, **92**, 189.
Willson, R. F., Kerdraon, A., Trottet, G., and Lang, K. R. 1990, *Ap. J.*, submitted.
Willson, R. F., and Lang, K. R. 1984, *Ap. J.*, **279**, 427.

MARGARET LIGGETT: Solar Astronomy, California Institute of Technology, Pasadena, CA 91125

ROBERT F. WILLSON and KENNETH R. LANG: Department of Physics and Astronomy, Robinson Hall, Tufts University, Medford, MA 02155

D1 RADIO EMISSION FROM QUIESCENT FILAMENTS

KENNETH R. LANG
Tufts University

IAU COLLOQUIUM NO. 117
DYNAMICS OF PROMINENCES
Hvar, Yugoslavia

September 25-29, 1989

ABSTRACT

Full-disk VLA synthesis maps of the quiet Sun indicate that filaments can be seen in emission at 91.6-cm wavelength; they are detected in absorption at shorter microwave wavelengths. The 91.6-cm emission has a brightness temperature of $T_B = 3 \times 10^5$ K. It is hotter, wider and longer than the underlying filament detected at Hα wavelengths, but the similarity between the shape, position, elongation and orientation of the radio and optical features suggests their close association. The 91.6-cm emission is attributed to the thermal bremsstrahlung of a hot transition sheath that envelopes the Hα filament and acts as an interface between the cool, dense Hα filament and the hotter, rarefied corona. The transition sheath is seen in emission because of the lower optical depth of the corona at 90-cm wavelength, and the width of this sheet is 10^9cm. A power law gradient in pressure provides a better match to the observations than a constant pressure model; definitive tests of theoretical models await simultaneous multi-wavelength studies of filaments at different observing angles. When the thermal bremsstrahlung is optically thin, the magnetic field strength in the transition sheath can be inferred from the observed circular polarization. Variable physical parameters of the sheath, such as width, electron density, and electron temperature, can explain controversial reports of the detection of, or the failure to detect, the meter-wavelength counterpart of Hα filaments.

Subject headings: Sun: filaments - Sun: prominences - Sun: radio radiation
Sun: coronal loops - Sun: magnetic fields

I. INTRODUCTION

Filaments are cooler than the surrounding corona, and therefore appear as depressions in the quiet Sun background at centimeter wavelengths (Gary, 1986; Kundu, Melozzi and Shevgaonkar, 1986); the cool filaments can also appear as depressions at millimeter wavelengths (Schmahl, Bobrowksy and Kundu, 1981). Regions that overlie filaments can now be detected using the VLA at the longer 91.6-cm wavelength; the higher temperatures produce regions of increased emission when compared with the surrounding quiet Sun background.

Previous observations have, however, led to an ongoing controversy about the optical counterparts of the quiescent, or non-flaring, solar radiation at meter wavelengths. A statistical study of numerous one-dimensional Nancay scans suggested that many quiescent meter-wavelength sources are associated with filament corridors as seen on Hα synoptic maps (Axisa et al., 1971), but subsequent two-dimensional maps indicated that most filaments have no radio counterpart at meter wavelengths (Alissandrakis, Lantos and Nicolaidis, 1985; Lantos et al., 1987).

The VLA provides an order-of-magnitude improvement in angular resolution over all previous meter-wavelength investigations of the quiet Sun and might therefore help resolve this controversy. The first VLA observations of the quiescent coronal at 92-cm wavelength indicated no systematic association of any of the radio sources with any optical counterpart, including active regions, filaments, sunspots and the magnetic neutral line in the underlying photosphere (Lang, Willson, and Trottet, 1987). Full disk VLA observations by Shevgaonkar, Kundu, and Jackson (1988) indicated that the 90-cm sources may be indentified as streamers above Hα filaments. However, our comparison of

their data with Hα observations (Solar Geophysical Data) indicates that many of the intense 90-cm sources do not overlie Hα filaments.

One probable source of confusion is noise storms, the most common form of solar activity at meter wavelengths. The numerous type I bursts and background continuum of noise storms have been associated with coronal loop structures detected during Skylab at soft X-ray wavelengths (Stewart and Vorpahl, 1977; Gergely, Kundu, Golub and Webb, 1980) as well as with large-scale EUV loops (Stewart, Brueckner and Dere, 1986). VLA observations at 91.6-cm wavelength confirm the location of noise storms in large-scale magnetic loops that either overlie coronal loops within individual active regions of connect these regions with more distant areas on the Sun (Lang and Willson, 1987); such conclusions were also anticipated by metric wavelength observations with the Nancay Radioheliograph (Lantos-Jarry, 1970; Mercier et al., 1984). Detection of the meter-wavelength counterpart of filaments requires observations when the intense noise storms are not present.

In this paper we present VLA 91.6-cm synthesis maps during quiescent periods without any noise storm activity. In Section II we show that there is an excellent association of some 91.6-cm sources with Hα filaments. The radio filaments are enhanced over the surrounding quiescent emission, rather than depressed. Not all Hα filaments, however, exhibit detectable 91.6-cm counterparts. In Section III we interpret some quiescent 91.6-cm sources in terms of the thermal radiation of a sheath overlying a Hα filament, and with temperatures intermediate between those of its Hα counterpart and the surrounding corona.

II. OBSERVATIONS

The Sun was observed with the VLA in the C/D hybrid configuration between 1315 and 1610 UT on 15 May 1988 using 27 antennas at 20.7-cm wavelength (1446 MHz) and 19 antennas at 91.6-cm wavelength (327.5 MHz) with respective bandwidths of 12.5 and 3.125 MHz. The full-disk synthesis maps at 20.7-cm are given elsewhere (Lang and Willson, 1989a), where they are used to identify active regions that interact via large-scale, trans-equatorial magnetic loops. Here we focus on the full-disk 91.6-cm synthesis map shown in Figure 1 (left). Although all four Stokes parameters were sampled, there was no detectable circular polarization, so our three-hour synthesis map refers to the total intensity, I. Burst data have been removed prior to making this synthesis map. The details of calibration procedures are given in Lang and Willson (1989b).

The contours of the resulting map (Figure 1, left) mark levels of equal brightness temperature, T_B, with an outermost contour of $T_B = 7.8 \times 10^4$ K, a contour interval of 7.8×10^4 K, and peak brightness tempeature of $T_B = 7.8 \times 10^5$ K. The mean brightness temperatures of the elongated sources marked A and B are, for example, estimated to Be $T_B \sim 3 \times 10^5$ K above the surrounding quiet Sun level of $T_B \sim 4 \times 10^5$ K, with an uncertainty of 20 percent.

An Hα photograph taken on the same day (15 May 1988) is also shown in Figure 1 (right); it contains several dark, elongated filaments. Two of these have counterparts in the 91.6-cm map with similar shapes, positions, elongations and orientations; they are designated by the letters A and B in the 91.6-cm map. The smaller filaments seen in the north-central regions also seem to have 91.6-cm counterparts, but there is no increased 91.6-cm emission in the vicinity of the dark filaments that lie near the north-east an south-east limbs (marked C and E on the 91.6-cm map).

The intense 91.6-cm emission detected near the equator on the east limb (marked D) may be due to a coronal streamer. Sacramento Peak coronagraph data (Solar Geophysical Data) show coronal material in this region, as well as those that have no detectable 91.6-cm radiation. No underlying active regions or filaments were visible as the Sun rotated and the limb region turned in to view during the following days.

Depressions in the 91.6-cm radiation are found in the central equatorial regions (hatched regions). They may be at least partly due to coronal holes, but the only available He 10830 data, taken on 14 May, do not exhibit a detectable equatorial coronal hole. Examination of the 91.6-cm maps for shorter time scales showed no evidence for variable features on time scales of a few tens of minutes.

III. DISCUSSION

The similarity in shape, position, elongation and orietation strongly suggests that the radio emision from soucres A and B is associated with the underlying dark filaments detected in the Hα photograph, but the radio emission could also be associated with bright Hα plage and their associated higher magnetic fields. The most intense emission from source A coincides with a dark filament rather than plage, and the most intense part of source B corresponds to the largest part of the underlying filament. Moreover, the weaker emission from both sources has the same shape and orientation as the associated narrow, elongated filaments. We therefore attribute the radio emission to these filaments, whle noticing that Hα plage might also play a role in enhanced 91.6-cm emission.

We therefore interpret the regions of increased 91.6-cm emission around filaments (sources A and B) in terms of a hot sheath that envelops the cooler Hα filaments; such a surrounding sheath is suggested by the fact that the radio wavelength features are similar in shape to, but wider, longer and hotter than, their optical counterparts. The mean 91.6-cm brightness temperatures of $T_B \sim 3 \times 10^5$ K, for example, lie between the electron temperatures of the cool Hα filaments and the electron temperature of the surrounding corona.

In order to gain a quantitative view of the transiton sheath, we compare our observations with the data and models given by Kundu, Melozzi and Shevgaonkar (1986). Their VLA observations at the shorter 6 and 20 cm wavelengths indicated radio depressions above Hα filaments, in comparison with the hot surrounding corona, but a transition sheath was indicated by the fact that the radio filaments are larger in size than their optical counterparts and that the brightness temperature, T_B, of the radio filaments

increases with wavelength from $T_B \sim 1.5 \times 10^4$ K at 6 cm to $T_B \sim 5 \times 10^4$ K at 20 cm. Our higher brightness temperature of $T_B \sim 3 \times 10^5$ K at the longer 91.6-cm wavelength can be explained by the larger optical depth of thermal bremsstrahlung from the transition sheath at longer wavelengths, and the fact that the 91.6-cm sheath is seen in emission can be explained by the relatively low optical depth of the low-density corona. The brightness temperature contribution of the corona has been taken into account by subtracting the background solar disk temperature in obtaining our filament brightness temperature of $T_B \sim 3 \times 10^5$K. If the transition sheath is observed as optically thin bremsstrahlung during future observations, the magnetic field strength can be inferred from the observed circular polarization.

We have assumed that the variation of temperature with height in the transition sheath is that given by Kundu, Melozzi and Shevgaonkar (1986); their data resulted from an assumed balance between the thermal energy conducted in from the corona and the energy radiated away. These temperatures, T, were then combined with three pressure models to infer the electron density, N, and the equation of transfer was solved assuming free-free emission with these values of temperature and density. The three models were a constant pressure model $P = NT = 3 \times 10^{14}$ cm^{-3} K, and two power law models $P = NT = aT^n$, with $a = 2.5 \times 10^{17}$, $n = -0.58$ and $a = 4 \times 10^{17}$, $n = -0.62$. The calculated brightness temperatures of these two models are shown in Figure 2 together with our measurements at 91.6 cm and those of other observers at shorter wavelengths. This figure indicates that the brightness temperature of the constant pressure model is too high at both 20 cm and 90 cm, with respective values of $T_B \sim 9 \times 10^4$ K and $T_B \sim 6 \times 10^5$ K. The power law models are more in accord with the observational data; at 20 cm

and 90 cm they both produce respective values of $T_B \sim 5 \times 10^4$ K and $T_B \sim 3 \times 10^5$ K. Also note that the 20 cm point is an average of several observations for different observing angles, so this difference cannot account for the result. Detailed model comparisons await future multi-wavelength studies of the same filament at the same time for different observing angles.

So, the observed 91.6-cm structures that are associated with these Hα filaments may be interpreted as the thermal bremsstrahlung of a hot (electron temperature $T_e \approx 3 \times 10^5$ K) sheath that envelops a Hα filament. Such a sheath acts as the boundary between the filament and the surrounding million-degree corona. A loop thickness of $L \approx 10^9$ cm, or about one fiftieth of the $10' \approx 5 \times 10^{10}$ cm extent of the radio sources A and B, has been inferred by deconvolving the observed radio width, to take into account the beamwidth, and using the convolution relation to subtract the observed width of the Hα filament. Such a thickness is consistent with the models of Kundu, Melozzi and Shevgaonkar (1986). If the hypothesized sheath were substantially thinner than the assumed thickness of $L \approx 10^9$ cm, then the optical depth for thermal bremsstrahlung would be much smaller, and the optically-thin sheath might not be detectable. And if the electron density of the sheath was only slightly higher, then its plasma frequency would exceed our observing frequency, and the sheath radiation could not propagate out to be observed. Variable physical parameters of the sheath might therefore easily explain why the elusive meter-wavelength counterpart of Hα filaments is only sometimes observed; just the right thickness, electron density and electron temperature are required for detection.

ACKNOWLEDGMENTS

Radio astronomical studies of the Sun at Tufts University are supported under grant AFOSR-89-0147 with the Air Force Office of Scientific Research. The Very Large Array is operated by Associated Universities, Inc., under contract with the National Science Foundation. The data presented in this paper were taken during collaborative long-wavelength solar observations by Tufts University and the Observatoire de Paris - Meudon, under the support of National Science Foundation grant INT-8602285 and Centre National de la Recherche Scientfique grant 920038.

REFERENCES

Alissandrakis, C.E., Lantos, P., and Nicolaidis, E. 1985, Solar Phys., 97, 267.

Axisa, F., Avignon, Y., Martres, M.J., Pick, M., and Simon, P. 1971, Solar Phys., 19, 110.

Gary, D.E. 1986, in Coronal and Prominence Plasmas, ed. A.I. Poland (NASA Conf. Pub. 2442), p. 121.

Gergely, T.E., and Kundu, M.R. 1980, in Radio Physics of the Sun. IAU Symposium No. 86, ed. M.R. Kundu and T.E. Gergely, p. 435.

Kundu, M.R., Melozzi, M., and Shevgaonkar, R.K., 1986, Astron. Ap., 167, 166.

Lang, K.R., and Willson, R.F. 1987, Ap.J., 319, 514.

Lang, K.R., and Willson, R.F. 1989a, Ap. J. (Letters) 344, L 77.

Lang, K.R., and Willson, R.F. 1989b, Ap. J. (Letters) 344, L 73.

Lang, K.R., Willson, R.F., and Trottet, G. 1988, Astron. Ap., 199, 325.

Lantos, P., Alissandrakis, C.E., Gergely, T., and Kundu, M.R. 1987, Solar Phys., 112, 325.

Lantos - Jarry, M.F. 1970, Solar Phys., 15, 40.

Mercier, C., Elgaroy, O., Tiamicha, A. and Zlobec, P. 1984, Solar Phys., 92, 375.

Schmahl, E.J., Bobrowksy, M., and Kundu, M.R. 1981, Solar Phys., 71, 311.

Stewart, R.T., Brueckner, G.E., and Dere, K.P. 1986, Solar Phys., 106, 107.

Stewart, R.T., and Vorpahl, J. 1977, Solar Phys., 55, 111.

FIGURE LEGENDS

FIG. 1. A three-hour Very Large Array (VLA) synthesis map of the total intensity, I, from the visible solar disk at 91.6-cm (left) is compared with an Hα photograph (right) taken at Boulder Solar Observatory - at 1415 UT on the same day (15 May 1988, courtesy of Pat McIntosh). The synthesized beamwidth is denoted by the small black spot in the lower right-hand corner; it has angular dimension of 80" x 55" at a position angle of -20°. The circle in the 91.6-cm map denotes the visible solar limb, and the tick marks denote solar north and south. Radio wavelength emission from dark, elongated filaments in the Hα photo are designated by A and B in the 91.6-cm map. Filaments C and E did not correspond to enhanced 91.6-cm emission while source D probably coincides with a coronal streamer. The hatched regions in the central equatorial regions correspond to depressions in the 91.6-cm emission.

FIG. 2. Calculated brightness temperatures for a constant pressure $P = 3 \times 10^{14}$ cm^{-3} K (dashed line) and a power law pressure $P = 2.5 \times 10^{17}$ $T^{-0.58}$ with $dT/dh = 0$ at height $h = 0$. The observed temperature at 91.6-cm (filled circle) is from this paper, whereas the other values (crosses, open circles, open squares and open triangles) are from Kundu, Melozzi and Shevgaonkar (1986) with their 6 and 20 cm measurements increased by a Factor of 1.7 due to the detection of a software calibration error. The brightness temperatures refer to mean values over the radio source.

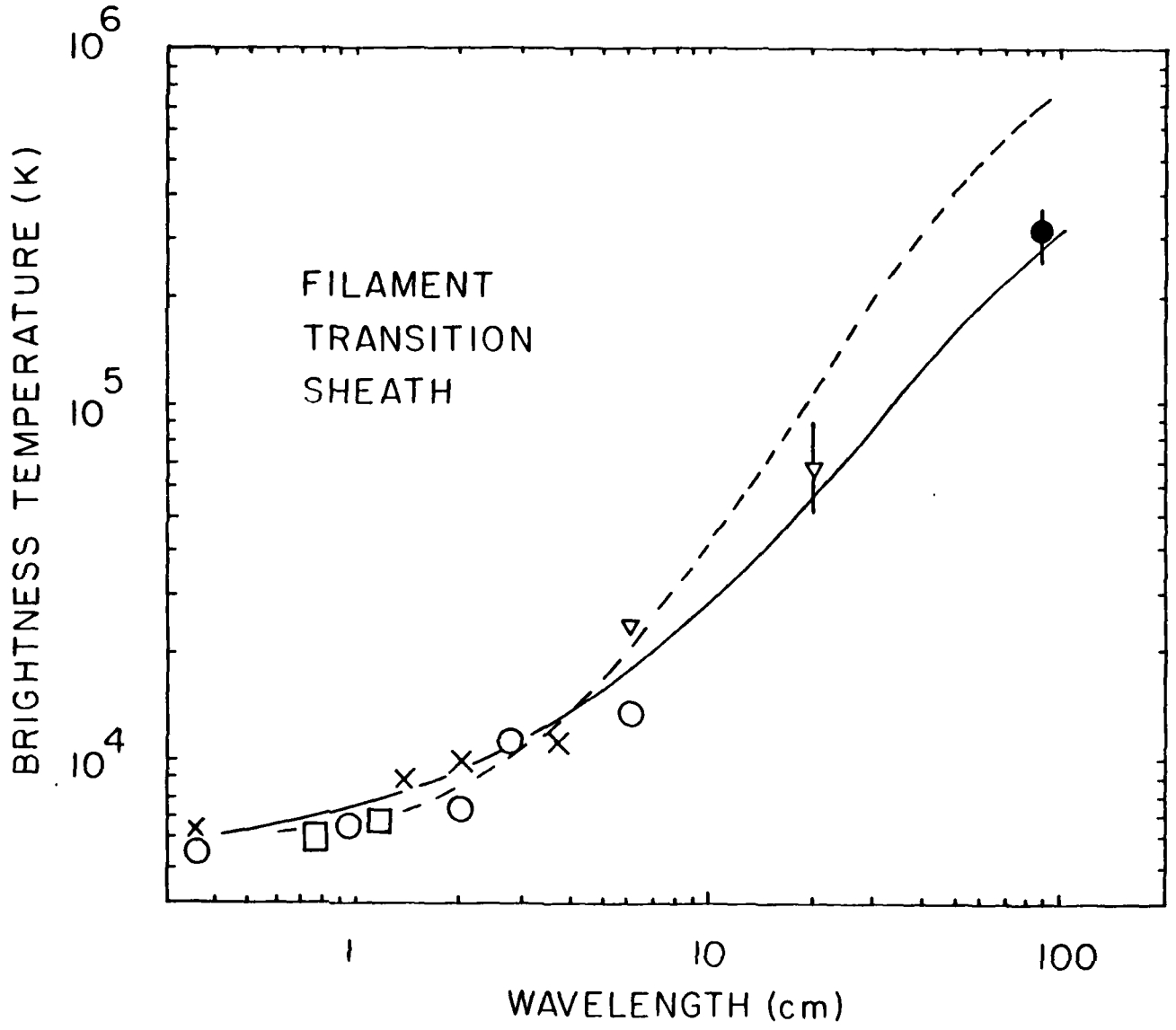
BRIGHTNESS TEMPERATURE (K)
10^6
10^5
10^4
FILAMENT
TRANSITION
SHEATH
1
10
100
WAVELENGTH (cm)

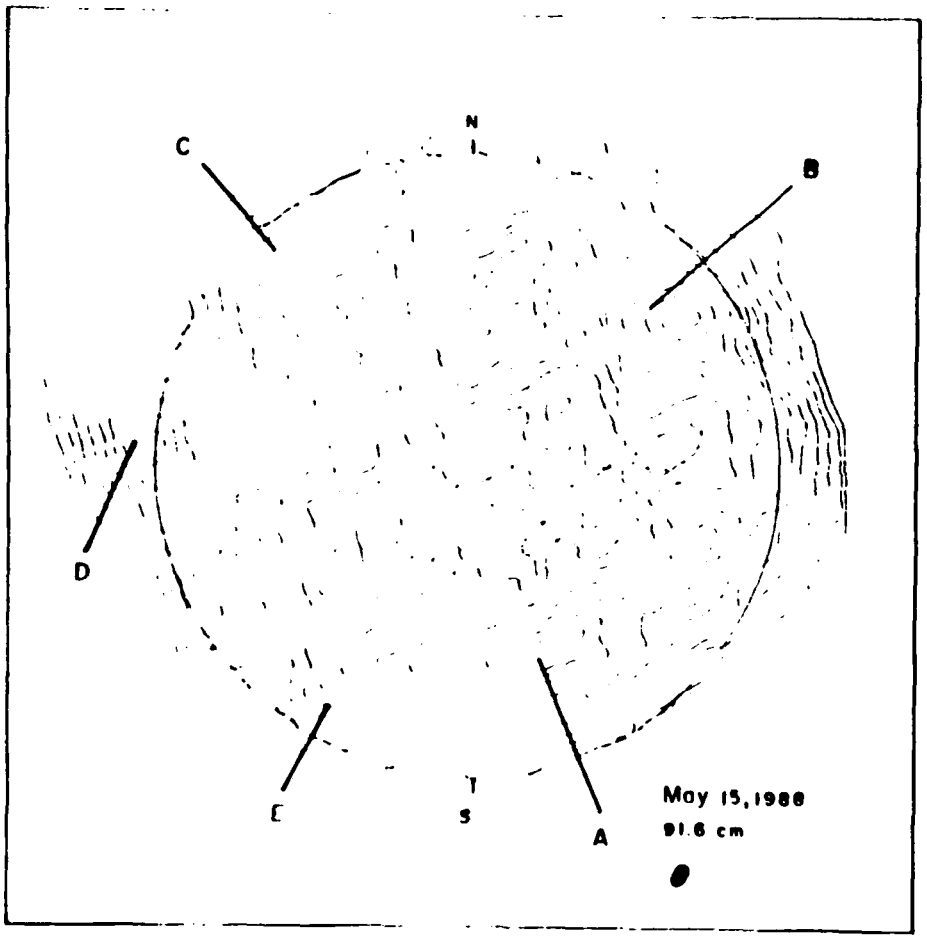
N
C
B
D
E
S
A
May 15, 1988
91.6 cm

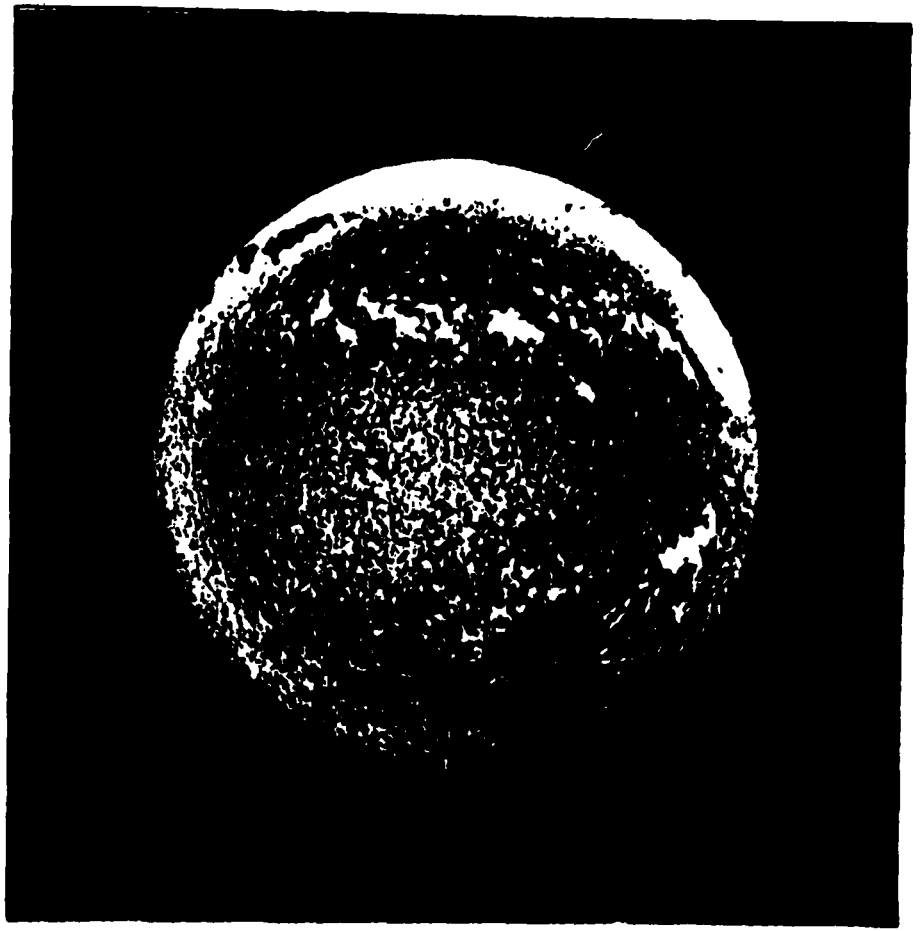

D2. FLARE STARS AT RADIO WAVELENGTHS

Kenneth R. Lang, Tufts University

Invited Review

I.A.U. SYMPOSIUM No. 137 - FLARE STARS

Byurakan, Armenia, USSR

October 23-27, 1989

FLARE STARS AT RADIO WAVELENGTHS

KENNETH R. LANG
Department of Physics and Astronomy
Tufts University
Medford, MA 02155
U.S.A.

ABSTRACT. The radio emission from dMe flare stars is discussed using Very Large Array and Arecibo observations as examples. Active flare stars emit weak, unpolarized, quiescent radio radiation that may be always present. Although thermal bremsstrahlung and/or thermal gyroresonance radiation account for the slowly-varying, quiescent radio radiation of solar active regions, these processes cannot account for the long-wavelength quiescent radiation observed from nearby dMe flare stars. It has been attributed to nonthermal gyrosynchrotron radiation, but some as yet unexplained mechanism must be continually producing the energetic electrons. Long-duration (hours), narrow-band ($\Delta\nu/\nu < 0.1$) radiation is also emitted from some nearby dMe stars at 20 cm wavelength. Such radiation may be attributed to coherent plasma radiation or to coherent electron-cyclotron masers. Impulsive stellar flares exhibit rapid variations (< 100 msec) that require radio sources that are smaller than the star in size, and high brightness temperatures $T_B > 10^{15}$ K that are also explained by coherent radiation processes. Quasi-periodic temporal fluctuations suggest pulsations during some radio flares. Evidence for frequency structure and positive or negative frequency drifts during radio flares from dMe stars is also presented.

1. INTRODUCTION

Pioneering single-dish observations in the 1970s showed that dwarf M flare stars occasionally emit radio bursts with extremely high flux densities and brightness temperatures of $T_B > 10^{12}$ to 10^{15} K if the radio source is comparable to the star in size (see Lang and Willson (1986b) and Kundu and Shevgaonkar (1988) for some historical details). Such powerful radio flares are extremely rare, sporadic and brief, however, leading many to suspect that they might be confused with terrestrial interferance. Moreover, identification by correlation with optical flares could not be relied on, for different radiation mechanisms often dominate in the two spectral domains.

Interferometric observations with the Very Large Array (VLA) have unambiguously differentiated stellar radio emission from terrestrial interferance, and the large collecting area of both the VLA and the Arecibo Observatory have enabled detection of the relatively weak radio flares that are presumably more frequent than the more powerful ones. One survey, for example, indicates that flaring emission can be detected for about 40% of flare stars nearer than 10 parsecs and visible with the VLA (White, Kundu and Jackson, 1990). Under the assumption that the radio source size is equal to the stellar radius, brightness temperatures of $T_B = 10^8$ to 10^{10} K and $T_B = 10^9$ to 10^{11} K have been inferred for the detected stars at 6 cm and 20 cm wavelength, respectively.

Although the observed radio luminosity from stellar flares is only about one thousandth the luminosity observed at X-ray or optical wavelengths, the radio emission is still thousands of times more powerful than solar radio flares, and it serves as an important diagnostic tool for studies of stellar coronae. Such studies have been carried out in detail for the most active dwarf M flare stars listed in Table 1. They are all nearby dMe stars that show evidence for chromospheric activity in the form of Ca II, Mg II and Hα emission lines.

Table 1. Accurate 6 cm positions, spectral type, Sp, quiescent flux density, S_{Q6}, at 6 centimeters wavelength, peak flaring flux density, S_{F20}, at 20 centimeters wavelength, distance, D, in parsecs, and the logarithm of the quiescent X-ray luminosity, log L_x, for radio-active flare stars.

Star	R.A.(1950.0) h m s	Dec.(1950.0) ° ′ ″	Sp	S_{Q6} (mJy)	S_{F20} (mJy)	D (pc)	log L_x (erg s^{-1})
L 726-8A**	01 36 33.314	- 18 12 23.20	dM5.5e	1.0	20	2.7	27.5
UV Ceti**	01 36 33.404	- 18 12 21.56	dM6e	3.2	100	2.7	27.5
YY Gem	07 31 25.691	+31 58 47.23	dM1e	0.4	1	14.5	29.5
YZ CMi	07 42 02.962	+03 40 30.39	dM4.5e	0.5	20	6.0	28.5
AD Leo	10 16 52.604	+20 07 17.59	dM3.5e	1.1	100	4.9	29.0
Wolf 630A,B	16 52 46.455	- 08 15 13.715	dM4.5e	0.9	3	6.2	
AT Mic†	20 38 44.4	- 32 36 49.5	dM4.5e	3.6	6	8.8	29.3
AU Mic	20 42 04.558	- 31 31 17.50	dM0e	0.8	26	8.8	29.8
EQ Peg A††	23 29 20.910	+19 39 41.11	dM5e	0.3	25	6.4	

*Adapted from Kundu et al. (1987), and Jackson, Kundu and White (1989) for the 6 cm data, with positions accurate to 0″.1 or better.

**The separation and position angle of L 726-8A and L 726-8B (UV Ceti) is 2″.080 ± 0″.080 at 38°.0 ± 1°.9.

†Southern component of a fully resolved binary whose components are both active radio emitters; the nothern component lies about 3″.6 away at a position angle of about 15°.

††Quiescent emission from both component of EQ Peg A, B has been previously detected with respective 6 cm fluxes of 0.7 and 0.4 mJy and an angular separation of about 3″.0 (see Gary (1985)).

This review will focus on these radio-active dMe stars. They include the very few cases in which we can detect the relatively weak (a few mJy), quiescent radio flux of the star (see Section 2). Long-duration, narrow-band radio flares (Section 3) have also been observed from several of these stars; they are unlike anything observed on the Sun.

Powerful (up to 200 mJy), impulsive (a few minutes) radio flares are also emitted by these stars. Such flares exhibit rapid variations (Section 4.1), quasi-periodic fluctuations (Section 4.2), both narrow-band and broad-band features (Section 5) and positive and negative frequency drifts (Section 5).

Figures 1 and 2 illustrate such flares for the dMe star EQ Pegasi. They are often up to 100% circularly polarized. Successive oppositely polarized flares have been detected for EQ Pegasi (Fig. 2) and AD Leonis (Willson, Lang and Foster (1988)), suggesting the presence of both magnetic polarities; but YZ Canis Minoris always exhibits left-handed circular polarization that remains the same over a wide range of wavelength (6 cm to 90 cm), suggesting a global, dipolar magnetic field that is viewed pole-on (Kundu and Shevgaonkar (1988)).

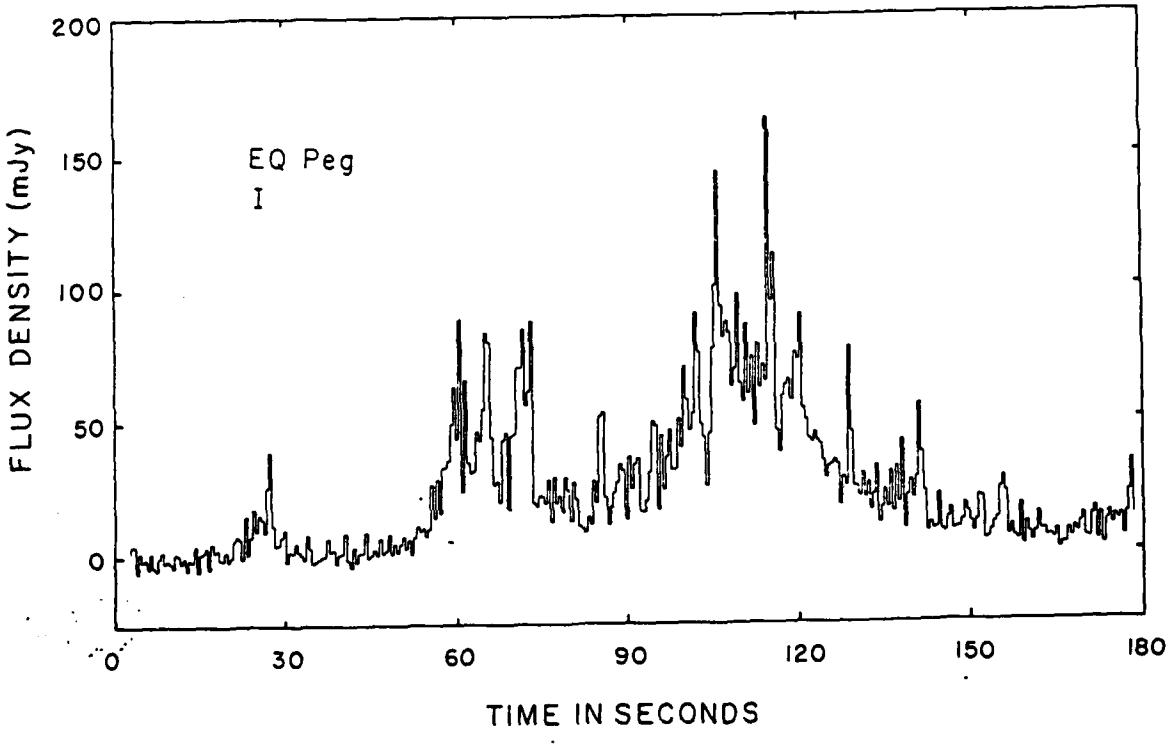

Figure 1. A previously unpublished VLA observation of the total intensity, I, at 1420 MHz (21 cm) from the dwarf M star EQ Pegasi. The flaring emission has a total duration of minutes, with components on shorter time scales of seconds or less. The radiation is up to 100 percent circularly polarized (see Fig. 2).

2. QUIESCENT RADIO EMISSION FROM dMe FLARE STARS

Unpolarized radio radiation that is nearly always present, and shows only slow variations with time, has been termed quiescent radio emission to distinguish it form the highly variable, brief radio flares that are often highly circularly polarized. The quiescent emission has flux densities of a few mJy at 6 cm wavelength (see Table 1 and Gary (1985)). It was at first attributed to thermal radiation from the same electron population that gives rise to the stellar X-ray emission (also see Table 1). If this were the case, it would be consistent with the Sun's slowly varying radiation at centimeter wavelengths, the solar radiation is due to either thermal bremsstrahlung or the thermal gyroresonance radiation of hot (10^6K) electrons trapped within coronal loops that radiate strongly at X-ray wavelengths.

Nevertheless, thermal emission from the stellar coronae observed in X-rays cannot easily account for the quiescent radiation. Thermal bremsstrahlung of the X-ray plasma is so optically thin at 6 cm wavelength that its flux density is one or two orders of magnitude below the detection limit of the VLA - even when the X-ray plasma covers the entire surface of the nearest flare star.

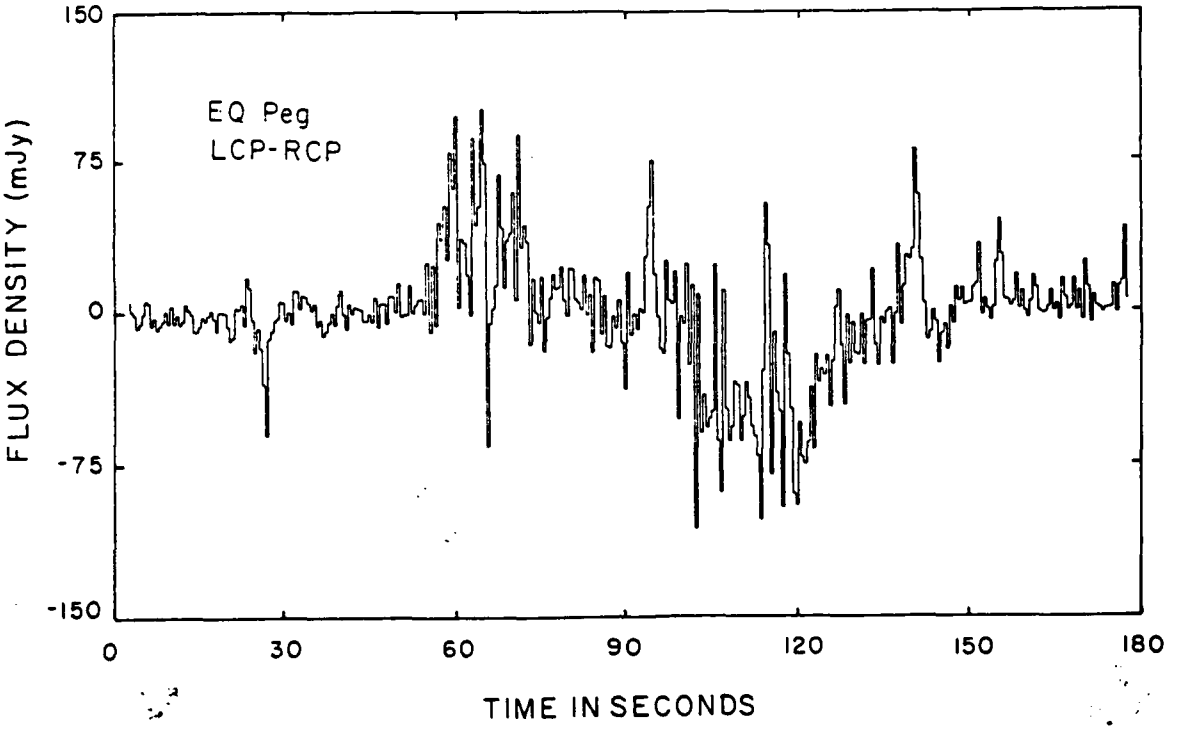

Figure 2. The difference between the left-hand circularly polarized (LCP) and right-hand-circularly polarized (RCP) radiation from the dwarf M star EQ Pegasi at 1420 MHz (21 cm). Up to 100 percent circularly polarized radiation is emitted with opposite senses, or directions, for successive bursts (courtesy of Robert F. Willson).

The optical depth can be enhanced for the gyroresonance of thermal electrons in relatively strong magnetic fields. Short-wavelength < 6 cm) quiescent emission might then be explained by optically thick gyroresonant radiation of the high-temperature tail of the X-ray emmitting plasma (Gudel and Benz, 1989). In this case, the radio data require electrons that are at a higher temperature than the average X-ray emitting electrons, and they are probably emitted from a source that is much larger than the star. The maximum observed flux density, S, is given by the Rayleigh-Jeans law, and the radius of the emitting source is therefore given by:

$$R^2 = 10^{13} \frac{SD^2}{\nu^2 T} \quad cm^2 ,$$

where S is the source flux denisty in Jy, D is the distance in cm, T_6 is the temperature in K, and the observing frequency is $\nu = 2.8 \times 10^6$ nH Hz for the n th harmonic in a magnetic field of strength H. Radii comparable to those of the dwarf M stars are only obtained for low flux densities, S = 1 mJy, short wavelengths, $\lambda < 6$ cm, high temperatures $T > 10^7$ K, and nearby dMe flare stars, D < 10 pc.

Thermal gyroresonance radiation cannot explain the long-wavelength, $\lambda > 20$ cm, quiescent radiation where higher flux densities of S = 2 to 20 mJy have been observed (Lang and Willson, 1986 a, Bastian and Brokbinder, 1987, Gudel and Benz, 1989). The radio source would have to be tens to hundreds of times larger than the star with implausibly intense magnetic fields at these remote locations. This long-wavelength radio emission has been attributed to nonthermal gyrosynchrotron radiation.

The gyrosynchrotorn hypothesis requires a hotter corona with smaller sizes and lower densities than the gyroresonance model, but there must be a currently - unexplained, steady source of energetic electrons. Both models have been discussed by Kundu et al. (1987); because the gravitational scale height is comparable to the height of the stellar coronae, magnetic structures are required to confine the radio-emitting plasma. The coronae of nearby dMe flare stars therefore bear a closer resemblance to the Earth's magnetosphere than to the Sun's corona. We do not know if the relevant magnetic structures on the flare stars are due to several small active regions or to a global dipolar field, and we do not know how the radio-emitting electrons interact with the X-ray emitting plasma. The long-wavelength quiescent radiation might alternatively be due to continued, low-level, narrow-band, coherent radiation that resembles radio flares from these stars.

3. LONG-DURATION, NARROW-BAND EMISSION

Relatively intense(S = 100 mJy), narrow-band ($\Delta\nu/\nu < 0.1$) radiation lasting for several hours has been observed at 20 cm wavelength in several flare stars (Lang and Willson, 1986; White, Kundu and Jackson, 1986; Kundu et al., 1987; Lang and Willson, 1988). These

long-duration events are slowly variable, so they might be more energetic version of the process that accounts for the quiescent radiation. However, the long-duration, narrow-band radiation is highly circularly polarized, so its polarization bears a closer resemblance to the stellar flares than to the unpolarized quiescent radiation.

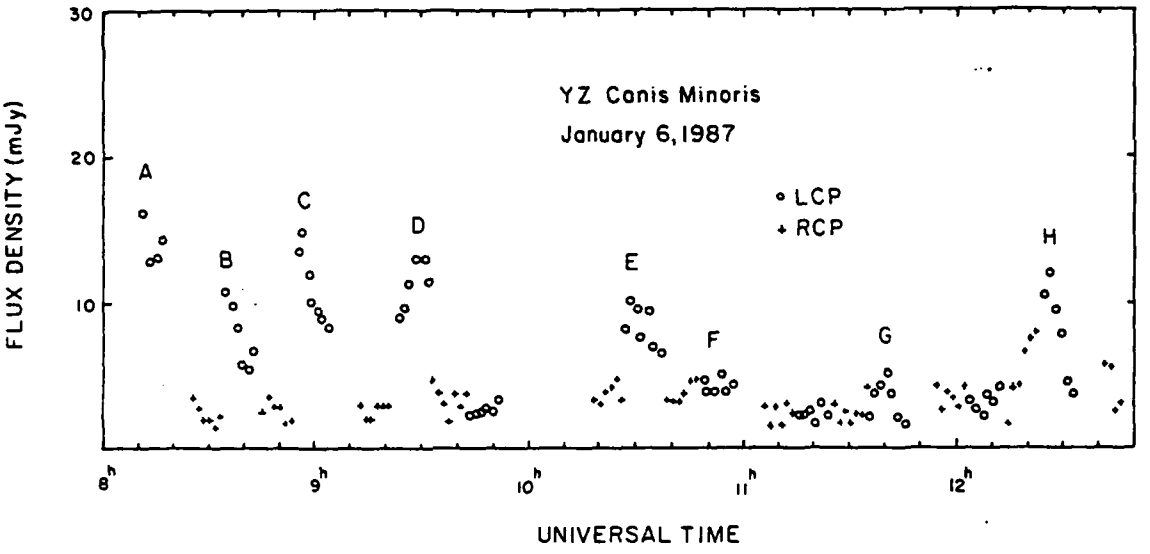

Figure 3. A five-hour VLA observation of the total intensity of the radiation from the dwarf M star YZ Canis Minoris in a 50 MHz bandwidth centered at 1464.9 MHz. The radiation is 100 percent left-hand circularly polarized. Its narrow-band frequency structure is illustrated in Fig. 4. (adapted from Lang and Willson (1986a)).

The long-duration, narrow-band highly polarized radiation (see Figures 3 and 4) is unlike any flares observed on the Sun, and cannot be easily explained using the solar analogy. The energy release mechanism lasts at least an order of magnitude longer than solar flares, and is difficult to understand if magnetic reconnection is the source of energy for the stellar flares (White, Kundu and Jackson, 1986). The narrow-band structure cannot be attributed to continuum emission processes such as thermal bremsstrahlung, thermal gyroresonant radiation, or nonthermal gyrosynchrotron radiation; it may be due to coherent mechanisms like electron-cyclotron masers or coherent plasma radiation. Both mechanisms require a magnetic field to produce the high circular polarization - either at the site of radiation production or during subsequent propagation of initially unpolarized radiation.

The coherent radiation processes provide constraints on the physical conditions in the coronae of flare stars (Lang, 1986). An upper limit to the electron density in the source is given by the requirment that the observing frequency must be greater than the

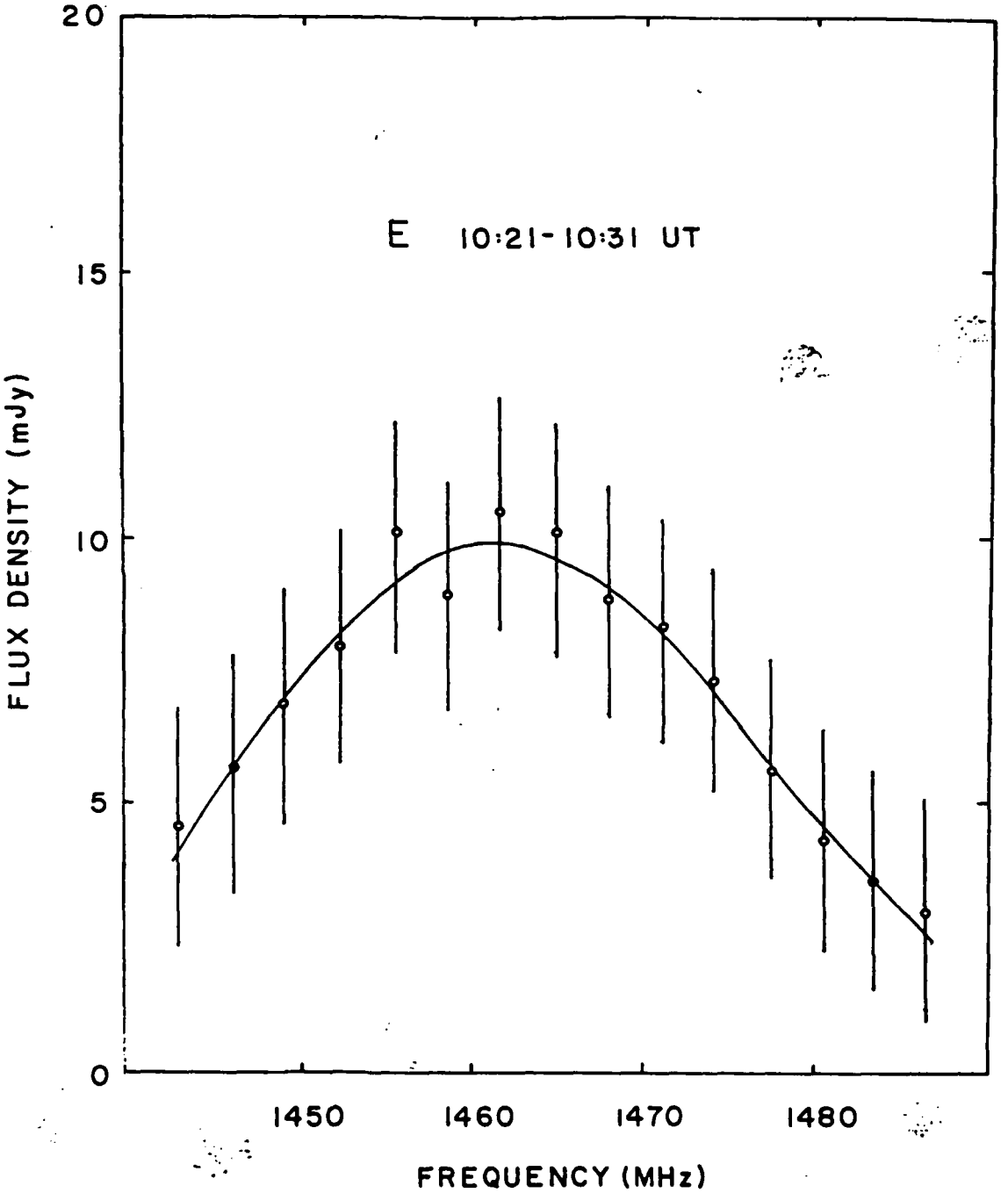

Figure 4. Frequency spectrum of the left circularly polarized radiation from YZ Canis Minoris for the interval marked E in Figure 1. Here the total intensity is plotted for 15 contiguous channels, each 3.125 MHz wide, for the 10-second interval. These data, as well as those for other intervals lettered in Fig. 3, show evidence for narrow-band radiation with a bandwidth $\Delta\nu < 30$ MHz, or $\Delta\nu/\nu = 0.02$. (Adapted from Lang and Willson (1986a)).

plasma frequency for the radiation to propagate out and reach the observer; at 20-cm wavelength this requires $N_e < 2.5 \times 10^{10}$ cm^{-3}. If an electron-cyclotron maser emits at the second or third harmonic of the gyrofrequency, then a coronal magnetic field strength of H = 250 G or 167 G is required to explain the 20 cm radiation. Coherent plasma radiation at the second harmonic of the plasma frequency requires an electron density of $N_e = 6 \times 10^9$ cm^{-3}. If coherent plasma radiation dominates, then the plasma frequency must be larger than the electron gyrofrequency, thereby providing an upper limit to the magnetic field strength H < 250 G.

4. TEMPORAL STRUCTURE OF RADIO FLARES

4.1 Rapid Variations

Radio flares from the dMe star AD Leonis near 20 cm wavelength consist of rapid (< 100 milliseconds), highly-polarized (up to 100% left-hand circularly polarized) spikes whose rise times provide stringent limits to the size and brightness temperature of the radio source. Such rapid variations were first observed by Lang et al. (1983) using the Arecibo Observatory (see Figure 5). They have been confirmed by Bastian et al. (1990) using the same radio telescope, and by Gudel, et al. (1989) whose simultaneous observations with the radio telescopes in Effelsberg, Jodrell Bank and Arecibo substantiated the common origin of the radiation and eliminated any remaining doubts about its stellar origin (the time coincidence of flares observed at the three sites was within 0.4 seconds).

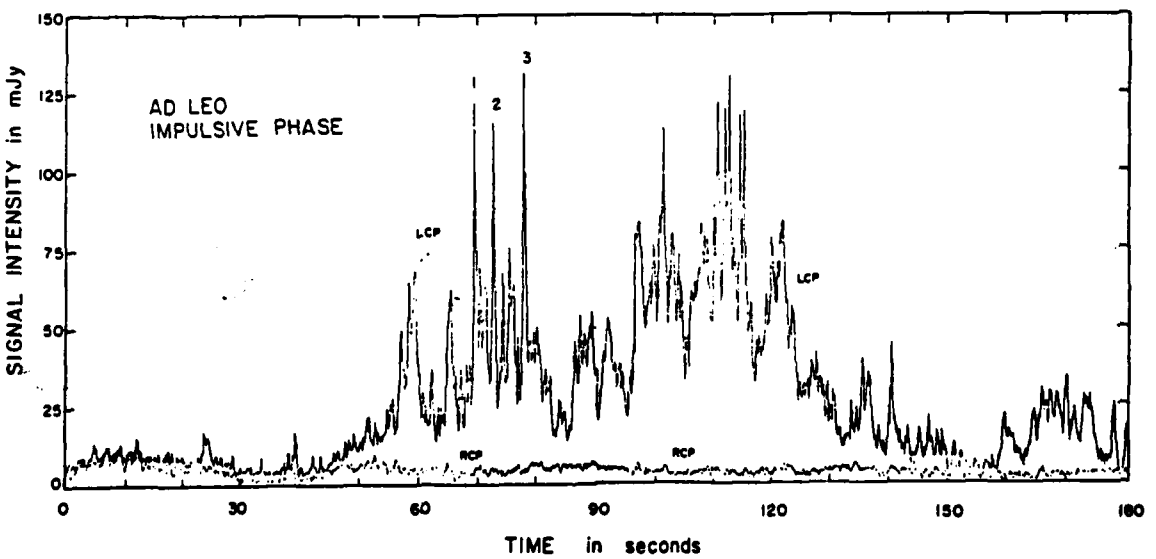

Figure 5. These observations, taken at 1400 MHz (21 cm) with the Arecibo Observatory, indicate that highly left-circularly polarized (LCP) radiation from the dwarf M star AD Leonis consists of rapid spikes whose duration τ < 100 milliseconds. The emitting source must be much smaller than the star in size.(Adapted from Lang et al. (1983)).

The spikes labeled 1,2 and 3 in Figure 5 have rise times $\tau < 200$ milliseconds, and upper limits of $\tau < 20$ milliseconds have been observed. An upper limit to the linear size, L, of the emitting region is provided by the distance that light travels in time, τ, or $L < c \times \tau$. A light-travel time of 20 milliseconds indicates $L < 6{,}000$ km, which is less than 1% of the stellar diameter. If the burst emitter is symmetric, it has an area less than 0.0003 of the stellar surface area, and the brightness temperature, T_B, is $T_B > 10^{15}$ K.

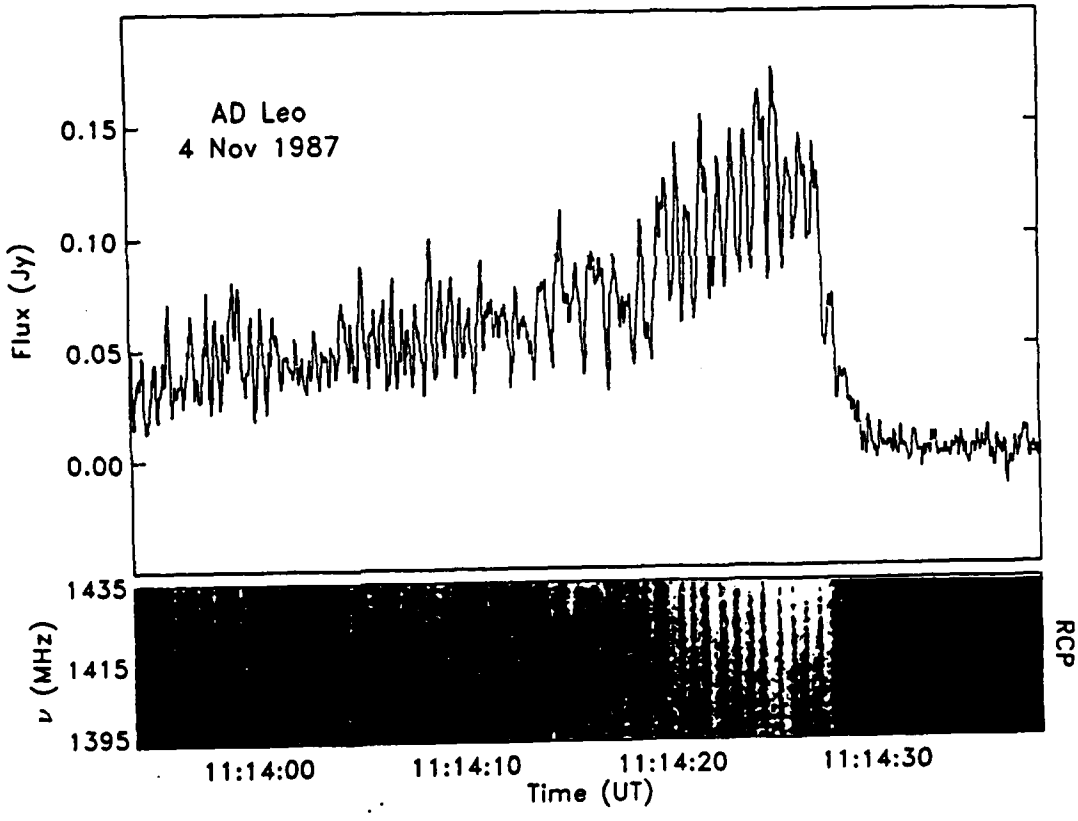

Figure 6. Observations of AD Leonis at 1415 MHz (21 cm) with the Arecibo Observatory indicate quasi-periodic pulsations with an amplitude modulation of ≈ 50 percent and a period of ≈ 0.7 seconds (top). The dynamic spectrum (bottom) indicates that the pulsations are broad-band with bandwidths $\Delta\nu > 40$ MHz. (Adapted from Bastian et al. (1990)).

4.2. Quasi-Periodic Fluctuations

Radio flare emission from AD Leonis has also been resolved into a multitude of broad-band, quasi-periodic fluctuations called pulsations. Such pulsations have been reported by Lang and Willson (1986), Gudel et al. (1989) and Bastian et al. (1990); and example is shown in Figure 6. The typical interval between pulses is about 1 second, which

is comparable to that of solar decimetric pulsations. The AD Leo pulsations are up to 100% circularly polarized; they are coherent across the observing bandwidths of up to 100 MHz. They might be attributed to oscillations in a coronal loop with dimensions of about 5,000 km, which is close to the upper size limit inferred from the light-travel time.

5. FREQUENCY STRUCTURE OF RADIO FLARES

Observations of the radio radiation intensity as a function of both time and frequency (dynamic spectra) can independently confirm the small size of the radio emitter and provide insights to the relevant plasma processes. Dynamic spectra of UV Ceti near 20 cm wavelength (Bastian and Bookbinder, 1987) indicated, for example, both broad-band (> 40 MHz) and narrow-band ($\Delta\nu/\nu < 0.002$) features. The narrow-band emission is most likely due to a coherent radiation mechanism. A spectral component with a width, $\Delta\nu$, of 0.2 percent of the central frequency, ν, puts an upper limit on the source diameter of 200 km, assuming a scale height of one stellar radius, the largest reasonable. If an electron-cyclotron maser is responsible, the magnetic field strength $H \approx 250$ G and the electron density $N_e < 10^9$ cm^{-3}.

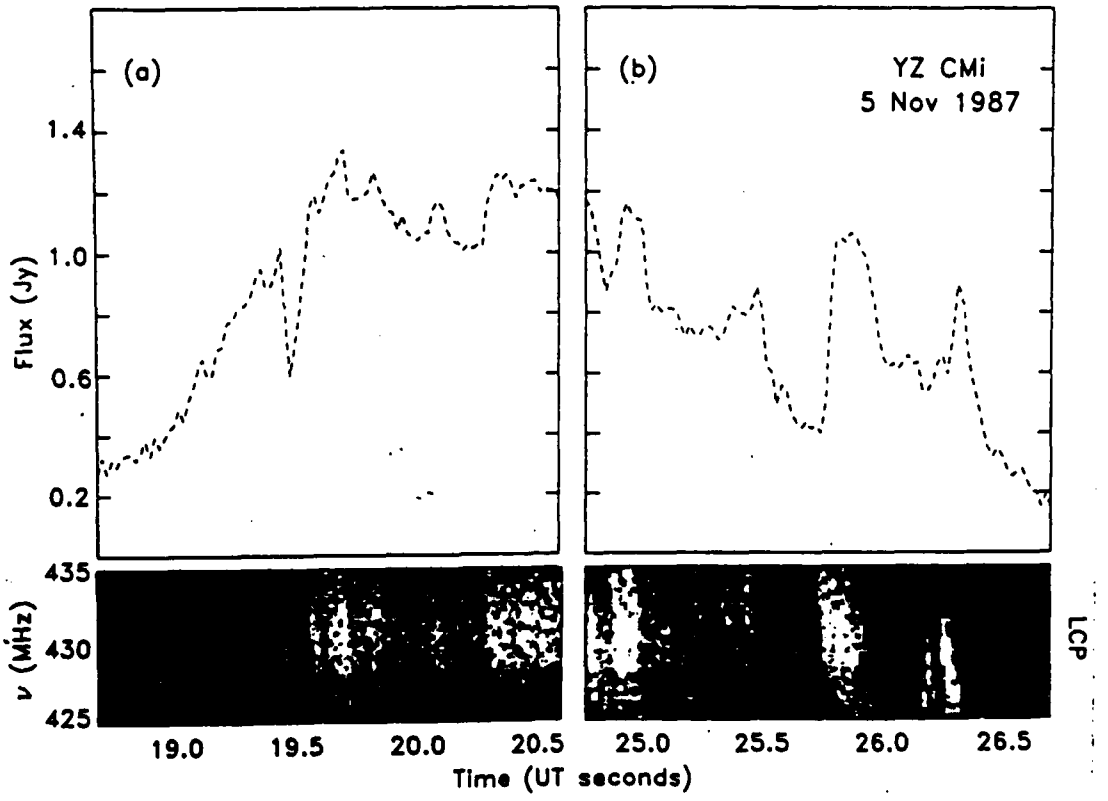

Figure 7. These Arecibo observations of the dynamic spectra (lower panel) of the 430 MHz (70 cm) radiation from the dwarf M star YZ Canis Minoris indicate a sudden reduction feature, in (a), with a drift in frequency of 250 MHz/s from high to low frequencies, as well as other narrowband and drifting features in (b). (Adapted from Bastian et al. (1990)).

Dynamic spectra of the radio radiation from the dMe flare stars AD Leo, YZ Cmi and UV Ceti show considerable complexity, with both narrow-band and broad-band features, and both positive and negative frequency drifts (Bastian and Bookbinder, 1987; Jackson, Kundu, and White, 1987; Bastian et al., 1990). The example shown in Figure 7 has a negative drift of 250 MHz per second from high to low frequencies. Such a negative drift is commonly observed in the Sun (eg. type II and type III bursts) suggesting electron beams or shock waves that propagate outwards in the stellar corona. But positive frequency drifts have also been observed for flare stars, suggesting a distrubance that propagates downward in the stellar corona and progressively excites plasma radiation at higher frequencies (larger electron densities).

Thus, there is clear evidence for apparent frequency drifts and narrow-band features in radio flares from dMe stars, but their interpretation is currently open to question. They could be due to the progagation of an exciter, group delays or some other cause.

6. DISCUSSION

To sum up, the quiescent radio radiation from dMe stars might be due to exceptionally hot thermal electrons, nonthermal electrons, or near continual coherent flaring. The high brightness temperatures, strong circular polarization and narrow frequency extent of long-duration radio events require a coherent plasma process, as does the more impulsive stellar radio flares. The cyclotron maser could explain many aspects of the flaring emission (Dulk, 1985), but several other coherent radiation processes might be involved (Kuijpers, 1989; Mullan, 1989). When the correct radiation mechanisms are identified, perhaps as the result of future observations with broader bandwidths, we can accurately specify the physical parameters in the stellar coronae.

Different processes probably dominate at different wavelengths, as they do on the Sun, and both solar and stellar flares must be related to magnetic fields. Past theoretical studies of solar radio radiation can therefore provide a useful background for exploring plausible radiation mechanisms. However, the direct analogy of the Sun as a radio flare star is probably a mistake; the Sun is the wrong spectral type, and its radio flares are so weak that they would be undetectable at the distance of the nearest star. In addition, solar flares have near-simultaneous signatures at optical, radio and X-ray wavelengths, while flaring radio emission from the dMe stars is often undetectable in other regions of the electromagnetic spectrum (see for instance Kundu et al. (1989)). The available evidence therefore indicates that radio flares from dwarf M flare stars are physically very different from those occuring on the Sun.

7. ACKNOWLEDGMENTS

Radio astronomical studies of the Sun and other nearby active stars at Tufts University are supported under grant AFOSR-89-0147 with the Air Force Office of Scientific Research. Related solar observations are supported by NASA grant NAG 5-501. The Arecibo Observatory is part of the National Astronomy and Ionosphere Center, which is operated by Cornell University under contract with the National Science Foundation (N.S.F.). The Very Large Array is operated by Associated Universities, Inc., under contract with the N.S.F.

8. REFERENCES

Bastian, T.S. and Bookbinder, J.A. (1987) 'First dynamic spectra of stellar microwave flares', Nature, 326, 678-680.

Bastian, T.S., Bookbinder, J., Dulk, G.A. and Davis, M. (1990) 'Dynamic spectra of radio bursts from flare stars', Astrophysical Journal, April 10, 1990 issue.

Dulk, G.A. (1985), 'Radio emission from the sun and stars', Annual Review of Astronomy and Astrophysics 23, 169-224.

Gary, D.E. (1985) 'Quiescent stellar radio emission', in R.M. Hjellming and D.M. Gibson (eds.), Radio Stars, D. Reidel, Boston, pp. 185-196.

Güdel, M. and Benz, A.O. (1989) 'Broad-band spectrum of dMe star radio emission', Astronomy and Astrophysics Letters, 211, L5-L8.

Güdel, M., Benz, A.O., Bastian, T.S., Fürst, E., Simnett, G.M. and Davis, R.J. (1989) 'Broadband spectral observation of a dMe star radio flare', Astronomy and Astrophysics Letters 220, L5-L8.

Jackson, P.D., Kundu, M.R. and White, S.M., (1987) 'Dynamic spectrum of a radio flare on UV Ceti', Astrophysical Journal Letters 316, L85-L90.

Jackson, P.D., Kundu, M.R. and White, S.M. (1989) 'Quiescent and flaring radio emission from the flare stars AD Leonis, EQ Pegasi, UV Ceti, Wolf 630, YY Geminorum, and YZ Canis Minoris', Astronomy and Astrophysics 210, 284-294.

Kuijpers, J. (1989) 'Radio emission from stellar flares', Solar Physics 121, 163-185.

Kundu, M.R., Jackson, P.D., White, S.M., and Melozzi, M. (1987) 'Microwave observations of the flare stars UV Ceti, AT Microscopii, and AU Microscopii', Astrophysical Journal 312, 822-829.

Kundu, M.R., Pallavicini, R., White, S.M., and Jackson, P.D. (1985) 'Co-ordinated VLA and EXOSAT observations of the flare stars UV Ceti, EQ Pegasi, YZ Canis Minoris and AD Leonis', Astronomy and Astrophysics 195, 159-171.

Kundu, M.R. and Shevgaonkar, R.K. (1988) 'Detection of the dMe flare star YZ Canis Minoris simultaneously at 20 and 90 centimeter wavelengths', Astrophysical Journal 334, 1001-1007.

Lang, K.R. (1986) 'Radio wavelength observations of magnetic fields on active dwarf M, RS CVn and magnetic stars', Advances in Space Research 6, No. 8, 109-112.

Lang, K.R., Bookbinder, J., Golub, L. and Davis, M.M. (1983) 'Bright, rapid, highly-polarized radio spikes from the M dwarf AD Leonis', Astrophysical Journal (Letters) 272, L15-L18.

Lang, K.R. and Willson, R.F. (1986a) 'Narrow-band, slowly varying decimetric radiation from the dwarf M flare star YZ Canis Minoris', Astrophysical Journal (Letters) 302, L17-L21.

Lang, K.R. and Willson, R.F. (1986b) 'Millisecond radio spikes from the dwarf M flare star AD Leonis', Astrophysical Journal 305, 363-368.

Lang, K.R. and Willson, R.F. (1988) 'Narrow-band, slowly varying decimetric radiation from the dwarf M flare star YZ Canis Minoris II', Astrophysical Journal 326, 300-304.

Mullan, D.J. (1989) 'Solar and stellar flares: questions and answers', Solar Physics 121, 239-259.

White, S.M., Jackson, P.D., and Kundu, M.R. (1989) 'A VLA survey of nearby flare stars', Astrophysical Journal Supplement, December 15, 1989.

White, S.M., Kundu, M.R., and Jackson, P.D. (1986) 'Narrow-band radio flares from red dwarf stars', Astrophysical Journal 311, 814 - 818.

Willson, R.F., Lang, K.R., and Foster, P. (1988) 'VLA observations of dwarf M flare stars and magnetic stars', Astronomy and Astrophysics 199, 255-261.

D3. VLA OBSERVATIONS OF THE CORONAL PLASMA

Kenneth R. Lang, Tufts University

IAU SYMPOSIUM No. 142

BASIC PLASMA PROCESSES ON THE SUN

Bangalore, India

December 1-5, 1989

VLA OBSERVATIONS OF THE CORONAL PLASMA

KENNETH R. LANG
Dept. of Physics and Astronomy
Tufts University
Medford, MA 02155
U.S.A.

ABSTRACT. VLA observations at 20-cm wavelength specify the brightness temperature and magnetic structure of plasma constrained within coronal loops in solar active regions. Comparisons with simultaneous SMM observations at soft X-ray wavelengths lead to measurements of physical parameters like electron density, electron temperature and magnetic field strength. Such comparisons also indicate coronal loops can be detected at either radio or X-ray wavelengths while remaining invisible in the other spectral domain, and that the dominant radiation mechanisms can be thermal bremsstrahlung or thermal gyroresonance radiation. VLA observations at the longer 90-cm wavelength reveal the thermal emission of a hot transition sheath enveloping a cooler, underlying Hα filament seen in absorption. The 20-cm VLA observations indicate that the precursor, impulsive and post-flare components of solar flares originate in spatially separated and resolved sources. The 90-cm VLA data indicate that time-correlated radio bursts can occur in active regions on opposite sides of the solar equator. These regions are apparently linked by large-scale, trans-equatorial magnetic loops at least 2.6×10^5 km (or 6') long; these loops act as magnetic conduits for relativistic electrons moving at one-third the velocity of light.

I. INTRODUCTION.

This paper provides a brief overview of recent discoveries by the Tufts University group using the Very Large Array (VLA) to study the coronal plasma under the support of the AFOSR and NASA (Section 6). More detailed accounts can be found in the references given in this introduction and in Section 7. Ground-based VLA observations at 20-cm wavelength can detect the hot coronal plasma previously detected by space-bourne X-ray telescopes; detailed comparisons of simultaneous data (SMM and VLA) indicate that physical parameters can be obtained (Section 2), but that some coronal loops are invisible in either spectral domain. (Lang, Willson, Smith and Strong 1987a,b). At the longer 91.6-cm wavelength, the VLA detects more extensive emission interpreted

as a hot 10^5 K interface between cool, dense Hα filaments and the hotter, enveloping rarefied corona (Section 3, Lang and Willson, 1989a). The unparalleled spatial resolution of the VLA at 20-cm wavelength has shown that the precursor, impulsive and post-flare components of solar bursts originate in nearby, but separate, coronal loops or systems of loops (Section 4, Willson, Lang and Liggett, 1990; Willson, Klein, Kerdraon, Lang and Trottet, 1990). Flaring emission detected at 90-cm wavelength reveals otherwize-invisible, trans-equatorial loops that act as magnetic conduits for relativistic electrons that trigger flares on opposite sides of the solar equator (Section 5, Lang and Willson, 1989b).

2. QUIESCENT 20 CM AND X-RAY EMISSION FROM CORONAL LOOPS

The development of aperture synthesis telescopes like the Very Large Array (VLA) has permitted ground-based observations of coronal loops at 20-cm wavelength; the quiescent, or non-flaring, loop emission has brightness temperatures, T_B, comparable to the million-degree coronal electron temperature. A comparison with simultaneous soft X-ray images of comparable angular resolution and field of view (Fig.1) indicates that X-ray coronal loops can be completely imaged at 20 cm.

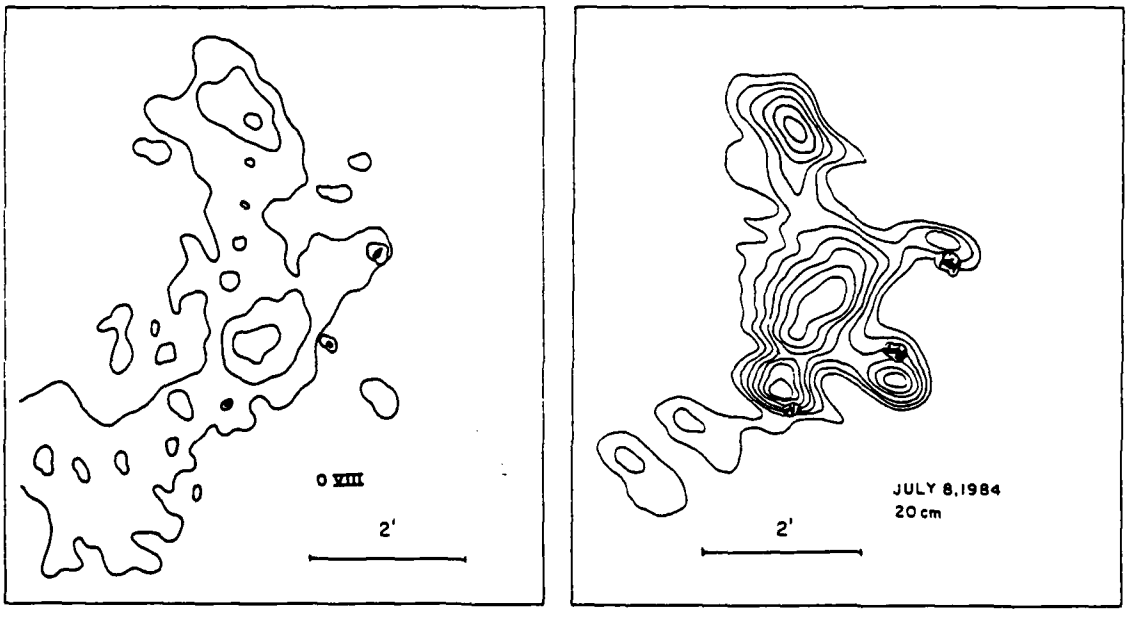

Figure 1. A comparison of soft X-ray (SMM FCS - left) and 20-cm (VLA-right) images of an active region. Here the sunspots are denoted by small black dots with a circle around them, and the identical angular scale for the two images can be inferred from the 120" spacing between the fiducial marks on the axes. The soft X-ray data were taken in the O VIII line (18.0 A); they show two regions of hot, million-degree plasma that are also detected at 20 cm. The radio image also shows hot regions near sunspots that are not detected with soft X-rays. The contours of the 20-cm map mark levels of equal brightness temperature corresponding to 0.4, 0.5, 0.6, ... 1.0 times the maximum brightness temperature of 1.4×10^6 K. (Adapted from Lang et al. (1987a)).

Soft X-ray spectral lines have been used to determine the electron temperature, T_e, and electron density, N_e, of the X-ray emitting plasma that spatially coincides with the 20-cm radiation; for the data shown in Fig. 1, average values of $T_e = 3.0 \pm 0.1 \times 10^6$ K and $N_e = 2.4 \pm 0.4 \times 10^9$ cm^{-3} were obtained. The quiescent X-ray radiation is attributed to thermal bremsstrahlung. The 20-cm emission is optically thin with optical depths $\tau = T_e/T_B = 0.3$. The thermal bremsstrahlung of the X-ray emitting plasma ought to be optically thin at 20 cm, but its thermal gyroresonance radiation should be optically thick at this wavelength. The low T_B is then explained if a higher, cooler plasma covers the hotter X-ray emitting plasma. Thermal gyroresonance radiation must account for the intense 20-cm radiation near and above sunspots where no X-ray radiation is detected (also see Fig. 1).

3. QUIESCENT 90 CM EMISSION FROM FILAMENTS.

Although 20-cm VLA observations of the quiet Sun reveal the ubiguitous coronal loops anchored within solar active regions, the VLA results at the longer 91.6-cm wavelength reveal quiescent emission from more extensive structures (angular sizes $\theta = 3'$) that are not associated with active regions (Fig. 2 right and left). The 91.6-cm features are similar in shape, position, elongation and orientation to dark Hα filaments; but the radio structures are wider and longer, and they are detected in emission rather than absorption. This 91.6-cm emission has been interpreted as the thermal bremsstrahlung of a hot (10^5 K), thin (10^4 km) transition sheath that envelopes the cooler Hα filaments and acts as an interface with the hotter surrounding corona; this sheath is seen in emission because of the relatively low optical depth of the low-density corona.

Comparisons of the observed brightness temperatures, as corrected for the contribution of the corona, with theoretical models, and with other observations at shorter radio wavelengths, indicate that a power-law gradient in pressure provides a better fit than a constant pressure model (Lang and Willson, 1989a). Variable physical parameters of the transition sheath can explain controversial reports of the detection of, or the failure to detect, the meter-wavelength counterpart of Hα filaments. If the sheath were substantially thinner, then the optical depth would not be large enough for detection of its 91.6-cm bremsstrahlung; and if the electron density of the sheath was much higher than $N_e = 10^9$ cm^{-3}, then its plasma frequency would exceed our observing frequency and the sheath radiation could not propagate out to be observed.

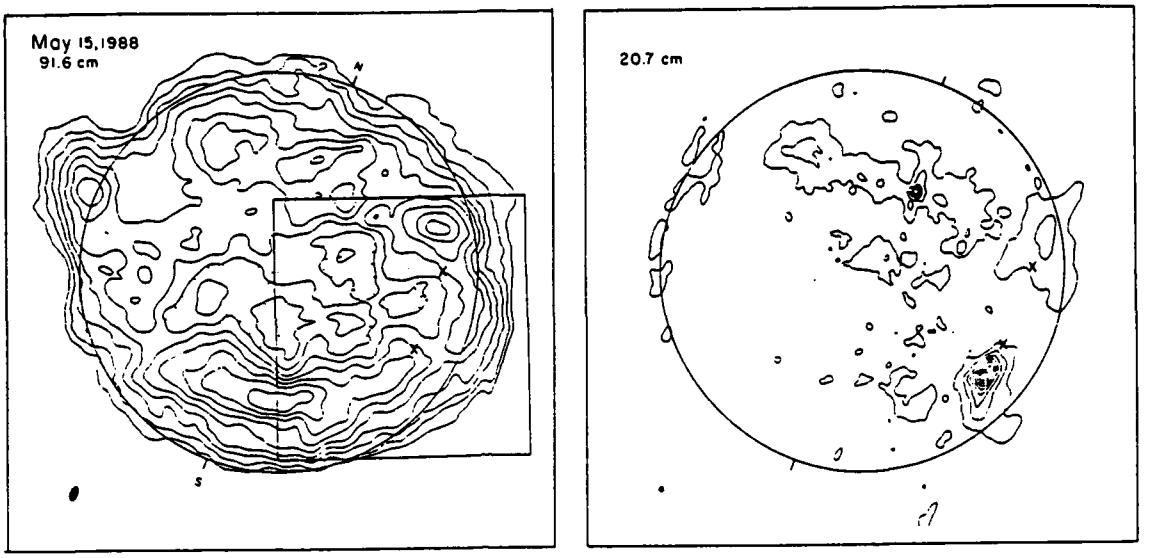

Figure 2. Three-hour VLA synthesis maps of the quiescent, or non-flaring, intensity from the visible solar disk at 91.6 cm (left) and 20.7 cm (right). The circle denotes the visible solar limb; the tick marks denote solar north and south; and the synthesized beamwidths are denoted by the dark spots in the lower left-hand corners. The 20.7-cm contours delineate active-region coronal loops with a peak brightness temperature of $T_B = 2.5 \times 10^6$ K, while the 91.6-cm contours show more elongated structures that are not associated with active regions and have a peak $T_B = 7.8 \times 10^5$ K. The dominant 91.6-cm emission in the southern hemisphere coincides with a dark, underlying Hα filament; the emission (91.6-cm) and absorption (Hα) features have a similar shape, position, elongation and orientation; but the 91.6-cm emission is wider and longer, suggesting a warm transition sheath that acts as an interface between the cool, dense Hα filament and the hot, rarefied enveloping corona. (Adapted from Lang and Willson (1989a)).

4. RESOLVING FLARE COMPONENTS

The classical time profile for the microwave or radio emission of solar flares, or eruptions, consists of a low-level precursor, and a rapid powerful impulsive component, followed by a more gradual post-burst, or decay, phase (see Fig. 3). The VLA has now been used to map these flaring components at 3-second time intervals, showing that they originate in spatially separated sources (Fig 4 and 5).

These results suggest that solar flares are triggered by interacting coronal loops; emerging coronal loops may interact with adjacent ones, leading to the explosive release of magnetic energy stored within them. The system of coronal loops then relaxes to a spatially-different configuration during the decay phase. Comparisons with various theoretical models indicate that a multithermal model with magnetic field strengths of H = 75 to 120 G can explain the impulsive component. Thermal gyroresonance emission from coronal loops with H < 270 G can explain the precursor source; both the 20.7-cm and hard

X-ray emission during the impulsive phase can be attrubuted to non-thermal electrons in the coronal and chromospheric portions of magnetic loops (Willson, Lang and Liggett, 1990; Willson et al., 1990).

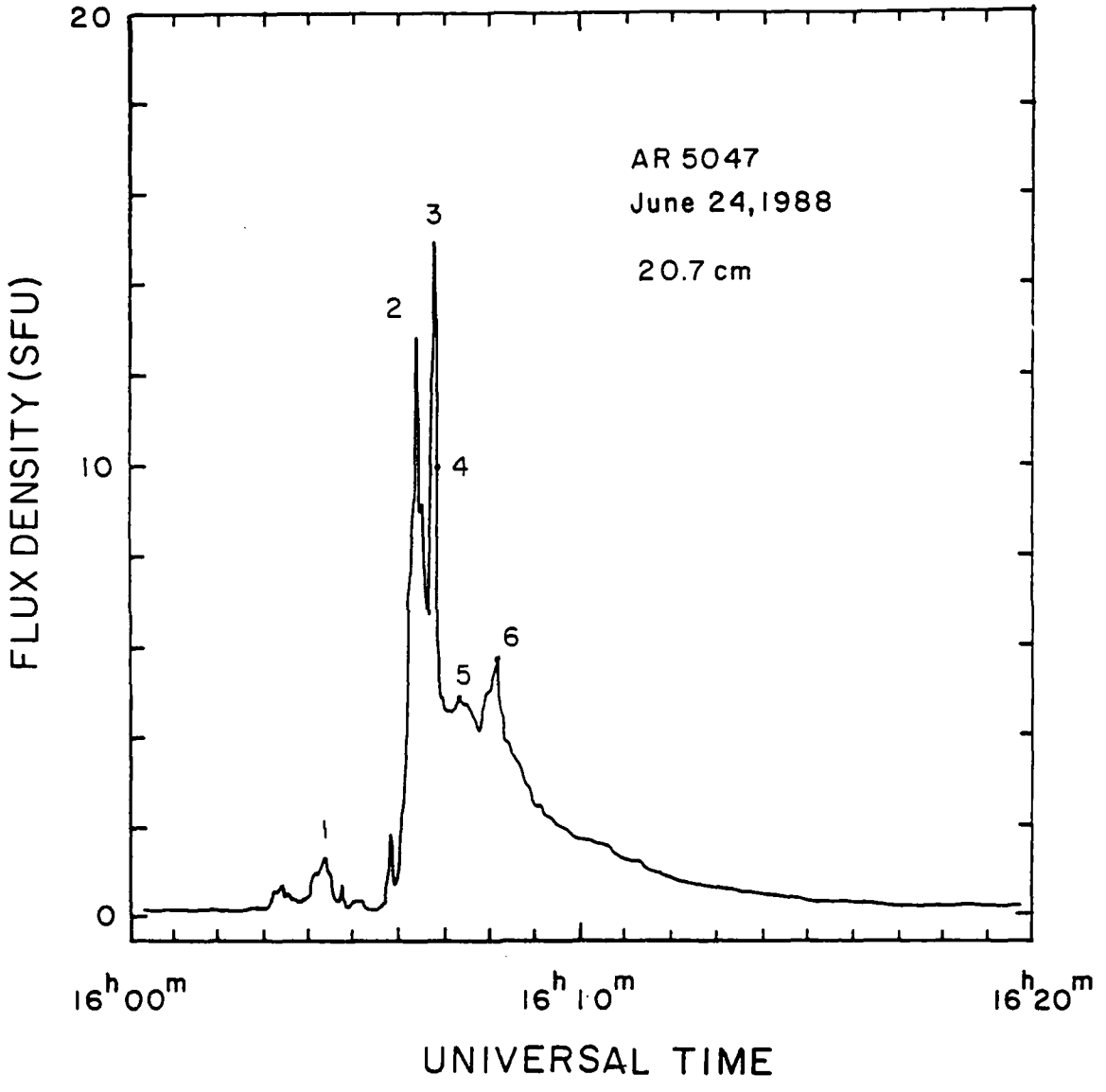

Figure 3. The time profile of a 20.7-cm burst showing the preburst (1), impulsive (2,3), and post-burst (4,5,6) phases. The VLA snapshot maps given in Fig. 4 indicate that these three phases originate from spatially separated, resolved components. (Adapted from Willson, Lang and Liggett (1990)).

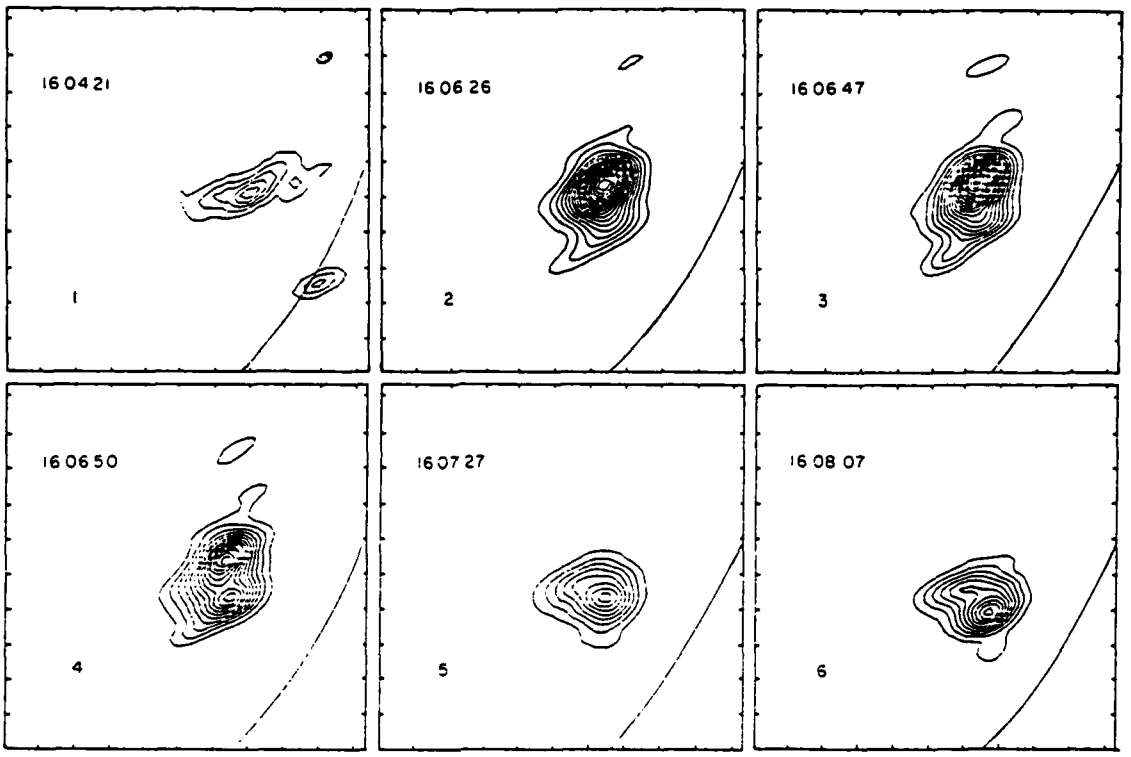

Figure 4. VLA snapshot maps of the total intensity, I, at 20.7-cm wavelength during 3.3-second intervals at the times denoted by 1 to 6 in Fig. 3. The precursor (1) is spatially separated from the subsequent impulsive bursts (2 and 3). The post-burst, or decay, phase (5,6) originates in another spatially separate source that first becomes detectable during the end (4) of the second impulsive burst (3). All three components are resolved with a synthesized beamwidth of 12" x 30"; the angular scale can be inferred from the 60" spacing between the fiducial marks on the axes. The contour intervals are in units of equal brightness temperature, T_B, with an outermost contour and contour interval of $T_B = 4.4 \times 10^5$ K for 1, and $T_B = 5.5 \times 10^6$ K for the others five images. The maximum value is $T_{Bmax} = 4.4 \times 10^6$, 1.0×10^8, 1.3×10^8, 7.7×10^7, 4.4×10^7 and 5.5×10^7 K for 1,2,3,4,5 and 6 respectively. (Adapted from Willson, Lang and Liggett (1990)).

5. TRIGGERING FLARES ACROSS TRANS-EQUATORIAL

Time-correlated radio bursts have been observed in active regions on opposite sides of the solar equator (Figs. 6 and 7). These regions are apparently linked by large-scale, trans-equatorial magnetic loops that are at least 2.6×10^5 km (or 6') long. Energetic electrons accelerated during a radio burst in one active region probably move along this magnetic conduit at velocities of about one-third the velocity of light, thereby triggering radio bursts in the other active region.

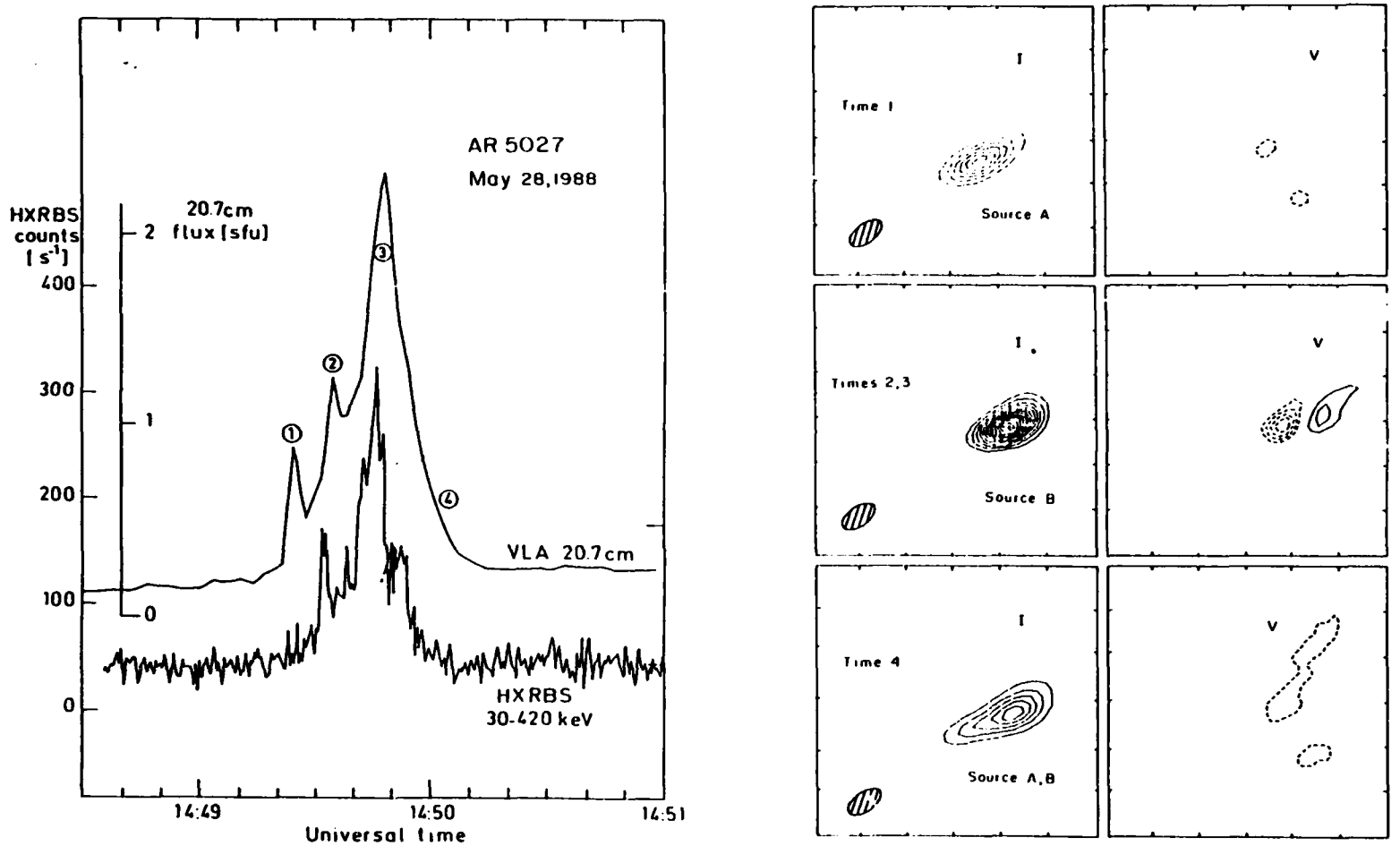

Figure 5. Time profiles (left) of the emission at 20.7-cm (VLA) and hard X-rays (SMM - HXRBS); and three-second VLA snapshot maps (right) of the total intensity, I, and circular polarization, V, at 20.7 cm for the times denoted 1 to 4 in the time profile. Although the first 20.7 cm peak (designated 1) is not detected at hard X-rays, the rest of the burst profile (2,3 and 4) in the two spectral domains is very similar. The snapshot maps show spatially separated resolved sources.

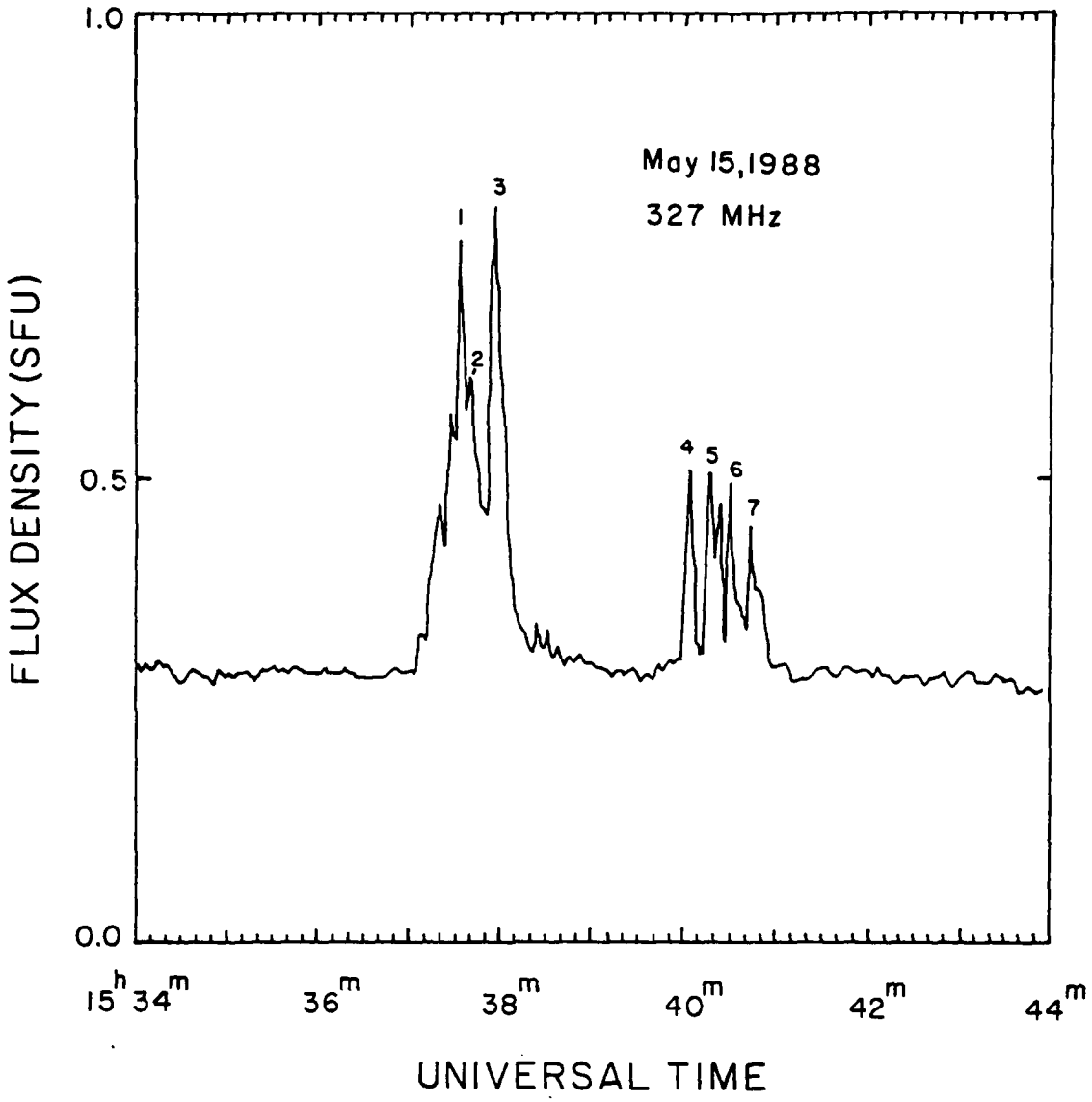

Figure 6. Time profile of the 91.6-cm (327 MHz) emission detected with one of the short VLA baselines (fringe spacing of about 5'). The VLA snapshot maps at times 1,2,3,4 and 5 are shown in Fig. 7. (Adapted from Lang and Willson (1989b)).

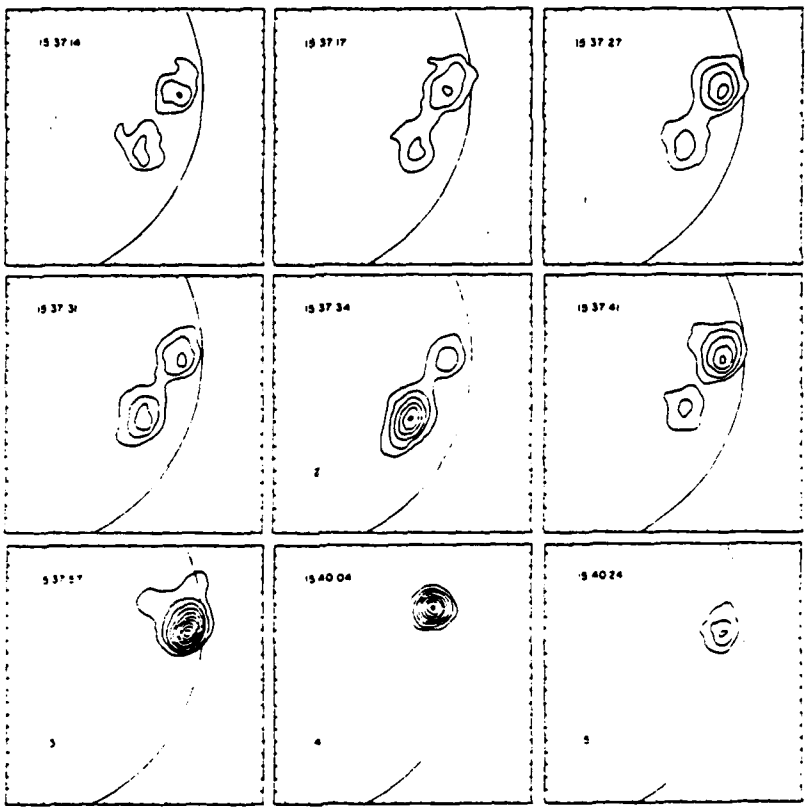

Figure 7. Three-second VLA snapshot maps at 91.6 cm for different times during the burst shown in Fig. 6. The emission comes from opposite sides of the solar equator in two regions separated by about 6', or 2.6 x 10^5 km; here the angular scale can be inferred from the 1' spacing between the fiducial marks on the axes. The contours mark intervals of equal brightness temperature, T_B, with an outermost contour and contour interval of 1 x 10^6 K. (Adapted from Lang and Willson (1989b)).

6. ACKNOWLEDGEMENTS.

Radio astronomical studies of the Sun at Tufts University are supported under grant AFOSR-89-0147 with the Air Force Office of Scientific Research. Related solar observations are supported by NASA grant NAG 5-501. The Very Large Array is operated by Associated Universities, Inc., under contract with the N.S.F.

7. REFERENCES.

Lang, K.R. and Willson, R.F. (1989a) 'Radio emission from quiescent solar filaments at 91.6 centimeter wavelength', Astrophysical Journal (Letters) 344, L73-L75.

Lang, K.R. and Willson, R.F. (1989b) 'Time-correlated bursts from widely separated solar active regions at 91.6 centimeter wavelength', Astrophysical Journal (Letters) 344, L77-L80.

Lang, K.R., Willson, R.F., Smith, K.L., and Strong, K.T. (1987a) 'Simultaneous SMM flat crystal spectrometer and Very Large Array Observations of solar active regions', Astrophysical Journal 322, 1035-1043.

Lang, K.R., Willson, R.F., Smith, K.L., and Strong, K.T. (1987b) 'Solar active region physical parameters inferred from a thermal cyclotron line and soft X-ray spectral lines', Astrophysical Journal 322, 1044-1051.

Willson, R.F., Klein, K.-L., Kerdraon, A., Lang, K.R., and Trottett, G. (1990) 'Multiple-wavelength analysis of energy release during a solar flare: thermal and non-thermal electron populations. Astrophysical Journal-submitted.

Willson, R.F., Lang, K.R., and Liggett, M. (1990) 'Impulsive microwave burst and solar noise storm emission resolved with the VLA', Astrophysical Journal, February 20, 1990.

THE ASTROPHYSICAL JOURNAL, 357:662–671, 1990 July 10

D4 MULTIPLE-WAVELENGTH ANALYSIS OF ENERGY RELEASE DURING A SOLAR FLARE: THERMAL AND NONTHERMAL ELECTRON POPULATIONS

ROBERT F. WILLSON,[1] KARL-LUDWIG KLEIN,[2] ALAIN KERDRAON,[2] KENNETH R. LANG,[1] AND GERARD TROTTET[2]

Received 1989 September 25; accepted 1990 January 15

ABSTRACT

Collaborative solar investigations by Tufts University and the Observatoire de Paris have resulted in simultaneous radio observations with the Very Large Array (VLA) and the Nançay Radioheliograph (NR), comparisons of this radio data with X-ray observations, and theoretical interpretations of the dominant radiation mechanisms during a weak impulsive solar flare observed on 1988 May 28. The VLA has mapped the flaring structures at time intervals of 3.3 s, showing that the preflash and flash-phase components of the impulsive emission originate in spatially separated sources. The 20.7 cm preflash source is ascribed to thermal gyroresonance emission from coronal loops with typical magnetic field strengths of up to 270 G; this emission is associated with heating and exhibits no detectable hard X-ray radiation above 30 keV. The flash-phase 20.7 cm source and the hard X-ray emission are attributed to nonthermal electrons in the coronal and chromospheric portions of a magnetic loop. The combination of imaging observations at 20.7 and 91.6 cm excludes emission from a confined hot plasma during the flash phase.

Subject headings: radiation mechanisms — Sun: corona — Sun: flares — Sun: radio radiation

I. INTRODUCTION

Energy release during solar flares proceeds through several, observationally distinguishable steps: soft X-ray and radio wave signatures of interacting magnetic structures and of the *heating* of coronal loops can be observed during the preflare phase, i.e., minutes before the onset of the impulsive energy release revealed by the hard X-ray onset (see reviews by Priest *et al.* 1986; Van Hoven and Hurford 1986; Kundu 1986). The frequent presence of suprathermal electrons in the corona during the preflare phase is revealed by decimeter-wave emission (Benz *et al.* 1983). During large bursts, the impulsive phase, which starts with the first detectable hard X-ray emission above about 30 keV, has been shown to consist of two parts, termed preflash phase and flash phase, respectively. Preflash emission is characterized by weak hard X-ray emission and by metric type III bursts. At the transition from the preflash phase to the flash phase, the hard X-ray spectrum starts hardening, the decimetric-to-metric radio wave emission is shifted to higher frequencies, and the full scale of electromagnetic emission from energetic particles, going from γ-rays to radio waves, appears nearly simultaneously (Benz *et al.* 1983; Raoult *et al.* 1985; Klein *et al.* 1987). Observational evidence in different wavelength ranges suggests that the interaction between magnetic structures is necessary to trigger the flash phase (Raoult *et al.* 1985; Machado *et al.* 1988).

There is general agreement—and observational evidence (e.g., Lin *et al.* 1981; Kattenberg *et al.* 1981)—that any physically reasonable process of energy release will both heat the plasma and produce suprathermal particles. However, the relative contribution of the two populations to the observed hard X-ray and microwave emission in the different parts of the impulsive phase is unknown. Fürst, Benz, and Hirth (1982) and Alissandrakis, Schadee, and Kundu (1988) argued that the microwave emission of the weak flares they studied was incompatible with bremsstrahlung from the soft X-ray emitting plasma ($T \approx 10^7$ K), but they did not discuss the potential role of a high-temperature plasma ($T \geq 10^8$ K). Quantitative analyses of the problem were carried out through the modeling of hard X-ray and microwave emissions (see the recent review by Pick, Klein, and Trottet 1989). When studying the correlation of peak fluxes in the two spectral ranges, most authors (Gary 1985; Kai 1986; Lu and Petrosian 1989) have recently favored the nonthermal over the thermal model (Batchelor *et al.* 1985; but see Batchelor 1989). More detailed analyses of individual events, using temporal, spectral, or spatial information, however, tried to include both thermal and nonthermal electron populations (Böhme *et al.* 1977; Klein, Trottet, and Magun 1986; Holman, Kundu, and Kane 1989). These studies did not lead to a unique conclusion on the role of the two electron populations, and they did not analyze the transition between the preflash and the flash phase.

In this paper we reconsider the analysis of different electron populations in the case of a weak impulsive flare with simple spatial structure. VLA observations at 20.7 and 91.6 cm, and soft and hard X-ray data from the spectrometers aboard the *GOES* and *SMM* (HXRBS) spacecraft, are used. The times and techniques of relevant observations are given in § II, and an overview of the radio observations of the active region is contained in § III. Section IV focuses on the flare observations: 20.7 cm emission during the preflash phase is spatially separated from the subsequent flash phase component. The preflash peak at 20.7 cm has no counterpart in the hard X-ray emission, while during the flash phase the radio emission is closely associated with that at hard X-ray wavelengths. These observations are interpreted in § V: thermal gyroresonance emission is shown to be the most probable process for the preflash emission at 20.7 cm wavelength, while the radio and hard X-ray observations during the remainder of the impulsive phase are shown to be inconsistent with a confined thermal electron population, but are more readily explained by the injection of nonthermal electrons. In our concluding section,

[1] Department of Physics and Astronomy, Tufts University.
[2] Observatoire de Paris, Section d'Astrophysique de Meudon.

we place these observations and their interpretation within the context of current research on energy release during solar flares.

II. OBSERVATIONS

The observations reported below were carried out conjointly with the Very Large Array (VLA), the Nançay Radioheliograph (NR; The Radioheliograph Group 1989), the hard X-ray burst spectrometer HXRBS on board the *Solar Maximum Mission* (*SMM*) Satellite (Orwig, Frost, and Dennis 1980), and the soft X-ray telescope aboard the *GOES* satellite. The VLA observations were made from 1435 UT to 1630 UT on 1988 May 28 in the C/D array. In this configuration, the outermost antennas of the southeast and southwest arms are located at a distance of 0.59 km from the array center, while the most remote antenna of the north arm is located at 1.9 km from the center. The NR observed the Sun from 0755 UT to 1449 UT. The characteristics of the instruments are summarized in Table 1. At all wavelengths, the beamwidths of the individual antennas cover the whole Sun.

The VLA data were calibrated using standard solar calibration procedures; uncertainties in this calibration have been discussed by Kundu, Schmahl, and Fu (1989) and by Shevgaonkar, Kundu, and Jackson (1988). One uncertainty results from a software error in the program that applies the system temperatures of solar calibration antennas to other antennas (Ray Gonzales, private communication). This uncertainty results in an underestimate of brightness temperatures by a factor of 1.8, and our data have been corrected for this error. Another uncertainty is attributed to measurements of the high-temperature noise diodes on the solar calibration antennas; they are not measured regularly enough at the VLA to assure accurate measurements of the system temperature. This problem leads to an uncertainty of no more than 20%–25% in the inferred brightness temperatures.

The brightness temperatures were derived from a flux calibration with the radio source 3C 48, which was observed for 5 minutes every 40 minutes; its flux density is 14.6 Jy and 47.0 Jy at 20.7 cm and 91.6 cm, respectively (VLA calibrator list).

TABLE 1

SUMMARY OF INSTRUMENTAL CHARACTERISTICS

Observed frequency (MHz)	Beam (FWHM)	Bandwidth (MHz)	Sampling time (s)
Very Large Array			
1446	23″ × 40″	12.5	3.33
327.5	75 × 135	0.781	3.33
Nançay Radioheliograph			
435	72	0.7	0.25
408	78	0.7	0.25
327	96	0.7	0.25
236.6	132	0.7	0.25
164	96/192	0.7	0.05/0.25

The calibrated VLA data were used together with the standard CLEAN procedure to make synthesis maps of the total intensity, I, and the circular polarization, or Stokes parameter V, for both the 2 hr observing interval and for 3 s snapshot intervals during the radio bursts, or flares.

The NR provides six independent data sets, at 164 MHz with both the east-west and north-south branches, and at four further frequencies (see Table 1) with the north-south branch.

III. OVERVIEW OF THE RADIO OBSERVATIONS

During the entire observing period covered by the two radio instruments, a noise storm continuum and type I bursts were visible at all frequencies up to 435 MHz. This emission dominates the 2 hr VLA synthesis map of total intensity at 91.6 cm (Fig. 1, left). It has an extent of 3.'7 × 7′, a peak brightness

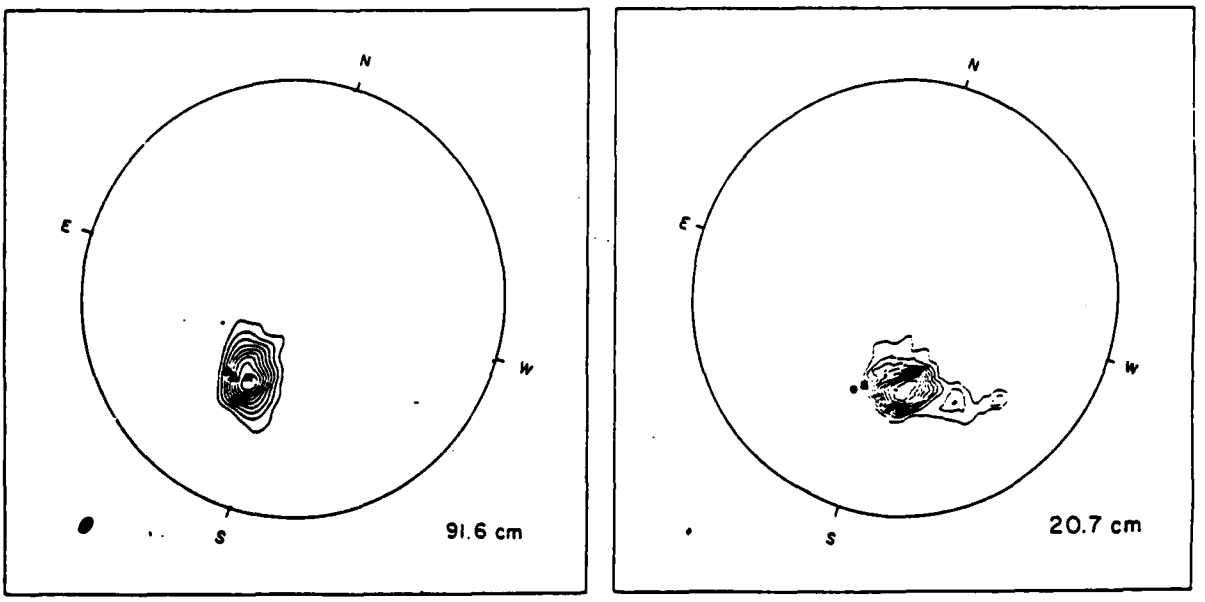

FIG. 1.—Two hour VLA synthesis maps at 91.6 cm (*left*) and 20.7 cm (*right*). Peak brightness temperature and contour intervals are 2.1 × 10^7 K, and 2.16 × 10^6 K (91.6 cm) and 2.9 × 10^6 K and 2.9 × 10^5 K (20.7 cm), respectively. The 91.6 cm emission is dominated by noise storm activity that is 90% right-hand circularly polarized, whereas the 20.7 cm map shows the quiescent, or nonflaring, emission of AR 5027. The 91.6 cm figure also shows the positions of the noise storm at 66, 91.6, and 183 cm, respectively designated by an open circle, cross and triangle (Nançay Radioheliograph); the filled circle and open square in the 20.7 cm image denote the positions of two bursts, designated as sources A and B, respectively. The synthesized beams at the two wavelengths are given as filled ellipses in the lower left-hand corner of each image, and the large circle denotes the limits of the photosphere.

temperature of $T_b = 2 \times 10^7$ K, and it is 90% right-hand circularly polarized. The open circle, cross, and triangle show the noise storm centroid at 66 and 91.5 cm, inferred from the rotation of the fringe pattern of the NR during the 7 hr observing period, and the average position at 183 cm measured with both branches of the radioheliograph. The dispersion of the noise storm source positions with wavelength is seen to be small, as is expected for a source close to disk center. The NR observations indicate a double source structure in the north-south direction, which is consistent with the elongated shape observed at 91.6 cm with the VLA. The two sources are more than 90% right-hand polarized at all observed frequencies. Comparison of the sense of polarization with the large-scale photospheric field pattern obtained from the Stanford magnetogram (*Solar-Geophysical Data*) indicates the association of the noise storm source with a region of negative magnetic polarity, which suggests radio emission in the ordinary mode. This is usually assumed to be the case in noise storms (e.g., Elgarøy 1977; Mercier *et al.* 1984).

Figure 1 (*right*) shows the 2 hr total intensity VLA synthesis map at 20.7 cm wavelength. The emission comes predominantly from an extended source (3′ × 9′) associated with the quiescent emission of active region AR 5027 (S29 W12). A weaker structure extends northward toward active region AR 5025 (S18 W12). The peak brightness temperature in the map is 2.9×10^6 K. No circular polarization was detected. The filled circle and open square in Figure 1 indicate the locations of the 20.7 cm bursts associated with a radio flare occurring around 14:49:20 UT; they are respectively designated source A and B in the subsequent text.

The remainder of this paper will discuss this flare-associated radio burst.

IV. FLARE-ASSOCIATED OBSERVATIONS

Figure 2 shows the time history, with 3.3 s integration time, of the flux densities at 20.7 and 91.6 cm (VLA), the hard X-ray count rate above 25 keV (HXRBS on board *SMM*, courtesy B. Dennis), and the soft X-ray flux in the 0.5–4 Å band as observed with the *GOES* satellite. The 20.7 cm and hard X-ray emissions are associated with a flare detected at Hα and soft X-ray wavelengths (importance SN/C1.3) located at S26 W01 (*Solar-Geophysical Data* 531 II). The flare-associated emission starts at 14:49:30 UT in hard X-rays above 30 keV and at 91.6 cm, 10 s earlier at 20.7 cm and in the first HXRBS channel (below 30 keV). The hard X-ray and radio bursts fade together, vanishing at about 14:50:10 UT. The enhanced 91.6 cm brightness between 14:49:00 UT and 14:49:20 UT (designated 5 in Fig. 2) is not associated with the flare but is due to the noise storm discussed in the previous section. The soft X-ray burst has its most rapid rise during the hard X-ray and radio bursts and attains its maximum about 40 s after the impulsive peaks in these wavelength ranges. The time history of the radio and soft X-ray emissions is typical for such flares (see Fürst, Benz, and Hirth 1982).

Figure 3 shows 3.3 s snapshot maps of total and circularly polarized brightness at 20.7 cm at three instants of the burst, together with the synthesized beam (hatched ellipse). Two sources can be distinguished: The first peak (marked 1 in Fig. 2) arises from a source termed A (Fig. 3, top), the second and third peak (marked 2 and 3 in Fig. 2) are from a source B displaced about 40″ from A (Fig. 3, middle). Besides their positions, A and B have other distinctive characteristics:

1. A is not associated with a detectable hard X-ray peak, but with smoothly rising low-energy emission; the radio source is unpolarized.

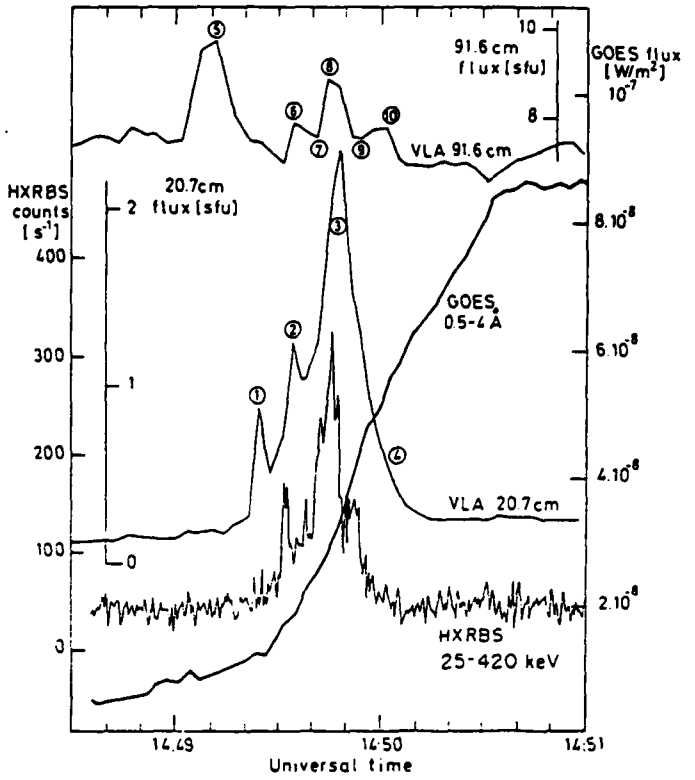

FIG. 2.—Time profiles of emission observed simultaneously at radio (VLA; 91.6 cm, 20.7 cm), hard X-ray (HXRBS/*SMM*; channels 1–15, $h\nu$ = 25–420 keV), and soft X-ray (*GOES*; 0.5–4 Å) wavelengths. Radio and soft X-ray data have been plotted with the same 3.3 s integration time, whereas 1 s integration was performed on the hard X-ray count rate in order to demonstrate that no essential feature of the burst has been lost in the VLA data. Although the first 20.7 cm peak (designated 1) is not detected at hard X-rays, the rest of the burst profiles (2 and 3) in the two spectral domains are very similar. The 91.6 cm profile shows fluctuating emission from a noise storm center (peak 5) that is spatially separated from the subsequent burst emission. The soft-X-ray data show a gradual increase, with some low-level fluctuations around the time of the first impulsive emission (1) at 20.7 cm. VLA snapshot maps for the times marked 1, 3, and 4 are given in Fig. 3, while those for the times marked 7, 8, and 9 are given in Fig. 5.

2. B appears and vanishes with the hard X-ray emission above 30 keV. It has a bipolar structure with a maximum circular polarization of about 20%. The source shape and polarization are conserved throughout the burst.

Source A is not visible during the phase of brightest emission (14:49:34–14:49:57 UT) but is detected again, together with B, at the end of the event (time marked 4 in Fig. 2, synthesis map in Fig. 3, bottom). A test consisting of convolving source A with the 40″ beam during the presence of source B shows that A would go undetected as long as $T_b(A) < 0.5 \times T_b(B)$, where $T_b(X)$ denotes the brightness temperature of source X.

In Figure 4 (Plate 15) we compare a 3.3 s snapshot map of the 20.7 cm burst at 14:49:54 UT with a SOON Hα image taken at 14:50:10 UT. Here the uncertainty in the coregistration of the two images is ±10″. This figure shows that the microwave burst is displaced ≈1′ east-southeast from the compact ($\theta \leq 30''$) Hα flare kernels located at the eastern end of the active region. The size of the 20.7 cm source (half-intensity level) is about twice that of the optical flare. The angular displacement of the microwave emission with respect

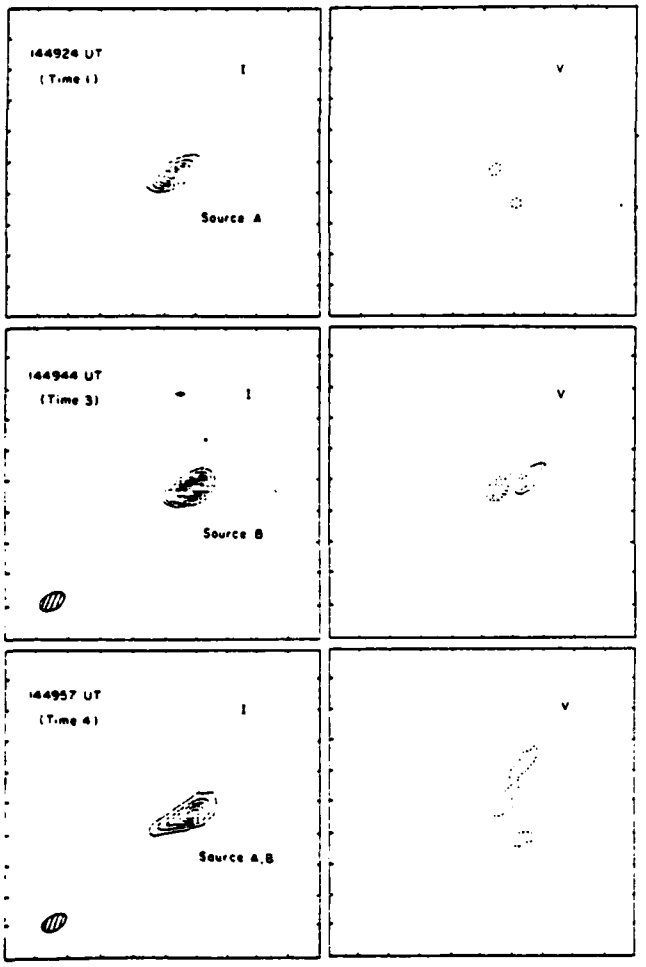

FIG. 3.—Three second VLA snapshot maps of the total intensity, I, and circular polarization, V, at 20.7 cm for the times denoted 1–4 in Fig. 2. They illustrate an unpolarized source A at time 1, a dipolar source B at time 3, and both sources A and B at a later time 4. Peak brightness temperature and contour intervals for the I maps are 2.0×10^7 K and 1.1×10^6 K, respectively. The outermost contour and contour interval of the V maps are equal to 5.5×10^5 K. The synthesized beam is denoted by the hatched ellipse in the lower left-hand corner. The angular scale may be inferred from the 60" fiducial marks on the axes.

to the Hα flare may be attributed to a projection effect (due by the greater height of the 20.7 cm source above the photosphere) if the source lies within a coronal loop that bends toward the east limb. A microwave source that lies radially above the flaring region would produce mostly a southward displacement, contrary to observation.

The 91.6 cm emission at time 5 in Figure 2 was highly circularly polarized (95%–100%) noise storm radiation whose spatial position and structure were identical to those of the 2 hr synthesis map shown in Figure 1 (*left*). Figure 5 shows 91.6 cm VLA snapshot maps for the time intervals 7–9 in Figure 2. Burst component 6 at 91.6 cm (Fig. 2) showed the same structure and position as burst 8. Peak 10 is an unpolarized burst from a position slightly southward of the western source seen at time 8. The less intense peaks at time 7 and 9 (also Fig. 2) were spatially identical and separated from burst sources 6, 8, and 10. At the times of peaks 6 and 8, two sources (C and D) with opposite polarization are observed. Component C of this burst was 55% ± 5% (left-hand) circularly polarized at 91.6 cm wavelength, while component D was nearly completely right-hand polarized. In the valleys of the total flux (time 7 and 9) only source D is visible in polarization. When measured in the valleys, the brightness temperature of source D decreases with time. No accurate determination of the brightness temperature of D is possible at the times of the peaks because the emission from C dominates the signal, but there seems to be a weak brightening of D at the time of peak 8. We infer from these maps that we observed one source (C), which was the seat of two partially polarized bursts (peaks 6, 8), one displaced unpolarized source bursting later (peak 10), and a third, totally polarized source (D). The brightness of D essentially decreases slowly between the first peak (6) and the time when the last snapshot map was taken. The bipolar structure at peaks 6 and 8 may hence be ascribed to the existence of two spatially separated sources which exhibit different temporal evolution, rather than to a single magnetic loop.

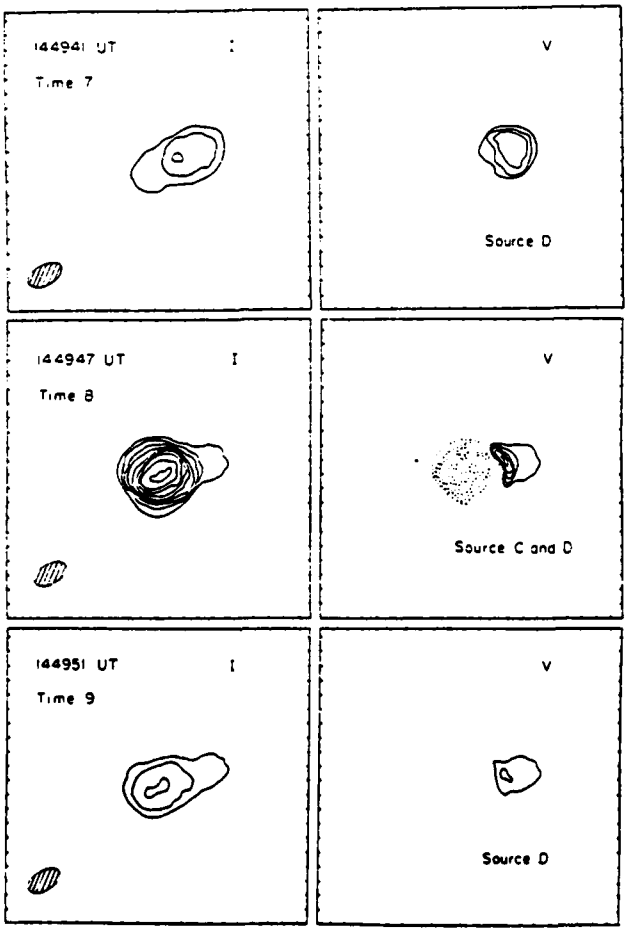

FIG. 5.—Three second VLA snapshot maps of the total intensity, I, and circular polarization, V, at 91.6 cm wavelength for the times denoted 6–10 in Fig. 2. They illustrate the same extended dipolar source (C and D) at the peaks 6, 8, or 10, and the same compact, unipolar source D at the valley 7 or 9. Peak brightness temperature and contour intervals for the I maps are 2.5×10^7 K and 2.75×10^6 K, respectively. The outermost contour and contour interval of the V maps are equal to 2.7×10^5 K and 1.37×10^5 K, respectively. The synthesized beam is denoted by the hatched ellipse in the lower left-hand corner. The angular scale may be inferred from the 60" fiducial marks on the axes.

V. INTERPRETATION OF THE FLARE-ASSOCIATED EMISSION

a) Flare-associated Emission at 91.6 cm

The lack of spatially resolved spectral observations in the decimenter-to-meter waveband precludes any detailed discussion of the 91.6 cm emission associated with the impulsive burst. The only spectral information available stems from single-frequency records at Sagamore Hill (*Solar-Geophysical Data* 527 I) and at Nançay (only paper records available). Sagamore Hill reports both type V and type IV from 1443 to 1453 UT. The impulsive nature of the emission seen at the VLA and on Nançay records suggests type III/V activity. This is also consistent with the similarity of the 91.6 cm time history and those at 20.7 cm and hard X-rays (Raoult *et al.* 1985; Suzuki and Dulk 1985). Assuming this spectral identification is correct, peaks 6, 8, and 10 are ascribed to type III electron beams, and the smoothly varying source D is ascribed to a type V continuum. The simultaneous start and end, to within the VLA time resolution, of these emissions and those of source B (see § V*b*) at 20.7 cm and hard X-ray wavelengths, indicates a common injection of nonthermal electrons into different magnetic structures (see Raoult *et al.* 1985). This does not imply a peak-to-peak correspondence. Peak 10, which occurs in the decay phase of the 20.7 cm burst at a site displaced from the preceding peak, has no clearly associated hard X-ray feature. The data set of Raoult *et al.* (1989), who study the relative timing of microwave bursts and metric type III emission, shows a similar behavior in the decay phase of microwave bursts.

The main objection against the type III/V interpretation of the 91.6 cm emission is the high degree of circular polarization. Opposite polarization of the type III and continuum sources has been observed at longer wavelengths (Suzuki and Dulk 1985), but with much lower degrees of polarization than in the present case. From one-dimensional images provided by the NR, Mercier (1989) finds that the degree of circular polarization of Type III bursts is most often below 30% in the 300–500 MHz range. If interpreted as plasma emission, the high polarization of source D suggests fundamental emission, so that ordinary mode polarization is expected at 91.6 cm, while the extraordinary mode is most likely for the underlying 20.7 cm gyrosynchrotron source. However, the bipolar sources at the two frequencies show the same sense of polarization. This implies that the underlying 20.7 cm source is situated in an oppositely directed magnetic field. Altogether the available information is confusing, and one cannot exclude the alternative interpretation of gyromagnetic emission, e.g., a cyclotron maser, for sources C and D. Whatever is the nature of the burst-associated emission at 91.6 cm, it reveals the injection of nonthermal electrons in the middle corona at the time of the hard X-ray burst into a structure which is larger than the 20.7 cm burst source. This will be an important constraint to the interpretation of the 20.7 cm and hard X-ray emission in § V*d*.

b) Measured Source Parameters at 20.7 cm *and X-Ray Wavelengths*

Measured quantities of the 20.7 cm and X-ray sources are summarized in Table 2. Column (1) gives the starting time of the sampling interval. Dimensions are given when sources A and B are clearly separated. Instants where both sources are observed are denoted by "A + B". The soft X-ray temperature and emission measure have been inferred from the two channels of the *GOES* detector using the formalism of Thomas, Starr, and Crannell (1985), which accounts for both bremsstrahlung continuum and the contribution of lines. In calculating these parameters, the preburst emission was first subtracted from the subsequent *GOES* data. The formal values of T, EM, and N given in Table 2 are those obtained from our calculations, but they are probably not determined to better than one significant figure. The hard X-ray spectral index γ likewise probably lies within ± 0.5 from the given value. The temperature is essentially constant during the radio and hard X-ray burst, while the emission measure smoothly rises from 2 to 9×10^{47} cm^{-3} between 14:49:19 UT and 14:49:50 UT. The injection spectrum [power law $F(E)dE \sim E^{-\gamma}dE$] and number of nonthermal electrons are derived from power-law fits to the observed hard X-ray spectrum using the thick-target

TABLE 2

MEASURED PARAMETERS OF X-RAY AND RADIO SOURCES

	VLA 20.7 cm		*GOES*		HXRBS			
TIME (1)	T_b (K) (2)	Size (3)	T (K) (4)	EM (cm^{-3}) (5)	γ (6)	N ($\geq$25 keV) (7)	T (K) (8)	EM (cm^{-3}) (9)
Source A								
14:49:21.....	1.1×10^6	...	8.6×10^6	1.8×10^{47}	...	...	...	...
14:49:24.....	6.6×10^6	30″ × 60″	8.0×10^6	2.0×10^{47}	...	$< 10^{31}$	...	...
14:49:27.....	3.3×10^6	...	8.3×10^6	2.6×10^{47}	...	...	...	...
Source B								
14:49:31.....	4.4×10^6	A + B	8.3×10^6	3.3×10^{47}	...	...	...	...
14:49:34.....	9.9×10^6	A + B	8.1×10^6	3.9×10^{47}	5.9	5.0×10^{34}	1.5×10^8	2.2×10^{44}
14:49:37.....	7.7×10^6	...	8.3×10^6	4.6×10^{47}	7.4	1.8×10^{35}	9.9×10^7	9.9×10^{44}
14:49:41.....	9.9×10^6	...	8.1×10^6	5.6×10^{47}	5.0	5.2×10^{34}	2.3×10^8	1.7×10^{44}
14:49:44.....	1.5×10^7	30″ × 60″	8.1×10^6	5.6×10^{47}	5.5	1.3×10^{35}	1.8×10^8	4.2×10^{44}
14:49:47.....	1.9×10^7	...	8.0×10^6	6.5×10^{47}	5.9	1.2×10^{35}	1.6×10^8	3.6×10^{44}
14:49:51.....	1.1×10^7	...	8.1×10^6	8.6×10^{47}	...	...	...	...
14:49:54.....	9.9×10^6	...	...	...	...	...	...	...
14:49:57.....	5.5×10^6	A + B	...	...	...	...	...	...
14:50:01.....	3.3×10^6	A + B	...	...	...	...	...	...
14:50:04.....	2.2×10^6	...	...	...	...	...	...	...

expressions of, e.g., Lin and Hudson (1976). The number of electrons is the product of the injected particle flux and the integration time of 3.3 s. The temperatures and emission measures in the last column are derived from an isothermal hard X-ray model (e.g., Batchelor *et al.* 1985, and references therein).

c) *Interpretation of the* 20.7 cm *Emission of Source A*

The lack of circular polarization and of any detectable hard X-ray emission above 30 keV suggests that the 20.7 cm emission from source A comes from a Maxwellian electron population with moderate temperature ($T < 10^7$ K). This is also consistent with the absence of a counterpart to source A at 91.6 cm. The failure to detect hard X-ray emission implies that less than 10^{-3} photons keV^{-1} cm^{-2} s^{-1} are emitted at 30 keV (Dennis *et al.* 1988: HXRBS Event listing). This puts an upper limit of the order of 10^{31} to the number of nonthermal electrons above 25 keV. Although this number would be sufficient to produce the observed brightness temperature in a magnetic field of the order of 100 G through gyrosynchrotron radiation, the nondetection of circular polarization is incompatible with such an interpretation.

Thermal microwave radiation is either bremsstrahlung or gyromagnetic emission. The electron temperatures inferred from the soft X-ray observations (Table 2) show that a moderately hot plasma does exist at the time of source A. However, the temporal evolutions of the radio and soft X-ray emissions are clearly different, which suggests that either the sources seen in these wavelength ranges are not the same, or that the radio brightness temperature depends sensitively on a parameter, such as the magnetic field, that does not affect the soft X-ray flux.

i) *The Radiation Mechanism*

The radio data yield an upper limit of the electron density, which is attained when the plasma frequency equals the observed frequency of 1500 MHz ($N_e = 2.8 \times 10^{10}$ cm^{-3}), and a lower limit of the electron temperature, given by the brightness temperature ($T = 7 \times 10^6$ K). Assuming that the source dimension along the line of sight does not exceed 2×10^9 cm, one finds that the observed 20.7 cm emission is compatible with the free-free mechanism if the electron density is at least 10^{10} cm^{-3}. The opacity of the radio emission is increased in the presence of a magnetic field. We compute the optical depth of a plasma with $T = 7 \times 10^6$ K, assuming gyroresonance emission from the top of the loop or loops seen at 20.7 cm, which implies a viewing angle close to 90°. Using equations 27 and 28 of Dulk (1985), the source is found to be optically thick at the third or fourth harmonic of the gyrofrequency in the extraordinary mode, at the second harmonic in the ordinary mode, for scale heights of the magnetic field above 10^7 cm and an electron density of the order of 2×10^9 cm^{-3}. Unpolarized emission will hence be observed from the summit of a nearly isothermal magnetic loop with a magnetic field that increases along the line of sight from roughly 130 G or 180 G at the top to 270 G. The 20.7 cm data do not allow us to decide whether source A emits predominantly free-free or gyroresonance emission. However, it will be shown below that the high electron density required by the free-free interpretation is inconsistent with the soft X-ray observations.

ii) *Temporal Evolution*

In light of the foregoing analysis, the temporal evolution of the radio emission from source A reflects either the rapid changes of the magnetic field, if the radiation process is gyromagnetic, or the heat exchange of the radio source with the cool lower atmospheric layers.

The upper limits of the temperature and density inferred from the radio observations yield a radiative cooling time $\tau_r \simeq 10^7 (T_e/N_e)$ greater than 2500 s. Thus, radiative cooling does not explain the observed rapid changes in source A.

Conductive cooling operates on a shorter time scale. The classical Spitzer-Härm theory, which is valid as long as the collisional mean free path of the electrons is smaller than 1% of the temperature scale height (e.g., Duijveman 1983, and references therein), is inapplicable in the case under discussion: When $T > 7 \times 10^6$ K, the density would have to be greater than 10^{12} cm^{-3} in order that the mean free path of the electrons be smaller than 1% of the characteristic scale length of the temperature required by the observed 4 s cooling time (e.g., Duijveman 1983). At such an electron density, no 1500 MHz emission would escape from the source.

An upper limit for the heat flux out of the loop is given by the free-streaming value (e.g., Duijveman 1983, eq. [8]). A conductive cooling time of 3 s is then achieved in a loop at 7×10^6 K. The free streaming will be inhibited if turbulence at the interface between the hot and the cool plasma confines the bulk of the hot plasma. The typical velocity of heat transport is then $5c_s$ (Smith 1986), where c_s is the sound velocity in the hot plasma. If source A as seen by the VLA represents a single loop, a cooling time of roughly 20 s will result from this interpretation, and the observed 4 s decay time would require a shorter loop length around 10^9 cm. In summary, conductive cooling can explain the fading of the emission from source A. This implies either that heat is transported in a nearly free-streaming situation or that the radio source observed by the VLA comprises several smaller magnetic loops. The heat transport interpretation appears more attractive than the hypothesis of transient variation of the magnetic field. No direct diagnostic tool has allowed us so far to probe the magnetic field on second time scales. Detailed radio spectra might give essential information on the field strength, but we do not have such observations in the present case. However, the radio observations suggest that the magnetic field configuration is not destroyed during the burst, because source A is seen again at the end of the impulsive phase. Furthermore, the dissipation of a magnetic field of 100 G in a volume of 10^{28} cm^{-3} would dump 4×10^{30} ergs into the plasma on a time scale of 4 s, and it is difficult to understand why this energy release would only appear as a small fluctuation superposed on a smoothly rising soft X-ray flux. Thus, the hypothesis that the temporal evolution of source A reflects that of the magnetic field cannot be corroborated.

iii) *Relation with the Soft X-Ray Emitting Plasma*

The thermal interpretation of source A poses the question of consistency of the observations at 20.7 cm wavelength and in soft X-rays. The 20.7 cm brightness temperature evolves on a 4 s time scale, while the bulk of the soft X-ray emission exhibits a smooth increase of the emission measure with an *e*-folding time around 20 s, with a low level of fluctuations at the shorter wavelengths around the time of source A (see Fig. 2). The different time histories in the radio and soft X-ray bands suggest that the sources are spatially distinct.

The 20.7 cm brightness temperature comprises a peak with a 4 s decay constant, which may be superposed on a smoothly rising emission similar to the soft X-ray and the low-energy hard X-ray flux in the first HXRBS channel (Fig. 2). The bulk

of the soft X-ray emission exhibits a smooth increase of the emission measure with an *e*-folding time around 20 s, and a low level of fluctuations at the shorter wavelengths around the time of source A (see Fig. 2). The different time histories of the 20.7 cm peak and of the soft X-ray emission suggests that at least part of the radio emission comes from a source which is spatially distinct from the soft X-ray emitting region.

The contribution of the soft X-ray emitting plasma to the 20.7 cm radiation of source A can be estimated from the soft X-ray emission measure and temperature in Table 2, together with the measured surface of the radio source (4×10^{18} cm^2, if one assumes that the large beam broadens the source by 40%). This yields a brightness temperature of $(1.5 \times 10^6 \text{ K})/\mu$ (μ is the refractive index), i.e., at least 20% of the peak brightness temperature of source A. This would agree with a slowly rising component underlying peak 1 in Figure 2. The peak of the 20.7 cm emission itself then would come from a cooler plasma ($T \leq 5 \times 10^6$ K), which would hardly be visible in the *GOES* data. On the other hand, if the whole of the emission of source A is attributed to a plasma distinct from the soft X-ray emitting plasma, the contribution of source A to the soft X-ray emission is estimated as follows: if the radio source observed with the VLA consists of a semicircular nest of loops with the projected dimension measured at 20.7 cm, a volume of 2×10^{28} cm^3 is derived, which together with an electron density of 5×10^9 cm^{-3} in source A yields an emission measure of 5×10^{47} cm^{-3}. With a temperature of 7×10^6 K, the soft X-ray emission would be 10^{-7} W m^{-2} and 5×10^{-9} W m^{-2} respectively, in the long- and short-wavelength ranges of *GOES*. These values comprise the bremsstrahlung continuum emission (Tucker and Koren 1971) and an estimated line contribution of 55% and 25%, respectively, in the two channels (Thomas, Starr, and Crannell 1985, Fig. 5). During the emission of source A, *GOES* measured excess fluxes which are slightly higher than these values. The thermal gyroresonance emission of source A hence appears consistent with the soft X-ray data, while the bremsstrahlung interpretation would require densities that should make source A a brighter soft X-ray emitter than actually observed. The fact that the 20.7 cm peak has no clear counterpart in the soft X-ray flux may be due to either of the following:

1. The magnetic field in the soft X-ray loops is low ($H \leq 130$ G), and the density is below 5×10^9 cm^{-3}, when a detection threshold of $T_b = 10^6$ K is assumed, or below 3×10^9 cm^{-3} for a threshold of 5×10^5 K. This implies that the bulk of the observed soft X-ray emission comes from a tenuous plasma in loops larger than those observed at 20.7 cm.

2. The bulk of the soft X-ray emission comes from dense structures ($N_e > 2.8 \times 10^{10}$ cm^{-3}), where 20.7 cm waves do not propagate. The simultaneous existence of hot structures with low and high density in flaring active regions is well established by X-ray observations with angular resolution (e.g., Hernandez *et al.* 1986).

In summary, the 20.7 cm observations of source A are consistent with thermal gyroresonance emission from a loop or a nest of loops with typical field strengths of 270 to 130 G. Since no spatially resolved X-ray observations are available, we cannot decide whether or not the soft X-ray source contributes to a smoothly evolving emission underlying the spike seen at 20.7 cm. The site of the radio spike itself must be spatially distinct from the soft X-ray source. The most probable interpretation of the fading of the spike is conductive cooling.

d) Interpretation of the 20.7 cm *Emission of Source B*

Source B is different from A by its position, its polarization characteristics, and by its close association with hard X-ray emission. The two latter points suggest gyromagnetic emission from an energetic electron population, either a very hot plasma ($T \geq 10^8$ K) or a suprathermal electron population. We compute the spatial distribution of the brightness temperature for both cases, using the gyrosynchrotron model of Klein and Trottet (1984) with the approximations of Klein (1987), and a power-law and relativistic Maxwellian distribution of the energetic electrons. The magnetic loop is represented by a collection of dipolar field lines, with the observer being situated in the meridional plane of the dipole (see Fig. 1 of Klein and Trottet 1984, with $\Lambda = 0$). The geometry of the radio source is fixed by the VLA observations. The dimensions of the model loop are given in Table 3. No variation of the source parameters were assumed perpendicular to the line of sight.

i) *Nonthermal Electrons*

We suppose that hard X-ray and microwave emission result from a common injection of electrons in the magnetic loop. Like Hernandez *et al.* (1986), we assume that equal numbers of particles travel upward and downward. Those injected downward give rise to the hard X-ray emission in the chromosphere, while those going upward generate radio waves in the coronal part of the loop and hard X-rays when penetrating into the chromospheric layers of the opposite leg of the loop. The number of electrons seen at 20.7 cm is then half the number derived from the hard X-ray observations. We suppose further that the electron distribution is isotropic in the corona and that the slope of the instantaneous energy spectrum of these particles is the same as that of the injection spectrum derived from the thick target hard X-ray emission. We adopt values of the electron population which are situated between those derived from the hard X-rays at 14:49:44 UT and 14:49:47 UT; these values are listed in Table 3.

Once the energy spectrum is fixed, the resulting emission depends on the magnetic field strength and—through their influence on free-free absorption and Razin suppression—on the temperature and density of the thermal electrons in the loop. We restrict, somewhat arbitrarily, the variation of the

TABLE 3

PARAMETERS OF MODEL SOURCE B

A. LOOP GEOMETRY

Parameter	Value
Height (cm)	2.4×10^9
Depth (cm)	1.3×10^9
Width (cm)	2.2×10^9
Volume (cm^3)	1.4×10^{28}

B. PLASMA PARAMETERS

	NONTHERMAL MODEL		THERMAL
PARAMETER	High H	Low H	MODEL
H_{top} (G)	105	32	20
H_{bottom} (G)	368	112	70
N_e (cm^{-3})	1.5×10^{10}	2×10^9	1.8×10^8
T (K)	2.0×10^6	2×10^6	1.7×10^6
γ	5.7	5.7	...
$n(\geq 25$ keV)(cm^{-3}) ...	4.4×10^6	4.4×10^6	...

field strength, H, in the coronal part of the loop to $H_{bottom} = 3.5 \times H_{top}$. It will turn out that the emission comes mainly from the legs of the coronal loop, so that the magnetic field strength at the top is of no crucial importance. It then appears that the observed brightness distribution can be represented by a wide set of parameters, ranging from a tenuous plasma where gyrosynchrotron radiation is efficiently emitted even in a rather weak field, to dense and/or cool plasmas, where the brightness is reduced by Razin suppression and free-free absorption, such that the observed brightness temperature can then only be produced if the magnetic field is intense.

Typical parameter sets which fit the observations after convolution with a Gaussian beam of 40" are given in Table 3 for two extreme cases, referred to as "High H" and "Low H," where H denotes the magnetic field strength. The two cases can *in principle* be distinguished observationally: the low magnetic field case produces a higher degree of circular polarization at a given frequency and a lower brightness at high frequencies than the strong field case. However, the polarization criterion does not effectively constrain the models, because the degree of circular polarization may be lowered by field inhomogeneities and effects of propagation which are not accessible to observations (see discussion by Alissandrakis and Preka-Papadema 1984). The spectral criterion cannot be fully exploited either, because short-wavelength observations of the burst are not available. Nevertheless, the model has to take into account that the 91.6 cm observations show no significant contribution from the electron population radiating the 20.7 cm emission. The source at long wavelengths is much larger than at 20.7 cm, and the emission is highly polarized and of similar brightness temperature as the 20.7 cm source. If there were an optically thick low-frequency counterpart of the 20.7 cm emission, bright and weakly polarized radiation from essentially the same source as seen at 20.7 cm should be observable at 91.6 cm. The failure to detect this signature suggests that Razin suppression or free-free absorption reduce the contribution of the gyrosynchrotron spectrum to the 91.6 cm emission. This can happen, e.g., when the thermal electron density in the radio-emitting loop is above 1.5×10^9 cm^{-3}, so that no 91.6 cm radiation can escape.

Figure 6 compares computed and observed brightness temperature distributions at the peak of the burst. For the purpose of illustration the "High H" mode of Table 3 is chosen. The computed 20.7 cm brightness temperature (Fig. 5, *top*, *solid line*) attains its highest value in the legs of the coronal loop, while the circular polarization (*dashed line*) is more pronounced in the feet of the loop, where the radiation propagates nearly parallel to the magnetic field. The circular polarization is computed assuming quasi-parallel propagation. This approximation breaks down close to the top of the loop, where the wavevector is perpendicular to the magnetic field. It was assumed that no circularly polarized emission arises from this region. For comparison with the observations, the computed brightness temperature profile is convolved with a Gaussian beam of 40" FWHM. The convolved brightness profile is shown in Figure 6 (*middle*), where it is favorably compared with the observed one (*bottom*). The convolution with the large beam makes the bright legs disappear, giving a brightness distribution with a peak at the top of the loop ($T_b = 1.7 \times 10^7$ K). The circular polarization, after convolution with the beam, gives two peaks of roughly 4×10^6 K in the legs of the loop, corresponding to a degree of polarization of 30%. This is about 1.5 times the observed value. The symmetry of the unconvolved source is a consequence of our assumption that the observer is located in the meridional plane of the dipole. However, the asymmetry between the legs of the loop, which would be seen by an observer outside this plane (see figures in Alissandrakis and Preka-Papadema 1984, and Klein and Trottet 1984), would not generate any observational difference after convolution with the large beam, but it would decrease the observed degree of polarization. The circular polarization is expected to be overestimated in the model computations anyway, because the assumed magnetic field structure is very regular, and depolarizing effects during propagation cannot be taken into account. It hence appears that radiation from a nonthermal electron population in a dense and/or cool magnetic loop is compatible with the whole set of available radio and hard X-ray observations.

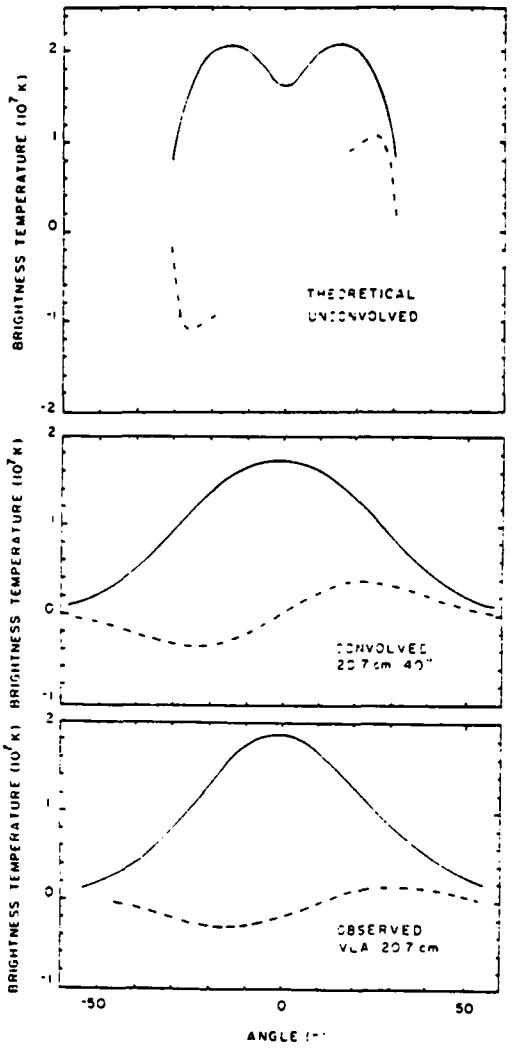

FIG. 6.—The computed spatial distribution of brightness temperature due to gyrosynchrotron radiation at 20.7 cm from a homogeneous and isotropic power-law electron spectrum in a magnetic loop (*top*) (*solid line*: total intensity I, *dashed line*: circular polarization V; parameters of the "High H" model of Table 3). The convolved distribution (*middle*) expected from the VLA (beamwidth 40" across the long axis of the source) represents the observed distribution (*bottom*). Notice that the presence or absence of intense emission from the legs or apex of magnetic loops depends on the source parameters as well as on the observing beamwidth.

ii) *Maxwellian Plasma*

When the hard X-ray and 20.7 cm emission are assumed to come from the same isothermal plasma, the magnetic field structure is the only free parameter left. The density of the hot plasma is determined by the emission measure derived from the hard X-ray observations, and the source volume is inferred from the 20.7 cm images (Table 3). A very tenuous source results ($N_e = 1.5 \times 10^8$ cm^{-3}), which is not uncommon in thermal microwave models (see Batchelor *et al.* 1985, Table 2). The observed brightness temperature distribution at 20.7 cm is well represented by a Maxwellian plasma with the magnetic field parameters given in the last column of Table 3. However, the long-wavelength spectrum expected from the thermal model is not easily reconciled with the 91.6 cm observations: the thermal plasma would be optically thick at 91.6 cm but sufficiently tenuous to enable the propagation of radiation at this wavelength. One thus expects a brightness temperature of roughly 10^8 K and very weak polarization from a source similar to that at 20.7 cm, contrary to what is observed. The only way to reconcile the radio and hard X-ray observations with emission from a hot plasma would be to locate the 20.7 cm source in an underdense structure so that the bright long-wavelength emission is totally absorbed in the ambient corona.

VI. DISCUSSION

In this paper, we have discussed observations of a weak impulsive flare. Since the lack of spatially resolved observations in the soft X-ray domain precludes any examination of the global energy balance of this flare, we will restrict our discussion to the hard X-ray and radio observations.

The 20.7 cm observations reveal the presence of two spatially distinct sources during the burst:

1. The radio emission during the early onset of the hard X-ray burst (detected only below 30 keV) originates from a source A. This preflash emission is most probably thermal gyroresonance emission from a 7×10^6 K plasma in a magnetic field of 130–270 G. This interpretation is consistent with the absence of detectable circular polarization, of a simultaneous hard X-ray peak and of burst emission at 91.6 cm.

2. From the onset to the end of the flash phase, the predominant 20.7 cm emission arises from a source B, which is different from A both in position and in polarization. The flash phase comprises several peaks observed in hard X-rays above 30 keV and at 20.7 cm and 91.6 cm.

As is again seen at the end of the impulsive phase, the preflash source A probably exists throughout the burst. Nevertheless, the large beam of the VLA in the C/D configuration does not enable us to determine whether the time history of source A resembles that of the dominant impulsive source B. Former VLA observations (Willson 1983; Holman, Kundu, and Kane 1989; Willson, Lang, and Liggett 1990) showed also that the precursor, impulsive, and decay phases of other flaring active regions originated in spatially separated sources. These findings are in agreement with results at metric (Raoult *et al.* 1985) and X-ray wavelengths (Hernandez *et al.* 1986; Machado *et al.* 1988). These sets of observations suggest that a destabilized coronal triggering source interacts with adjacent coronal loops, leading to the explosive release of energy during the flash phase.

While in the burst discussed in the present paper preflash emission at 20.7 cm seems to be consistent with a thermal electron population, the flash phase emission is in conflict with a perfectly confined hot plasma. The decimetric observations turn out to be a crucial criterion for distinguishing the two populations: while, in order to be detectable at high photon energies, the thermal plasma must have a temperature of at least 10^8 K, the low emission measure required, together with the measured dimension of the radio source, implies a low electron density (see Batchelor *et al.* 1985, Table 2, for other examples of weak hard X-ray bursts). If the high-energy tail of the hot electron population were confined around the apex of the loop by ion conduction fronts, bright, weakly polarized gyrosynchrotron emission should be seen at 91.6 cm at the location of the 20.7 cm source. This has not been observed in the present case. Hence, if the energetic electrons yielding the hard X-ray and radio emission originate from bulk energization of coronal plasma, they cannot be part of a confined Maxwellian. On the other hand, the injection of energetic electrons into different structures, where they emit hard X-ray, microwave, and decimetric emission through different mechanisms, might be easier to understand in terms of a process which generates a population of suprathermal electrons. This is consistent with the quantitative analysis of § V. The present work suggests that the acceleration of electrons is the main process responsible for the hard X-ray and radio emission associated with the flash phase.

Radio astronomical studies of the Sun at Tufts University are supported under grant AFOSR-89-0147 with the Air Force Office of Scientific Research. Simultaneous Very Large Array and *Solar Maximum Mission* observations of the Sun are supported by NASA grant 5-501 to Tufts University. The VLA is operated by Associated Universities, Inc., under contract with the National Science Foundation (NSF). Collaborative solar observations by Tufts University and the Observatoire de Paris are supported by NSF grant INT-8602285 and Centre National de la Recherche Scientifique (CNRS) grant 920038. The authors are indebted to B. R. Dennis for providing the hard X-ray spectral data and to C. Alissandrakis and J. Kuijpers for helpful discussions. We also thank R. Schwartz and G. Labow for their help with the analysis of the HXRBS data.

REFERENCES

Alissandrakis, C. E., and Preka-Papadema, P. 1984, *Astr. Ap.*, 139, 507.
Alissandrakis, C. E., Schadee, A., and Kundu, M. R. 1988, *Astr. Ap.*, 195, 290.
Batchelor, D. A. 1989, *Ap. J.*, 340, 607.
Batchelor, D. A., Crannell, C. J., Wiehl, H. J., and Magun, A. 1985, *Ap. J.*, 295, 258.
Benz, A. O., Barrow, C. H., Dennis, B. R., Pick, M., Raoult, A., and Simnett, G. 1983, *Solar Phys.*, 83, 267.
Böhme, A., Fürstenberg, F., Hildebrandt, J., Saal, O., Krüger, A., Hoyng, P., and Stevens, G. A. 1977, *Solar Phys.*, 53, 139.
Dennis, B. R., *et al.* 1988, *NASA-TM* 4036.
Duijveman, A. 1983, *Solar Phys.*, 84, 189.
Dulk, G. A. 1985, *Ann. Rev. Astr. Ap.*, 23, 169.
Elgarøy, Ø. 1977, *Solar Noise Storms* (Oxford: Pergamon Press).
Fürst, E., Benz, A. O., and Hirth, W. 1982, *Astr. Ap.*, 107, 178.
Gary, D. E. 1985, *Ap. J.*, 297, 799.
Hernandez, A. M., Machado, M. E., Vilmer, N., and Trottet, G. 1986, *Astr. Ap.*, 167, 77.
Holman, G., Kundu, M. R., and Kane, S. R. 1989, *Ap. J.*, 345, 1050.
Kai, K. 1986, *Solar Phys.*, 104, 235.
Kattenberg, A., Allaart, M., de Jager, C., Schadee, A., Schrijver, J., Shibasaki, K., Švestka, Z., and van Tend, W. 1981, *Solar Phys.*, 88, 315.
Klein, K.-L. 1987, *Astr. Ap.*, 183, 341.
Klein, K.-L., Pick, M., Magun, A., and Dennis, B. R. 1987, *Solar Phys.*, 111, 225.
Klein, K.-L., and Trottet, G. 1984, *Astr. Ap.*, 141, 67.
Klein, K.-L., Trottet, G., and Magun, A. 1986, *Solar Phys.*, 104, 243.
Kundu, M. R. 1986, *Adv. Space Res.*, 6, No. 6, 93.
Kundu, M. R., Schmahl, E. J., and Fu, Q.-J. 1989, *Ap. J.*, 336, 1078.

Lin, R. P., and Hudson, H. S. 1976, *Solar Phys.*, **50**, 153.
Lin, R. P., Schwartz, R. A., Pelling, R. M., and Hurley, K. C. 1981, *Ap. J. (Letters)*, **251**, L109.
Lu, E. T., and Petrosian, V. 1989, *Ap. J.*, **338**, 1122.
Machado, M. E., Moore, R. L., Hernandez, A. M., Rovira, M. G., Hagyard, M. J., and Smith, J. B. 1988, *Ap. J.*, **326**, 425.
Mercier, C. 1989, *Solar Phys.*, in press.
Mercier, C., Elgarøy, Ø., Tlamicha, A., and Zlobec, P. 1984, *Solar Phys.*, **92**, 375.
Orwig, L. E., Frost, K. J., and Dennis, B. R. 1980, *Solar Phys.*, **65**, 25.
Pick, M., Klein, K.-L., and Trottet, G. 1989, *Ap. J. Suppl.*, in press.
Priest, E. R., Gaizauskas, V., Hagyard, M. J., Schmahl, E. J., and Webb, D. F. 1986, in *Energetic Phenomena on the Sun*, ed. M. Kundu and B. Woodgate (NASA CP-2439), p. 1.
The Radioheliograph Group 1989, *Solar Phys.*, **120**, 193.
Raoult, A., Correia, E., Lantos, P., Kaufmann, P., Klein, K.-L., and de Genouillac, G. 1989, *Solar Phys.*, **120**, 125.
Raoult, A., Pick, M., Dennis, B. R., and Kane, S. R. 1985, *Ap. J.*, **299**, 1027.
Shevgaonkar, R. K., Kundu, M. R., and Jackson, P. D. 1988, *Ap. J.*, **329**, 982.
Smith, D. F. 1986, *Ap. J.*, **302**, 836.
Suzuki, S., and Dulk, G. A. 1985, in *Radiophysics of the Sun*, ed. D. J. McLean and N. R. Labrum (Cambridge: Cambridge University Press), p. 289.
Thomas, R. J., Starr, R., and Crannell, C. J. 1985, *Solar Phys.*, **95**, 323.
Tucker, W. H., and Koren, M. 1971, *Ap. J.*, **168**, 283.
Van Hoven, G., and Hurford, G. J. 1986, *Adv. Space Res.*, **6**, No. 6, 83.
Willson, R. F. 1983, *Solar Phys.*, **83**, 285.
Willson, R. F., Lang, K. R., and Liggett, M. 1990, *Ap. J.*, **350**, 856.

ALAIN KERDRAON, KARL-LUDWIG KLEIN, and GÉRARD TROTTET: Observatoire de Paris, Section d'Astrophysique de Meudon, CNRS UA 324, F-91925 Meudon Principal Cédex, France

KENNETH R. LANG and ROBERT F. WILLSON: Department of Physics and Astronomy, Robinson Hall, Tufts University, Medford, MA 02155

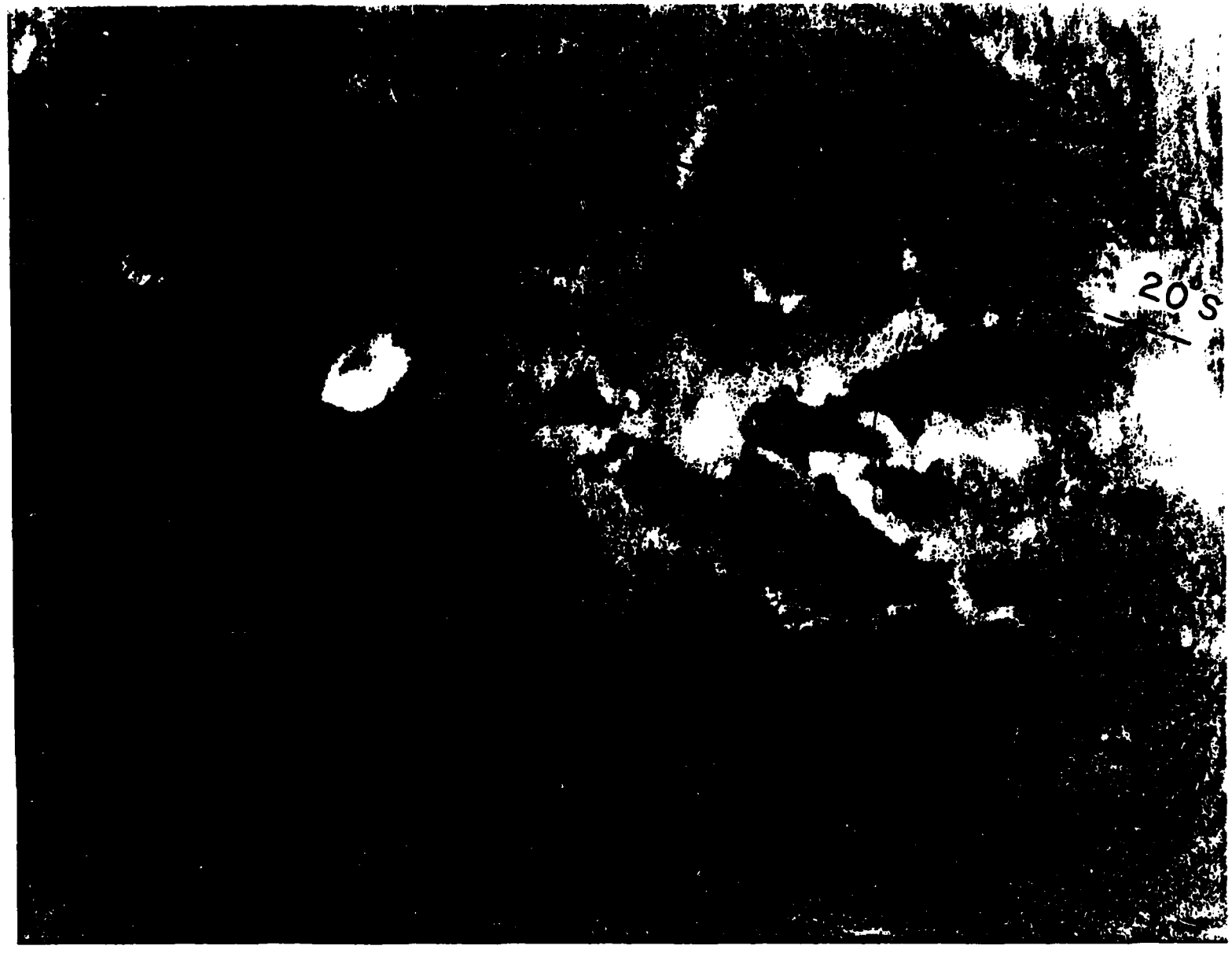

FIG. 4.—A VLA 3.3 s snapshot map of the 20.7 cm burst at 14:49:54 UT is compared with a SOON Hα image taken at 14:50:10 UT. The contours of the snapshot map denote levels of equal brightness temperature, with an outermost contour and contour interval of $T_b = 1.1 \times 10^6$ K. The dashed lines denote heliocentric latitude and longitude, and the angular scale may be determined from the 1′ horizontal bar. The two arrows show the locations of Hα kernels which are displaced westward from the position of the 20.7 cm burst.

WILLSON *et al.* (*see* 357, 664)

D5 VLA-PHOENIX OBSERVATIONS OF A NARROW-BAND DECIMETRIC BURST

Robert F. Willson
Dept. Of Physics and Astronomy
Tufts University
Medford, MA 02155
USA

Arnold. O. Benz
Institute of Astronomy
ETH, CH-8092
Zurich
Switzerland

ABSTRACT We discuss observations of a highly-circularly polarized multiply-impulsive microwave burst detected by the Very Large Array and the Phoenix Digital Radio Spectrometer. The VLA was used to resolve the burst in two dimensions, while PHOENIX provided high time resolution information about its spectral properties. During part of the burst, positive frequency drifts were detected, suggesting inwardly propagating beams of electrons emitting Type III-like radiation.

1. INTRODUCTION

It is generally believed that gyrosynchrotron radiation from nonthermal electrons can explain the properties of most solar microwave bursts, including their brightness temperature, polarization and bandwidth. Recent observation using wide-band dynamic spectrographs have, however, discovered multiply-impulsive ($\tau < 100$ msec) bursts including spikes, pulsations and decimetric type III bursts whose narrow bandwidths and frequency drifts require a different explanation such as plasma radiation or electron-cyclotron maser emission (eg. Stähli and Benz 1987). Practically nothing is known about the spatial properties of these events since they have only been detected with single dish instruments with poor angular resolution. Here we discuss some spatially resolved observations of a narrow band decimetric burst using the VLA and the Phoenix Digital Radiospectrometer.

2. COORDINATED OBSERVATIONS OF MICROWAVE BURSTS

The Very Large Array was used to observe the Sun between 1300-2300 UT on June 25 and 27, 1989 as part of the Max 91 Campaign. Observations were made simultaneously at 1446 MHz (20.7 cm) and 327 MHz (91.6 cm) with a time resolution of 1.67 s. They were coordinated with observations at the Nancay Radioheliograph (164 and 327 MHz) and with the PHOENIX Digital Radio Spectrometer (ten frequencies each between 301 and 356 MHz and 1265 and 1525 MHz- 20 msec time resolution) in order to study the spatial, temporal and spectral properties of decimetric bursts.

Figure 1a shows an example of a burst detected by the VLA and PHOENIX at 1446 MHz. It consists of several impulsive spikes, each of 20-30 seconds in duration, covering a period of a few minutes. There was no

evidence for burst emission at 327 MHz, nor was there a soft or hard X-ray burst detected by the SMM or GOES satellites. Snapshot maps (Fig. 1b) show that the bursts are compact (θ= 25-30") and highly circularly polarized (ρ_c = 90-100 %). Co-registration of these maps with a SOON Hα image taken at 1617 UT showed that the burst was located above a faint optical flare lying between two active regions (~N25, E21)

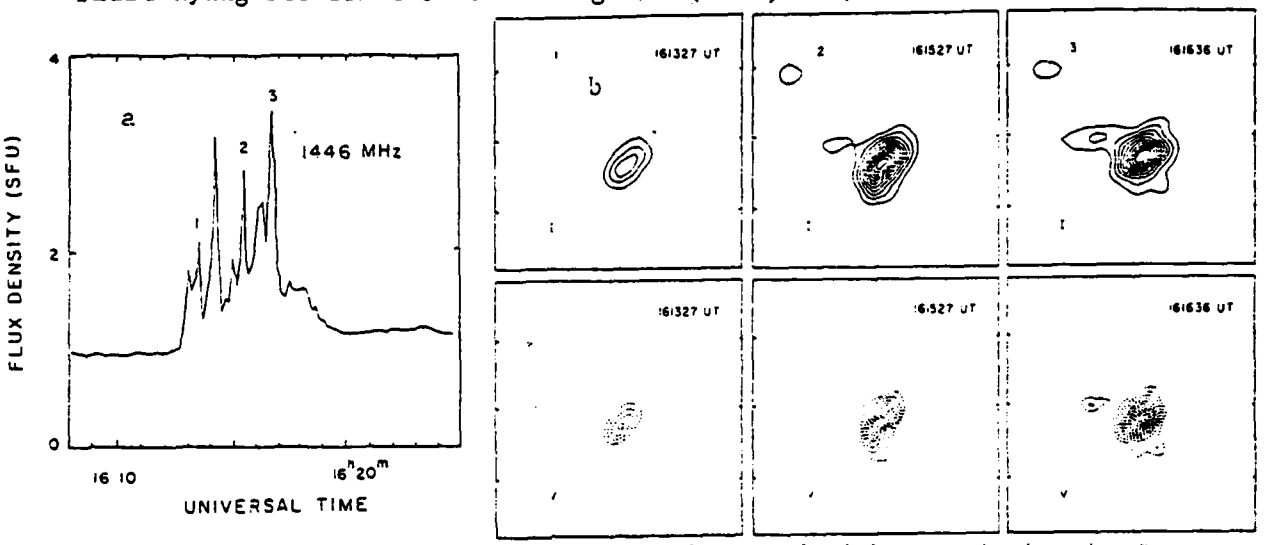

Figure 1. a) Time profile of the burst detected with one of the short VLA baselines on 1989 June 25. b) VLA 3.3 s snapshot maps at times 1, 2 and 3 shown in Fig. 1a. The brightness temperature contours for the I and V maps are drawn at intervals of T_b = 8 x 10^5 and 4 x 10^5 K, respectively. Fiducial marks on the axes are drawn every 60".

The PHOENIX spectral data showed that the emission drifted from high to low frequencies near the time of the most intense peak (3) (~+750 MHz/sec) suggesting an inwardly-propagating beam of electrons. Broadband emission was detected at most other times. Although the positions of the bursts shifted from peak to peak ($\Delta\theta$~10"), these changes were not systematic, as would be expected for a source moving through the corona. Nevertheless, this event may be related to the decimetric type III events (Stähli and Benz 1987) whose narrow bandwidths and frequency drifts suggest a coherent emission mechanism, such as plasma radiation or electron-cyclotron maser emission.

3. ACKNOWLEDGEMENTS

Radio astronomical studies of the Sun at Tufts University are supported under grant AFOSR-89-0147 with the Air Force Office of Scientific Research, and by NASA grant NAG-5-501.

4. REFERENCE

Stähli, M., and Benz, A.O. (1987) 'Microwave Emission of Solar Electron Beams', Astronomy and Astrophysics 175, 271-276.

THE ASTROPHYSICAL JOURNAL, 378:360–371, 1991 September 1

D6. MULTI-WAVE BAND *SMM*–VLA OBSERVATIONS OF AN M2 FLARE AND AN ASSOCIATED CORONAL MASS EJECTION

ROBERT F. WILLSON,[1] JOAN T. SCHMELZ,[2] RAYMOND D. GONZALEZ,[3] KENNETH R. LANG,[1] AND KERMIT L. SMITH[4]

Received 1989 December 21; accepted 1991 March 13

ABSTRACT

An M2 flare and an associated coronal mass ejection (CME) were observed by instruments on the *Solar Maximum Mission* as well as by the Very Large Array and other ground-based observatories on 1988 September 30 as part of the International Solar Month campaign. The multi-wave band data show a gradual, slowly changing event which lasted several hours. The microwave burst emission originates in compact ($\theta = 10''$–$30''$), moderately circularly polarized ($\rho_c \leq 60\%$) sources ($T_b = 0.5$–20×10^6 K) located near the sites of bright Hα and soft X-ray emission. These data were combined with estimates of electron temperature ($T_e = 1.5 \times 10^7$ K) and emission measure (EM $\approx 2.0 \times 10^{49}$ cm^{-3}) obtained from Ca XIX and Fe XXV spectra to show that the microwave emission can be attributed to thermal gyrosynchrotron radiation in regions where the magnetic field strength is $H = 425$–650 G. The CME was observed by both ground- and space-based coronagraphs and a good estimate of the acceleration at low altitudes could be measured: 0.1240 ± 0.0466 km s^{-2}. From these observations, the flare and CME start times appear to be simultaneous. The event can be described by a "cartoon" where a global magnetic disturbance both triggers the flare and opens the field lines allowing the filament cavity to rise. After the mass ejection, the open field lines begin to reconnect. The low-lying loops are heated first and the deposited energy travels down to the surface and appears as bright Hα parallel ribbons. Higher and higher loops are heated until reconnection is complete.

Subject headings: Sun: corona — Sun: flares — Sun: radio radiation — Sun: X-rays

1. INTRODUCTION

Multiple-wavelength VLA observations of solar radio bursts may be used to locate the sites of energy release at different heights above flaring active regions and to provide information about preburst heating and magnetic interactions which may trigger the impulsive phase (e.g., Kundu et al. 1982; Kundu & Lang 1985). The emission at short wavelengths ($\lambda \leq 6$ cm) generally occurs along the legs of coronal loops, whereas the emission at longer wavelengths usually occurs near the top (Marsh & Hurford 1980; Lang & Willson 1983; Kundu, Schmahl, & Velusamy 1982a). Centimeter-wavelength emission is thought to be the gyrosynchrotron radiation of thermal or nonthermal electrons trapped in magnetic loops; because the shape of the brightness temperature spectrum depends critically on the magnetic field strength (Dulk & Marsh 1982; Dulk 1985), spatially resolved observations at different wavelengths may be used to infer variations in field strength along the flaring loop.

When VLA observations are compared with data at X-ray wavelengths, they also reveal information about the size and location of energy release in the two spectral domains. Soft X-ray data from the X-ray Polychromator (XRP) aboard the *Solar Maximum Mission* satellite, for example, can be used to estimate the electron temperature and electron density of the hot ($T_e \approx 10^7$ K) thermal plasma, while data from the Hard X-Ray Burst Spectrometer (HXRBS) may be used to derive the number density and energy distribution of the nonthermal electrons accelerated during the impulsive phase. By combining this information with the brightness temperature, size, and polarization of the VLA sources, it is possible to deduce the radio emission mechanism and to constrain plasma parameters, such as the magnetic field strength (e.g. Schmahl et al. 1990; Willson et al. 1990a).

Previous multiwavelength VLA observations of solar radio bursts have been made at 2 and 6 cm (Shevganonkar & Kundu 1985; Dulk, Bastian, & Kane 1986; Kundu, Velusamy, & White 1987) and at 6 and 20 cm (Melozzi, Kundu, & Shevgaonkar 1985; Velusamy et al. 1987). These observations therefore referred to regions either near the legs of loops or at the tops, but not both. Moreover, because these studies did not involve spatially resolved X-ray images, they provided no clues to the sizes and relative positions of thermal and nonthermal plasmas.

In this paper, we discuss multi-wave band VLA and *SMM* observations of an X-ray burst and an associated coronal mass ejection (CME) which occurred during International Solar Month (1988 September). Our VLA observations were made at wavelengths of 2, 3.5, 6.1, and 20.7 cm and therefore potentially cover both the high-frequency and low-frequency sides of the microwave burst spectrum. Snapshot maps at 3.3 s time intervals delineated the time evolution of the burst structure over a greater range of heights than was possible during previous investigations, while comparisons with soft X-ray data provided better constraints on plasma parameters and emission mechanisms. In addition, the occurrence of a coronal mass ejection gave us the opportunity to determine which came first, the start of the flare or the initiation of the mass ejection (see, for example, Harrison et al. 1989). Finally, comparisons with

[1] Department of Physics and Astronomy, Tufts University, Medford, MA 02155.
[2] Applied Research Corporation under subcontract to Lockheed. Postal address: NASA/Goddard Space Flight Center, SMM-XRP Code 602.6, Greenbelt, MD 20771.
[3] National Radio Astronomy Observatory, P.O. Box O, Socorro, NM 87801.
[4] Lockheed Palo Alto Research Laboratory, 3251 Hanover Street, Palo Alto, CA 94304.

soft X-ray and Hα images allowed us to investigate the related magnetic reconnection processes which is observed as apparent motion of an X-ray loop and dark filament.

In §§ 2 and 3 we discuss VLA observations of the preburst, impulsive, and decay phases of this event. The high spatial resolution of the snapshot maps allowed us to locate the microwave emission with respect to Hα flare kernels and ribbons, soft X-ray loops, and coronal potential field lines. The radio burst has a relatively simple structure, whose size systematically increases with wavelength. In § 3 we also present *SMM*–XRP soft X-ray maps as well as light curves and spectra of the flaring emission. The soft X-ray images were used to study the structural evolution of the thermal plasma, while the spectra provided estimates of its electron temperature and emission measure. Finally, we discuss observations of the coronal mass ejection using images from the Coronagraph Polarimeter (C/P) aboard *SMM* and from the K-Coronometer in Mauna Loa.

In § 4.1, we combine the *SMM*, VLA and other ground-based observations to show that the radio emission can be best explained as thermal gyrosynchrotron radiation from regions where the magnetic field strength is $H = 425$–650 G. These values of H are in good agreement with those inferred from potential field calculations. To our knowledge, these are the first such comparisons of magnetic field strengths involving VLA burst observations. In § 4.2 we discuss observations of an expanding X-ray arch, a dark Hα filament, and the CME in light of recent ideas about the initiation of coronal mass ejections and their relationship to other flare-related phenomena. In § 5, we summarize our conclusions.

2. OBSERVATIONS

Active Region AR 5171 (S26 E25 at 1300 UT) was chosen as the International Solar Month target for 1988 September 30, having produced a number of M-class *GOES* flares during the preceding several days. (*GOES*, the *Geostationary Operational Environmental Satellite*, has a full disk X-ray monitor with a soft X-ray channel [1–8 Å] and a harder channel [0.5–4 Å]). At ≈1900 UT, an M2 flare erupted from the region which was detected with several instruments on *SMM*, the VLA, and other ground-based observatories participating in the campaign. The *GOES* data shown in Figure 1 indicate a simple burst profile, consisting of a relatively slow rise (≈5–10 minutes) followed by a gradual decay lasting several hours. In this figure, the times of the VLA and *SMM* observations are also shown. The VLA observed the preburst, impulsive, and decay phases of the flare. *SMM*, which had been tracking the region for 2 days, was eclipsed by the Earth until 1907 UT and, therefore, missed the impulsive phase.

2.1. *Radio Observations*

The VLA observed AR 5171 in the D configuration between 1815 and 2300 UT on 1988 September 30. The observations were made at wavelengths of 2.0, 3.6, 6.1, and 20.7 cm (14934, 8484, 4816, and 1496 MHz) with bandwidths of 12.5 MHz. At these four respective wavelengths, the individual antenna beamwidths are 3'.2, 6'.0, 9'.7, and 32' with synthesized beamwidths of ≈5″, 10″, 16″, and 40″. Our observing sequence consisted of consecutive 8–10 minute observations at 2, 3.6, and 6.1 cm, with a 5–7 minute observation at 20.7 cm about every 90 minutes. This strategy allowed us to image both the quiescent active region and emission from different phases of the relatively long-lasting burst.

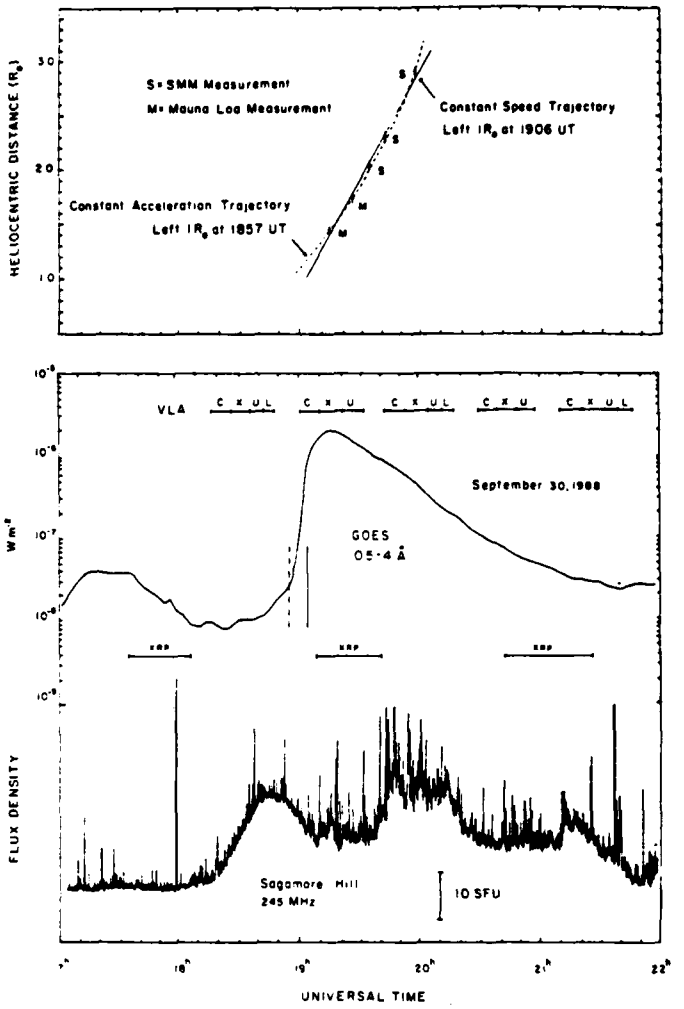

FIG. 1.—*Bottom*: Time profiles of the burst obtained by the 0.5–4.0 Å detector on *GOES* and by the Sagamore Hill station of the Air Force Solar Radio Patrol at 245 MHz. The times and bands that the VLA observed are shown at the top. The times of the *SMM* orbits are given at the bottom. Here the VLA band designations of U, X, C, and L correspond to wavelengths of 2, 3.6, 6.1 and 20.7 cm, respectively. *Top*: Time-height plot of the CME as detected by the Mauna Loa Mark III K Coronometer (M) and by the *SMM* Coronagraph/Polarimeter (S). The solid and dashed lines represent, respectively, constant speed and constant acceleration fits to the data.

The gains and phases of the antennas were calibrated every 35 minutes using 2 minute observations of PKS 1252+119, with 3C 286 used to establish the flux density scale at all wavelengths. All four Stokes parameters were sampled every 3.3 s in order to study rapid changes in the structure and polarization. The data were calibrated using the standard VLA reduction programs and then used to make CLEANed maps at all wavelengths. Uncertainties in the calibration of solar observations at the VLA have been discussed by Kundu, Schmahl, & Fu (1989), Shevgaonkar, Kundu, & Jackson (1989), and Lang & Willson (1989).

This burst was also detected by the Sagamore Hill and Palehua stations of the Radio Solar Telescope Network (RSTN), operated by the US Air Force. The total solar flux is measured at eight wavelengths between 122 and 1.94 cm. The 122 cm data (Fig. 1) show intense burst emission before and during the M2 flare which may be attributed to a Type I noise

storm. A Type II burst was also reported from 1916 to 1936 UT by the Sagamore Hill Observatory (Solar Geophysical Data). Unfortunately these data provide no spatial information and, because the VLA was not operating at 90 cm, we cannot say whether this long-wavelength activity was associated with the X-ray burst or the CME. However, recent simultaneous VLA observations of another event at 20.7 and 91.6 cm did show that a noise storm continuum source began to increase in intensity about 30 minutes prior to the onset of an impulsive burst, possibly indicating an interaction between large- and small-scale coronal loops (Willson, Lang, & Liggett 1990b).

2.2. *SMM Observations*

The XRP (Acton et al. 1980) Flat Crystal Spectrometer (FCS) can be centered on resonance lines between 1.5 and 20.0 Å. These lines are sensitive to different plasma temperatures and ratios of the line fluxes can be used to determine various physical parameters of the plasma. The wavelength drive which scans the crystals and centers them on different spectral lines, could, unfortunately, not move freely in September. The strategy adopted was to park the drive at the Fe XVII resonance line (peak formation temperature $T_e = 5 \times 10^6$ K) at 15.01 Å, the most sensitive line for active region studies. The FCS was centered on AR 5171 and rastered continuously over a 4′ × 4′ field of view in steps of 10″ or 15″. Successive images provide a time history of the active region.

Temperature and emission measure estimates of the flaring plasma are available from the XRP Bent Crystal Spectrometer (BCS), a nonimaging instrument with a 6′ × 6′ (FWHM) field of view. The BCS monitors the high-temperature ($T_e \geq 10^7$ K) component of the plasma through light curves and spectra of Ca XVIII–XIX lines (peak formation temperature $T_e = 35 \times 10^6$ K) near 3.18 Å and Fe XXIV–XXV lines (peak formation temperature $T_e = 70 \times 10^6$ K at 1.91 Å). The electron temperature can be determined from the ratio of the dielectronic satellite line flux to the collisionally excited resonance line flux for each ion: k/w in Ca XVIII/Ca XIX and j/w in Fe XXIV/Fe XXV (using the notation of Gabriel 1972). The emission measure can then be found by using the ion emissivity curves with the derived electron temperature. The atomic physics calculations of Bely-Dubau et al. (1982 and references therein) were used to derive these plasma parameters.

The *SMM* Coronagraph/Polarimeter (C/P) was built and operated by the High Altitude Observatory and described in detail by MacQueen et al. (1980). It imaged the solar corona between 1.5 and 6 $R_\odot$ using a broad band green filter. On 1988 September 30, the first C/P image of the southeast limb after the M2 flare revealed only the relatively quiet corona. The CME was detected in an image taken at 1936 UT and its evolving structure was observed in two subsequent images (1944 and 2001 UT) before it moved out of the C/P field of view. These images were, unfortunately, not ideal since the CME was at the edge of the field of view in two of the images and a portion was blocked by the occulting disk pylon shadow in the third. Nevertheless, measurements of the CME properties could be made and, thus, the event is interesting because of the multi-wave band data taken of the associated flare.

3. RESULTS

3.1. *Preburst Active Region Emission*

Because of the large number of short interferometer spacings in the D configuration, we were able to make snapshot maps of the preburst emission with a reasonably high dynamic range of about 20 to 1. Figure 2 shows maps of total intensity, *I*, and

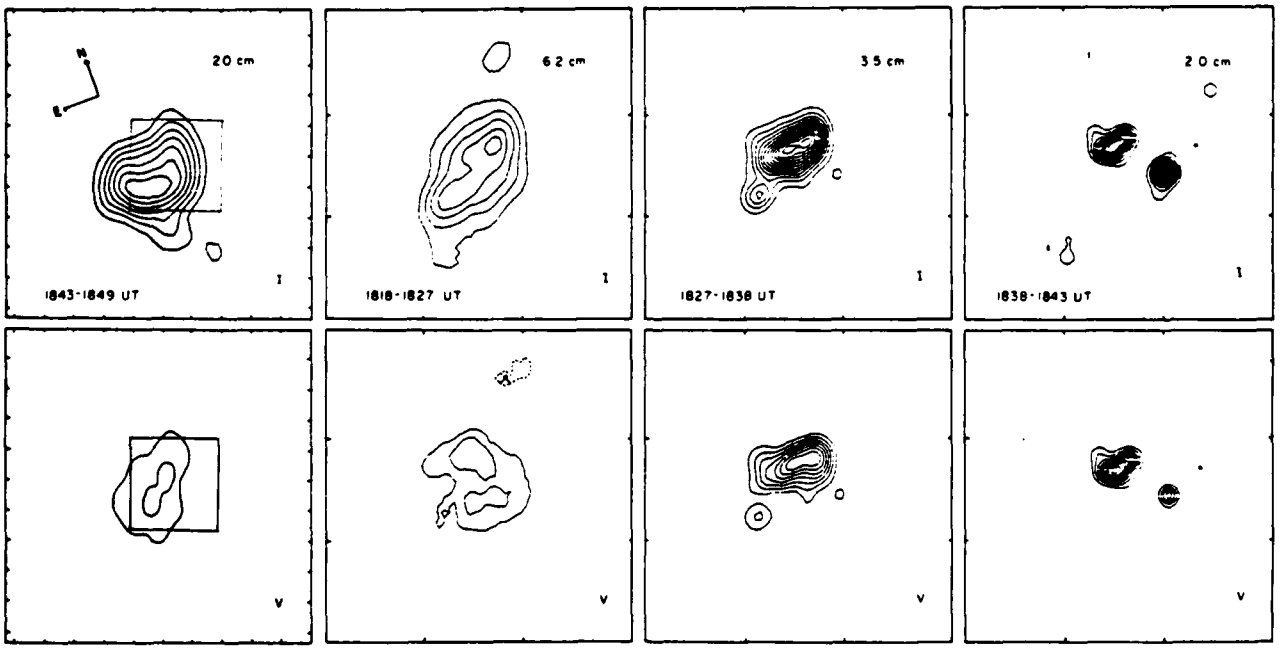

FIG. 2.—VLA maps of total intensity, *I*, and Stokes parameter, *V*, showing the preburst emission at 2, 3.6, 6.1, and 20.7 cm wavelength. The fiducial marks on the axes are drawn at 60″ intervals. The direction of the north and east solar limbs are denoted by arrows. The box on the 20.7 cm map marks the 3′ field of view of the maps at the shorter wavelengths. The contours mark levels of equal brightness temperature, with an outermost contour and contour interval of $T_b = 3.1 \times 10^5$ K, 2.7×10^5 K, 1.7×10^5 K, and 3.6×10^6 K, at 20.7, 6.1, 3.6, and 2.0 cm. The peak brightness temperatures at these four respective wavelengths are $T_b = 2.2 \times 10^6$ K, 1.4×10^6 K, 2.1×10^6 K, and 5.0×10^6 K.

TABLE 1

PARAMETERS OF THE PREBURST EMISSION

Wavelength (cm)	Brightness Temperature (K)	Polarization	Angular Size
2.0.....	5.0×10^5	90%	12″ × 25″
3.6.....	2.1×10^6	60	20 × 40
6.1.....	1.4×10^6	40	30 × 75
20.7.....	2.2×10^6	≤ 10	170 × 175

circular polarization, V, and Table 1 gives the peak brightness temperature, size, and degree of circular polarization at all wavelengths. Here, the uncertainties in the values of the brightness temperatures are approximately 15%–20%. As shown in Figure 2, the emission at 3.6, 6.1, and 20.7 cm is contained in a single component whose size systematically increases and whose polarization decreases with increasing wavelength. These systematic variations are also apparent at 2.0 cm, except that there is an additional component that has no counterpart at longer wavelengths. The peak brightness temperatures (Table 1) are typical of those observed in quiescent active regions (e.g., Lang, Willson, & Gaizauskas 1983); and unless the actual brightness temperatures of the quiescent emission are abnormally low, this suggests that there was no significant preburst heating on time scales of a few tens of minutes before the burst, as has been observed for some active regions (Willson 1984; Kundu et al. 1987). Such enhanced emission, for example, could occur because of the emergence or reorientation of magnetic flux resulting in the heating of the plasma and the triggering of bursts (Heyvaerts, Priest, & Rust 1977; Priest et al. 1986 and references therein).

The VLA maps have been co-aligned with an Hα image and a Kitt Peak magnetogram (provided courtesy of Jack Harvey) of the active region. In Figure 3, we mark the locations of the sunspots and regions of bright plage as found on a Solar Optical Observing Network (SOON) Hα image made at 1841 UT. Figure 3 shows contours of the longitudinal magnetic fields obtained from the Kitt Peak magnetogram taken earlier in the day (1454 UT). Here we also show the configuration of magnetic field lines that have been extrapolated into the corona using the Kitt Peak data and sunspot field measurements from the Mount Wilson Observatory as boundary conditions. The method of extrapolation used for these calculations has been discussed by Sakurai (1981) who kindly provided us with his computer code.

A comparison of Figures 2 and 3 shows that the emission at 2, 3.6, and 6.1 cm is associated with relatively short magnetic loops connecting the dominant leading spot ($B \approx 2400$ G) of positive polarity to the smaller negative polarity ($B \approx 1000$ G) spots located $\approx 30''$ to the south. The more extended 20.7 cm emission is partly associated with these short loops, but mostly extends in the direction of the large-scale loops connecting the spots with regions of weaker magnetic fields ($B \approx 500$ G) to the southeast. The relatively high degree of (right-hand) circular polarization of the 2 cm ($\rho_c \approx 90\%$) and 3.6 cm ($\rho_c \approx 60\%$) emission suggests optically thin emission that is probably attributable to extraordinary-mode gyroresonance emission from the legs of loops anchored to the dominant spot.

SMM began tracking AR 5171 at ≈ 1300 UT on 1988 September 28 as the region was rotating over the east limb. Several hours later, AR 5171 produced two M flares and recovered quickly to a semiquiescent state, producing only small events before the VLA observations. The bulk of the Fe XVII X-ray emission is associated with the large-scale loops in the southeast. This is not surprising, as previous simultaneous VLA–XRP observations show a close correspondence between the structure of coronal loops at 20 cm and at X-ray wavelengths (Lang et al. 1987a, b). In addition, there is another more compact source located $\approx 30''$ south of the sunspots. The southward (or limbward) shift can be attributed to a projection effect due to the greater height of the soft X-ray emission above the underlying spots.

3.2. *Burst Emission*

Figures 4*a* and 4*b* show a series of VLA snapshot maps of total intensity, I, and circular polarization, V, which depict the evolution of the burst during the impulsive phase. The maps at 6.1, 3.6, and 2 cm represent 10 s of data, beginning at the time indicated. Maps made at shorter intervals (3.3 s) showed no detectable changes in structure. Table 2 gives the peak brightness temperature, size, and degree of circular polarization of these sources. The maps at 6.1 cm, made near the peak of the soft X-ray emission, show that the source has an elongated structure with an angular size of $\approx 20'' \times 38''$ at the half-

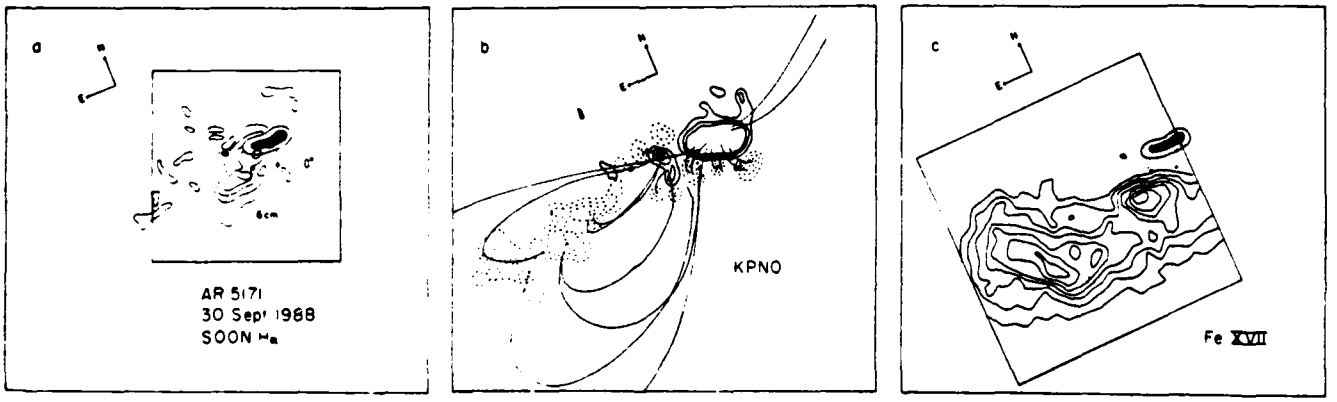

FIG. 3.—(*a*) A drawing showing the locations of the sunspots and brightest regions of plage as obtained from a SOON Hα image of AR 5171 at 1841 UT. For comparison, the 6.1 cm preburst map shown in Fig. 4 is superposed. (*b*) Potential magnetic field lines superposed on contours ($H = 200$, 400, 600 G) of the photospheric fields as obtained from a Kitt Peak magnetogram. (*c*) An XRP-FCS image of Fe XVII emission made during the preburst interval from 1738 to 1758 UT. The contours correspond to 10, 20, 30... counts s^{-1}.

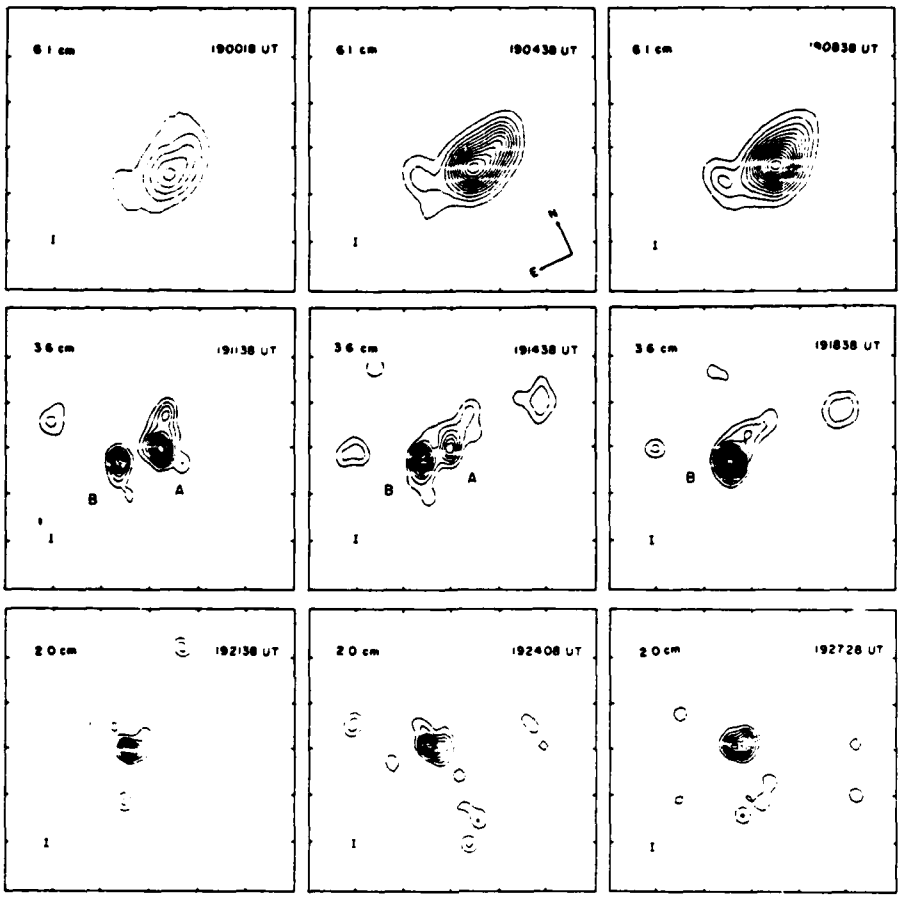

FIG. 4a

FIG. 4.—VLA snapshot maps of I (*a*) and V (*b*) at 6.1, 3.6, and 2.0 cm wavelength. The contours mark levels of equal brightness temperature, with an outermost contour and counter interval of $T_b = 1.3 \times 10^6$, 3.6×10^5, and 2.0×10^5 K for the maps at 6.1, 3.6, and 2.0 cm, respectively. The fiducial marks on the axes are drawn every 30″.

intensity level. Its centroid lies ≈30″ south of the preburst 6 cm peak, suggesting that the energy release took place in an adjacent source. There was no detectable change in the location of the 6 cm burst peak, although there is some indication of either a lengthening of the source or the emergence of a separate peak to the southeast. The peak brightness temperature of $T_b \approx 20 \times 10^6$ K is somewhat higher than the electron temperature inferred from the BCS spectra and the *GOES* data (see below).

The 3.6 cm maps show that, initially, there were two components, A and B, both of which were displaced eastward from the peak of the 6 cm burst. By ≈1900 UT, component A had disappeared, while component B had intensified. Component

TABLE 2

PARAMETERS OF THE BURST SOURCES

UT Time	Wavelength (cm)	Brightness Temperature (K)	Size	Polarization
190018	6.1	6.5×10^6	26″ × 37″	30%
190438	6.1	1.6×10^7	25 × 39	30
190838	6.1	1.8×10^7	25 × 30	20
191138A	3.6	3.2×10^6	15 × 18	55
191138B	3.6	2.5×10^6	12 × 15	≤10
191438A	3.6	2.1×10^6	12 × 17	50
191438B	3.6	4.7×10^6	12 × 14	≤10
191838B	3.6	6.1×10^6	12 × 14	≈15
192138	2.0	1.6×10^6	10 × 12	25
192408	2.0	2.2×10^6	10 × 12	27
192728	2.0	1.6×10^6	10 × 12	60
201100	20.7	4.6×10^6	100 × 130	≤15
213800	20.7	3.1×10^6	125 × 150	≤15

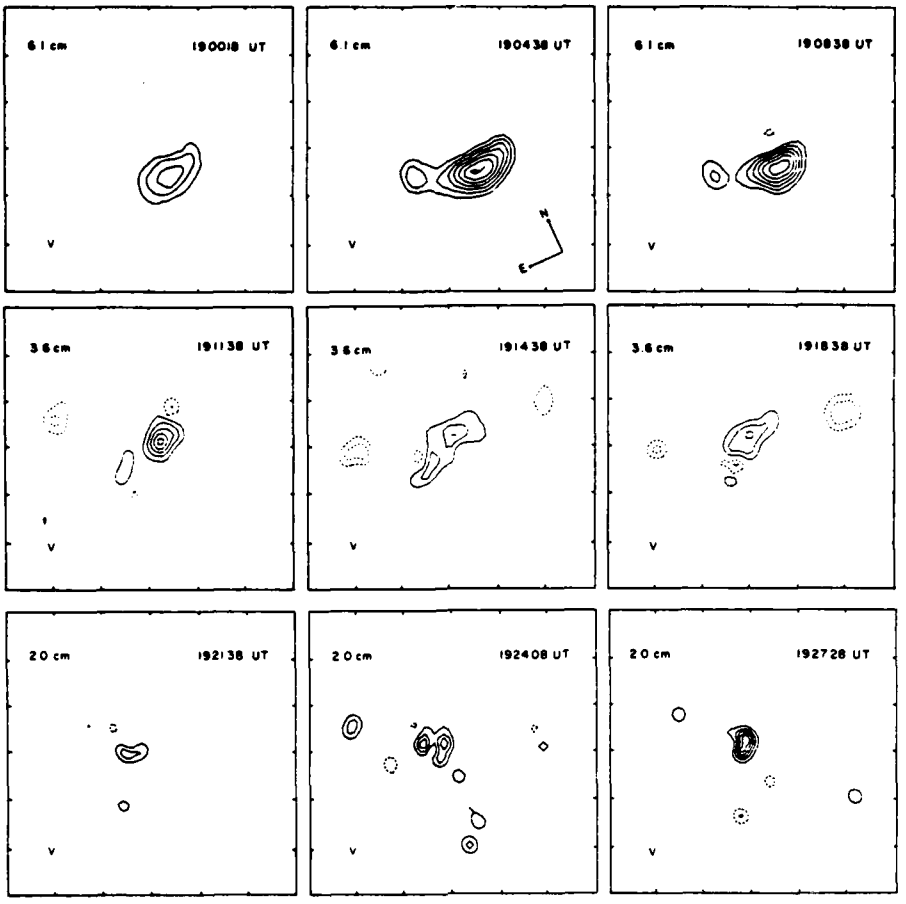

FIG. 4*b*

A had a circular polarization of ≈50% (RCP) while the peak of component B was only weakly polarized. The 2 cm maps made a few minutes after the peak of the impulsive phase indicate a single component (size ≈10″) whose center lies ≈15″ north of the 3.6 cm peak B. It shows circular polarization ($\rho_c \approx 25\%$ RCP) whose sense coincides with that at 6 and 3.6 cm, but which is smaller than at these other two wavelengths.

The electron temperature of the flaring plasma can be determined as a function of time from the k/w line ratio observed in the BCS Ca XIX spectra. The flux ratio as a function of temperature has been determined by Bely-Dubau et al. (1982). At 1907 UT, just after the impulsive phase of the M2 flare (as *SMM* moved out of Earth's shadow), the electron temperature determined by the k/w ratio was about 14×10^6 K with a statistical error of about $\pm 0.3 \times 10^6$ K. As shown in Figure 5, the temperature fell gradually, typical for long-duration X-ray events, to 11×10^6 K at 1940 when *SMM* entered the South Atlantic Anomaly. The volume emission measure increased from 0.05 to 0.15×10^{50} cm^{-3} in this period. The results from the j/w line ratio observed in the BCS Fe XXV spectra gave slightly higher temperatures and lower emission measures; the *GOES* data show the opposite effect. This indicates that flaring plasma was produced at a range of temperatures and each is most sensitive to a slightly different value.

3.3. *Evolution of the X-Ray Plasma and Postburst Motion*

At 1936 UT, C/P detected a faint coronal mass ejection above the southeast limb at a position angle of ≈150°. A second image (1944 UT) shows a bright loop with a dark feature trailing the front. The outer edge of the loop is determined in these images and a third (2001 UT) at a uniform position angle of 145 degrees. From these three images, a

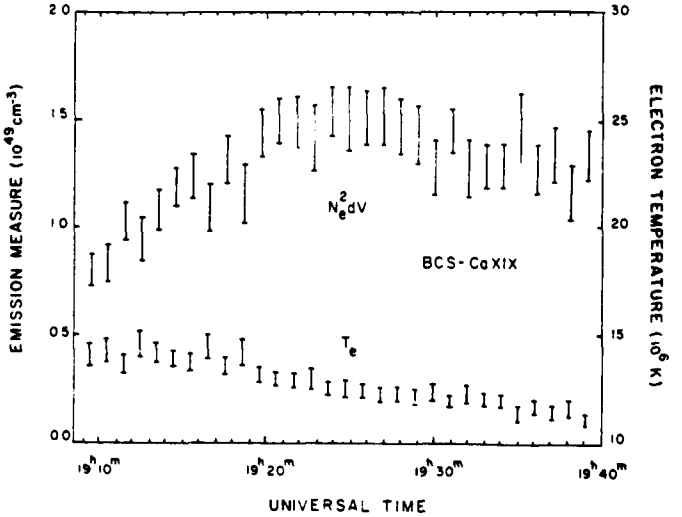

FIG. 5.—Plots of the electron temperature and emission measure derived from analysis of the BCS Ca XIX spectra. The error bars denote 1 σ uncertainties in the measurements.

height-time diagram was constructed, and a linear speed (projected onto the plane of the sky) of 378 ± 17 km s^{-1} is determined for the CME. A linear extrapolation of this speed yields a start time of $\approx$1905 UT (A.J. Hundhausen, private communication). The location of this event in the C P field of view and the extrapolated initiation time of the mass ejection establish its association with the M2 flare from AR 5171. A careful examination of the Mauna Loa Mark III K-Coronameter data for 1988 September 30 reveals two images of the event as it developed between 1.2 $R_\odot$ and the lower radius of the C/P field of view. Figure 1 shows that a constant acceleration trajectory, rather than a constant speed trajectory, best fits the five data points (all measured at 145°). This quadratic fit gives an extrapolated start time of 1857 ± 0001 UT and an acceleration of 0.1240 ± 0.0466 km s^{-2}.

Figures 6 and 7 show the evolution of the Fe XVII X-ray emission and the SOON Hα emission. Also shown in Figure 6 are the locations of the microwave burst peaks. Near the peak of the impulsive phase (1912–1922 UT), the X-ray emission is dominated by two relatively compact ($\approx$45″) sources, X_1 and X_2, which lie, respectively, southwest and southeast of the major sunspot. These limbward-shifted sources may represent loops whose feet are marked by the underlying Hα emission. There are two other peaks, X_3 and X_4, located in the eastern portion of the active region, which are also shifted with respect to the Hα emission. After 1922 UT, the peaks X_1 and X_2 appear to merge forming a large-scale loop that extends across much of the active region. The 2, 3.6, and 6 cm sources are located close to the Hα kernels near the sunspots and under this large-scale X-ray loop. During the flare decay, the X-ray emission begins to move limbward with an apparent projected speed of $\approx$7 km s^{-1} (Fig. 7). By 2309 UT, it has disappeared from the field of view, leaving a hole or depression $\approx$1′ south of the preburst, spot-associated X-ray component. These data suggest the outward movement of a postflare loop or the successive brightening of a set of loops at different altitudes. *Skylab* data showed similar motions (Kahler 1977; Pallavicini, Serio, & Vaiana 1977). Svestka et al. (1982), Svestka (1984), and de Jager & Svestka (1985) have discussed similar observations of postflare X-ray loops seen in *SMM* HXIS data which appeared to ascend into the corona following intense flares, and, in one case, a coronal mass ejection. They attributed these observations to coronal heating and particle acceleration caused by successive magnetic field line reconnection.

Inspection of the SOON Hα film indicated a limbward motion of the filament lying above the flare ribbon following the burst. Comparison of these images (Fig. 7) shows a close correspondence between the position, overall shape, and orientation of the filament and X-ray loop. Analysis of subsequent Hα images shows that the filament also appears to move laterally across the Sun together with the X-ray loops. Figure 8 shows the trajectory of the loops/filament system as measured from the bright Hα flare ribbon shown in Figure 6. The filament first appears at about 2014 UT with an initial limbward velocity (on the plane of the sky) of about 10 km s^{-1}. It soon decelerated to zero velocity ($\dot{v} = -8.2 \times 10^{-4}$ km s^{-2}) and became undetectable in the Hα images taken after 2230 UT. The X-ray loops show a clear, limbward displacement (relative

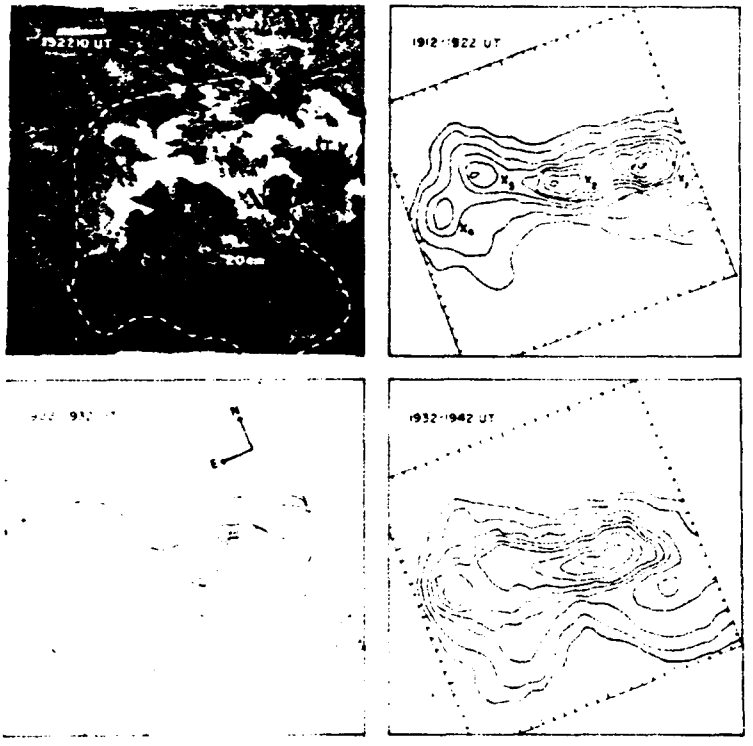

FIG. 6.—A SOON Hα image (*top left*) showing the location of the optical flare emission is compared with a sequence of XRP Fe XVII images depicting the evolution of the soft X-ray plasma. The locations of the VLA burst sources at 2.0, 3.6, 6.1, and 20.7 cm (Figs. 4 and 8) are superposed on the optical image. The contour levels of the XRP maps correspond to 100, 200, 400, 600, 800, 1000, 1400, 1800, 2200, 2600, and 3000 counts s^{-1} above the background level. The angular scale can be inferred from the 10″ spacing between the fiducial marks. The dashed line in the upper left-hand panel denotes the outermost contour of the 20.7 cm map at 2011 UT (see Fig. 9).

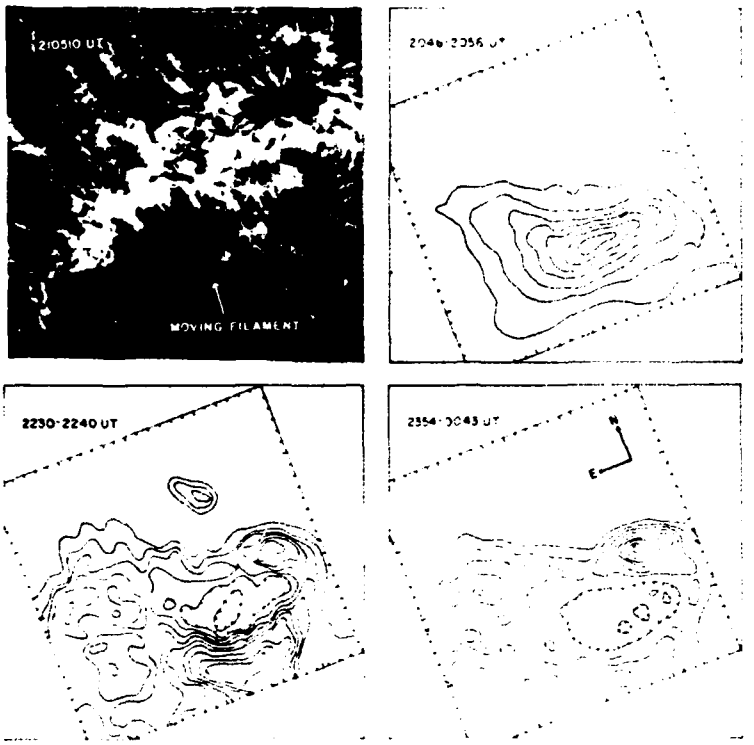

FIG. 7.—A comparison of Hα (*top left*) and soft X-ray (XRP–Fe XVII) images during the decay phase of the burst. A dark filament appearing to move outward with a projected speed of ≈ 7 km s^{-1} is coincident with an expanding X-ray loop which eventually disappears from the field of view. The contour levels of the Fe XVII image from 2046 to 2056 UT correspond to 100, 200, ... counts s^{-1} above the background level. The contour levels of the later maps are drawn at 10, 20 ... counts s^{-1} above the background level.

to the flare peak) in the first image taken after *SMM* emerged from Earth's shadow at 2042 UT. The loops display a decelerating motion similar to that of the filament until they disappear out of the XRP field of view at approximately 2300 UT.

In contrast, the 20 cm emission peak during the early decay phase (2011–2018 UT) is coincident with that of the preburst source (Fig. 9), suggesting energy release in the same region. A later map shows that, by 2138 UT, the peak has shifted $\approx 40''$ north while also developing a discernible "tongue" extending to the southeast. This new component could represent the microwave component of postflare loops, often detected in X-rays after bursts (Velusamy & Kundu 1981). Although this southward extension was outside the 2 cm field of view, there was no evidence for 3.6 or 6.1 cm emission in this region ($T_b \leq 0.5 \times 10^6$ K).

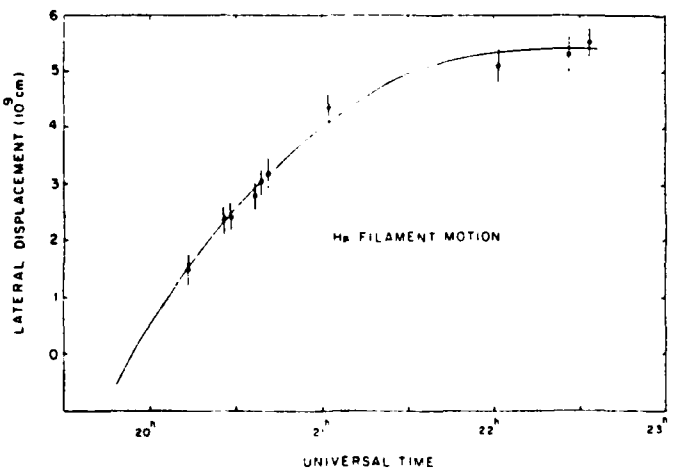

FIG. 8.—The lateral displacement of the Hα filament relative to the bright flare ribbon taken at 192210 UT (Fig. 6). The error bars correspond to an uncertainty of $\approx 5''$ in determining the position of the leading edge of the filament on each SOON image. A quadratic fit to the data (*solid line*) yields a velocity and deceleration of $v = 10.2$ km s^{-1} and $\dot{v} = -8.2 \times 10^{-4}$ km s^{-2}, respectively.

4. DISCUSSION

4.1. *Interpretation of the Microwave Emission*

In this section we will derive estimates of the magnetic field strength in the burst by comparing VLA brightness-temperature spectra with theoretical expectations from thermal and nonthermal distributions of electrons. A recent application of this technique was made by Gary & Hurford (1989) who used one-dimensional Owens Valley Radio Observatory interferometric observations to study the magnetic field structure of a simple solar microwave burst.

Our four-frequency observations are an improvement over some previous dual frequency studies (e.g., Shevgaonkar & Kundu 1985; Dulk et al. 1986) because they cover a wider range of wavelengths and therefore provide better constraints on radiation mechanisms and plasma parameters. A homogeneous source emitting thermal gyrosynchrotron radiation, for example, will have a constant brightness temperature, T_b, equal to the electron temperature, T_e, at frequencies $\nu \leq \nu_t$ where the emission is optically thick. At higher frequencies, corresponding to optically thin emission T_b will decrease rapidly with frequency as $\approx \nu^{-10}$ (see Dulk & Marsh 1982; Dulk 1985). The

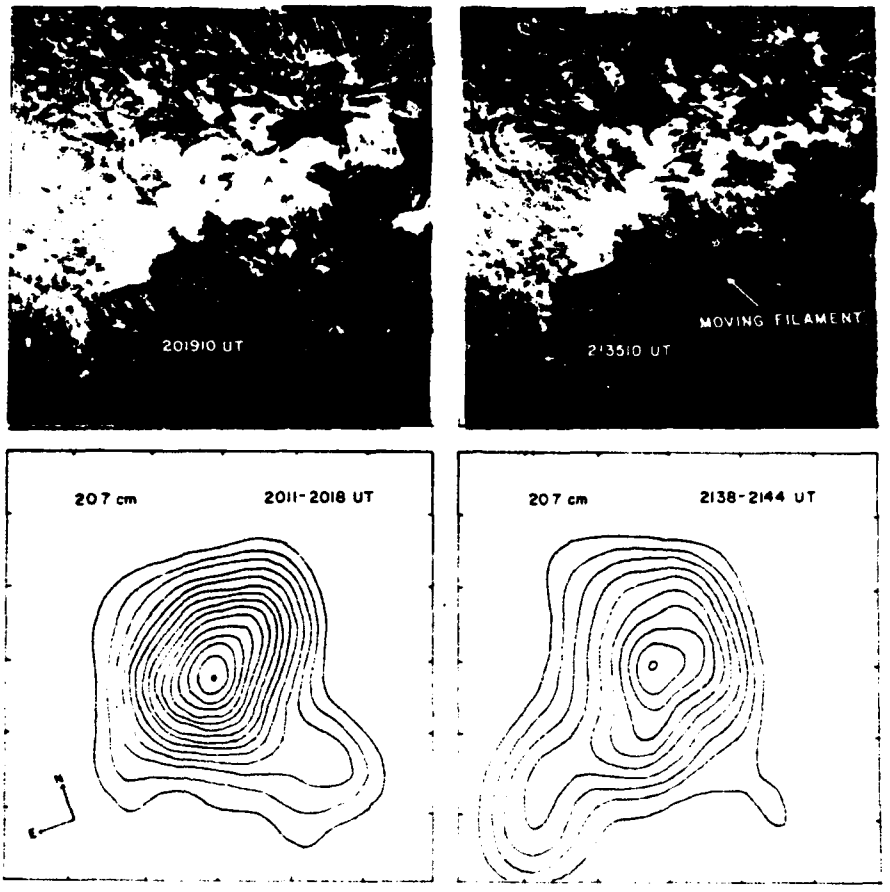

FIG. 9.—A comparison of SOON Hα images (*top*) and VLA 20.7 cm maps during the postimpulsive phase. Here the contours mark levels of equal brightness temperature with an outermost contour of 6.2×10^5 K and a contour interval of 3.1×10^5 K. The angular scale can be inferred from the 60" spacing between the fiducial marks on the axes. Note that the 20.7 cm emission has developed a distinct southeastward extension during the same time that the dark filament is seen to move outward.

turnover frequency depends critically on the magnetic field strength, B, the electron temperature, T_e, and the angle, θ, between B and the line of sight. For a nonthermal distribution of electrons, the brightness temperature will have a maximmum at a single frequency, ν_{peak}, whose value depends on B, δ, the energy spectral index, and the column density of nonthermal electrons, $N_{nt}L$. Here, N_{nt} is the number density of electrons with energy $E \geq E_0$, usually taken as 10 keV, and L is the path length through the source. The degree of circular polarization, ρ_c, for both thermal and nonthermal gyrosynchrotron emission also depends on these physical parameters. Given independent estimates of these quantities, the problem reduces to adjusting the magnetic field strength to give satisfactory agreement between the observed and modeled brightness-temperature spectra.

Figure 10 shows brightness-temperature spectra along three lines of sight through the source. Because the wavelengths were observed sequentially, we must assume that the brightness temperatures at the other wavelengths could be scaled by the variations in the total flux density, S_λ, as given by the RSTN data. That is, for any two times t_1 and t_2, $T_{b\lambda}(t_1) = T_{b\lambda}(t_2) * S_\lambda(t_1)/S_\lambda(t_2)$. This method is valid if the size of the emitting region does not change with time, as appears to be the case for the relatively simple sources at 2 and 6 cm and at 3.6 cm after 1918 UT.

As shown in Figure 10, the observed brightness temperatures at 6.1, and 20.7 cm are (1) comparable to the electron temperatures ($T_e = 6$–18×10^6 K) derived from the BCS Ca XIX and Fe XXV spectra and from the *GOES* data and (2) always higher or equal to those at 3.8 and 2.0 cm. This suggests that the emission is due to a thermal, rather than a nonthermal, gyrosynchrotron-emitting distribution of electrons.

To test this idea, we used the equations of Dulk (1985) to calculate theoretical brightness-temperature spectra from both thermal and nonthermal gyrosynchrotron emission for a range of B, T_e, δ, and θ. For both models, a source thickness of $L = 4.3 \times 10^9$ cm, corresponding to the approximate angular size ($\theta \approx 1'$) of the 6 cm emission, was assumed. The electron density was taken to be $N_e = (EM/L^3)^{0.5}$, where the emission measure was obtained from the BCS data. With EM ≈ 0.5–1.5×10^{49} cm^{-3}, and $L = 4.3 \times 10^9$ cm, $N_e \approx 0.8$–1.4×10^{10} cm^{-3}, a value consistent with those typically found in flaring loops. Included in our thermal model calculations is the contribution from thermal bremsstrahlung radiation, using the equation for optical depth given by Lang (1974). The *SMM* Hard X-Ray Burst Spectrometer data could, in principle, have been used to derive both δ and n_{nt} by fitting the observed photon energy distribution as a function of energy. However, because *SMM* was eclipsed by Earth until the very end of the impulsive phase, the data show no significant emission above the second energy channel ($E \geq 50$ keV) and standard fitting was not possible (B. R. Dennis, private communication). This suggests that

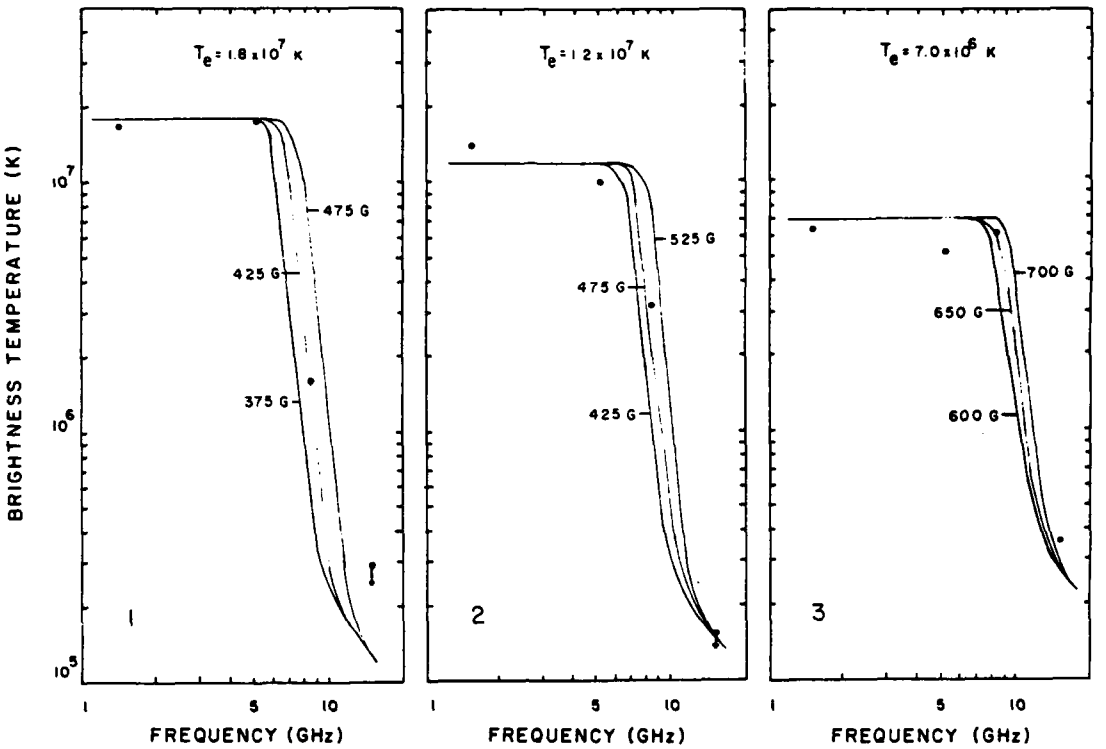

FIG. 10.—Brightness temperature spectra for three lines of sight through the microwave burst source. Spectra 1, 2, and 3 refer, respectively, to the peaks of the 6 cm source at 190838 UT, the 3.6 cm source A at 191138 UT, and the 3.6 cm peak B at 191738 UT. Theoretical spectra of the combined thermal gyrosynchrotron radiation and thermal bremsstrahlung emission for different values of magnetic field strength and electron density are also shown. These spectra were computed for an angle $\theta = 65°$ and electron densities of $N_e = 1.2 \times 10^{10}$ cm^{-3} (1 and 2) and 1.5×10^{10} cm^{-3} (3).

the hard X-ray emission was largely the high-energy tail of a low-temperature thermal distribution or, at least, that the number of nonthermal electrons in this event was low. From the relationship between photon and electron energy given by Lin & Hudson (1976), an upper limit of 10^{-2} photons cm^{-2} s^{-1} keV between 50 and 70 keV gives an upper limit to the total number of thick-target electrons with $E \geq 10$ keV equal $N_{nt} \leq 10^{34}$ and 1.5×10^{35}, respectively, for $\delta = 4.5$ and 6.0.

The results of our calculations indicate that the brightness temperatures and polarization can be fitted by a thermal spectrum with magnetic field strengths of 425–650 G, electron temperatures of $T_e = 7$–18×10^6 K, and observing angles of $\theta \approx 60°$. Spectrum 1, for example, could be well fitted with $H = 425$ G and $T_e = 18 \times 10^6$ K, values that are, respectively, somewhat lower and higher than along the direction of the 3.6 cm peak A (spectrum 2; $H = 475$ H, $T_e = 12 \times 10^6$ K). Spectrum 3, corresponding to the 3.6 cm peak at $\approx$1918 UT, shows that the brightness temperature at this wavelength ($T_b = 6.1 \times 10^6$ K) is approximately equal to that at 6 cm and 20.7 cm. A satisfactory fit to these data was found for an magnetic field strength of $H = 650$ G, except that the emission at 2 cm ($T_b = 0.36 \times 10^6$ K) was attributed not to thermal gyrosynchrotron emission, but to optically thin ($\tau \approx 0.04$) thermal bremsstrahlung radiation. The low degree of circular polarization of the 2 cm emission ($\rho_c \approx 25\%$) results from a propagation effect which increases the optical depth of the extraordinary mode of thermal bremsstrahlung over that of the ordinary mode in a magnetoactive plasma (Ratcliffe 1962).

These magnetic field strengths are in good agreement with those inferred from our potential field extrapolations. Field strengths of $H = 400$–500 G at heights of $h = 1$–1.5×10^9 cm are found above the smaller spots (see Fig. 3) that lie in the vicinity of the 2, 3.5, and 6.1 cm sources. Of course, it is difficult to make detailed comparisons between the different sets of values because of the unknown height of the radio emission. However, we are reasonably confident that the generation of strong non-potential fields was not required to explain the gyrosynchrotron radiation from this burst. To our knowledge, this is the first time that such comparisons of field strengths have been made for bursts observed with the VLA.

As shown by other recent multi-wavelength studies (Schmahl, Kundu, & Dennis 1985; Gary & Tang 1985; Dulk et al. 1986), nonthermal gyrosynchrotron radiation might also explain the brightness temperatures of solar microwave bursts. For example, with $\delta = 3.5$ and $N_{nt} L = 2.5 \times 10^{15}$ corresponding to a thickness of 1–4×10^8 cm ($\theta = 5''$) the predicted brightness temperatures at 6.1, 3.8, and 2.0 cm are 13×10^6, 1.8×10^6, and 0.18×10^6 K, in good agreement with those for spectrum A. However, the predicted brightness temperature at 20.7 cm is 6.8×10^8 K, about a factor of 40 higher than observed. A higher magnetic field strength of larger column density of nonthermal particles would increase T_b at all wavelengths. Absorption by a thermal gas with $T_e = 7 \times 10^6$ K, $N_e = 1.2 \times 10^{10}$ cm^{-3}, and $L = 5 \times 10^9$ cm would decrease the predicted brightness temperature by only a factor of 18 at 20.7 cm. For this reason, we believe that the microwave burst emission is probably better explained by thermal, rather than nonthermal, gyrosynchrotron emission.

We note that Gary & Hurford (1989) have also interpreted the microwave emission from a relatively simple burst in terms of a thermal model with a somewhat higher electron temperature and magnetic field strength derived here. For this

event they showed that the spectrum could be well fitted by a homogeneous, though expanding, thermal source with a peak electron temperature of $T_e = 7.1 \times 10^7$ K and a magnetic field strength of $B \approx 770$ G. Comparisons with *GOES* soft X-ray data also showed that the electron density increased by an order of magnitude during the burst, in contrast to smaller changes in N_e that we find for our event.

4.2. *Evolution of the Expanding X-Ray Arch, the Dark Filament, and the CME*

Recent work by Simnett & Harrison (1985) and Harrison et al. (1990) investigates the relative timing of flares and associated CMEs. Earlier models (Wu et al. 1983; Maxwell, Dryer, & McIntosh 1985) have assumed that flares preceded and drove mass ejections but those more recent revisionist models suggest quite the opposite: that the CME may precede and actually trigger the flare. We attempted to test this cause-and-effect relationship between the flare and the CME for the 1988 September 30 event; it is one of about a dozen events where both the C/P and the K-coronometer data were available (A.J. Hundhausen, private communication). With the combined data set, the development of the mass ejection can be tracked beginning at a much lower height in the corona. For these few events, a linear fit seems to be a very poor representation of the CME velocity at low altitudes; using this fit extrapolated to 1 $R_\odot$ would give an incorrect start time because (1) the CME may be accelerating (as in MacQueen 1985) at low altitudes; this effect would give an earlier start time; and (2) the CME structure may have already existed below the C/P field of view so the "front" would not start from 1 $R_\odot$ but from a higher altitude; this would give a later start time. As in Figure 1 a constant acceleration trajectory, rather than a constant speed trajectory, is a much better representation of the data for this event.

A. J. Hundhausen (private communication) finds, that, within the uncertainties of the measured quantities, the start of the flare and the initiation of the mass ejection are nearly coincident: the extrapolated CME start time is approximately 1857 UT with an error on the *fit* of ± 1 minute; this assumes that the event began at a height of 1 $R_\odot$. However, since the active region was at S26 E25, the CME was certainly "anchored" here at about 0.6 $R_\odot$, with the "front" at some unknown height between this position and 1 $R_\odot$. This could result in a start time which was, at most, 8 minutes earlier (assuming a constant acceleration) but was, more likely, a few minutes later. We conclude (1) that the CME start time was between 1848 and 1858 UT; (2) the start time recorded at the Holoman SOON site in Hα was 1857 UT; (3) the Palehua SOON site could record the start time as only *before* 1900 UT; (4) the Ramey SOON site recorded *before* 1910 UT; (5) the Sagamore Hill RSTN station recorded a burst beginning *before* 1904 UT; and (6) the *GOES* soft X-ray event began at 1859 UT; this is the time listed for both *GOES* 6 and 7 despite the fact that there seems to be a small rise in the X-ray level about 10–15 minutes before this (Fig. 1). This enhancement in the X-rays may be part of the event in question or, since *GOES* is a full disk monitor, an independent small event from another location which is related to the main flare only in time. No matter which possibility is correct, it seems impossible to determine which came first, the CME or the flare, and, based on the data available, we must agree with A. J. Hundhausen that these events are nearly coincident.

We suggest, on the other hand, a slightly different scenario in the form of a "cartoon" which is put together in part from Hundhausen (1987) and Zirin (1988) which (with some modifications) describes both the relative timing and morphology of 1988 September 30 event: As the magnetic field loops attempt to redistribute themselves to a more relaxed configuration, the global disturbance both triggers the flare and opens the field lines. The filament cavity along the neutral line, which is normally buoyant but is held down by the magnetic pressure of the loops on top of it, begins to rise, plowing through coronal material which builds up ahead of the cavity. This configuration (1) the built-up material, (2) the cavity, and (3) the filament or prominence becomes the "three-part" structure of a typical" CME: (1) a bright outer loop surrounding (2) a dark cavity with (3) bright material at the center. After the CME is ejected, the open field lines begin to reconnect. In the "typical" two-ribbon flare scenario, this reconnection first heats the low-lying loop arcades, injecting energy into each flux tube; this energy reaches the loop footpoints and is revealed in Hα images as two (ideally) parallel bright ribbons. As reconnection continues, higher loops are heated; these loops would (again ideally) have footpoints further from the neutral line, and the bright parallel ribbons in the Hα image would appear to move apart.

There is some evidence of the global magnetic disturbance before the 1988 September 30 event: There appears to be a precursor in the *GOES* light curve (Fig. 1), peaking at about 1740 UT, as well as an event at 245 MHz in the RSTN data, peaking about an hour later. The *GOES* event was untagged (according the Solar Geophysical Data) and it was not observed by FCS or BCS which were tracking the region (if the event had been from AR 5171, FCS and BCS would have detected it easily). Also, the VLA saw no preflare heating during the 245 MHz event. This enhanced emission may be the result of a change in the large-scale structure of the global magnetic field or from a footpoint hidden behind the limb (Harrison 1986). We favor the first possibility since it is likely that the entire loop structure was large enough to be outside the BCS field of view but not large enough to extend behind the limb since the region was only 25° from central meridian. Either scenario, however, would be consistent with Harrison (1986).

Although many CMEs show a distinct and striking three-part structure, this is not always the case. In fact, only about half of the CMEs observed by C/P show this "classic" structure (Hundhausen 1987). In the photographs of the 1988 September 30 CME, only the fuzzy faint outer loop and trailing dark cavity can be seen, so the structure is not "typical" and therefore differs from the cartoon above. As the field lines opened up, the buoyant cavity began to rise and collect material in front of it but the active region filament does not seem to have escaped: The filament as well as the X-ray arch, are still at the site of the M2 flare (Fig. 6) at this time. It is not until over an hour later, when the CME is well beyond the C/P field of view, that the filament begins to move (Figs. 7 and 8). Because this active region was well on the disk, the proper motion of both the filament and the loops is well measured. They are moving together, toward the limb in the direction of the CME, with an initial speed (in the plane of the sky) of about 10 km s^{-1}. Then the filament/loop system decelerates and virtually stops at approximately 2230 UT. If we assume a simple loop geometry and that these loops expand radially away from the surface, the total velocity of about 25 km s^{-1} is not high enough to escape the Sun's gravitational field. Quite the

opposite is true for the CME: assuming the same simple loop geometry and radial expansion, the total initial velocity is about 900 km s^{-1}, well above the escape velocity of the photosphere.

It seems, however, that the X-ray loops may not actually be moving but that the FCS images show a successive brightening of a set of loops at different altitudes as in the above, "ideal," two-ribbon flare scenario. Each X-ray image shows its brightest point at the peak of the the loop system. This brightening is evidence of reconnection at higher altitudes. (Unfortunately, there is not a good estimate of the temperature at this point since the FCS was able to image only in Fe XVII.) The report from the Holoman observatory SOON site actually described the event and a "parallel ribbon" flare. It seems, therefore, that the cartoon outlined above is a reasonable, generic description of the 1988 September 30 event; it is not perfect since no filament was observed as part of the CME but then, many events are probably only slightly different from the "typical" event described by this cartoon.

5. CONCLUSIONS

The M2 flare of 1988 September 30 during International Solar Month was well observed by *SMM*, the the VLA, and other ground-based instruments. The primary energy release at the short microwave wavelengths took place in a set of compact loops located near the sites of the brightest Hα and soft X-ray emission. There was no evidence for preburst heating of the coronal plasma on timescales of a few tens of minutes before the burst. Microwave spectra, together with estimates of electron temperature and emission measure derived from BCS data, suggest that the microwave emission can be attributed to thermal gyrosynchrotron radiation in regions of magnetic field strength $H = 425$–650 G. The inferred values of H are in reasonable accord with those obtained from coronal magnetic field extrapolations. Although the associated CME was rather unspectacular, the width, speed, and (in conjunction with Mauna Loa coronameter observations) acceleration of this event could be measured. This is one of the few mass ejections for which an unambiguous initiation time is obtained. Although only a single event, the resulting near-coincidence of the CME and the flare initiation times must seriously question earlier models of CME dynamics where the flare provides the "driver" for the mass ejection. Taken in conjunction with other multi-wave band data, we believe the event to be rather interesting. We propose that this event seems to be well described by a "cartoon" where a global magnetic disturbance opens the field lines allowing the filament cavity to rise and plow through coronal material. This configuration becomes the bright outer loop surrounding the dark cavity which is observed by the K-coronameter and C/P. After the CME is ejected, the open field lines begin to reconnect. The low-lying loop arcades heat first and the deposited energy travels down to the photosphere and appears as bright Hα parallel ribbons. As reconnection continues, higher and higher loops are heated until the system is stable again, a process which took several hours.

Radio astronomical studies of the Sun at Tufts University are supported under grant AFOSR-89-0147 with the Air Force Office of Scientific Research. Simultaneous Very Large Array and *Solar Maximum Mission* observations of the Sun are supported by NASA grant NAGW-2383. J. T. S. and K. L. S. acknowledge support by NASA contracts NAS5-30431 and NAS5-28713 and the Lockheed Independent Research Program. J. T. S. thanks O. C. St. Cyr and A. J. Hundhausen for helpful discussions on CMEs and J. L. R. Saba for reading this manuscript. We also thank the referee for suggesting improvements to our paper. NRAO is operated by Associated Universities, Inc., under contract with the National Science Foundation. The XRP data used in this work were available only because of the repair of the *SMM* spacecraft by the crew of the Challenger on mission 41-C. The pilot for that mission, and the commander of Challenger's last flight, was Francis R. Scobee. This work is dedicated to his memory.

REFERENCES

Acton, L. W., et al. 1980, Solar Phys., 65, 53
Bely-Dubau, F., Dubau, J., Faucher, P., & Gabriel, A. H. 1982, MNRAS, 198, 239
de Jager, C., & Svestka, Z. 1985, Solar Phys., 100, 435
Dulk, G. A. 1985, ARA&A, 23, 169
Dulk, G. A., Bastian, T. S., & Kane, S. R. 1986, ApJ, 300, 438
Dulk, G. A., & Marsh, K. A. 1982, ApJ, 259, 350
Gabriel, A. H. 1972, MNRAS, 162, 99
Gary, D. E., & Hurford, G. J. 1989, ApJ, 399, 1115
Gary, D. E., & Tang, F. 1985, ApJ, 288, 385
Harrison, R. A. 1986, A&A, 162, 283
Harrison, R. A., Hildner, E., Hundhausen, A. J., Sime, D. G., & Simnett, G. M. 1990 J. Geophys. Res., 95, A2, 917
Heyvaerts, J., Priest, E. R., & Rust, D. M. 1977, ApJ, 216, 123
Hundhausen, A. 1987, Proc. 6th Internat. Solar Wind Conference, 1, 181
Kahler, S. 1987, Rev. Geophys., 25, 663
Kundu, M. R., & Lang, K. R. 1985, Science, 228, 9
Kundu, M. R., Schmahl, E. J., & Fu, Q.-J. 1989, ApJ, 336, 1078
Kundu, M. R., Schmahl, E. J., Velusamy, T., & Vlahos, L. 1982, A&A, 108, 188
Kundu, M. R., Velusamy, T., & White, S. M. 1987, ApJ, 321, 593
Lang, K. R. 1974, Astrophysical Formulae (New York: Springer)
Lang, K. R., & Willson, R. F. 1983, Adv. Space Res., Proc. the 24th Plenary Meeting of COSPAR (Committee on Space Research), vol. 2, No. 11, 91
———. 1989, ApJ, 344, L73
Lang, K. R., Willson, R. F., & Gaizauskas, V. 1983, ApJ, 267, 455
Lang, K. R., Willson, R. F., Smith, K. L., & Strong, K. T. 1987a, ApJ, 322, 1035
———. 1987b, ApJ, 322, 1044
Lin, R. P., & Hudson, H. S. 1976, Solar Phys., 50, 153
MacQueen, R. M. 1985, Solar Phys., 95, 359
MacQueen, R. M., et al. 1980, Solar Phys., 65, 91
Marsh, K. A., & Hurford, G. 1980, ApJ, 240, L11
Maxwell, A., Dryer, M., & McIntosh, P. 1985, Solar Phys., 97, 401
Melozzi, M., Kundu, M. R., & Shevgaonkar, R. K. 1985, Solar Phys., 97, 345
Pallavicini, R., Serio, S., & Vaiana, G. S. 1977, ApJ, 216, 108
Priest, E. R., et al. 1986, Energetic Phenomena on the Sun (NASA CP-2439), ed. M. R. Kundu and B. Woodgate, chap. 1
Ratcliffe, J. A. 1962, The Magneto-ionic Theory (Cambridge: Cambridge Univ. Press)
Sakurai, T. 1981, Solar Phys., 76, 301
Schmahl, E. J., Kundu, M. R., & Dennis, B. R. 1985, ApJ, 299, 1017
Schmahl, E. J., Schmelz, J. T., Saba, J. L. R., Strong, K. T., & Kundu, M. R. 1990, ApJ, 358, 654
Shevgaonkar, R. K., & Kundu, M. R. 1985, ApJ, 292, 733
Shevgaonkar, R. K., Kundu, M. R., & Jackson, P. D. 1989, Solar Phys., 71, 311
Simnett, G. M., & Harrison, R. A. 1984, Adv. Space Res., 4, 279
Svestka, A. 1984, Solar Phys., 94, 171
Svestka, Z., et al. 1982, Solar Phys., 75, 305
Velusamy, T., & Kundu, M. R. 1981, ApJ, 243, L103
Velusamy, T., Kundu, M. R., Schmahl, E. J., & McCabe, M. 1987, ApJ, 319, 984
Willson, R. F. 1984, Solar Phys., 92, 189
Willson, R. F., Klein, K.-L., Kerdraon, A., Lang, K. R., & Trottet, G. 1990, ApJ, 357, 662
Willson, R. F., Lang, K. R., & Liggett, M. 1990b, ApJ, 350, 856
Wu, S. T., Wang, S., Dryer, M., Poland, A. I., Wolfson, C. J., Orwig, L. E., & Maxwell, A. 1983, Solar Phys., 85, 351
Zirin, H. 1988, Astrophysics of the Sun (Cambridge: Cambridge Univ. Press)

Note added in proof.—In a recent paper, D. Smith, E. Hildner, and P. Kuin (*Solar Phys.*, submitted [1991]) relate the Martens-Kuin filament eruption model to observations of CMEs. The current directions were reversed, resulting in mass ejection velocities and properties consistent with observations. The filament motion, however, is delayed, consistent with observations presented here.

D7. VLA SUPPORTING OBSERVATIONS FOR SOLAR-A

Kenneth R. Lang
Dept. of Physics & Astronomy, Robinson Hall
Tufts University, Medford, MA 02155, USA

ABSTRACT

High-resolution VLA maps at 20-cm wavelength can be used to resolve coronal loops within individual active regions and thereby reveal the coronal magnetic interaction that can trigger solar flares. These VLA maps can complement simultaneous SXT SOLAR-A observations. Simultaneous VLA and SOLAR-A observations can extend and amplify VLA results that resolve the preflare, impulsive and post-flare components of solar flares into nearby, but spatially-separated, sources. If this result is confirmed and found to be generally applicable, it will rule out previous theoretical work that confines all of these aspects of flare activity to a single coronal loop. VLA synthesis maps at 91.6-cm wavelength indicate that widely-separated active regions are apparently linked by large-scale, transequatorial magnetic loops 100 thousand to a million kilometers (2 to 20 arcminutes) long. Three-second VLA snapshot maps at this wavelength suggest that energetic electrons, accelerated during a flare in one active region, can move within these global magnetic conduits at nearly the velocity of light, thereby triggering bursts along the large-scale loops or in distant active regions. The SXT telescope aboard SOLAR-A should routinely observe the entire Sun to sample these global magnetic structures. SXT or HXT SOLAR-A observations with a limited field of view within individual active regions should be compared with simultaneous, full-disk VLA observations that can connect the localized satellite results with related activity in distant regions.

QUIESCENT EMISSION FROM CORONAL LOOPS WITHIN INDIVIDUAL ACTIVE REGIONS

Ground-based observations with the Very Large Array (VLA) at 21-cm wavelength detect the hot coronal plasma previously detected by space-bourne X-ray telescopes (Lang, 1990). The radio brightness temperatures are often lower than that expected from X-ray measurements of the electron temperature and density, suggesting that there is a cool sheath enveloping the hotter million-degree plasma that is constrained within magnetic loops joining sunspots within an active region.

A million-degree plasma is also detected at 21-cm wavelength near or above sunspots, but it is below the detection threshold at soft X-ray wavelengths. Thermal gyroresonance radiation is used to describe the radio emission above sunspots; magnetic field strengths can also be inferred from the radio data when its spectrum is known.

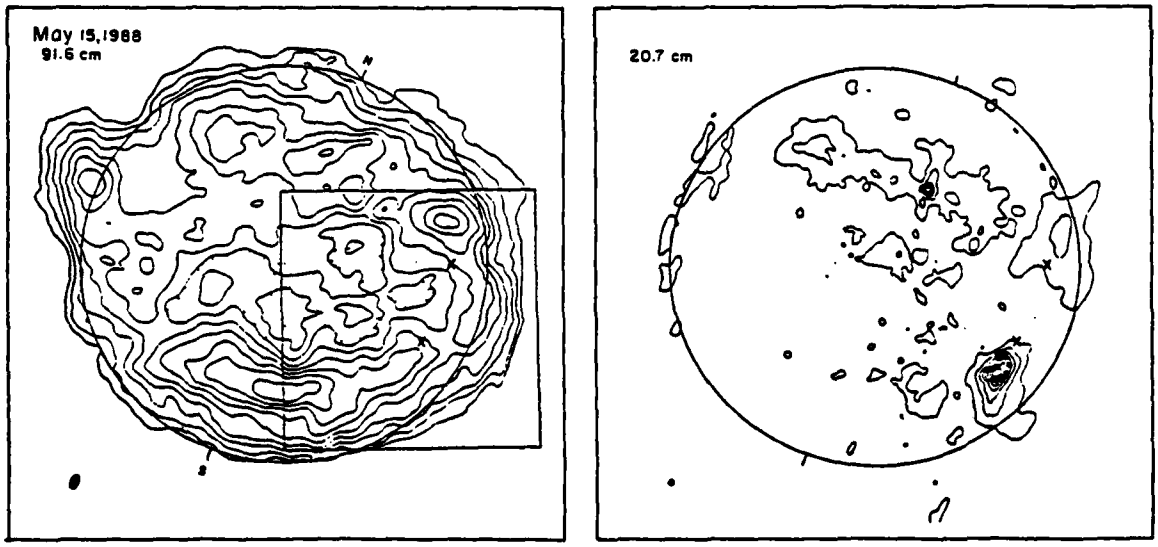

Figure 1. VLA maps of quiescent solar radio emission. The 21-cm contours delineate active-region coronal loops with a peak brightness temperature of 2.5 million degrees, while the 91-cm contours show more elongated structures that have a peak brightness temperature of 780,000 degreees.

Although 21-cm VLA observations of the quiet Sun reveal the ubiquitous coronal loops anchored within solar active regions (Fig. 1 right), the 91-cm VLA maps delineate quiescent emission from more extensive structures that are either associated with filaments and/or interconnect solar active regions (Fig. 1 left). Some of the 91-cm features have been interpreted in terms of a hot 100,000 degree transition sheath that envelopes the cooler filaments and acts as an interface with the hotter surrounding corona (Lang and Willson, 1990a).

SPATIAL LOCATION OF PRE-FLARE, IMPULSIVE AND POST-FLARE EMISSION

The increased intensity of the 21-cm emission before and during flares permits high-resolution VLA maps at time intervals of three seconds. These maps have shown that coronal magnetic interaction can trigger flares. Simultaneous SOLAR-A SXT and VLA observations can be compared with vector magnetographs to establish the relative importance of coronal and photospheric magnetic fields in the release of magnetic energy during solar flares.

The classical time profile for the radio emission of solar flares consists of a low-level, pre-flare component, a rapid, powerful impulsive component, and a more gradual post-flare, or decay, component (Fig. 2). The VLA has now been used at 21-cm wavelength to map these flaring components at three-second time intervals, showing that they originate in nearby, but spatially separated, sources (See Fig. 3 , Willson, Lang and Liggett, 1990, and Willson et al., 1990).

Simultaneous VLA and SOLAR-A observations can extend and amplify this result; if it is confirmed and found to be usually applicable, it will rule out extensive previous theoretical work that confines all aspects of flare activity to a single coronal loop or arcade of loops.

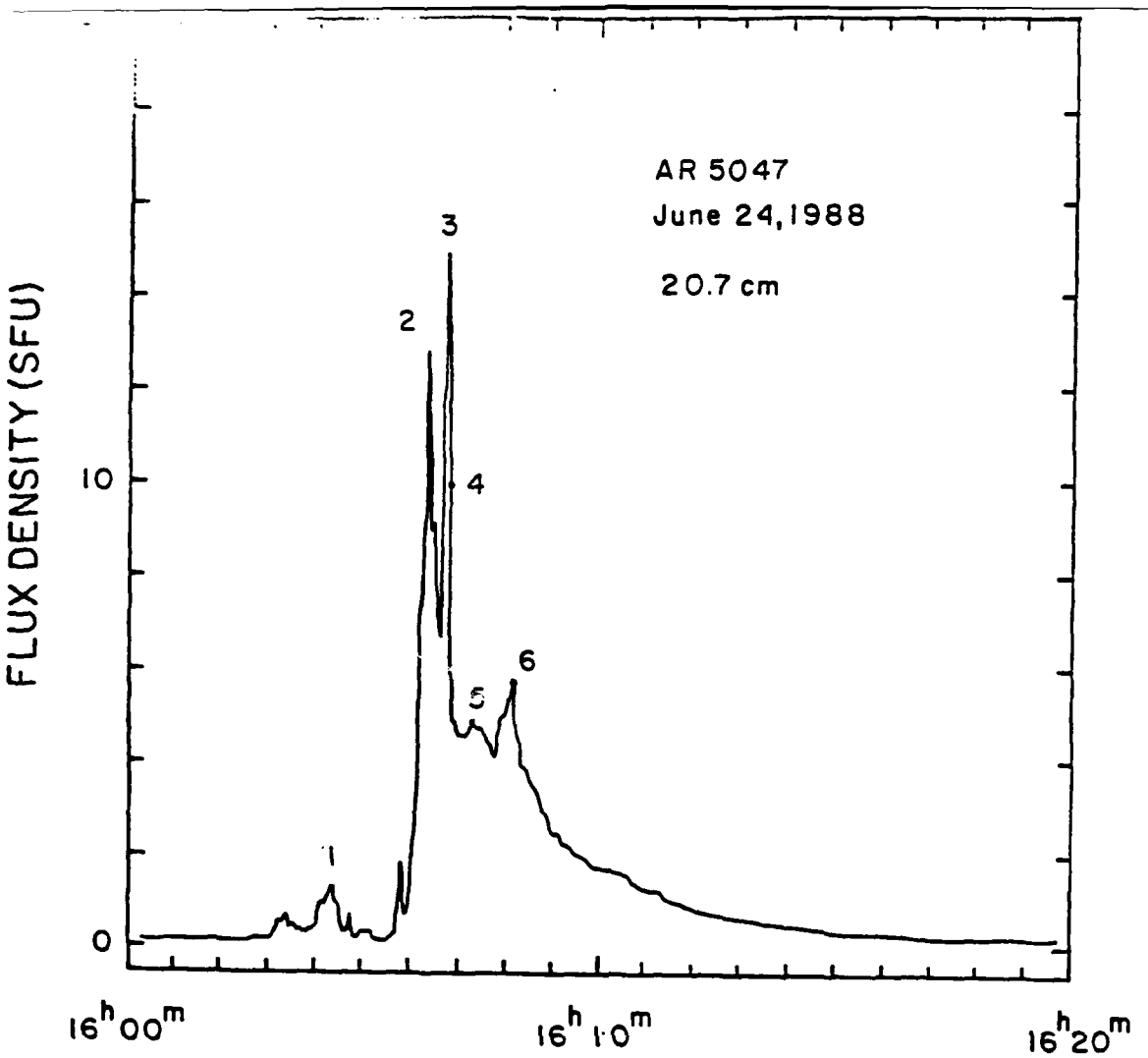

Figure 2. The time profile of a 21-cm burst showing the pre-flare (1), impulsive (2,3), and post-flare (4, 5, 6) components. See Fig. 3 for VLA maps of these components.

GLOBAL CORONAL STRUCTURES AND ACTIVITY

The existence of magnetic loops interconnecting separate active regions on opposite sides of the solar equator was first shown in soft X-ray images obtained during the Skylab mission (Svestka et al., 1977). Such transequatorial loops can now be detected from the ground using the VLA at the longer 91-cm wavelength (Fig. 4).

Three-second VLA maps at 91-cm wavelength have also revealed time-correlated radio bursts in active regions on opposite sides of the solar equator (Fig. 5, Lang and Willson,

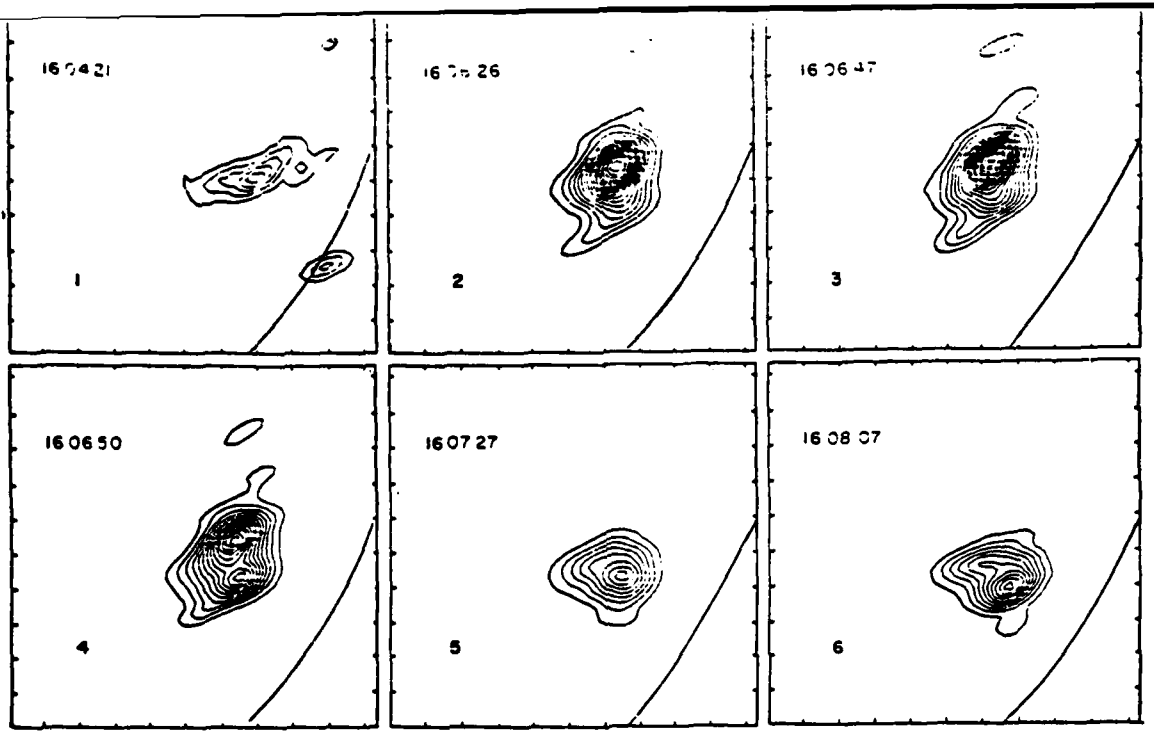

Figure 3. VLA snapshot maps of the total intensity at 21-cm wavelength during 3.3-second intervals at the times denoted by 1 to 6 in Fig. 2. The pre-flare component (1) is spatially separated from the subsequent impulsive bursts (2 and 3), which are in turn spatially separated from the nearby post-flare component (4, 5, 6). There is 60 arcsecond spacing between the fiducial marks on the axes.

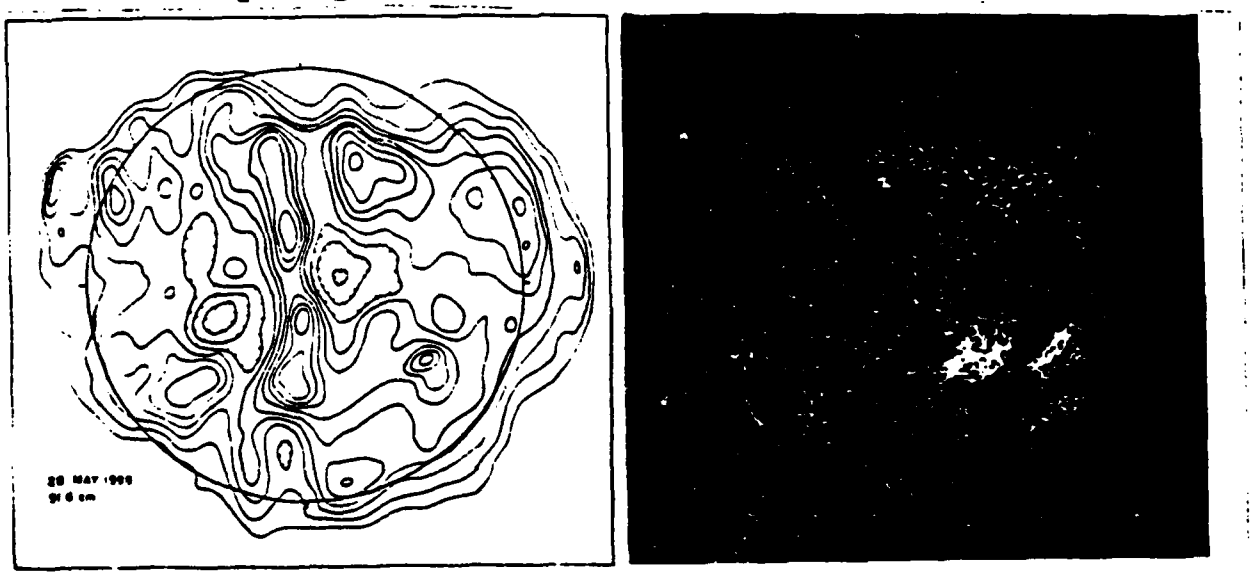

Figure 4. A VLA 91-cm map (left) is compared with a Kitt Peak magnetogram (right) on the same day. A transequatorial loop apparently joins two active regions.

1990b). These regions are apparently linked by large-scale, otherwise-invisible magnetic loops that are at least 260,000 km in length, or 6 arcminutes in angular extent. Energetic electrons accelerated during a radio burst in one active region probably move along this magnetic conduit at a velocity of about one-third of the velocity of light, thereby triggering a burst in the other active region.

Other 91-cm VLA observations show that flares can be triggered along the large-scale loops that connect widely-separated active regions, and not just at the loop footpoints.

The SXT telescope aboard SOLAR-A should routinely observe the entire Sun to sample these global magnetic structures. SXT or HXT SOLAR-A observations with limited field of view within individual active regions should be compared with simultaneous, global VLA snapshot maps.

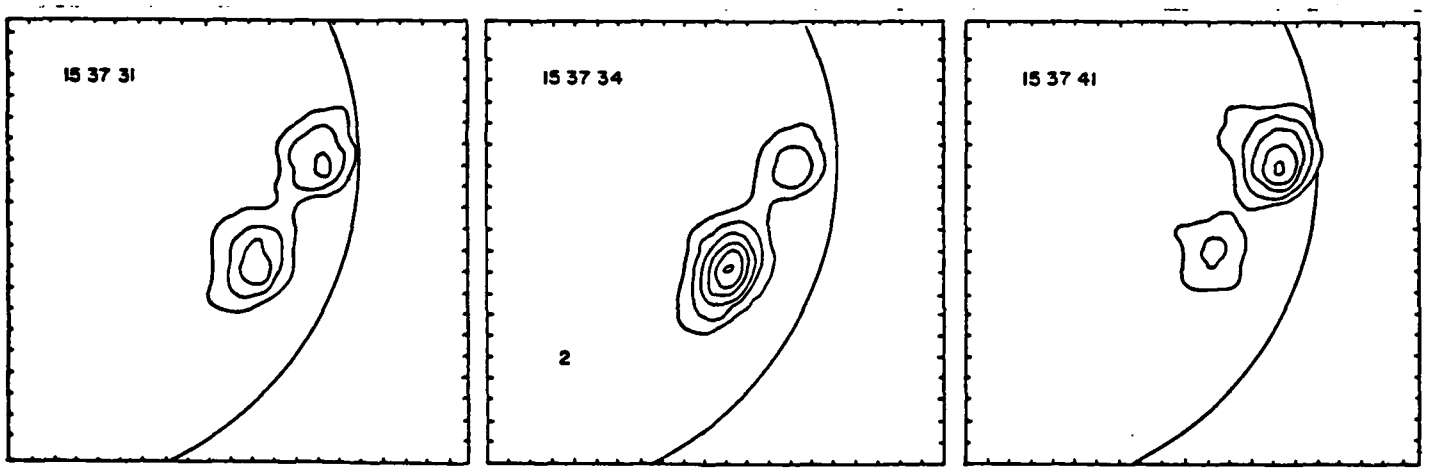

Figure 5. VLA snapshot maps (3.3 sec) at 91-cm for different times noted in each frame. The angular scale can be inferred from the 1 arcminute spacing between the fiducial marks on the axes; the two burst locations on opposite sides of the solar equator are also shown by two X marks in Fig. 1 (left). The contours mark intervals of equal brightness temperature with an outermost contour and contour interval of a million degrees Kelvin

Such VLA observations can connect the localized satellite observatiolns with related activity in distant active regions that are outside the satellite's field of view.

ACKNOWLEDGMENTS

Radio astronomical studies of the Sun at Tufts University are supported under grant AFOSR-89-0147 with the Air Force Office of Scientific Research. Related comparisons of VLA and SMM data are supported by NASA grant NAG 5-501. This paper was presented when the author was on leave from Tufts University and serving as a JPL Visiting Senior Scientist (VSS) assigned to the Space Physics Division at NASA Headquarters; he gratefully acknowledges travel support from the VSS Program.

REFERENCES

Lang, K.R., "VLA Observations of the Coronal Plasma," In *Basic Plasma Processes on the Sun, Proceedings of IAU Symposium No. 142* (eds. E.R. Priest and V. Krishan), Boston: Kluwer, 1990.

Lang, K.R. and Willson, R.F., *Astrophysical Journal (Letters)* **344**, L73-L75 (1990a).

Lang, K.R. and Willson, R.F., *Astrophysical Journal (Letters)* **344**, L77-L80 (1990b).

Svestka, Z., Krieger, A.S., Chase, R.C., and Howard, R., *Solar Physics* **52**, 69-90 (1977).

Willson, R.F., Lang, K.R., and Liggett, M., *Astrophysical Journal* **350**, 856-867 (1990).

Willson, R.F., Klein, K.-L., Kerdraon, A., Lang, K.R., and Trottet, G., *Astrophysical Journal* **357**, 662-671 (1990).

D8.

CoMStOC IV: Multiwaveband Observations of Sunspot and Plage-Associated Coronal Emission

Jeffrey W. Brosius
Laboratory for Astronomy and Solar Physics, NASA/GSFC
and
ST Systems Corporation

Robert F. Willson
Tufts University

Gordon D. Holman
Laboratory for Astronomy and Solar Physics, NASA/GSFC

Joan T. Schmelz
Applied Research Corporation and Lockheed

To appear in *The Astrophysical Journal*, February 1992

Abstract

Simultaneous observations of an active region located near central meridian were obtained with the Very Large Array, the Solar Maximum Mission X-Ray Polychromator, and the Beijing Observatory magnetograph on 18 December 1987, during the Coronal Magnetic Structures Observing Campaign (CoMStOC). An asymmetric loop-like structure connects the strong leading sunspot with a nearby region of opposite polarity. Both 6 and 20 cm emission lie along this structure, rather than over the sunspot, with higher frequency emission originating closer to the footpoint inside the sunspot. The 20 cm emission is due to a superposition of 2nd and 3rd harmonic gyroemission, where the field strength is 160 G – 300 G, while the 6 cm emission is due to 3rd harmonic gyroemission from a region where the magnetic field strength ranges from 547 G – 583 G. A high value of the Alfven speed, $\sim$ 40,000 km/sec, is obtained at the location of the 6 cm source, with somewhat lower values, $\sim$ 10,000 – 20,000 km/sec, at the location of the 20 cm emission. At the location of the 6 cm source, the plasma temperature diminishes with height from 2.5×10^6 K at $\sim$ 5000 km to 1.3×10^6 K at $\sim$ 15,000 km.

The X-ray data associated with an area of trailing plage were used to predict the brightness temperature structure due to thermal bremsstrahlung emission in the 6 and 20 cm wavebands. The predicted 6 cm brightness temperature in and around the location of the X-ray peak is low, consistent with our lack of observed 6 cm plage emission. The predicted 20 cm brightness temperature is consistent with that observed in the central portions of the plage, but the high 20 cm polarization requires the presence of cool ($T_e \leq 5 \times 10^5$ K), absorbing plasma overlying the hot plasma observed in X-rays. Two different models for interpreting these observations are described.

1 Introduction

Observations of coronal loops taken with the Very Large Array (VLA) show that emission at different wavelengths originates at different heights, with longer wavelengths corresponding to higher levels. Synthesis maps at 20 cm wavelength, for example, outline loop-like structures that stretch across regions of opposite magnetic polarity (Lang, Willson, and Rayrole 1982) while observations at shorter wavelengths (2 and 6 cm) generally indicate sources that lie along the legs of loops (Alissandrakis and Kundu 1982; Lang and Willson 1982; Lang, Willson and Gaizauskas 1983; Strong, Alissandrakis and Kundu 1984). The 20 cm loops are similar to their X-ray counterparts, for the loops detected have similar sizes, shapes, and brightness temperatures.

Although the X-ray emission is attributed to thermal bremsstrahlung and atomic line emission from hot ($T_e \sim 3 \times 10^6$ K) coronal plasma, the microwave emission may be due to either thermal bremsstrahlung or to gyroresonance emission from thermal electrons spiralling along coronal magnetic field lines. In order to determine which of these mechanisms is dominant, it is necessary to know the electron temperature and emission measure of the plasma so that the brightness temperature at a particular wavelength can be calculated and compared with the observed values. Observations of soft X-ray spectral lines obtained by the X-ray Polychromator (XRP) aboard the Solar Maximum Mission (SMM) satellite, for example, can yield estimates of the electron temperature, emission measure, and density in quiescent loops. These parameters have been combined with plausible estimates for the magnetic scale height and the harmonic to show that the microwave-emitting plasma can be optically thick to either thermal bremsstrahlung or gyroresonance emission at 20 cm wavelength (Lang, Willson, and Rayrole 1982; McConnell and Kundu 1983; Shevgaonkar and Kundu 1984; Gary and Hurford 1987).

Direct comparison of 6 cm and soft X-ray emission has confirmed the importance of gyroresonance emission at this wavelength. However, the brightest 6 cm sources are usually not associated with the brightest X-ray sources and the detailed correspondence between the radiation at these two wavelengths is poor (Schmahl et al. 1982; Webb et al. 1983). The reason for this is that 6 cm gyroresonance emission typically occurs in the strong magnetic fields above sunspots, while the X-ray emission is usually most intense between regions of opposite magnetic polarity. Thermal bremsstrahlung at 6 cm is often too optically thin to be detected.

More recent comparisons between simultaneous 20 cm and XRP images have shown better agreement between the emission at these wavelengths, although there are significant differences (Webb et al. 1987; Lang et al. 1987a,b; Nitta et al. 1991 – CoMStOC I). The 20 cm maps suggest the presence of both cool and hot plasmas in different regions that are not detected in X-rays, and there is X-ray emitting plasma that remains invisible at 20 cm. Although thermal bremsstrahlung could explain the bulk of the 20 cm emission, the detection of a line-like enhancement in the brightness spectrum at the apex of one coronal loop suggests the dominance of gyroresonance emission in that part of the loop (Willson 1985).

In this paper we describe the results of simultaneous VLA and XRP observations of a solar active region obtained during the Coronal Magnetic Structures Observing Campaign (CoMStOC). The primary objective of CoMStOC was to obtain quantitative information about the plasma and magnetic field structure above solar active regions by comparing the microwave and soft X-ray data with theoretical models (Holman and Kundu 1985, Brosius and Holman 1988, 1989) and

photospheric magnetic field measurements. In Section 2 we present and discuss the coordinated observations: VLA observations at four different frequencies in each of the 6 and 20 cm wavebands, XRP spectral and image data, and a photospheric longitudinal magnetogram from Beijing Observatory. In Section 3 we analyze and interpret the VLA, XRP, and magnetograph data in terms of physical models. In Section 4 we summarize our conclusions and their implications.

2 Observations and Data Analysis

2.1 VLA Observations

The VLA (B configuration) was used to observe the active region AR 4906 (S34.5, E17.7 at 1300 UT) between 1440 UT and 2300 UT on 18 December 1987. The entire array of 27 antennas was used at four frequencies in the 20 cm band (1375, 1420, 1550, and 1665 MHz) and four in the 6 cm band (4600, 4700, 4800, and 4900 MHz) with bandwidths of 12.5 MHz. The half-power beamwidth of the individual antennas ranged between 29′ and 34′.7 at 20 cm, with synthesized beamwidths of 4″. At 6 cm, the primary beamwidths ranged from 9′.7 to 10′.4, with synthesized beamwidths of 1″. One pair of frequencies was observed for about 5 minutes, so that all eight could be observed in about twenty minutes. The data were sampled every 10 s and calibrated using observations of PKS1655+078. Corrections were made for the difference in the signals from high temperature noise diodes located on four of the antennas. The temperatures of these sources were measured across each band prior to the observations. The data were edited and calibrated with the standard solar procedures at the VLA, and used to make synthesis maps of both the total intensity, I, and Stokes parameter, V, during the 8.5 hour interval at all eight frequencies. Examination of the fringe visibility on several baselines indicated no variations that could be attributed to solar bursts or interference.

Figure 1a shows the frequency-averaged 20 cm map with two main components: the source on the right is associated with the sunspot and the one on the left, which is $\sim$ 50% left-hand circularly polarized, is associated with the plage. Individual maps at the four 20 cm frequencies (Fig. 2) show that there is a systematic difference in the structure of the 20 cm emission at these frequencies. The sharply defined peak of the sunspot source systematically shifts by $\sim$ 10″ in the direction of the 6 cm source (Fig. 1b) from 1375 MHz to 1665 MHz. This is a manifestation of gyroresonance as the dominant emission mechanism: as the observing frequency changes, the magnetic field strength required to stimulate gyroresonance emission also changes; the appropriate field strength is at a slightly different location, resulting in a shift of the radio source with observing frequency.

In the B-configuration VLA, the maximum fringe spacing is $\sim$ 225″ at 20 cm and 66″ at 6 cm. No information is available concerning sources larger than these critical limits, so possible extended, low brightness temperature structures will be resolved out (see CoMStOC I for a more detailed discussion). The 6 and 20 cm sources seen in Figure 1a,b are smaller than their respective critical sizes, suggesting that no emission from the sources seen in these maps was resolved out. Furthermore, no significant changes in structure or brightness temperature ($<$ 15%) were found between the maps produced using the standard CLEAN algorithms and those produced using the Maximum Entropy Method (MEM) (Cornwell 1986, Bastian 1987). The MEM algorithm is better able to restore large-scale structure (as long as it is smaller than the maximum fringe spacing)

than is CLEAN. Thus the similarity of the MEM and the CLEAN maps indicates that there is no evidence for unresolved large-scale structure in either the 6 or 20 cm maps. Neither CLEAN nor MEM, of course, is capable of restoring the quiet sun background contribution, which is $\sim 4 \times 10^4$ K at 6 cm and $\sim 1 \times 10^5$ K at 20 cm.

2.2 XRP Observations

The XRP Flat Crystal Spectrometer (Acton et al. 1980), collimated to 14″ FWHM, could build images by rastering over a portion of a 4′ × 4′ area with a minimum pixel spacing of 5″, or scan a series of spectral lines at one or more spatial locations. XRP mapped AR 4906 in the Fe XVII resonance line at 15.01 Å, the most sensitive line at active region temperatures. This map (Fig. 1c) shows two peaks of emission: the weaker source on the right lies between the sunspot and a nearby region of opposite polarity; the stronger source on the left is associated with the trailing area of plage (see Fig. 1d).

A spectroscopic scan (between 13 and 19 Å) was done at the brightest Fe XVII pixel (marked with an "X" in Fig. 1) in the SMM orbit beginning at 0343 UT on 1987 December 18. Analysis of these spectral data follows the procedure outlined in CoMStOC I. The emissivity calculations from Mewe, Gronenschild, and van den Oord (1985) and the coronal abundances of Meyer (1985) were used to calculate the electron temperatures from five selected line flux ratios. Each of these ratios varies by a factor of 10 or more in the temperature range of interest (2-4 $\times 10^6$ K); this steep gradient makes the ratio sensitive to small changes in temperature and relatively insensitive to systematic uncertainties such as relative flux calibrations, elemental abundance variations, or errors in the atomic parameters. (See CoMStOC I for a detailed discussion of these calculations and possible sources of error.) These values and their uncertainties (statistical only) are listed in Table 1. The uncertainties in the weighted mean include systematic as well as statistical uncertainties. The column emission measure corresponding to each temperature in Table 1 was computed using the O VIII line flux, which has an emissivity curve with a broad, flat response in the range of interest; therefore, the emission measure determined using this line is relatively insensitive to possible errors in temperature. Once again, the uncertainties on the individual entries are statistical only (dominated by the uncertainty in the O VIII line flux) while the weighted mean includes systematic as well as statistical uncertainties.

XRP mapped AR 4906 at the peaks of five bright resonance lines—O VIII, Ne IX, Fe XVII, Mg XI, and Fe XVIII—in the SMM orbit beginning at 1134 UT on 1987 December 18. Ratios of these images can be used to determine the spatial structure of the plasma parameters across the region (as was done in CoMStOC I). Unfortunately, AR 4906 was relatively weak and, although Fe XVII was observed throughout the region, significant counts were observed in only one other line, O VIII, near the brightest central areas of the plage. The O VIII/Fe XVII flux ratio varies by only a factor of about five in the temperature range 2-4 $\times 10^6$ K, making it more sensitive to errors in flux calibration, elemental abundance, and atomic parameters than the line ratios available at the brightest Fe XVII pixel. Even though the data were taken 8 hours apart, the resulting electron temperatures and emission measures obtained with the O VIII/Fe XVII flux ratio from the spectroscopic and image data were equal at the same location. This indicates that the active region was stable during the observation period. Also, GOES soft X-ray data show no significant activity at or between the times of these observations.

A comparison of electron temperatures obtained from various line flux ratios at the location of the spectroscopic scan leads to the conclusion that the Fe XVII emissivity is inconsistent with that of the other lines by a factor of ~ 2.75. For greater detail see CoMStOC I, where the factor was found to be lower (~ 2.25), but the difference is within the uncertainty of the measurements. This emissivity "correction factor" is used to obtain temperature and emission measure maps (Figures 1e and 1f) from the O VIII/Fe XVII map flux ratios. Maps of the predicted microwave brightness temperatures at 20 cm and 6 cm are also shown (Figures 1g and 1h) and discussed further in Section 3.3. These maps were smoothed with a 3 x 3 boxcar to remove statistical noise, and the calculations were done only for those pixels with significant count rates, $> 3\sigma$, in both lines. It is difficult to obtain a meaningful, quantitative estimate of the error in the map temperatures and emission measures other than to note that they are expected to be larger than at the Fe XVII peak (Table 1).

2.3 Beijing Magnetogram

Figure 1d shows a photospheric longitudinal magnetogram of AR 4906 on 18 December 1987, obtained from the Beijing Observatory (courtesy of H. Zhang and H. Wang). The sunspot is the oval-shaped pair of solid contours to the right of map center. The maximum line-of-sight umbral magnetic field strength is ~2600 G, and the noise level is ~100 G. Comparison of the umbral field strength with data taken at the Mt. Wilson Observatory shows good agreement, indicating that the magnetogram did not saturate. Just left (east) of the sunspot is a nearby region of opposite polarity with a maximum, inward directed field of $\sim$ 790 G. Farther to the left is the trailing plage with a maximum, inward field of ~930 G.

Figure 1d also shows field lines obtained with the potential field extrapolation code developed by Sakurai (1982); this code solves Laplace's equation to calculate current-free magnetic field lines using the line-of-sight photospheric fields as boundary conditions. A cluster of field lines in the lower left portion of the sunspot terminates in and around the nearby, relatively strong region of opposite polarity. These field lines outline a loop-like structure (or bundle of loops) which is quite asymmetric. For several representative field lines, we list pairs of total extrapolated photospheric magnetic field strengths (in Gauss), where the first element corresponds to the footpoint inside the sunspot and the second to the footpoint in the region of opposite polarity: (1800,33), (1500,280), (1400,550). The corresponding photospheric footpoint separations for the above field lines are 5.06, 4.64, and 3.80 $\times 10^4$ km.

3 Results

3.1 Analysis of the Sunspot

The Sakurai code was modified to obtain the total extrapolated magnetic field strength in a grid of locations all at the same specified height above the photosphere. Contour maps at heights of 0, 5000, 10000, and 15000 km are shown in Figure 3. The vertical gradient of the total magnetic field strength near the center of the umbra for heights between 0 and 5000 km is $\sim$ 0.30 G/km. (This

is less than but comparable to the gradient of 0.41 – 0.67 G/km obtained by Henze et al., 1982, for the longitudinal magnetic field in the transition region and photosphere of a sunspot umbra.) The average horizontal gradient in the total photospheric magnetic field strength is $\sim$ 0.11 G/km. Knowing the height variation of the maximum total extrapolated sunspot field and assuming that this field can be described by that of a vertically oriented point dipole buried below the photosphere, we obtain a depth of 1.76×10^4 km and a dipole moment of 7.45×10^{15} G-km^3.

These dipole parameters are used to calculated contours of constant magnetic field strength which extend well into the corona. Figure 4 shows magnetic field contours corresponding to the 1st through 5th harmonics of 1665 MHz and 4900 MHz. The dipole field is compared with the field calculated with the Sakurai code. Specifically, the radii in the x-direction of several field strength contours in the point dipole field (Fig. 4) were compared with the radii of these same contours in the four extrapolated maps of Figure 3. At these four heights, the corresponding contour radii are equal to better than 10% for magnetic fields $\gtrsim$ 300 G and we find that the point dipole field is a good approximation of the extrapolated potential field within this three-dimensional structure; this approximation simplifies the calculation of microwave emission from sunspot models. For locations in which B<300 G, nearby pockets of magnetic field perturb the sunspot field from that of a point dipole.

Figure 5 shows the theoretical I and V maps for 1665 MHz and 4900 MHz obtained using the point dipole approximation and the model sunspot atmosphere described in Brosius and Holman (1989). The failure of this simple model to reproduce the sunspot microwave structure provides insight into the temperature, density, and field structure above the sunspot: 1) The coronal temperature and/or density must be relatively low over large portions of the sunspot and 2) the microwave emission must emanate from some coronal structure other than the sunspot in order to explain the observed 6 and 20 cm I and V structure. The loop-like structure is explored in the next sub-section.

An overlay of the intensity maps in the 20 cm waveband (Fig. 2) with the magnetogram reveals that the 20 cm intensity contours do not cover the entire sunspot. The potential field extrapolations (Fig. 3) show that magnetic fields which are high enough to produce 2nd harmonic gyroemission at all four frequencies in the 20 cm waveband (245 - 297 G) occur at heights of 5000 - 15000 km, where coronal temperatures ($> 10^6$ K) and densities ($\sim 10^9$ cm^{-3}) are expected to persist (Papagiannis and Kogut 1975, Hildebrandt et al. 1987). Indeed, 2nd harmonic gyroemission is expected to emanate from the portion of the sunspot for which the observed brightness temperature is less than the lowest observed intensity contour (5.3×10^5 K). Ways to obtain brightness temperatures this low from the 2nd harmonic gyroemission mechanism are 1) the density in the emission region is extremely low ($< 10^5$ cm^{-3} for a 2×10^6 K plasma), 2) the temperature in the emission region is less than 5.3×10^5 K, or 3) both the temperature and the density in the emission region are low. To obtain a density less than 10^5 cm^{-3} in the corona over a large fraction ($\sim$ 1/3) of a sunspot area seems unlikely, but it cannot be ruled out. Thus we find that a lower temperature and/or density exists over a portion of both the sunspot umbra and penumbra on the side of the sunspot away from the center of AR 4906. This is consistent with the results of Gary and Hurford (1987) and with Strong, Alissandrakis, and Kundu (1984).

3.2 Analysis of the Loop Structure Connecting the Sunspot with the Nearby Region of Opposite Polarity

An overlay of the intensity maps in the 20 cm waveband (Fig. 2) with the magnetogram field lines (Fig. 1d) reveals that the peak of the sunspot-associated source in all four of the 20 cm intensity maps lies along the loop structure joining the sunspot with the nearby region of opposite polarity. Figure 6 shows the locations of the centers of the 20 cm peak intensity contours, along with the 6 cm I and V sources, on the magnetogram. The higher the frequency, the farther down the leg of the loop (on the side of the sunspot) the intensity peak occurs. Assuming the emission in the 20 cm peaks to be dominated by 2nd harmonic gyroemission, we estimate a magnetic field gradient $\sim$ 0.0068 G/km along the loop in the plane of the sky. Assuming 3rd harmonic, the field gradient is $\sim$ 0.0047 G/km. Both of these gradients are factors of 2 to 3 less than the gradients calculated along the individual extrapolated field lines which pass through the 20 cm emission peaks. Based upon the potential field extrapolation, the 20 cm peak emission region is comprised of a superposition of 2nd and 3rd harmonic gyroemission arising from the loop structure. The magnetic field strength ranges from 160 to 300 G in the 20 cm source region.

The 6 cm emission originates farther down the leg of the loop (on the side toward the sunspot) since much higher fields are required for gyroresonance emission at 6 cm than at 20 cm. The polarization structure shows two V sources – one on either side of the I source – such that the I and V sources all lie roughly along the length of the loop. The polarization is $\sim$60% close to the edges of the I source. Such structure appears in the microwave loop models of Holman and Kundu (1985) and arises from the gyroresonance emission mechanism: the ordinary mode (O-mode) of a given harmonic becomes optically thin toward the harmonic edge more rapidly than does the extraordinary mode (X-mode). Assuming the emission in the 6 cm peak to be dominated by 3rd harmonic gyroemission (see next paragraph), we estimate an average magnetic field gradient (between the 6 and 20 cm source regions) $\sim$ 0.020 G/km along the loop in the plane of the sky. This is less than but comparable to the average field gradient $\sim$ 0.028 G/km calculated along the individual extrapolated field lines which pass through the 6 and 20 cm emission peaks.

In principle, the harmonic number of the 6 cm emission can be determined by comparing the observations with models. Although a simple dipole loop model does not accurately portray the asymmetry of the extrapolated field lines, we are only interested in reproducing the emission from one leg of the loop (the sunspot side of the loop in Fig. 6; the right half of Figure 7), so the magnetic field structure of the loop elsewhere is of little consequence. The density is selected so that the brightness temperature calculated for the portion of the loop away from the desired 6 cm source remains less than the lowest observed 6 cm brightness temperature contour, as observed. Both thermal bremsstrahlung and thermal gyroemission were included in the calculations and theoretical I and V maps at 6 cm were produced for three cases where the 2nd, 3rd, and 4th harmonic emission region was in the footpoint at a height of $\sim$ 5000 km. The 6 cm I and V structure and magnitude could not be produced with 4th harmonic emission. For 2nd harmonic, the density required is low: $\sim 5 \times 10^6$ cm^{-3}. If the density were higher, the overlying 3rd harmonic emission region would yield too high a brightness temperature from a large area of the loop and would destroy the desired V structure. For 3rd harmonic, the density is $\sim 10^9$ cm^{-3}. This is reasonable in light of the sunspot atmosphere model of Hildebrandt et al. (1987) where a density of $\sim 8 \times 10^8$ cm^{-3} occurs $\sim$ 5000 km above the photosphere. The emission measure for the model loop with density $\sim 10^9$ cm^{-3} is $\sim 10^{27}$ cm^{-5}, less than but comparable to the value of $\sim 10^{28}$ cm^{-5} estimated from the very weak

Fe XVII flux measured by XRP at the location of the 6 cm source (and assuming $T_e = 2.5 \times 10^6$ K). The corresponding value for the model loop with density $\sim 5 \times 10^6$ cm^{-3} is $\sim 2 \times 10^{22}$ cm^{-5}, substantially less than the observed value. Thus our model, combined with XRP observations, indicates that the observed 6 cm I and V structure is indeed due to 3rd harmonic gyroemission. Accounting for the four frequencies at which the 6 cm emission was observed, this translates into magnetic field strengths ranging from 547 G to 583 G. At the location of the 6 cm source the potential field extrapolation yields a field $\sim$ 600 G at a height $\sim$ 5000 km, consistent with our deduced values.

These magnetic field and density results can be used to estimate the Alfven speed and its variation within the loop. The magnetic field strength required for the highest frequency source in the 6 cm band, 583 G, gives an electron gyrofrequency of 1.63 GHz. The 6 cm source model is consistent with the observations when the electron density is between 5×10^8 cm^{-3} and 2×10^9 cm^{-3}, giving a plasma frequency of 0.2 - 0.4 GHz. Hence, the ratio of the gyrofrequency to the plasma frequency is found to be in the range 4 - 8 and the Alfven speed falls within the 28,000 - 57,000 km/sec range. (The estimated density of 1×10^9 cm^{-3} gives an Alfven speed of 40,000 km/sec.) The 160 G - 300 G range for the magnetic field strength in the 20 cm source region gives an electron gyrofrequency ranging from 0.45 GHz to 0.84 GHz. The electron density is not as well established. With an estimated value of 1×10^9 cm^{-3}, the ratio of the gyrofrequency to the plasma frequency ranges from 1.5 to 3, and the Alfven speed ranges from 10,000 km/sec to 20,000 km/sec. Hence, the Alfven speed in this coronal loop is highest near the sunspot and decreases toward the apex of the loop.

In wave heating theories of the corona, the heating rate is proportional to the Alfven speed and the square of the wave velocity amplitude. The Alfven speeds derived here are significantly greater than the generally quoted value of 1000 - 2000 km/s. This implies that the same heating rate can be achieved with a smaller wave amplitude. However, for resonant waves in a loop (as in resonant absorption theories), the period of the driving wave must be shorter. For a loop length of 100,000 km and an Alfven speed of 20,000 km/sec, the wave period must be 10 sec or less. Moreover, the gyrofrequency is generally assumed to be less than the plasma frequency, the opposite of what is found here and in other CoMStOC results. The value of this ratio determines which plasma instabilities are important.

At the location of the 6 cm peak, where the brightness temperature is $\sim 2.5 \times 10^6$ K, the 20 cm brightness temperature is lower, $\sim 1.3 \times 10^6$ K. Because lower frequencies require lower fields for the thermal gyroemission mechanism and, because the magnetic field diminishes with increasing height in the atmosphere, the 20 cm emission must originate higher in the atmosphere than the 6 cm emission. Indeed, fields high enough for 20 cm 2nd harmonic gyroemission (245 - 297 G) occur over the 6 cm source at heights in excess of 15,000 km. If the brightness temperature is $\sim 1.3 \times 10^6$ K and the 2nd harmonic is optically thin, the 20 cm emission should be polarized since the O-mode is less optically thick than the X-mode. This polarization is not observed and we conclude that the observed 20 cm brightness temperature is due to optically thick 2nd harmonic gyroemission in a region where $T_e \sim 1.3 \times 10^6$ K. This means that the plasma temperature at the height of formation of the 6 cm emission is higher than the plasma temperature at the height of formation of the 20 cm emission. Thus, at the location of the 6 cm intensity peak, the plasma temperature *diminishes with height.*

3.3 Analysis of the Plage

The electron temperature and column emission measure values obtained from the XRP data can be used to compute the thermal bremsstrahlung microwave emission from the X-ray emitting plasma. The optical depth due to thermal bremsstrahlung (free-free) absorption is

$$\tau_{ff}^{X,O} = \frac{9.786 \times 10^{-21}(EM)\ln(47T_e/\nu)}{n_\nu T_e^{1.5}(\nu \mp \nu_B \cos\theta)^2}, \quad (1)$$

where T_e is the electron temperature in K, EM is the emission measure in cm^{-5}, ν is the observation frequency in GHz, n_ν is the index of refraction (~ 1 for plasma and field conditions here), ν_B is the electron gyrofrequency ($\nu_B = 2.8 \times 10^{-3}B$, where B is in Gauss and ν_B is in GHz), θ is the angle between the field and the line of sight, and the minus sign refers to X-mode while the plus sign refers to O-mode. The thermal bremsstrahlung brightness temperature predicted for each mode can be calculated using

$$T_{B;X,O}^{PRED} = T_e[1 - \exp(-\tau_{ff}^{X,O})]. \quad (2)$$

In a magnetized plasma, the optical depth, and hence the predicted brightness temperature, of the X-mode emission is expected to be higher than that of the O-mode. The predicted total intensity I^{PRED} is simply the average brightness temperature of the two modes which, depending on the direction of the magnetic field, are associated with right circular polarized (RCP) or left circular polarized (LCP) emission.

At the location of the Fe XVII peak, where the XRP spectroscopic scan data used to generate Table 1 were obtained, the electron temperature of the plasma observed by XRP was $2.95 \pm 0.20 \times 10^6$ K and the log of the column emission measure was 28.85 ± 0.19. These values entered into the equations above yield the predicted intensities listed in Table 2. The uncertainties are due to the errors associated with the electron temperature and emission measure values in Table 1. At this same location in the plage, the VLA observed an intensity $I_{20}^{OBS} \sim 1.2 \times 10^6$ K at all four frequencies in the 20 cm waveband, and $I_6^{OBS} < 0.42 \times 10^6$ K in the 6 cm waveband. Our predicted intensities in the 6 cm waveband are all consistent with the VLA observations. Our predicted intensities in the 20 cm waveband are about 1.4 to 1.9 times higher than the corresponding observed intensities. Thus it appears that thermal bremsstrahlung plays a significant role in the observed plage emission.

The picture becomes considerably more complex when the observed polarization is considered. Table 2 lists the observed intensity and the LCP and RCP brightness temperatures ($T_{B,L}^{OBS}$ and $T_{B,R}^{OBS}$) for each of the four frequencies in the 20 cm waveband at the location of the XRP spectroscopic scan. The X-mode corresponds to the RCP emission for outward directed fields, and to the LCP emission for inward directed fields; the O-mode corresponds to the LCP emission for outward directed fields and to the RCP emission for inward directed fields. The LCP emission is reasonably consistent with the predicted thermal bremsstrahlung brightness temperature (I^{PRED}). However, the observed RCP emission is considerably lower, by a factor of 2 to 4, than the predicted value. Thus, some mechanism is required to explain the reduction of the expected RCP emission to its observed value. The only way to reduce the expected brightness temperatures of $\sim 2 \times 10^6$ K to the observed value $\sim 7 \times 10^5$ K is to have cooler absorbing plasma along the line of sight between the emission region and the observer.

One possible model which explains the discrepancy between the observed and the predicted polarization is that the source region consists of two layers of hot plasma separated by an inter-

vening layer of cooler plasma. The lowest layer contains the highest column emission measure and, therefore, is responsible for the majority of both the X-ray emission and the predicted thermal bremsstrahlung microwave emission. The intervening layer of cooler plasma absorbs out the microwave emission from this lower hot layer, leaving only the microwave emission from the uppermost hot layer to be detected by the VLA (see Figure 8a). The uppermost hot layer, optically thin to thermal bremsstrahlung, is embedded in a magnetic field such that thermal gyroemission, capable of producing the observed high polarization, produces the observed 20 cm microwave emission. The cool intervening layer must have a temperature $\leq 5 \times 10^5$ K in order to reduce the predicted RCP emission at 1665 MHz from 1.75×10^6 K to its observed value of 5×10^5 K. If, for example, the cool absorbing plasma has a temperature of 10^5 K, it needs log EM = 27.5 to get $\tau_{ff} \sim 5$ at 1665 MHz. This means that if the cool absorbing layer forms a sheath $\sim$ 3500 km thick, it needs a reasonable density $\sim 3 \times 10^9$ cm^{-3} in order to be an effective absorber. If gyroabsorption contributes to the opacity of this cool layer, the required emission measure may be lower. In order for the uppermost hot layer to both emit strongly in the 20 cm waveband and produce polarization as high as $\sim$ 50%, the layer must contain magnetic fields sufficiently high for gyroemission. From our potential field extrapolation at and near the location of the XRP spectroscopic scan, we find that the requisite magnetic field strengths are present, indicating that the observed 20 cm emission could originate in a gyroresonance emission layer between heights of $\sim$ 5000 and $\sim$ 15,000 km. Since the radiation is emitted primarily in the X-mode and the longitudinal field direction is inward, the emitted radiation will be LCP, as observed (Figure 2).

Plasma and magnetic field parameters in the uppermost hot layer can be calculated. The optical depth of the uppermost hot layer $\tau_{UH}^{X,O}$ can be estimated by solving

$$T_B^{X,O} = T_c \exp(-\tau_{UH}^{X,O}) + T_e[1 - \exp(-\tau_{UH}^{X,O})] \tag{3}$$

for $\tau_{UH}^{X,O}$, where $T_B^{X,O}$ are the observed X- (LCP) and O- (RCP) mode brightness temperatures at a particular frequency, T_c is the brightness temperature of the optically thick, underlying cool absorbing plasma ($T_c \leq 5 \times 10^5$ K), and T_e is the electron temperature of the uppermost hot layer ($T_e > 2 \times 10^6$ K). Solving for $\tau_{UH}^{X,O}$ we obtain

$$\tau_{UH}^{X,O} = \ln[(T_e - T_c)/(T_e - T_B^{X,O})]. \tag{4}$$

Assuming $T_e = 3 \times 10^6$ K and $T_c = 1 \times 10^5$ K, we obtain $\tau_{UH}^{X} = 0.80$ and $\tau_{UH}^{O} = 0.15$ for the observed brightness temperatures at 1665 MHz. Now the optical depth due to gyroresonance absorption can be written (e.g., Kundu 1965, Zheleznyakov 1970)

$$\tau_{gr}^{X,O} = 0.052 \frac{s^{2s}}{2^{s+1} s!} n_e \nu^{-1} L_B (1.77 \times 10^{-10} T_e)^{s-1} (1 \pm \cos\theta)^2 \sin^{2s-2}\theta, \tag{5}$$

where s is the harmonic number, n_e is the electron density, ν is the frequency, L_B is the magnetic scale height ($B/\nabla B$), T_e is the electron temperature, θ is the angle between the field and the line of sight, and the plus sign refers to X-mode while the minus sign refers to O-mode. The ratio

$$\tau_{UH}^{X}/\tau_{UH}^{O} = (1 + \cos\theta)^2/(1 - \cos\theta)^2 \tag{6}$$

yields the angle between the field and the line of sight which is required in order to produce the calculated X- and O-mode optical depths in the upper hot layer. For the case discussed above, the calculated angle is 66°, comparable to the angle obtained from the extrapolated coronal magnetic field.

The magnetic scale height L_B can also be calculated from the potential field extrapolation. It is 0.94×10^9 cm in the 2nd harmonic gyroemission region, 1.4×10^9 cm in the 3rd, and 1.8×10^9 cm in the 4th. Using $\tau_{UH}^X \sim 0.8$, $T_e = 3 \times 10^6$ K, $\nu \sim 1500$ MHz, and $\theta \sim 60°$, we calculate the electron density n_e required in the upper hot layer if the emission process is due to 2nd harmonic gyroemission ($n_e = 3.0 \times 10^4$ cm^{-3}), 3rd harmonic gyroemission ($n_e = 6.8 \times 10^6$ cm^{-3}), and 4th harmonic gyroemission ($n_e = 1.2 \times 10^9$ cm^{-3}).

A second possible model consists of two layers of plasma: the lower hot layer seen by XRP and a cooler overlying layer where gyroresonance absorption takes place. In this cool absorbing layer, neither mode is optically thick and since the X-mode is more attenuated than the O-mode, the resulting emission is dominated by O-mode. The observed emission, however, seems to be X-mode (it is left-circularly polarized, with an inward-directed underlying photospheric field). Nevertheless, the microwave emission can undergo a polarization inversion upon traversing a "quasi-transverse" (QT) layer in the coronal magnetic field (see Fig. 8b). This QT layer occurs where the magnetic field becomes transverse to the line of sight, i.e., the longitudinal field component B_z becomes zero. Previous studies have provided evidence for such polarization inversion (Kundu et al. 1977, Webb et al. 1983, Alissandrakis and Kundu 1984). The observed polarization is inverted when coupling between the polarization modes is weak.

Zheleznyakov (1970), using the WKB method, obtains the following expression for the coupling parameter, given here in the notation of Bandiera (1982):

$$C = \frac{2 \ln 2}{\pi^2} \frac{(m_e c)^4}{e^5} \frac{\omega^4}{N_e B^3} \mid \frac{d\theta}{ds} \mid, \tag{7}$$

where m_e and e are the rest mass and charge on an electron, c is the speed of light, ω is the observation angular frequency, N_e is the electron number density, B is the magnetic field strength, and $d\theta/ds$ is the gradient of the angle between the field and the line of sight; all units are in CGS. The microwave emission undergoes a polarization inversion when $C \ll 1$, or

$$4.766 \times 10^{-18} \frac{\nu^4}{N_e B^3} \mid \frac{d\theta}{ds} \mid \ll 1. \tag{8}$$

In and near the location of the XRP spectroscopic scan, the Sakurai code yields a QT layer at a height of ~75,000 km. The average total magnetic field strength obtained from the code is 17 G, and the angular gradient along the line of sight is 1.1×10^{-10} rad/cm. Inserting these values into the expression for the coupling parameter and using the highest observing frequency in the 20 cm waveband (1.665 GHz), we find that the polarization inversion will take place if the electron density in the QT layer exceeds 8.4×10^5 cm^{-3}. The model plage electron density of Hildebrandt et al. (1987) at a height of 75,000 km is 1.4×10^9 cm^{-3}, and the model electron densities in all of the coronal structures in Hildebrandt et al. (1987) and Pagagiannis and Kogut (1975) exceed 5.4×10^7 cm^{-3} at the same height. Thus it is reasonable to expect polarization inversion to occur for the 20 cm microwave emission from the plage: the 20 cm emission exiting the cool absorbing plasma, dominated by the O-mode (RCP), is inverted in the QT layer so that the O-mode emission becomes LCP, as observed.

Plasma and magnetic field parameters in the cool absorbing layer can be calculated. The optical depths of the cool absorbing layer $\tau_c^{X,O}$ can be estimated by solving

$$T_B^{X,O} = T_B^{PRED} \exp(-\tau_c^{X,O}) + T_c[1 - \exp(-\tau_c^{X,O})] \tag{9}$$

for $\tau_c^{X,O}$, where $T_B^{X,O}$ are the observed X- and O- mode brightness temperatures at a particular frequency (prior to polarization inversion), T_B^{PRED} is the brightness temperature due to thermal bremsstrahlung predicted from the X-ray observations, and T_c is the electron temperature of the cool absorbing layer. Solving for $\tau_c^{X,O}$ we obtain

$$\tau_c^{X,O} = \ln[(T_c - T_B^{PRED})/(T_c - T_B^{X,O})]. \quad (10)$$

For the average observed brightness temperatures in the 20 cm waveband, we obtain $\tau_c^X = 1.44$ and $\tau_c^O = 0.18$ for $T_c = 3 \times 10^5$ K, which leads to $\theta \sim 62°$. This angle is comparable to the angle obtained from the extrapolated field. Using $\tau_c^X \sim 1.44$, $T_c = 3 \times 10^5$ K, $\nu \sim 1500$ MHz, and $\theta \sim 60°$, we calculate the electron density n_e required in the cool absorbing layer if the absorption process is due to 2nd harmonic gyroabsorption ($n_e = 5.5 \times 10^5$ cm^{-3}), 3rd harmonic gyroabsorption ($n_e = 1.2 \times 10^9$ cm^{-3}), and 4th harmonic gyroabsorption ($n_e = 2.1 \times 10^{12}$ cm^{-3}). The 2nd-harmonic density is considerably less than canonical low coronal density values, but cannot be ruled out. The 3rd-harmonic density is consistent with canonical low coronal density values, and is also consistent with the density requirement for polarization inversion in the QT layer (although the QT layer is $\sim$ 70,000 km higher in the atmosphere). The 4th-harmonic density is so high that plasma suppression would prohibit the propagation of 20 cm electromagnetic radiation, so this can be ruled out. The absorption which produces the observed polarization at the location of the XRP spectroscopic scan most likely occurs in the 3rd harmonic gyroresonance absorption region.

The situation is somewhat different at the location of the 20 cm intensity peak in the plage. Here, $\sim$ 30,000 km west of the location of the XRP spectroscopic scan, the predicted and the observed 20 cm intensity peaks are cospatial. The predicted brightness temperature is 2.2×10^6 K, while the observed LCP brightness temperature is 1.9×10^6 K and the observed RCP brightness temperature is 0.9×10^6 K. The maximum predicted 6 cm brightness temperature is 7×10^5 K, while the observed is $< 4.2 \times 10^5$ K. This, again, requires the presence of cooler absorbing plasma overlying the hot plasma observed by XRP. Here, however, the coronal potential field is not sufficient for the gyroemission mechanism to operate. The photospheric field is less than 100 G, and between heights of 5000 and 15,000 km the total extrapolated field ranges from $\sim$ 60 to $\sim$ 90 G. This suggests quite strongly that the extrapolated field is substantially less than the actual magnetic field in the corona. This is possibly a manifestation of instrumental insensitivity to photospheric longitudinal magnetic fields less than $\sim$ 100 G. It is quite possible that compact, highly intense photospheric magnetic field regions were not detected due to inadequate instrumental resolution. It also cannot be ruled out that electric currents, and hence non-potential magnetic fields, are present in the corona.

These models represent the two simplest ways to describe and interpret the simultaneous, multi-waveband data taken of AR 4906. Simpler models can, of course, explain the microwave images, the X-ray spectra, or the magnetic extrapolations individually or even explain any two of these, but the two models explained in detail above and depicted in Figure 8 can describe the entire data set.

4 Conclusions

A number of important conclusions concerning the plasma and magnetic field structure of an active region, as well as the observational methods, result from this study:

(1) The temperature in the corona over an active region can diminish with height; this occurs over both the sunspot and the plage in AR 4906 where a different line of reasoning leads to this conclusion for each structure. In the case of the sunspot, the cospatial microwave emission in the 6 and 20 cm wavebands have substantially different brightness temperatures. The emission in both wavebands is attributed to optically thick thermal gyroemission in the high magnetic field of the sunspot. The 6 cm emission requires higher fields than the 20 cm emission and, hence, originates lower in the sunspot atmosphere. Where the 6 and 20 cm emission overlap, the 6 cm brightness temperature is 2.5×10^6 K while the 20 cm brightness temperature is 1.3×10^6 K. Thus the sunspot atmospheric temperature diminishes from 2.5×10^6 K at the height of the 6 cm emission to 1.3×10^6 K at the height of the 20 cm emission. In the case of the plage, the conclusion is based upon the discrepancy between the observed RCP emission at 20 cm and the brightness temperature predicted from the XRP line flux ratios. Specifically, this requires the presence of overlying cool, absorbing plasma in order to reduce its predicted brightness temperature of $T_B^{PRED} \sim 2 \times 10^6$ K to its observed value of $T_{B,R}^{OBS} \sim 0.7 \times 10^6$ K. The overlying, cool plasma must have a temperature $\leq 5 \times 10^5$ K.

(2) A loop or loop-like structure connects the sunspot with a nearby region of opposite polarity in the east. The peaks of the 6 and 20 cm emission lie along this loop, with higher frequency emission originating farther down the leg of the loop on the side of the sunspot. Based upon the potential field extrapolation, the 20 cm emission is due to a combination of 2nd and 3rd harmonic gyroemission, putting the magnetic field strength in this region in the range 160 – 300 G.

(3) Based upon a comparison of the 6 cm and X-ray observations with calculations of the emission from a model loop, we deduced the plasma and magnetic field parameters at the location of the 6 cm source. An electron temperature $T_e = 2.5 \times 10^6$ K, an electron density $N_e \sim 1 \times 10^9$ cm^{-3}, and a magnetic field strength of 583 G (3rd harmonic gyroemission at 4900 MHz) result. The potential field extrapolation yields this magnetic field strength at a height $\sim$ 5000 km above the photosphere.

(4) These results have allowed us to obtain good estimates of the Alfven speed at two locations within the loop. At the 6 cm source near the sunspot, an Alfven speed $\sim$ 40,000 km/sec is obtained. Higher in the loop, at the location of the 20 cm emission, the Alfven speed is found to range from 10,000 km/sec – 20,000 km/sec. These values are substantially higher than the 1000 – 2000 km/sec typically quoted for the Alfven speed in the corona. At both locations the electron gyrofrequency exceeds the plasma frequency.

(5) The extrapolated potential sunspot field can be approximated by that of a vertically oriented point dipole for locations in which $B \gtrsim 300$ G. For locations in which $B < 300$ G, nearby pockets of magnetic field perturb the sunspot field from that of a point dipole.

(6) The electron temperature and/or density are lower over the western portion of the sunspot (away from the center of the active region) than they are over the eastern portion of the sunspot.

(7) In the plage, the ratios of X-ray emission lines are used to calculate the electron temperature and column emission measure. The most accurate determination of these parameters is at the location of the Fe XVII peak flux, where spectroscopic scan data were obtained. The Fe XVII emissivity needs to be divided by a correction factor $\sim$ 2.75. This is somewhat higher than but comparable to the $\sim$ 2.25 factor obtained in CoMStOC I.

(8) The predicted 20 cm brightness temperature in the plage is reasonably consistent with the observed for the LCP emission but is much higher for the RCP emission. We have proposed two possible models to explain this discrepancy. Both models are as simple as possible yet still incorporate all three sets of data for AR 4906: The first model has a low layer of hot plasma (where the X-ray emission originates) covered by an optically thick cool, absorbing layer. On top of this cool plasma is a second hot layer which is optically thin to thermal bremsstrahlung but emits strong, polarized microwave emission since it is embedded in a magnetic field sufficient for gyroresonance emission at 20 cm. Since the longitudinal component of the magnetic field inverts at a height of ~75,000 km, the density at this height cannot exceed $\sim 8 \times 10^5$ cm^{-3}; otherwise, the polarization will invert in this QT layer and the sense of polarization will be opposite that observed. (It should be pointed out that the model coronal densities of Hildebrandt et al., 1987, and Papagiannis and Kogut, 1975, greatly exceed 8×10^5 cm^{-3} at a height of 75,000 km.) The second model has a layer of cool, but not fully thick, absorbing plasma overlying the hot plasma from which the predicted microwave emission originates. This cool plasma, embedded in a magnetic field sufficient for gyroresonance absorption, attenuates the X-mode more strongly than the O-mode. The polarization is subsequently inverted in the overlying QT layer in the magnetic field. Appropriate coronal magnetic field strengths, as well as the QT layer, are extrapolated from the photospheric longitudinal magnetogram with the Sakurai (1982) code. A similar result has been obtained from the analysis of the CoMStOC II data (Schmelz et al. 1991).

(9) Elsewhere in the plage, at the observed 20 cm intensity peak, we find that the magnetic field required to explain the observations is higher than the coronal potential field extrapolated from the photospheric longitudinal magnetogram. A similar discrepancy has been found in the analysis of other CoMStOC data.

Acknowledgements. We gratefully acknowledge the assistance of Dr. Haimin Wang in the acquisition of the Beijing Observatory magnetogram. Radio astronomical studies of the Sun at Tufts University are supported under grant AFOSR-89-0147 with the Air Force Office of Scientific Research. Simultaneous VLA and SMM observations of the Sun are supported by NASA grant NAGW-2383 to Tufts University. JTS acknowledges support by NASA contracts NAS5-30431 and NAS5-28713 and the Lockheed Independent Research Program. JWB and GDH acknowledge support by the SMM Guest Investigator Program and NASA RTOP 170-38-53-16. The success of the SMM CoMStOC observations depended on the efforts of many persons at the SMM Experimenters Operations Facility. The VLA is operated by Associated Universities Inc., under contract with the National Science Foundation. The XRP data used in this work were available only because of the repair of the SMM spacecraft by the crew of the Challenger on mission 41-C. The pilot for that mission, and the commander of Challenger's last flight, was Francis R. Scobee. This work is dedicated to his memory.

TABLE 1
Plasma Parameters from XRP Spectroscopic Scan Data

Line Ratio	T_e (MK)[1]	log(EM) (cm^{-5})[2]
O VIII/Mg XI	3.01 ± 0.16	28.85 ± 0.08
O VIII/Fe XVIII	2.83 ± 0.19	28.87 ± 0.09
Ne IX/Fe XVIII	2.94 ± 0.22	28.85 ± 0.09
Mg XI/Fe XVIII	2.61 ± 0.50	28.89 ± 0.24
Fe XVII/Fe XVIII	3.12 ± 0.27	28.83 ± 0.06
weighted mean[3]	2.95 ± 0.20	28.85 ± 0.19

[1] The quoted uncertainties on the individual values of T_e reflect counting statistics only.

[2] The column emission measure is computed from the O VIII flux only; the quoted uncertainties on the individual values reflect counting statistics only.

[3] The quoted uncertainties on the weighted means of T_e and EM are the root mean squares of the statistical and systematic uncertainties. For temperature, the systematic uncertainty is estimated as the standard deviation of the individual values. For the emission measure, the systematic uncertainty is estimated as the standard deviation of the emission measures calculated for the O VIII, Ne IX, Mg XI, and Fe XVIII fluxes at the mean T_e.

TABLE 2

Predicted Microwave Intensities from XRP Spectroscopic Scan Data And Observed Microwave Intensities from the VLA

Freq. (MHz)	I^{PRED} (MK)	I^{OBS} (MK)	$T_{B,L}^{OBS}$ (MK)	$T_{B,R}^{OBS}$ (MK)
1375	2.17 ± 0.49	1.2	1.5	0.9
1420	2.10 ± 0.49	1.1	1.5	0.7
1550	1.91 ± 0.49	1.4	2.0	0.8
1665	1.75 ± 0.49	1.1	1.7	0.5
4600	$0.31\ ^{+0.17}_{-0.11}$	<0.42	—	—
4700	$0.30\ ^{+0.16}_{-0.11}$	<0.42	—	—
4800	$0.29\ ^{+0.16}_{-0.10}$	<0.42	—	—
4900	$0.28\ ^{+0.15}_{-0.10}$	<0.42	—	—

References

Acton, L. W., et al. 1980, *Solar Phys.*, **65**, 53.

Alissandrakis, C. E., and Kundu, M. R. 1982, *Ap. J. (Letters)*, **253**, L49.

Alissandrakis, C. E., and Kundu, M. R. 1984, *Astr. Ap.*, **139**, 271.

Bandiera, R. 1982, *Astr. Ap.*, **112**, 52.

Bastian, T. 1987, Ph.D. thesis, University of Colorado.

Brosius, J. W., and Holman, G. D. 1988, *Ap. J.*, **327**, 417.

Brosius, J. W., and Holman, G. D. 1989, *Ap. J.*, **342**, 1172.

Cornwell, T. 1986, in *Synthesis Imaging* (NRAO Summer School Course Notes), p. 117.

Gary, D. E., and Hurford, G. J. 1987, *Ap. J.*, **317**, 522.

Henze, W., Jr., Tandberg-Hanssen, E., Hagyard, M. J., Woodgate, B. E., Shine, R. A., Beckers, J. M., Bruner, M., Gurman, J. B., Hyder, C. L., and West, E. A. 1982, *Solar Phys.*, **81**, 231.

Hildebrandt, J., Kruger, A., Urpo, S., and Terasranta, H. 1987, *Observation and Interpretation of Solar S-Component Radiation at Millimeter Waves* (Helsinki Univ. of Technology Radio Lab., Rept. S170).

Holman, G. D., and Kundu, M. R. 1985, *Ap. J.*, **292**, 291.

Kundu, M. R. 1965, *Solar Radio Astronomy* (New York: Interscience).

Kundu, M. R., Alissandrakis, C. E., Bregman, J. D., and Hin, A. C. 1977, *Ap. J.*, **213**, 278.

Lang, K. R., and Willson, R. F. 1982, *Ap. J. (Letters)*, **255**, L111.

Lang, K. R., Willson, R. F., and Gaizauskas, V. 1983, *Ap. J.*, **267**, 455.

Lang, K. R., Willson, R. F., and Rayrole, J. 1982, *Ap. J.*, **258**, 384.

Lang, K. R., Willson, R. F., Smith, K. L., and Strong, K. T. 1987, *Ap. J.*, **322**, 1035.

Lang, K. R., Willson, R. F., Smith, K. L., and Strong, K. T. 1987, *Ap. J.*, **322**, 1044.

McConnell, D., and Kundu, M. R. 1983, *Ap. J.*, **269**, 698.

Mewe, R., Gronenschild, E. H. B. M., and van den Oord, G. H. J. 1985, *Astr. Ap. Suppl.*, **62**, 197.

Meyer, J.-P. 1985, *Ap. J. Suppl.*, **57**, 173.

Nitta, N., White, S. M., Kundu, M. R., Gopalswamy, N., Holman, G. D., Brosius, J. W., Schmelz, J. T., Saba, J. L. R., and Strong, K. T. 1991, *Ap. J.*, **374**, 374 (CoMStOC I).

Papagiannis, M. D., and Kogut, J. A. 1975, *Brightness Temperatures and Polarizations of Solar Active Regions at 3.8 cm - Theory and Observations* (AFCRL-TR-75-0430).

Sakurai, T. 1982, *Solar Phys.*, **76**, 301.

Schmahl, E. J., Kundu, M. R., Strong, K. T., Bentley, R. D., Smith, J. B., Jr., and Krall, K. R. 1982, *Solar Phys.*, **80**, 233.

Schmelz, J. T., Holman, G. D., Brosius, J. W., and Gonzalez, R. D. 1991, *Ap. J.*, in preparation (CoMStOC II).

Shevgaonkar, R. K., and Kundu, M. R. 1984, *Ap. J.*, **283**, 413.

Strong, K. T., Alissandrakis, C. E., and Kundu, M. R. 1984, *Ap. J.*, **277**, 865.

Webb, D. F., Davis, J. M., Kundu, M. R., and Velusamy, T. 1983, *Solar Phys.*, **85**, 267.

Webb, D. F., Holman, G. D., Davis, J. M., Kundu, M. R., and Shevgaonkar, R. K. 1987, *Ap. J.*, **315**, 716.

Willson, R. F. 1985, *Ap. J.*, **298**, 911.

Zheleznyakov, V. V. 1970, *Radio Emission of the Sun and Planets*, ed. J. S. Hey (Oxford: Pergamon Press).

Figure Captions

Figure 1. Observations of the CoMStOC IV active region, AR 4906. Celestial north is up, and west is to the right. All eight boxes cover the same field of view, for ease in coalignment. The tick spacing is one minute of arc, the crosses mark the locations of the phase center of the VLA observations, and "X" marks the location of the XRP spectroscopic scan. (**a**) Frequency-averaged map of I (intensity) at 20 cm. The contour levels are 0.21, 0.41, 0.62, 0.83, 1.03, 1.24, 1.45, 1.66, 1.86, and 2.07 $\times 10^6$ K. (**b**) Frequency-averaged map of I at 6 cm. The contour levels are 0.42, 0.63, 0.84, 1.05, 1.26, 1.47, 1.68, 1.89, and 2.10 $\times 10^6$ K. (**c**) XRP soft X-ray map of AR 4906 in the bright Fe XVII line at 15.01 A. The image was accumulated during a 4′ square raster with 10″ steps which took 10 min to complete. The map has been smoothed with a 3 x 3 boxcar to improve statistics. Contour levels are 5, 10, 15, 20, 25, 30, 35, and 40 counts/s. (**d**) Photospheric longitudinal magnetogram obtained from the Beijing Observatory, with superimposed magnetic field lines calculated with the potential field extrapolation code of Sakurai. The contour levels are 200 and 500 G, where the dashed contours represent inward directed fields and the solid contours represent outward directed fields. (**e**) Electron temperature and (**f**) log of the column emission measure calculated from line flux ratios of emission lines observed with XRP. The contours in (**e**) are 2.2, 2.4, 2.6, 2.8, and 3.0 $\times 10^6$ K; the contours in (**f**) are 28.7, 28.9, and 29.1. The temperature and emission measure diagnostics were available only in the plage. (**g**) Brightness temperature map at 20 cm calculated for the thermal bremsstrahlung emission mechanism using the electron temperature and column emission measure maps in (e) and (f). The contours are 1.7, 1.9, and 2.1 $\times 10^6$ K. (**h**) Brightness temperature map at 6 cm calculated for the thermal bremsstrahlung emission mechanism using the electron temperature and column emission measure maps in (e) and (f). The contours are 0.1, 0.3, and 0.5 $\times 10^6$ K.

Figure 2. I and V maps at each of the four frequencies in the 20 cm waveband. The I contour levels are 0.53, 0.79, 1.05, 1.31, 1.57, 1.83, 2.09, and 2.35 $\times 10^6$ K for all frequencies. The V contour levels are 0.29 and 0.38 $\times 10^6$ K at 1375 MHz; 0.27, 0.36, and 0.46 $\times 10^6$ K at 1420 MHz; 0.31, 0.41, 0.51, and 0.61 $\times 10^6$ K at 1550 MHz; and 0.40, 0.53, and 0.66 $\times 10^6$ K at 1665 MHz. Celestial north is up, and west is to the right. The tick spacing is one minute of arc, and the crosses mark the location of the phase center of the VLA observations.

Figure 3. Sequence of contour maps showing the extrapolated magnetic field strength at heights of (**a**) 0 km, (**b**) 5000 km, (**c**) 10000 km, and (**d**) 15000 km above the photosphere. Celestial north is up, and west is to the right. The numbers along the axes are distances from solar disk center in units of 10^4 km in the plane of the sky. The contour levels in (**a**) and (**b**) are 150, 250, 350, 500, and 800 G. The contour levels in (**c**) and (**d**) are 150, 200, 250, 350, and 500 G. Crosshairs mark the phase centers of the VLA 6 and 20 cm maps, to assist in coaligning images. A 40″ line segment is shown in (d) to assist in scaling and coaligning.

Figure 4. Magnetic field of a model sunspot consisting of a vertically oriented point dipole buried below the photosphere. Numbers along the x and y axes represent the distance from the point dipole in units of 10^4 km. The x-axis is in the plane of the photosphere, and the y-axis is perpendicular to that plane. Solid lines are field lines, dashed lines numbered 1 through 5 are contours of constant magnetic field strength, and the dotted horizontal lines represent heights above the photosphere of 5000, 10000, and 15000 km. In (**a**) the dashed lines are magnetic field contours corresponding to the 1st through 5th harmonics of 1665 MHz: 594, 297, 198, 149, and 119 G. In (**b**) the dashed lines are magnetic field contours corresponding to the 1st through 5th harmonics

of 4900 MHz: 1749, 875, 583, 437, and 350 G.

Figure 5. I and V maps calculated for 1665 MHz and 4900 MHz for the sunspot model whose magnetic field is shown in Figure 4. Numbers along the x and y axes are in units of arcsec, and the crosshairs intersect at the center of the sunspot. Contour line thickness increases with increasing contour value. In (**a**) the 1665 MHz I contours are 0.84, 1.37, and 1.90 $\times 10^6$ K, and in (**b**) the 1665 MHz V contours are 0.27, 0.53, and 0.80 $\times 10^6$ K. In (**c**) the 4900 MHz I contours are 0.66, 1.28, and 1.90 $\times 10^6$ K, and in (**d**) the 4900 MHz V contours are 0.31, 0.62, and 0.93 $\times 10^6$ K.

Figure 6. Portion of the magnetogram showing the locations of the 6 and 20 cm emission along the field lines which outline the loop-like structure connecting the sunspot with the nearby region of opposite polarity. Celestial north is toward the top, and west is toward the right. A segment of 10″ length is shown for scaling purposes. Shaded areas show where the photospheric longitudinal field exceeds 200 G. The solid magnetic field contours represent outward directed fields of 200 and 500 G, while the short-dashed magnetic field contours represent inward directed fields of 200 and 500 G. The sunspot is the large shaded area in the upper right. The long-dashed contour corresponds to an intensity I of 0.79 x 10^6 K at the representative 20 cm microwave frequency of 1375 MHz. The "+" symbols mark the locations of the peak brightness temperature of each of the four closely-spaced frequencies in the 20 cm waveband. The location of the peak brightness temperature shifts systematically closer to the footpoint inside the sunspot with increasing frequency: the "+" farthest to the left corresponds to the 1375 MHz emission, and the "+" farthest to the right corresponds to the 1665 MHz emission. The dotted contour corresponds to an intensity I of 1.56 x 10^6 K at 4900 MHz in the 6 cm waveband. The dot-dash contours correspond to a V of 0.39 x 10^6 K at 4900 MHz.

Figure 7. Theoretical 4900 MHz I and V maps for the model loop described in the text. The height of the loop apex (16000 km), the footpoint separation (50000 km), and the loop thickness at the apex (7700 km) were all estimated from the extrapolated potential field lines. The cross section of the loop is taken to be circular at the apex. The model loop has a constant temperature of 2.5 x 10^6 K, a density of 1 x 10^9 cm^{-3}, and a field strength of 583 G (3rd harmonic) in the footpoints at a height of $\sim$ 5000 km above the photosphere. The I contours are 0.52, 1.04, 1.56, and 2.34 $\times 10^6$ K. The V contours are 0.39, 0.52, 0.64, and 1.00 $\times 10^6$ K. The model I and V sources on the right side of the figure reproduce the observed 6 cm I and V sources fairly well.

Figure 8. Illustration of the two models used to explain the observed polarization of the 20 cm microwave emission from the plage. The arrows labeled with an "R" correspond to RCP emission and the arrows labeled with an "L" correspond to LCP emission. The propagation mode is indicated by an "X" or an "O" in parentheses. The propagation mode is determined by the orientation of the local magnetic field, indicated by arrows labeled B_z. The lengths of the arrows labeled R and L indicate the relative brightness temperatures of the emergent emission in the given mode of polarization. (**a**) The hot/cool/hot layer model. Emission with high brightness temperature and low polarization ($T_B^{X,O} \sim 2 \times 10^6$ K) emerges from the lowest layer. This emission is then absorbed by the overlying cooler layer, from which low brightness temperature emission ($T_B^{X,O} < 5 \times 10^5$ K) emerges. Highly polarized emission ($T_B^X \sim 2 \times 10^6$ K, $T_B^O \sim 7 \times 10^5$ K) emerges from the highest layer, which is a hot plasma embedded in a magnetic field which is sufficiently strong for gyroresonance emission. (**b**) The hot/cool/QT layer model. Emission with high brightness temperature and low polarization ($T_B^{X,O} \sim 2 \times 10^6$ K) emerges from the lowest layer. This emission is then attenuated in the overlying cooler layer, in which magnetic fields sufficient

for gyroresonance absorption cause the optical depth (and hence the attenuation) to be greater for the X-mode (L) than for the O-mode (R). This results in the emission of O-mode-dominated (R) emission. The polarization is then inverted to its observed (L) value upon traversal of the overlying quasi-transverse (QT) layer in the magnetic field overlying the plage.

Postal Addresses

Jeffrey W. Brosius and Gordon D. Holman
Code 682.1
NASA/Goddard Space Flight Center
Greenbelt, MD 20771

Joan T. Schmelz
Code 602.6
NASA/Goddard Space Flight Center
Greenbelt, MD 20771

Robert F. Willson
Physics and Astronomy Dept.
Tufts University
Medford, MA 02134

Fig. 1

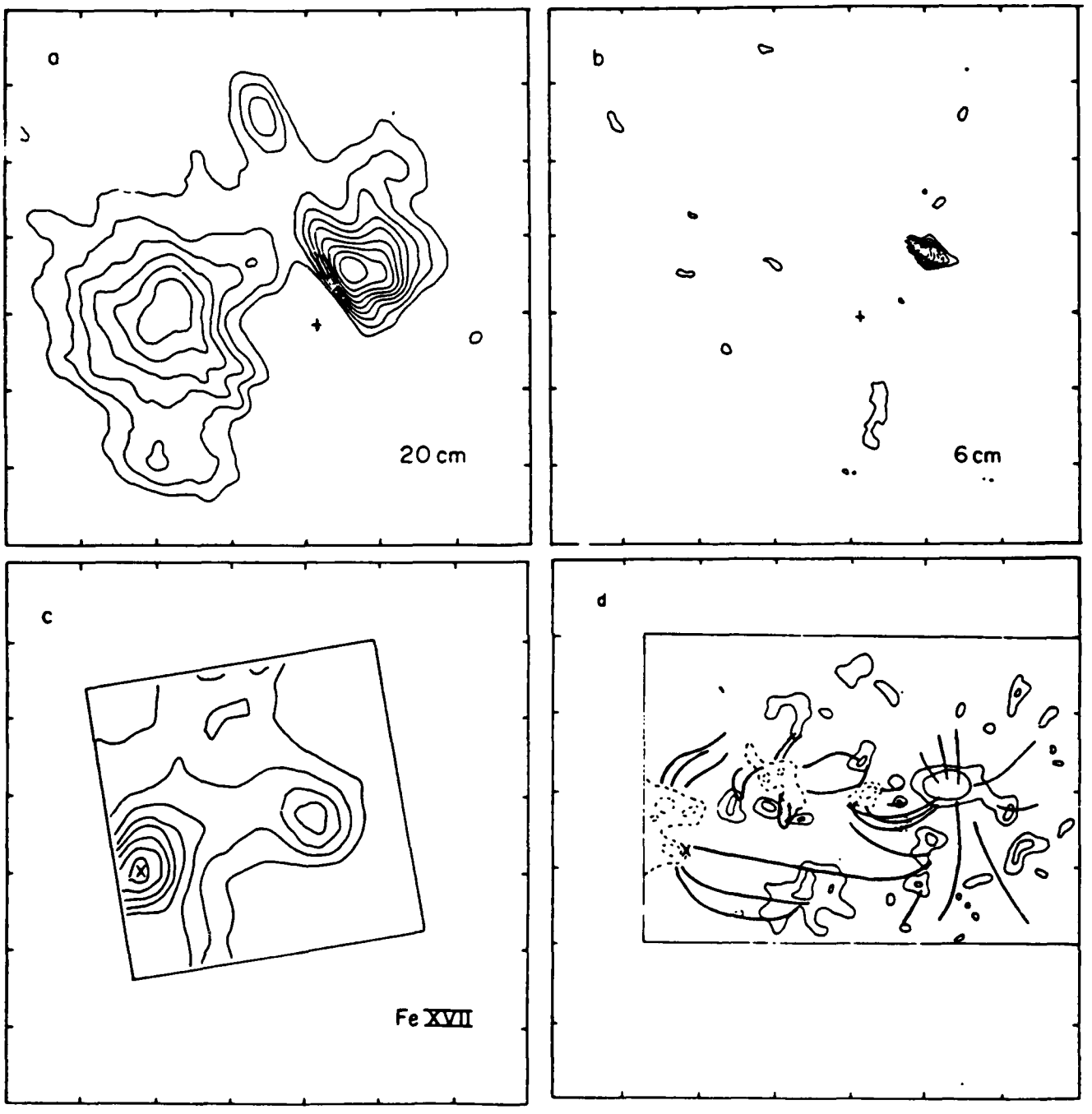

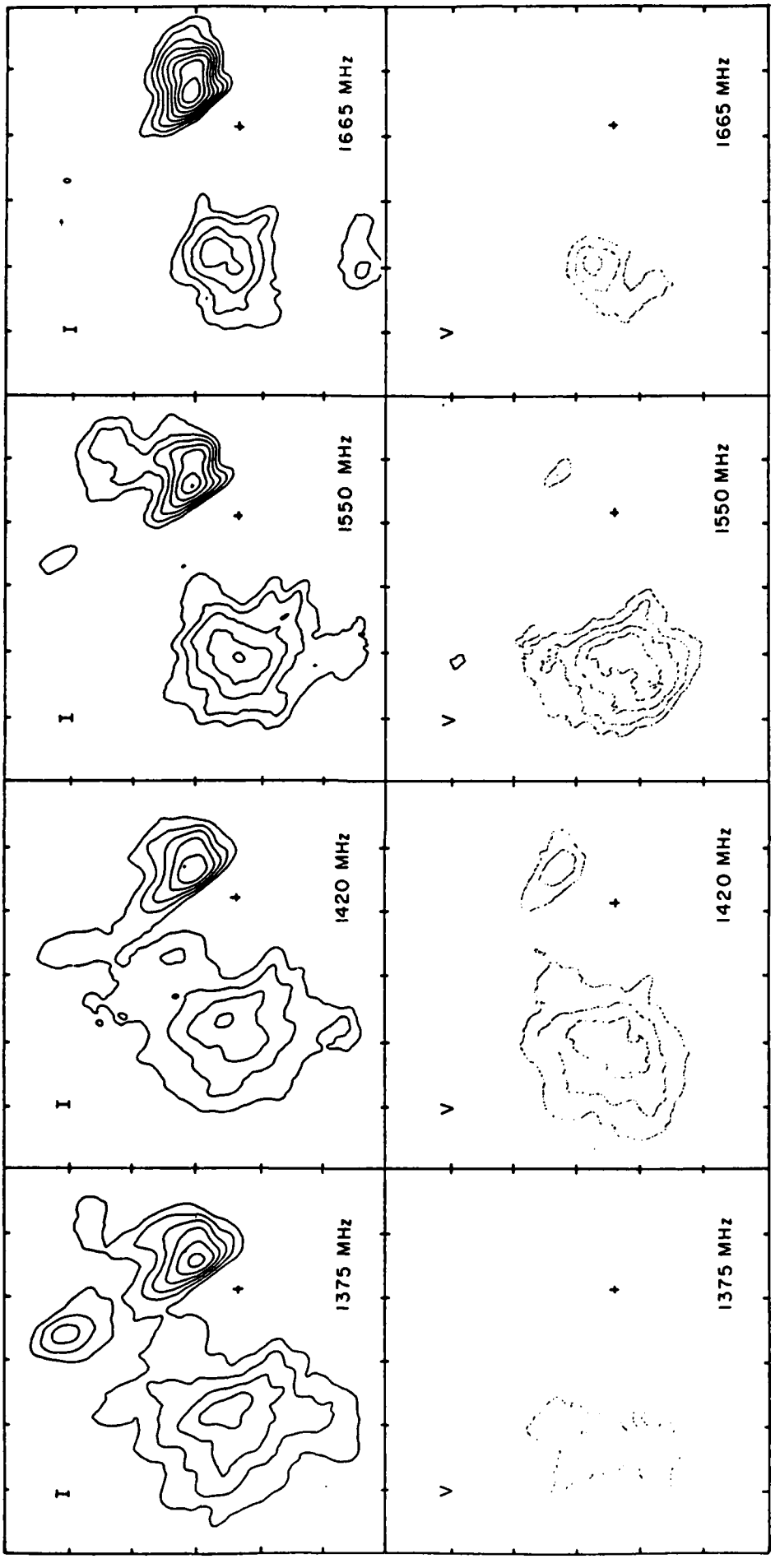
I
1665 MHz
V
1665 MHz
I
1550 MHz
V
1550 MHz
I
1420 MHz
V
1420 MHz
I
1375 MHz
V
1375 MHz

Fig. 2

Fig. 3

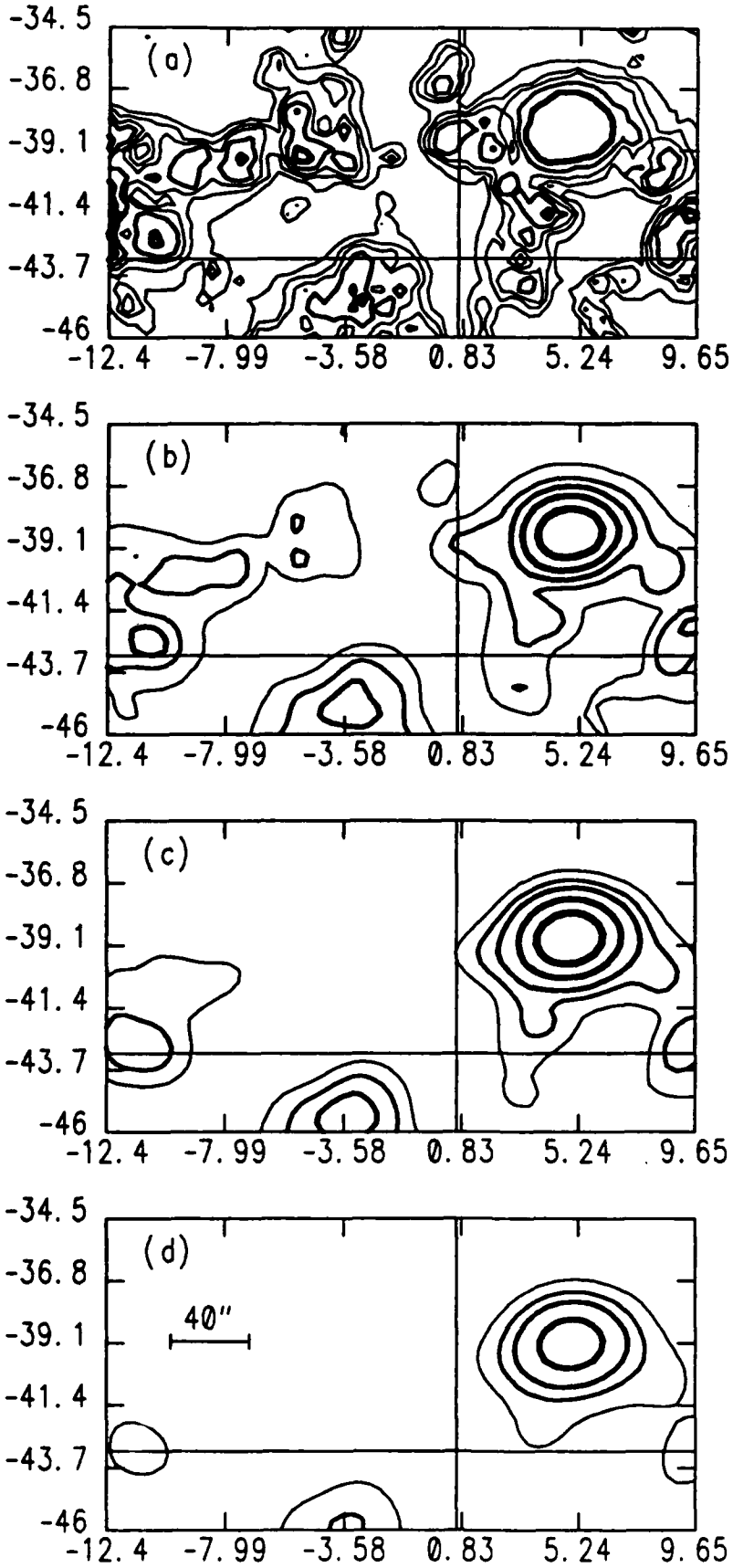

Fig. 4

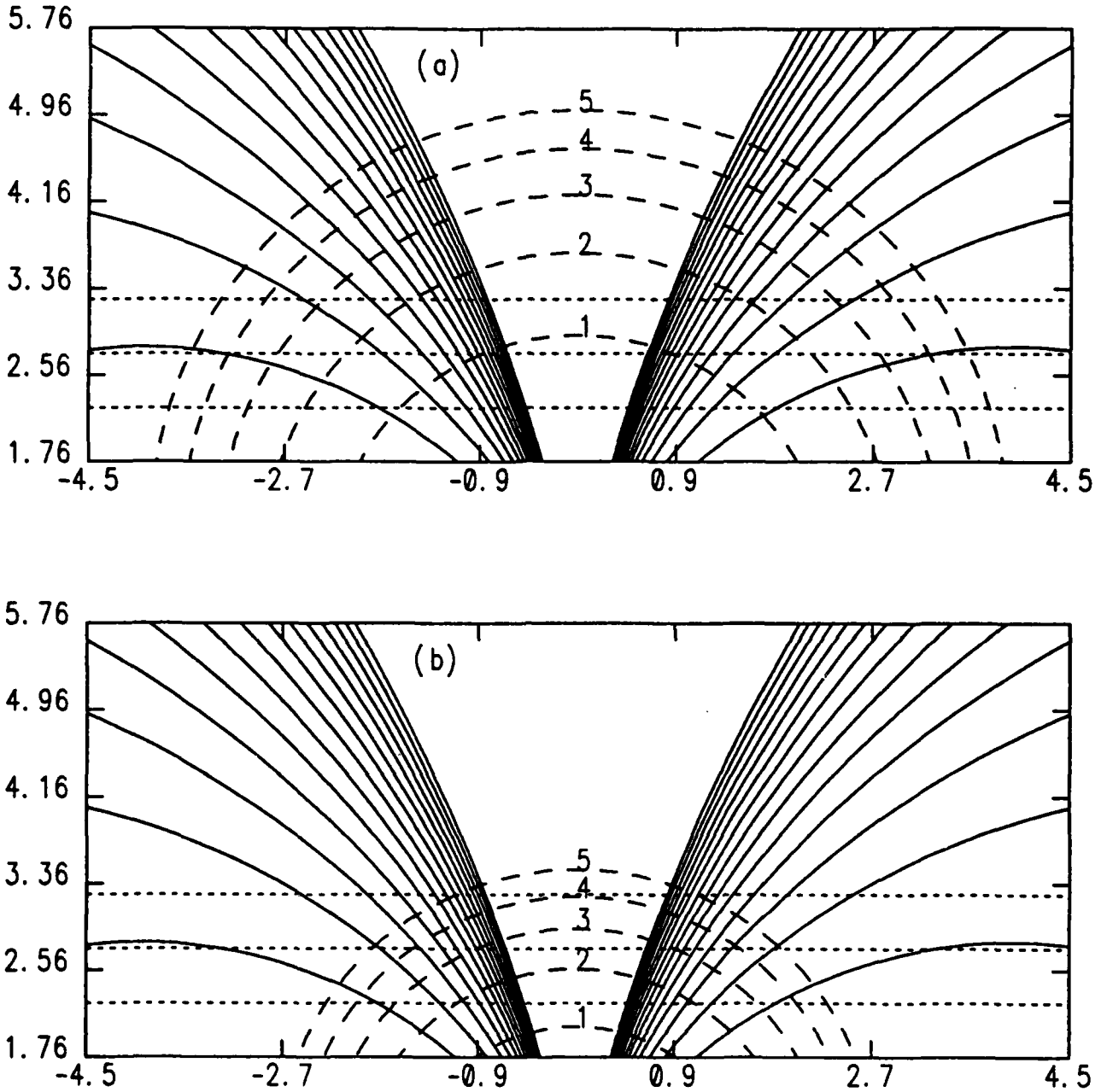
5.76
4.96
4.16
3.36
2.56
1.76
(a)
5
4
3
2
1
-4.5
-2.7
-0.9
0.9
2.7
4.5
5.76
4.96
4.16
3.36
2.56
1.76
(b)
5
4
3
2
1
-4.5
-2.7
-0.9
0.9
2.7
4.5

Fig. 5

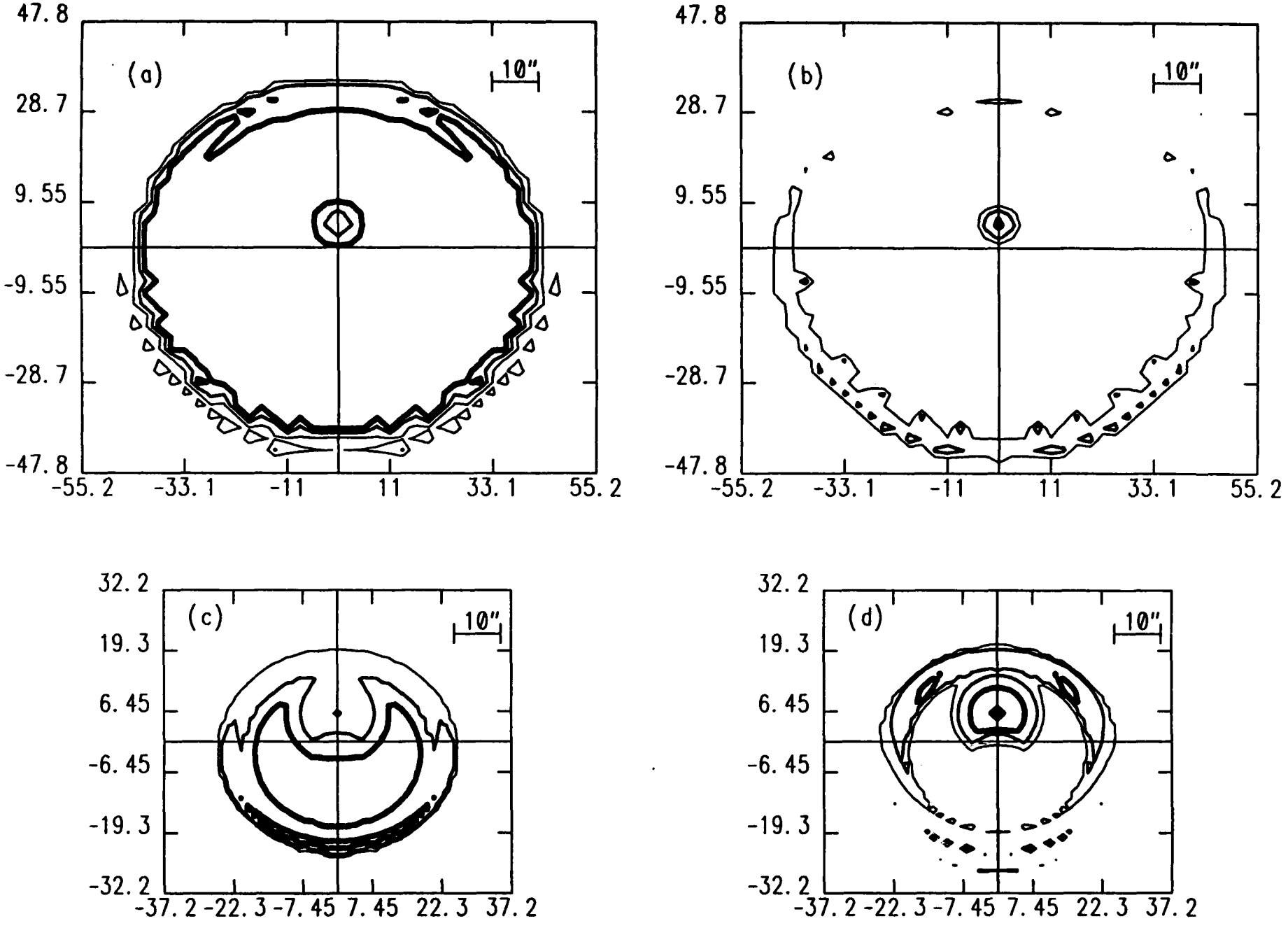
(a)
10"
47.8
28.7
9.55
-9.55
-28.7
-47.8
-55.2
-33.1
-11
11
33.1
55.2
(b)
10"
47.8
28.7
9.55
-9.55
-28.7
-47.8
-55.2
-33.1
-11
11
33.1
55.2
(c)
10"
32.2
19.3
6.45
-6.45
-19.3
-32.2
-37.2
-22.3
-7.45
7.45
22.3
37.2
(d)
10"
32.2
19.3
6.45
-6.45
-19.3
-32.2
-37.2
-22.3
-7.45
7.45
22.3
37.2

Fig. 6

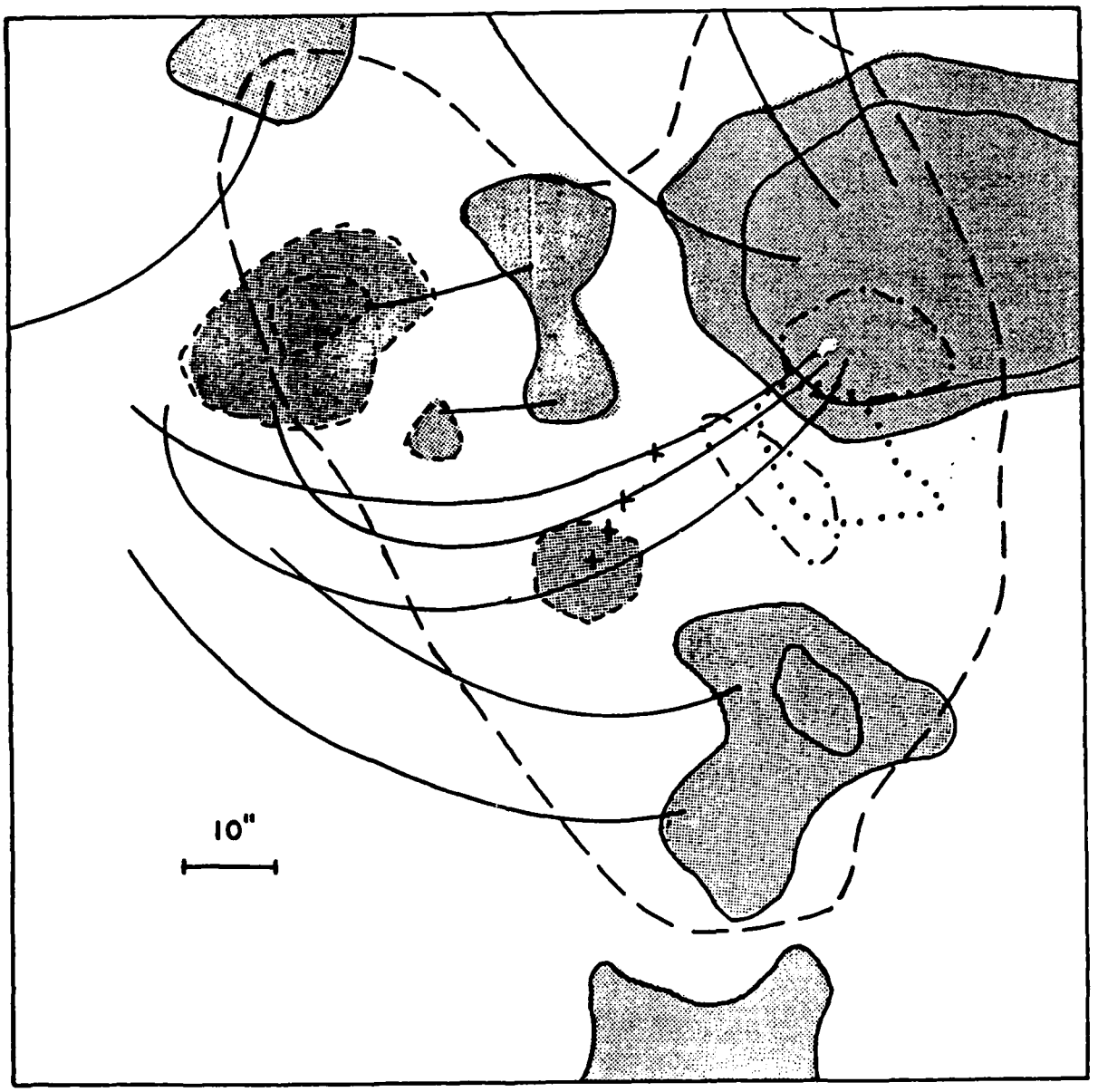

Fig. 7

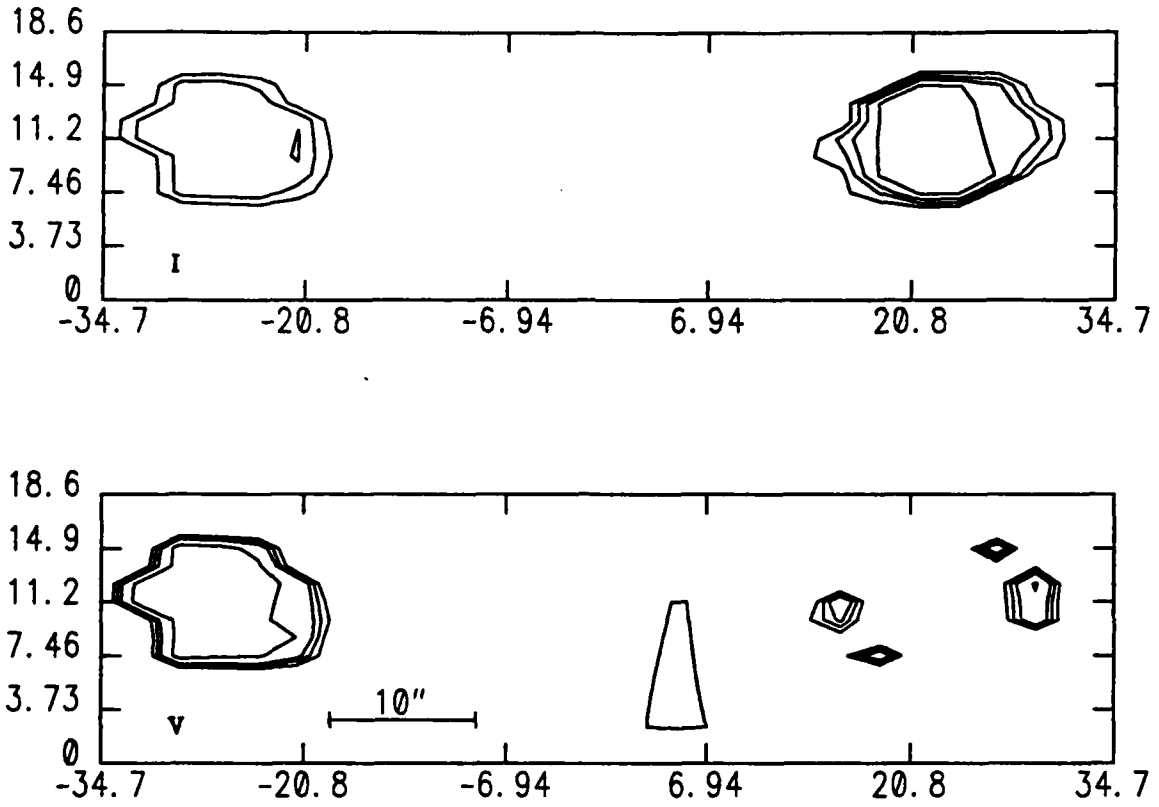
18.6
14.9
11.2
7.46
3.73
0
I
-34.7
-20.8
-6.94
6.94
20.8
34.7
18.6
14.9
11.2
7.46
3.73
0
V
10"
-34.7
-20.8
-6.94
6.94
20.8
34.7

Fig. 8

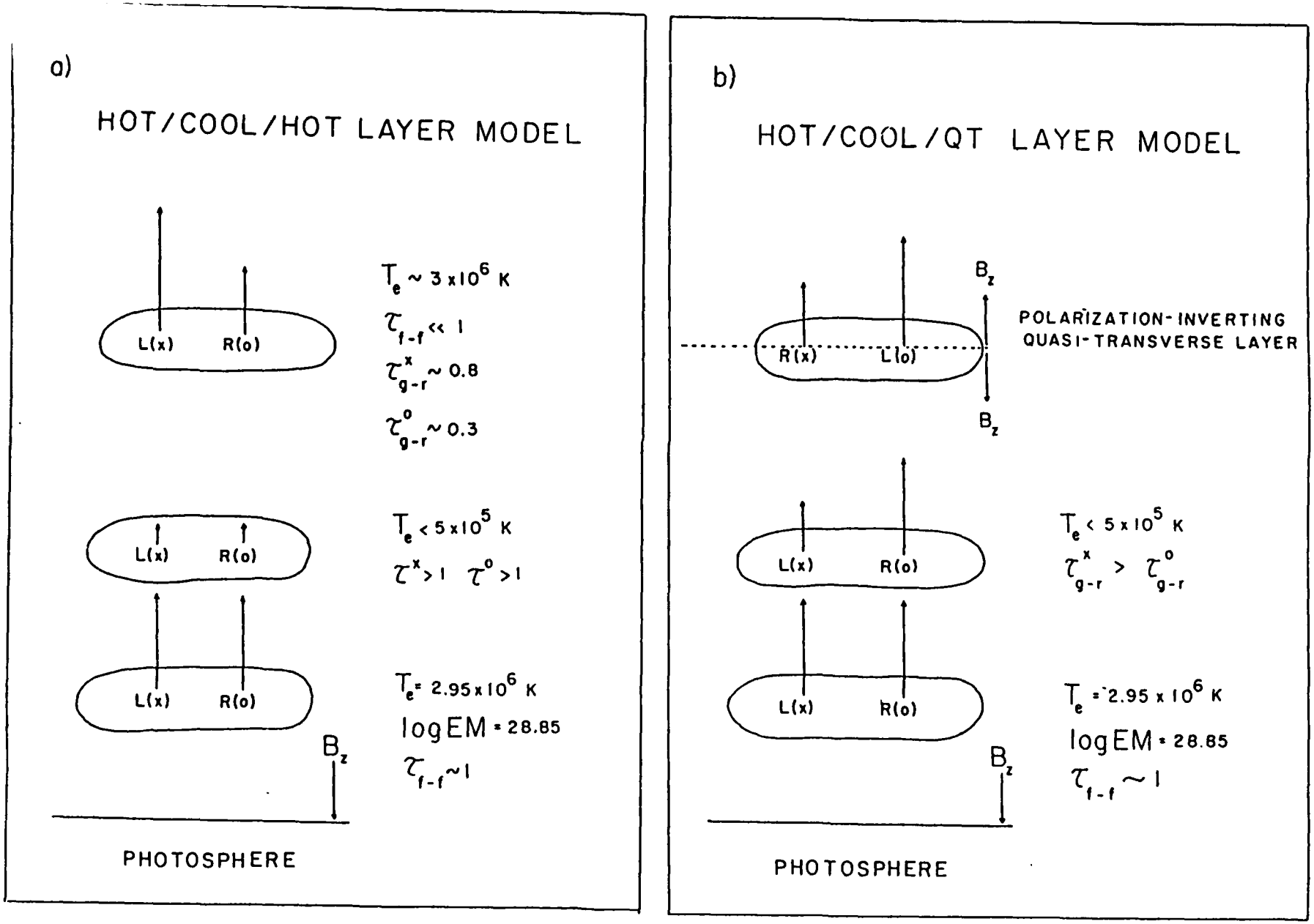
a)
HOT/COOL/HOT LAYER MODEL
L(x)
R(o)
$T_e \sim 3 \times 10^6$ K
$\tau_{f-f} \ll 1$
$\tau^x_{g-r} \sim 0.8$
$\tau^o_{g-r} \sim 0.3$
$T_e < 5 \times 10^5$ K
$\tau^x > 1$ $\tau^o > 1$
$T_e = 2.95 \times 10^6$ K
log EM = 28.85
$\tau_{f-f} \sim 1$
B_z
PHOTOSPHERE
b)
HOT/COOL/QT LAYER MODEL
R(x)
L(o)
POLARIZATION-INVERTING
QUASI-TRANSVERSE LAYER
$T_e < 5 \times 10^5$ K
$\tau^x_{g-r} > \tau^o_{g-r}$
$T_e = 2.95 \times 10^6$ K
log EM = 28.85
$\tau_{f-f} \sim 1$

Astron. Astrophys. 251, 298-306 (1991)

ASTRONOMY AND ASTROPHYSICS

D9.

Acceleration of electrons outside flares: coronal manifestation and possible origin

J.P. Raulin [1], R.F. Willson [2], A. Kerdraon [1], K.-L. Klein [1], K.R. Lang [2], and G. Trottet [1]

[1] Observatoire de Paris, Section de Meudon, DASOP and CNRS-URA 324, F-92195 Meudon, France
[2] Department of Physics and Astronomy, Robinson Hall, Tufts University, Medford, MA 02155, USA

Received March 11, accepted April 8, 1991

Abstract. Imaging observations at decimetric and metric wavelengths of the solar corona are used to investigate a short-lasting noise storm and the associated changes of the underlying active region plasma. It is shown that a new source appears in the active region in close temporal and spatial coincidence with the onset of the noise storm in the middle corona. The onset of the noise storm is delayed at longer wavelengths. At a given wavelength, the noise storm source undergoes a systematic slow movement with a significant component perpendicular to the magnetic field lines above the active region. The observations are tentatively attributed to the emission of nonthermal electrons in a system of expanding coronal loops, the expansion being initiated by the appearance of the new 21 cm source in the low atmosphere. The derived velocity of expansion is about 80 to 150 $km\,s^{-1}$. It is shown that the electrons emitting the noise storm cannot be provided by the high-energy tail of the Maxwellian in the new active region source, but originate either from a nonthermal population in this source or from acceleration at higher altitudes, in the structures which give rise to the noise storm. The new source in the active region underneath the noise storm is then considered as triggering the expansion of the overlying loop system in which the noise storm is emitted.

Key words: acceleration mechanisms – Sun: activity – Sun: bursts – Sun: corona – Sun: radio radiation

1. Introduction

Noise storms at decimetric and metric wavelengths are the oldest known evidence of particle acceleration (electrons of some keV to several tens of keV) in a stellar corona outside violent transient processes such as flares. This type of emission consists of a continuum and superposed short-lasting, narrow-band (~1 s, 1 MHz) bursts. Noise storms occur mostly above active regions and can be maintained over timescales of hours or even days. The reader is referred to Elgarøy's monograph (1977), to Benz & Zlobec (1982) and Kai et al. (1985) for more detailed information.

Despite fourty years of investigation the origin of noise storms, i.e. the radiation mechanism and the energy source, have still not been definitely identified. A general consensus exists nevertheless that the radiation is emitted at or close to the plasma frequency. No *systematic* association with chromospheric or photospheric phenomena has been disclosed so far. Some observations show that a violent perturbation of the coronal magnetic field can coincide with particularly intense noise storms. This evidence includes the eruption of prominences (McLean 1973; Webb & Kundu 1978; Kundu & Gopalswamy 1990) and the launch of a white-light coronal transient (Lantos et al. 1981; Lantos 1982; Hildner et al. 1986, Sect. 6.2.1.5). These phenomena are particularly energetic and are neither a necessary nor a sufficient condition for noise storm onsets.

A more systematic relationship between noise storms and morphological changes in the corona has been discovered with sensitive imaging observations: Stewart et al. (1986) showed that the onset of noise storms follows the formation of extended, dense loops in the middle corona. The timing of the noise storm onset with respect to the appearance of an active region in X-rays (Stewart et al. 1986) and to the intensification of microwave emission ascribed to the gyroresonance process (Kai & Sekiguchi 1973; Sakurai 1975) suggests that the conditions for a noise storm to occur are set up by changes in the magnetic structure of the underlying active region. The time difference between the modification of the magnetic field structure and the onset of the noise storm is of the order of 1 d, corresponding to the expansion of the magnetic flux into the corona at a velocity of ~1 $km\,s^{-1}$.

On shorter timescales noise storm onsets and enhancements are related to the addition of new material to the corona (Kerdraon et al. 1983). This process evolves on timescales of the order of 1 h at most. In the study by Kerdraon and coworkers it was not possible to state whether the addition of matter was a signature of a local re-arrangement of the coronal magnetic field or the consequence of processes in the lower atmosphere.

Given the different types of association found so far, it may be speculated that a spectrum of dynamical changes of the corona is related to noise storms, and that the less spectacular modifications related to weak and average noise storms most often escape detection. Structural changes of the white-light corona below noise storm sources have not been accessible to space-borne coronagraphs so far. Interferometric observations in the microwave range can image active regions on both the disk and the limb with sufficient temporal resolution. They are sensitive enough to detect small changes in the brightness and the structure of the active region outside flares.

Using multiple-wavelength observations at decimetric and metric wavelengths with the Very Large Array and the Nançay Radioheliograph, we provide evidence that a short noise storm is triggered from the low atmosphere: A new source is seen at 21 cm wavelength in the active region underneath the location of and

Send offprint requests to: J.P. Raulin

immediately preceding a noise storm in the middle corona. The timing at all wavelengths and the movement of the noise storm source are interpreted in a scenario where the noise storm occurs in a system of expanding loops. The observations then suggest that the expansion is initiated by the appearance of the new structure revealed at 21 cm. The outline of the paper is as follows: Sect. 2 summarizes the properties of the instruments. The observational results are presented in Sect. 3, and a tentative interpretation is given in Sect. 4. Section 5 summarizes the results and discusses the role of the new source in the active region in the excitation of the noise storm.

2. Instruments

The observations reported below were carried out conjointly with the Very Large Array (VLA) and the Nançay Radioheliograph (NRH; The Radioheliograph Group 1989). The VLA observations were carried out at 327 and 1446 MHz, from 13:30 UT to 16:30 UT on 1988 June 8, in the C/D array. In this configuration, the outermost antennas of the southeast and southwest arms are located at a distance of 0.59 km from the array centre, while the most remote antenna of the north arm is located at 1.9 km from the centre. The NRH observed the Sun from 8 UT to 15:50 UT. It provides six independent data sets, at 164 MHz with both east-west and north-south arrays, and at four further frequencies with the north-south array. The characteristics of the instruments are summarized in Table 1. At all wavelengths the beamwidths of the individual antennas cover the whole Sun.

Both instruments were calibrated according to their own standard procedure (Bastian 1989; The Radioheliograph Group 1989). The radio source 3 C 48 was observed by the VLA for 5 min every 40 min. Its flux density is 14.6 Jy and 47.0 Jy at 20.7 cm and 91.6 cm, respectively (VLA calibrator list). A good agreement was found between fluxes measured at 327 MHz with both instruments. VLA maps were made by the standard CLEAN algorithm provided by the AIPS package. Self calibration was tested on a few 21 cm maps, but gave no improvement.

3. Observational results

3.1. Overview of the radio emission from AR 5036

The radio sources studied below are associated with AR 5036, which is located S 17 E 35 on 1988 June 8. Figure 1 a shows the Hα

Table 1. Summary of instrumental characteristics

Observed frequency (MHz)	Clean beam (FWHM)	Bandwidth (MHz)	Sampling time (s)
Very Large Array			
1446	27″ × 70″	12.5	3.33
327.5	80″ × 300″	0.781	3.33
Nançay Radioheliograph			
339	92″	0.7	0.25
327	96″	0.7	0.25
322	97″	0.7	0.25
236.6	132″	0.7	0.25
164	96″/192″	0.7	0.05/0.25

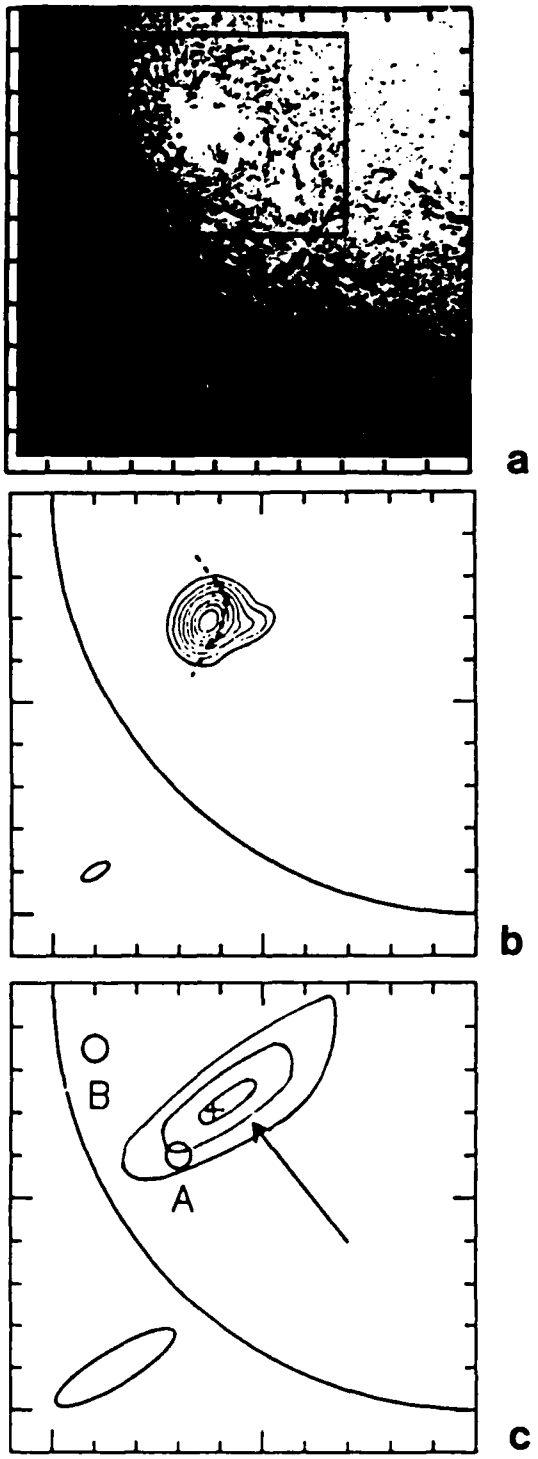

Fig. 1. a Hα image taken with the Meudon Spectroheliograph on 1988 June 8 at 7:12 UT. AR 5036 is surrounded by the frame in which maps at 21 cm-λ are plotted in Fig. 3. b Quiescent emission at 21 cm, observed between 13:30 UT and 14:40 UT with the VLA. Peak brightness temperature 1.6 10^6 K, first level 4.8 10^5 K, contour interval 1.6 10^5 K. The dashed line denotes the inversion of the magnetic field along the line of sight. The half-power level of the beam is drawn in the lower left corner. c Noise storm sources prior to 15 UT: Map at 92 cm synthesized between 13:30 UT and 14:50 UT with the VLA (first level 7 10^6 K, contour interval 2.7 10^6 K, peak 1.9 10^7 K). The cross and circles give the centroid positions at 92 and 127 cm, respectively, observed with the NRH between 8 UT and 13 UT. The arrow indicates the first position of the new noise storm observed at 92 cm with the VLA after 15 UT. The half power level of the beam is drawn in the lower left corner

image taken at Meudon at 07:12 UT. The box represents the frame around the active region in which 21 cm maps will be plotted below (Fig. 3). The active region is of $\beta\gamma$ type in the Mt. Wilson classification (Solar Geophysical Data 558 I). The radio emissions from AR 5036 prior to the noise storm analyzed below are summarized in Figs. 1 b and c. Figure 1 b shows the 21 cm radio emission observed with the VLA between 13:30 UT and 14:40 UT. This emission comes from a source with dimensions of roughly $1' \times 1'$, with a westward extension. An Hα flare is reported in AR 5036 between 13:40 UT and 13:50 UT with maximum at 13:41 UT (Solar Geophysical Data). The VLA did not observe the sun between 13:43 UT and 13:50 UT due to a calibration period. In the minutes preceding and following the calibration, the flux varies by about 10%, but no change is detected in the structure of the active region and in the location of the brightest emission until 14:50 UT. The dashed line in Fig. 1 b is the main line of inversion of the (line of sight) magnetic field. The maximum uncertainty of the alignment of the VLA maps with the optical image is about 10", i.e. much smaller than the beam width. Hence at 21 cm the brightest emission of the active region appears to come from a source overlying the line of field reversal. No significant circular polarization was detected. The extension of the 21 cm source points to a region where a parasitic polarity is detected in the magnetograms. It is close to this parasitic polarity that a new source will appear around 14:50 UT, immediately preceding the onset of the noise storm which will be discussed below.

At decimetre- and metre-wavelengths a noise storm is observed since 8 UT by the NRH and since 13:30 UT by the VLA. The VLA map at 92 cm-λ (327 MHz) is plotted in Fig. 1 c together with positions of the centroids of the sources at different wavelengths observed with the NRH. The cospatial sources at 68 cm (435 MHz), 73 cm (408 MHz) and 92 cm are indicated by the cross. Positions at 1.27 m (236.6 MHz) are shown by the circles "A" and "B". The centroid positions have been derived from earth rotation synthesis of 1 D scans of the NRH north-south branch during four hours (cf. Radioheliograph Group 1989). No emission at 1.83 m (164 MHz) is observed from this noise storm. At 1.27 m-λ source A is part of the noise storm observed at shorter wavelengths. The emission is 80% left hand circularly polarized at all wavelengths corresponding to the ordinary mode with respect to the dominating photospheric field in the leading part of the active region. Source B is located at a position shifted north-east with respect to AR 5036. This emission is right hand cricularly polarized, consistent with a magnetic structure anchored in the trailing part of AR 5036. We did not investigate whether a physical link exists between sources A and B or whether they belong to different noise storms. The ensemble of noise storm sources described above will be referred to as "permanent" in the following, whenever it will be necessary to distinguish them from the noise storm starting around 15 UT, which is of prime interest in this paper.

3.2. Noise storm emission and modification of the structure of the active region after 14:45 UT

3.2.1. Overview of the noise storm emission

At metre- and decimetre-wavelengths the flux density starts to rise around 15 UT and maintains an enhanced level for 50 min or longer, depending on the wavelength. The VLA did not observe the onset of the emission at 92 cm because of a calibration period between 14:58 and 15:08 UT. In the first 1 min map thereafter, emission is seen from a new source southwest of the preexisting noise storm, as indicated by the arrow in Fig. 1 c. The time profile of the flux density (Fig. 2) consists of two components: a slowly varying continuum extending from wavelengths shorter than 88 cm to 1.83 m, and superposed shortlasting bursts which dominate the time profile at longer wavelengths. Both the continuum and most of the bursts are nearly 100% polarized. The emission is rather weak so that terrestrial interference may be noticeable. This probably causes the quasiperiodic variations of the flux density seen at 88 cm wavelength. The brightness temperature rises from $2\ 10^7$ to $6\ 10^8$ K at 92 cm. No Hα flare or prominence eruption is reported in association with this event. These properties characterize the radio event as a noise storm (of rather short duration). The noise storm will be analyzed with more detail in Sects. 3.2.3 and 3.2.4.

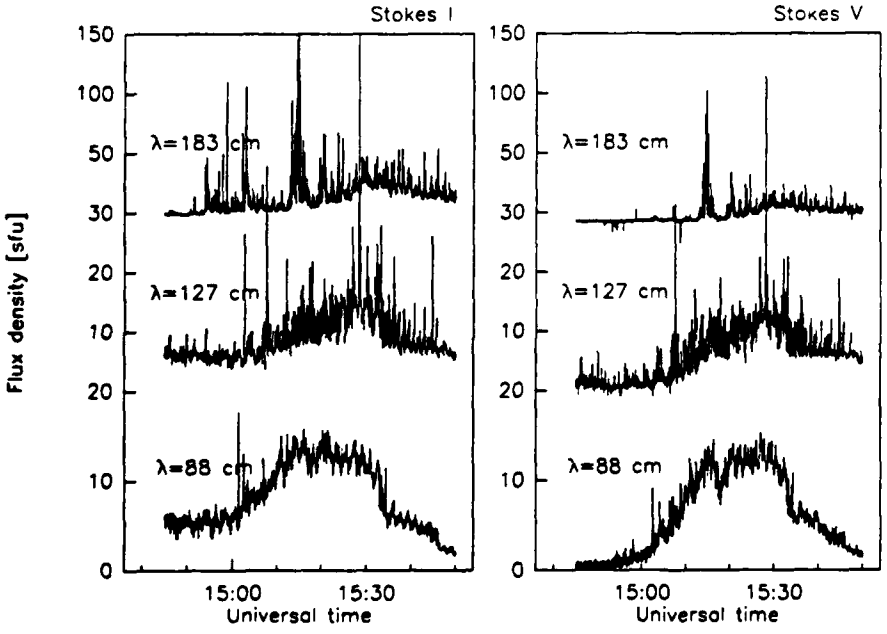

Fig. 2. The time profiles of noise storm emission observed with the Nançay Radioheliograph in total (left panel) and circularly polarized (right panel) flux densities. Observations with the east-west branch are shown at 1.83 m, with the north-south branch at the other wavelengths. Integration time is 1 s. The emission consists of a wide-band continuum with superposed bursts. The quasiperiodic fluctuations at 88 cm are probably due to terrestrial interference

Bursts are visible at 1.83 m prior to the onset of the noise storm continuum (Fig. 2). These as well as some of the bursts occurring during the continuum are unpolarized. Isolated unpolarized bursts are observed at similar positions already 30 min before the period shown in Fig. 2. Both the timing and the polarization characteristics suggest that the unpolarized bursts are not related to the noise storm studied in this paper. They will not be further discussed.

3.2.2. Magnetic structure of the underlying corona

The onset of the noise storm in the middle corona is preceded by a change in the emission from the thermal plasma of the active region observed at 21 cm. While a rather constant level of emission from a simple source was observed before 14:47 UT (Fig. 1b), the flux density rose and a new source appeared around 14:50 UT in the southwestern part of the previously existing, and persisting, source, near the extension seen in Fig. 1b. The new emission comes from a site which in projection on the solar disk is close to the source of the new noise storm at longer wavelengths. It persists at the same location until 16:10 UT, after which time it is covered by the background of growing emission from the main active region source. Contours of equal brightness temperature of the 21 cm source are plotted in Fig. 3. The map at 14:50 UT shows the situation of the active region immediately prior to the appearance of the new source. The centroids of noise storm positions at 92 and 183 cm are indicated in the later maps. While the structure of the active region remains qualitatively unchanged from the appearance of the new source until 16:10 UT, the noise storm sources are seen to gradually shift towards north-east during the event. This motion will be further discussed in Sect. 3.2.4.

3.2.3. The timing of emissions at different wavelengths

In order to identify the onset time of the emission at different wavelengths we compute time-averaged values of the flux densities at (or near) the sites of the new sources during some minutes prior to their appearance, and look for the instant when the average value was exceeded by 3 standard deviations. This instant is called the starting or onset time at a given wavelength.

At 21 cm the determination of the onset is made difficult by the variation of the underlying previously existing source of quiescent emission. Figure 4 shows the relative variations of the flux densities for the quiescent source and the new source. It is seen that emission from the new source begins to increase relative to the main source between 14:49 and 14:51 UT. We therefore consider 14:50 UT as the time where the new source appears.

The noise storm occurs at a position which in projection onto the north-south baseline of the NRH is close to the permanent noise storm observed since 8 UT. To estimate the onset time of the new noise storm continuum, we attempt to eliminate the bursts: At a given position of the one dimensional brightness distribution an average (running mean) intensity is computed over a specified time interval. The intensity attributed to the position at the instant under consideration is the minimum of the original and the average value. This procedure is applied to the whole spatial extent of the source during the event. It is iteratively performed with increasingly large time intervals (3, 5, and 7 s). After that the intensities are averaged with one minute integration time. The time histories of the flux densities computed after this procedure, after subtraction of the contribution from the quiet Sun and after correction of terrestrial interference are plotted in Fig. 5a. The flux densities have been multiplied by a factor which corrects for

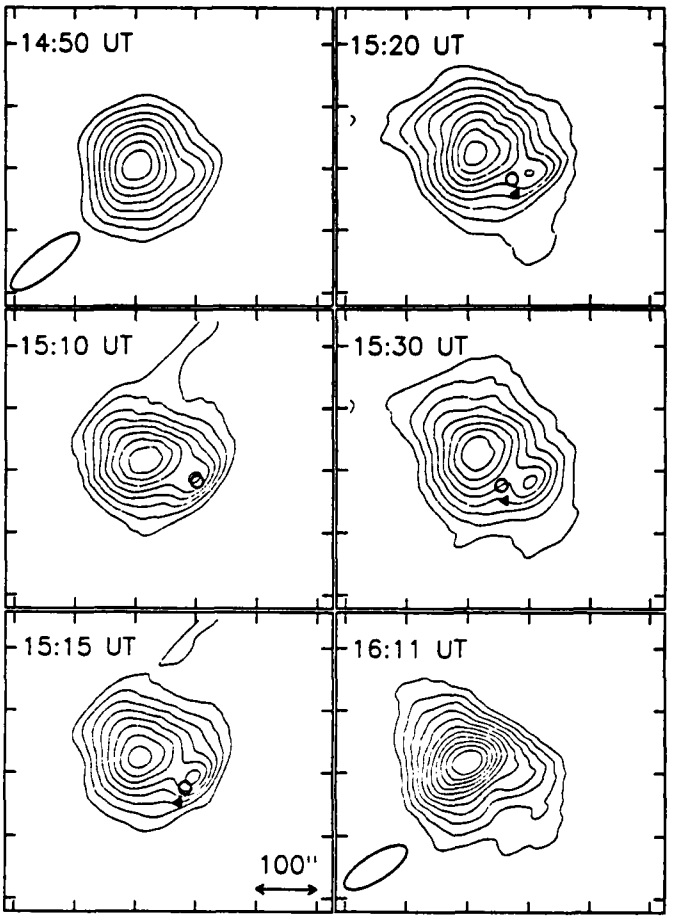

Fig. 3. Maps of the active region at 21 cm and centroid positions of the noise storm at 92 (circles) and 183 cm (triangles). The frame used is overlaid upon the Hα photograph in Fig. 1a. The same contours of equal brightness temperature are used in each plot. The lowest level of each map is 1.25 10^6 K, the contour interval 4.2 10^5 K. The peak brightness temperature before 16 UT is 2.9 10^6 K at 15:30 UT. The half-power level of the beam at 21 cm is drawn in the lower left corner of the first and the last map

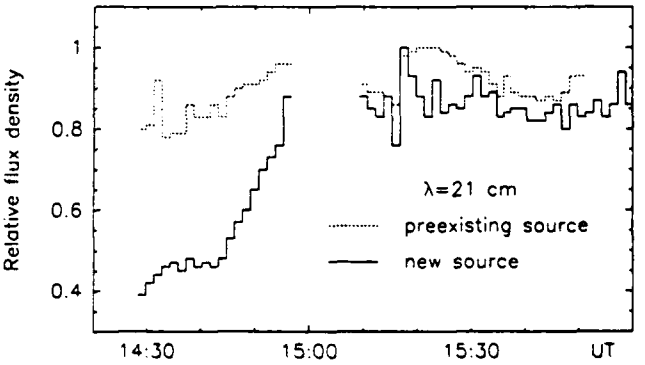

Fig. 4. Time history of the relative flux densities of the quiescent active region source (dashed line) and the new source (solid line) at 21 cm. The flux densities have been calculated around the brightest points of each of the two sources and normalized to their maximum values (1.2 and 0.6 sfu for 30" × 30" boxes around the quiescent and the new source, respectively)

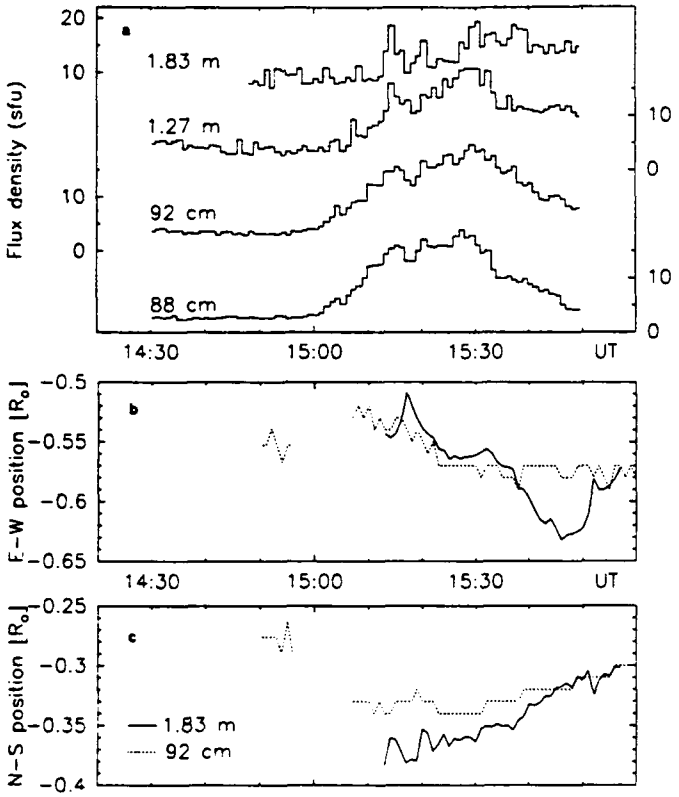

Fig. 5. **a** Time profiles of the flux densities of the noise storm continuum (1 min averages, NRH). Rapidly (~ 1 s) varying emissions have been removed prior to the integration (cf. Sect. 3.2.3).
b and c Heliographic east-west and north-south positions of the centroids of the noise storm sources at 92 cm (VLA, dashed line) and 1.83 m (NRH, solid line)

the decrease of the signal due to the fact that the antennas of the north-south branch stop tracking the sun at 15:15 UT (D. Rigaud, priv. comm.). The accuracy of the correction has been checked by comparison with the flux densities observed with the east-west branch of the NRH at 1.83 m and with the VLA at 92 cm. For the sake of homogeneity of the data observations with the north-south branch of the Radioheliograph are used at all wavelengths. Due to an unfavorable baseline orientation a different noise storm on the western hemisphere is also within the instrumental beam. However, comparison with the flux densities observed with the east-west branch at 1.83 m and with the VLA at 92 cm shows that the only effect due to this overlapping is the constant level of emission at 1.83 m seen in Fig. 5a after 15:40 UT. The other aspects of the time profiles are due to the noise storm under study. The following features in these time profiles are noteworthy:

1. the emission starts later at longer wavelengths,
2. the emission fades earlier at shorter wavelengths,
3. there are indications of common features at different wavelengths, like the peak at 15:15 UT and the valley around 15:18 UT.

The onset times of the emissions are summarized in Table 2. Once the emission has started at all observed wavelengths, there is no indication of spectral changes on the timescale seen in the onset delays. Before 15:18 UT, the spectral maximum is at wavelengths shorter than 90 cm, including some temporal variation which we cannot trace in detail with the available observations. Between 15:18 UT and 15:50 UT the spectral maximum of the continuum lies near 1.10 m, without any significant change.

Table 2. Onset times of radio emissions

14:47	Rise of the flux density at 21 cm
14:50	Appearance of a new source at 21 cm
15:01	Onset of the noise storm at 88 and 92 cm
15:07	Onset of the noise storm at 1.27 m
15:13	Onset of the noise storm at 1.83 m

3.2.4. Structure and movement of the noise storm sources

The sources of the noise storm are simple both at 92 cm (VLA) and at 1.83 m (NRH). Their sizes are somewhat greater than the instrumental beam. No variation of the size by more than 30% could be detected during the noise storm at either wavelength. The source motion seen in Fig. 3 is shown with more detail in Fig. 5b, c, where the temporal evolution of the centroid positions is plotted separately for the heliographic east-west and north-south directions. At both wavelengths an irregular motion is superposed upon a general trend towards north-east, with a change of direction in the late phase of the emission. At 92 cm (dashed line) the noise storm undergoes a systematic eastward displacement at constant north-south position until 15:23 UT ($v = 26\,\mathrm{km\,s^{-1}}$). Observations with the north-south branch of the NRH suggest that this movement starts at the onset of the noise storm at 92 cm, but two-dimensional maps are not available at this time. This movement occurs during the first rise and fall of the flux density until 15:18 UT. Then the source remains at the same east-west position, while slowly shifting towards heliographic north ($v = 15\,\mathrm{km\,s^{-1}}$) throughout the phases of maximum and decreasing flux density. At 1.83 m (solid line) the source exhibits an initial eastward displacement, with an irregular behaviour along the north-south axis. After 15:17 UT it undergoes a systematic shift northward with four periods of different motion in the east-west direction: two periods of eastward motion from 15:17 to 15:25 UT ($v = 75\,\mathrm{km\,s^{-1}}$) and from 15:32 to 15:46 UT ($v = 71\,\mathrm{km\,s^{-1}}$) are separated by seven minutes at roughly constant east-west position, and followed by a reversed motion (westward) after 15:47 UT ($v = 96\,\mathrm{km\,s^{-1}}$). At both 92 and 183 cm the most intense emission occurs after the first period of motion.

In Fig. 6a, b the source positions at 92 and 183 cm are overlaid upon a drawing of field lines computed from a current-free extrapolation of the photospheric magnetic field (code and Kitt Peak Solar Observatory magnetic field data kindly provided by Drs. T. Sakurai and J. Harvey, respectively). The picture suggests that the initial source motions (before the reversals at 15:24 UT at 92 cm and at 15:47 UT at 183 cm) make a significant angle with the coronal magnetic field lines. Inspection of Big Bear magnetograms between 14 and 17 UT (courtesy S. Martin and H. Wang) did not reveal any significant changes of the magnetic structure.

3.3. Soft X-ray emission

No soft X-ray event has been reported during the period of the noise storm emission. However, inspection of the GOES fluxes shows that during the period 14:30 to 16 UT the emission in the 1–8Å band varies between minima of $6.5\,10^{-7}\,\mathrm{W\,m^{-2}}$ at 14:48 and 15:47 UT, and peak levels of $7.3\,10^{-7}\,\mathrm{W\,m^{-2}}$ and $7.1\,10^{-7}\,\mathrm{W\,m^{-2}}$, respectively, at 15:14 and 15:22 UT. The flux increase of the event is hence similar to the soft X-ray burst accompanying the filament eruption and noise storm onset reported by Kundu & Gopalswamy (1990) and of the event preceding the noise storm onset reported by Lang & Willson

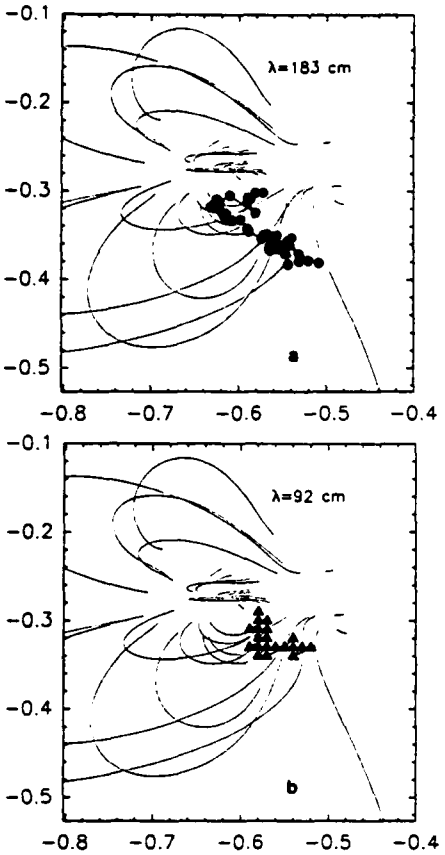

Fig. 6a and b. Heliographic positions of source centroids at 92 cm (b) and 1.83 m (a) are superposed upon field lines derived from a current-free extrapolation of the photospheric magnetic field observed at Kitt Peak Observatory at 15:43 UT (code courtesy Dr. T. Sakurai, field measurements courtesy Dr. J. Harvey). The movement of the radio sources is eastward (north-eastward), then northward (westward) at 92 (183) cm

(1987). In both cases the soft X-ray event is clearly identified because of the low level of activity at the time of these observations.

A detailed spectral analysis of the GOES observations of 1988 june 8 is not possible because the relevant signal is smaller than the presumable background (cf. discussion by Bornmann 1990). Assuming $T = 7\ 10^6$ K as observed with HXIS in another case of noise-storm associated X-ray emission (Švestka et al. 1982a) yields an emission measure of $2\ 10^{47}\ cm^{-3}$.

4. Interpretation

4.1. Brightening of a new source at 21 cm

The key feature of the reported observations is the brightening of a new structure in the active region underneath the location of, and prior to, the development of the noise storm. The new source appears close to a parasitic polarity in the magnetic field of the leading part of the active region. The physical nature of the modification of the active region cannot be elucidated from the available observations. The properties of the 21 cm emission are consistent with bremsstrahlung from the thermal plasma. The absence of significant ($> 30\%$) circular polarization throughout the period where the secondary source exists suggests that gyroresonance emission is unimportant. The brightness temperature of the new source does not seem to exceed $2\ 10^6$ K, so that the emission is probably not optically thick (note, however, that the exact determination of the brightness temperature is made difficult by the underlying emission from the main source in the active region). The brightening of the secondary source can then be attributed to the emergence of a new structure, to mass input into a pre-existing structure, or to a combination of both. Either of these processes may serve as a trigger of mechanisms which lead to the acceleration of electrons eventually seen in the noise storm emission at greater heights. Habbal et al. (1989) observed that in coincidence with a noise storm onset the brightest emission of the underlying active region at 21 cm changes from its previous location and starts wandering around between different points within a complex spatial pattern. However, in their case of a complex active region structure it seems difficult to associate a specific feature of the active region with the brightening of the storm emission.

4.2. Frequency drift and source motion at fixed wavelengths

The delay of the onset of radio emission at subsequently longer wavelengths indicates that either the energetic electrons radiate in sources of successively lower density, or that the low frequency radiation can escape from the source only in the later phases of its evolution. Judging from the large delay between the onset times, the access to the regions of lower density is opened on timescales which are long compared with timescales of particle propagation along magnetic field lines, and rather correspond to particle diffusion perpendicular to the magnetic field or to hydrodynamic processes. Similarly long delays have been observed precedingly (McLean 1973; Akinyan et al. 1978; Lantos et al. 1981; Kundu & Gopalswamy 1990). Such delays were generally attributed to the emergence of magnetic flux into the solar corona or to the expansion of magnetic loops (which confine the radiating electrons). In the event reported by Lantos et al. the expanding loop scenario was corroborated by the observation of a white-light coronal transient. As a consequence of the expansion, the density in the loop decreases, in competition with mass injection into the loop, and the loop propagates into an environment of ever lower density. When mass injection is negligible, a given plasma level is expected to sink in the course of the expansion. This would be visible on maps at radio wavelengths. The inward motion of noise storm sources observed by Dulk & Altschuler (1971) and McLean (1973) may be indicative of this. The source motion observed by Lantos et al. was explained by a combination of downward motion due to the rarefation and outward motion due to the expansion of the field lines (cf. Hildner et al. 1986, Fig. 6.2.16).

Such a geometry does not seem to fit with the 1988 June 8 noise storm. Besides an apparent upward motion along extended loops, sources both at 92 and 183 cm seem to have a significant velocity component perpendicular to the field lines of the extrapolated potential field. If this is the correct interpretation of Fig. 6, emission during the whole duration of the noise storm comes from the legs of magnetic loops anchored in the vicinity of the new source at 21 cm. Emission from the legs is also consistent with the constant and high degree of circular polarization observed throughout the duration of the noise storm. If the displacement of the noise storm sources at fixed wavelengths reflects the displacement of the corresponding plasma levels, this configuration is qualitatively consistent with a scenario where the active region in the middle corona consists of a three-dimensional system of magnetic loops where the density decreases both with height and

with distance on either side of a central plane containing the long axis of the active region. If the system of loops expands in a nearly isotropic way, a given plasma level will carry out an inward motion, approaching the central plane. This movement will proceed as long as the considered density level has not attained the inner region of the loop system where the initial density was highest. Once this region has been reached, any further quasi-horizontal shift would lead into regions of lower density. At this place a given plasma level will sink towards the photosphere. This scenario is interesting in that it explains qualitatively the two most evident features of the observed movement at 92 and 183 cm:

1. the initial motion, which in the described scenario is directed towards the central plane of the loop system as a consequence of the expansion;

2. the evolution of the movement in the late phase of the noise storm, where an apparent downward movement ($\lambda = 1.83$ m) or a sharp directional change ($\lambda = 92$ cm) of the source are seen.

The onset of the noise storm and its delay at longer wavelengths might be explained by injection of energetic electrons into relatively dense loops, which do not allow emission at long wavelengths to escape before appropriate densities have been established in the course of expansion. In order to estimate the required expansion velocity, we suppose a loop system rises into the corona at constant speed v_{exp}. Its height at time t is given by

$$h(t) = h_0 + v_{exp}(t - t_0). \quad (1)$$

Its volume is supposed to vary as h^α, where for a loop with height small compared with the gravitational scale height $\alpha = 1$ describes expansion with constant cross section, $\alpha = 3$ expansion with constant diametre-to-height-ratio of the loop. If the loop height is greater than the gravitational scale height, the latter case is described by $\alpha = 2$. Assuming that the injection of matter is negligible, the plasma frequency will vary as

$$\left[\frac{\nu_p(t_0)}{\nu_p(t)}\right]^{2/\alpha} = 1 + \frac{v_{exp}}{h_0}(t - t_0) \quad (2)$$

Figure 7 shows the observed time delays of Table 2 for various α. The abscissa is the time delay with respect to the onset of the emission at 92 cm (327 MHz). The ordinate displays the left hand side of Eq. (2), with $\nu_p(t_0) = 327$ MHz. The length of the horizontal bars denotes the 1 min integration time. The dashed lines give the least-squares fit of Eq. (2) to the data. It is seen that the time sequence of the onset of the noise storm at different wavelengths is consistent with a loop volume expanding like the square or the third power of its height. The expansion velocities derived from the measured onset times and Eq. (2) range from 80 to 150 km s^{-1} for an initial loop height of 10^4 km. Extrapolating this expansion back to the low atmosphere, the height of the loop system at the time where the new source appears at 21 cm is found to be smaller than $5 \cdot 10^4$ km. This comprises the altitude range where the 21 cm sources are expected. This result strengthens the conclusion that a close link exists between the appearance of the new source at 21 cm and the rising loop system in the overlying corona. It does not imply that the structure seen at 21 cm takes itself part in the expansion. The fact that a stable source is observed at least until 16 10 UT (and may exist afterwards) suggests on the contrary that the magnetic field structure is conserved. However, the timing of all these emissions is consistent with triggering of the process in the low corona, in the vicinity of the source seen at 21 cm.

Once the plasma has become sufficiently tenuous to support emission at all wavelengths, common features may occur at

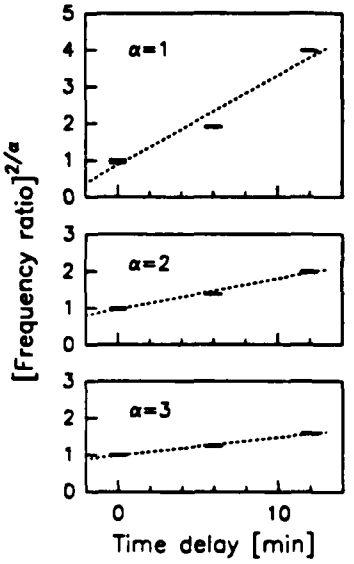

Fig. 7. Evolution of the onset times of plasma emission at different frequencies. The fraction $(327\text{ MHz}/\nu)^{2/\alpha}$ is plotted for $\alpha = 1, 2, 3$ (from top to bottom) as a function of the onset time of the corresponding emission listed in Table 2. α is a parameter describing the expansion of the emitting volume (cf. Sect. 4.2). The width of the horizontal bars is the 1 min integration time. The dashed line is a least squares fit of the four data points to a straight line

different wavelengths, in accordance with the observations. The continued expansion of the loop system becomes noticeable at the end of the noise storm through the change of direction of the movement. At 1.83 m a movement towards the photosphere is suggested by Fig. 6a. Assuming a hydrostatic stratification along the direction of motion, the downward velocity derived from our simple geometrical model is found to lie in the range 55 ($\alpha = 2$) to 75 ($\alpha = 3$) km s^{-1} (for an assumed scale height of 10^4 km), which is of the order of the observed value of 100 km s^{-1} (in projection on the disk).

5. Discussion and conclusion

Imaging observations over a wide range of radio wavelengths have been presented which show a temporal sequence of a modification of the structure of an active region and the onset of a noise storm at subsequently longer wavelengths in the overlying corona. The main characteristics of the noise storm are

1. the onset time increases with increasing wavelength at a mean rate of frequency drift of about 0.2 MHz s^{-1} between 92 and 183 cm;

2. at a given wavelength the noise storm source exhibits a motion with components along and across the large-scale magnetic field lines with a projected velocity of a few tens of km s^{-1}.

Simple considerations qualitatively suggest that both frequency drift and source motions can result from the three-dimensional expansion of a nest of loops, provided the electron density decreases with distance from the centre of the nest of loops.

The major and unexpected feature of the observations is the appearance of a new bright source at 21 cm. A causal link with the development of the noise storm at greater altitudes is suggested by

1. the proximity of the newly appearing structure in the active region and the noise storm,

2. the timing of the appearance of the new source in the active region with respect to the onset of the noise storm at different wavelengths, i.e. different altitudes.

The new structure might be considered as the energy reservoir for the noise storm. Such a model predicts a close relationship between the emission from the active region and from the nonthermal particles, which has occasionally been reported in the literature (Lantos et al. 1981; Švestka et al. 1982a, b). Two agents of the energy transport to the noise storm source may then be envisaged: diffusion of electrons or waves.

Achterberg & Kuijpers (1984) have considered the transport of electrons perpendicular to magnetic field lines due to low-frequency magnetic turbulence. They show that this process is far more efficient in the cross-field transport than regular (curvature, gradient) drifts. The particles can then either propagate directly across field lines from the active region to the noise storm source, or else diffuse over a relatively short distance into the feet of field lines connected with the noise storm in the middle corona, which they then reach by propagating parallel to the field lines. In either case the electrons would have to travel over distances of the order of 10^5 km in a medium with density larger than the critical plasma density at the emitting wavelength ($1.3\ 10^9\ cm^{-3}$ at 92 cm). Only energetic electrons ($E \geq 50$ keV) could achieve this. However, only 10^{-7} electrons with the appropriate energies can actually be supplied instantaneously by the thermal plasma at $7\ 10^6$ K. The energy they carry is negligible compared with the electromagnetic energy radiated by the noise storm. Hence if the energy needed to maintain the noise storm emission is directly supplied by the underlying active region, a suprathermal tail of particles is required in the low atmosphere. Then either the suprathermal particles themselves diffuse into the noise storm emitting structures or they generate electromagnetic waves (e.g. by the loss-cone instability) which subsequently accelerate electrons in the structures emitting the noise storm (cf. Sprangle & Vlahos 1983). In either case where the new 21 cm source is considered as the energy reservoir of the noise storm the energy requirements tend to be bigger than if the electrons drew their energy from the large-scale coronal magnetic field, because the energy losses in the relatively dense plasma at low altitudes are higher than in the middle corona. An observational clue to the presence of nonthermal electrons prior to the onset of the noise storm continuum would be impulsive decimetric emission around the time of appearance of the new source in the active region. No such emission shows up in our observations, but their spectral coverage is insufficient to definitely exclude this possibility. The type I bursts seen at 1.83 m before the onset of the continuum do probably not imply sufficient energy to be of relevance here.

As an alternative interpretation we speculate that the new source at 21 cm may be indicative of flux emergence by which the overlying large-scale magnetic structure is forced to expand or is driven unstable. Emerging magnetic flux is considered as an efficient means to provide the energy necessary to maintain noise storm emission (Spicer et al. 1981; Wentzel 1982). MHD analyses have shown that emerging flux can indeed drive an overlying magnetic arcade unstable (Zwingmann 1984; Ali 1990, 1991). For the noise storm studied in the present paper such a scenario is supported by the fact that the source appears above a parasitic polarity in the leading part of the active region. It is also consistent with previous observations by Stewart et al. (1986) which indicate that significant changes occur in the loop structure before the onset of the noise storm. These changes are correlated with the emergence of new magnetic flux in the vicinity of the active region. The delay between the first sign of newly emerging flux and the onset of the noise storm may indicate that the coronal arches must have a minimum size before they contribute to the re-arrangement of the magnetic field structures in which the noise storm is emitted (Brueckner 1983). Multiple wavelength observations at microwaves of active regions during the hours preceding the onset of noise storms would be of great interest to clarify this point.

We would finally note that there is some similarity of the onset of the noise storm reported in this paper with the onset behaviour of flares and coronal mass ejections: The emission in such events seems to imply the presence, and probably interaction, of observationally distinguishable magnetic structures (cf. Raoult et al. 1985; Machado et al. 1988; Harrison & Sime 1989; Willson et al. 1990). The difference lies in the timescales (minutes for noise storms and coronal transients rather than seconds in the case of flares) and in the energy budget, which is much smaller for the noise storm than for observable flares.

Acknowledgements. The authors acknowledge helpful dicussions with Drs. C. Alissandrakis, P. Lantos and C. Mercier. We also are grateful to Drs. J. Harvey, S. Martin and H. Wang for supplying the Kitt Peak and Big Bear Solar Observatory magnetograms. Radio astronomical studies of the Sun at Tufts University are supported under grant AFOSR-89-0147 with the Air Force Office of Scientific Research. Analysis of simultaneous Very Large Array and Solar Maximum Mission observations of the Sun are supported by NASA grant NAGW-2383. NRAO is operated by Associated Universites, Inc., under contract with the National Science Foundation. Collaborative solar observations by Tufts University and the Observatoire de Paris are supported by NSF grant INT-8602285 and CNRS grant 920038.

References

Achterberg A., Kuijpers J., 1984, A&A 130, 111
Akinyan S.T., Chertok I.M., Fomichev V.V., Korolev O.S., Böhme A., 1978, Phys. Solariterr. Potsdam 7, 5
Ali J.J., 1990, Phys. Fluids B2, 1928
Ali J.J., 1991, in Flares 22 Workshop Dynamics of Solar Flares, Schmieder B., Priest E. (eds.), Paris Observatory Publication, p. 29
Bastian T., 1989, in Synthesis imaging in radio astronomy, Perley R.A., Schwab F.R., Bridle A.H. (eds.), Astron. Soc. of the Pacific, p. 399
Benz A.O., Zlobec P., 1982, Proc. 4th CESRA Workshop on Solar Noise Storms, Trieste Observatory Publication
Bornmann P.L., 1990, ApJ 356, 733
Brueckner G.E., 1983, Solar Phys. 85, 243
Dulk G.A., Altschuler M.D., 1971, Solar Phys. 20, 438
Elgarøy O., 1977, Solar Noise Storms, Pergamon Press, Oxford
Habbal S.R., Ellman N.E., Gonzalez R., 1989, ApJ 342, 594
Harrison R.A., Sime D.G., 1989, J. Geophys. Res. 94, 2333
Hildner E., Bassi J., Bougeret J.L., et al., 1986, in Energetic Phenomena on the Sun, Kundu M.R., Woodgate B.E. (eds.), NASA CP-2439, p. 6-1
Kai K., Melrose D.B., Suzuki S., 1985, Radio Physics of the Sun, McLean D.J., Labrum N.R. (eds.), Cambridge University Press, Cambridge, p. 415
Kai K., Sekiguchi H., 1973, Proc. Astron. Soc. Australia 2, 217
Kerdraon A., Pick M., Trottet G., Sawyer C., Illing R., Wagner W., House L., 1983, ApJ 265, L19
Kundu M.R., Gopalswamy N., 1990, Solar Phys. 129, 133
Lang K.R., Willson R.F., 1987, ApJ 319, 514

Lantos P., 1982, in: Proc. 4th CESRA Workshop on Solar Noise Storms. Benz A.O., Zlobec P. (eds.) Trieste Observatory Publication, p. 247
Lantos P., Kerdraon A., Rapley C.G., Bentley R.D., 1981, A&A 101, 33
Machado M.E., Moore R.L., Hernandez A.M., Rovira M.G., Hagyard M.J., Smith J.B., 1988, ApJ 326, 425
McLean D.J., 1973, Proc. Astron. Soc. Australia 2, 222
Radioheliograph Group, 1989, Solar Phys. 120, 193
Raoult A., Pick M., Dennis B.R., Kane S.R., 1985, ApJ 299, 1027
Sakurai K., 1975, Planet. Spa. Sci. 23, 1344
Spicer D.S., Benz A.O., Huba J.D., 1981, A&A 105, 221
Sprangle P., Vlahos L., 1983, ApJ 273, L95
Stewart R.T., Brueckner G.E., Dere K.P., 1986, Solar Phys. 106, 107
Švestka Z., Stewart R.T., Hoyng P. et al., 1982a, Solar Phys. 75, 305
Švestka Z., Dennis B.R., Pick M., Raoult A., Rapley C.G., Stewart R.T., Woodgate B.E., 1982b, Solar Phys. 80, 143
Webb D.F., Kundu M.R., 1978, Solar Phys. 57, 154
Wentzel D.G., 1982, in: Proc. 4th CESRA Workshop on Solar Noise Storms. Benz A.O., Zlobec P. (eds.) Trieste Observatory Publication, p. 145
Willson R.F., Klein K.-L., Kerdraon A., Lang K.R., Trottet G., 1990, ApJ 357, 662
Zwingmann W., 1984, Thesis. Ruhr Universität Bochum

E1. VLA, PHOENIX and BATSE Observations of an X1 Flare

Robert F. Willson, Dept. of Physics and Astronomy, Tufts University, Medford, MA 02155
Markus J. Aschwanden, NASA/GSFC, Code 602.6, Greenbelt, MD 20771
Arnold O. Benz, Institute for Astronomy, ETH, CH-8082 Zürich, Switzerland

ABSTRACT: We present observations of an X1 flare (July 18, 1991) detected simultaneously with the Very Large Array (VLA), the PHOENIX Digital Radio Spectrometer and the Burst and Transient Source Experiment (BATSE) aboard the Gamma Ray Observatory (GRO). The VLA was used to produce snapshot maps of the impulsive burst emission on timescales of 1.7 sec at both 20 and 91 cm. Our results indicate electron acceleration in the higher corona ($h \approx 0.4$ - $0.5 R_\odot$) several minutes before the onset of the hard X-ray burst detected by BATSE. Comparisons with high spectral ($\Delta\nu = 3$ MHz) and temporal ($\Delta t = 40$ ms) observations by PHOENIX reveal a variety of radio bursts at 20 cm, such as type III bursts, intermediate drift bursts, and quasi-periodic pulsations during differnt stages of the X1 flare. From the drift rates of these radio bursts we derive information on local density scale heights, the speed of radio exciters, and the local magnetic field. Radio emission at 90 cm shows a type IV burst moving outward with a constant velocity of 240 km/s.

The described X1 flare is unique in the sense that it appeared at the east limb (N06/E88), providing the most accurate information on the vertical structure of different flare tracers visible in radio wavelengths.

1. GOES and BATSE/GRO data

We present some preliminary data from the sofar largest flare simultaneously observed by VLA, PHOENIX and GRO, which occurred on July 18, 1991. A GOES X1-class soft X-ray event was reported near the east limb (North 06 , East 88) in NOAA/USAF active region 6734, starting at 1425 UT, with maximum at 1441 UT, and ending at 1519 UT. An Hα flare with importance 1N was detected during this time, associated with eruptive prominences and sprays.

BATSE recorded enhanced hard X-ray emission (> 25 keV) after 1425:34, which was interrupted by GRO spacecraft night from 1430:10 until 1503:00 UT, and lasted until 1510:10 UT. The BATSE hard X-ray time profile (Fig. 1) shows two peaks in the early rise of the impusive phase, and the end of the decay phase, while most of the main flare phase was missed during spacecraft night. The major HXR peak at 1429-1430 UT is correlated with a group of fast-drifting bursts at > 1.3 GHz.

2. VLA observations

The VLA observations were made at $\nu = 1441.6$ MHz (20.8 cm) and 333 MHz (90 cm) with bandwidths of 3.25 MHz and a time resolution of 1.66 seconds. At the time of these observations, the VLA was in the A configuration which provided synthesized beamwidths of $\approx$ 1" at 20.8 cm and $\approx$5" at 90 cm.

Radio emission at 90 cm indicates impulsive and relatively low-intensity bursts (10-15 SFU) beginning at 14:19 UT, or about three minutes after the first enhancements of soft X-ray emission and about six minutes before the start of the BATSE hard X-ray burst. These metric bursts are located at different locations at heights of h = 0.4 - 0.5 $R_\odot$ above the limb (Fig. 2). They have angular sizes of $\approx$ 1.5' and peak brightness temperatures of T_b = 3.4 - 6.7 x 10^7 K.

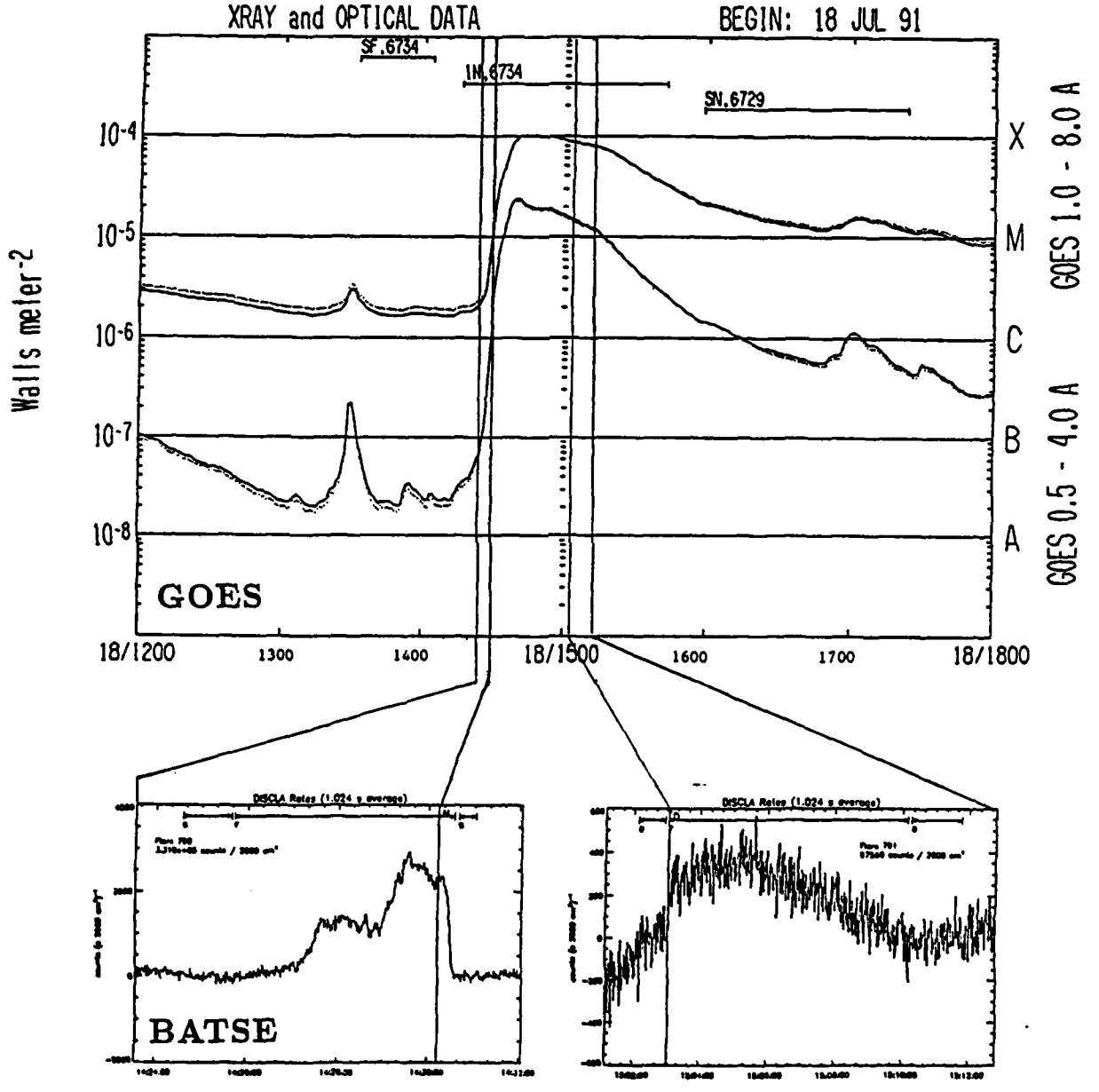

Fig. 1: *Time profile of the GOES soft X-ray data (0.5-4.0 and 1.0-8.0 Angstrom) and BATSE/GRO hard X-ray data (25-1000 keV) during the X1 class event on 1991 July 18, 1425-1510 UT. GRO observations are intermitted by spacecraft night from 1430 to 1503 UT.*

Between 14:40 - 14:50 UT, an intense 90 cm burst was observed to move systematically outward from the Sun with a velocity of $\approx$ 240 km s^{-1} (Fig. 3). This outward movement is characteristic for a moving Type IV burst. 90 cm sources associated with slowly-varying emission during the decay phase of the soft X-ray burst show no systematic movement, but again, are located at heights of h$\approx$ 0.4$R_\odot$ above the limb.

The time profile of 20 cm emission is depicted in Fig. 4 (top). Maps of the 20 cm emission during the times of maximum brightness (14:35:19 UT, 14:35:53 UT) show that the burst consists of at least two components (T_b = 2.8 x 10^7 K) which are located at heights of h $\approx$ 0.2$R_\odot$ (Fig. 2). The PHOENIX spectrometer data reveal a "broadband, quasi-periodic pulsation event" during this period of time.

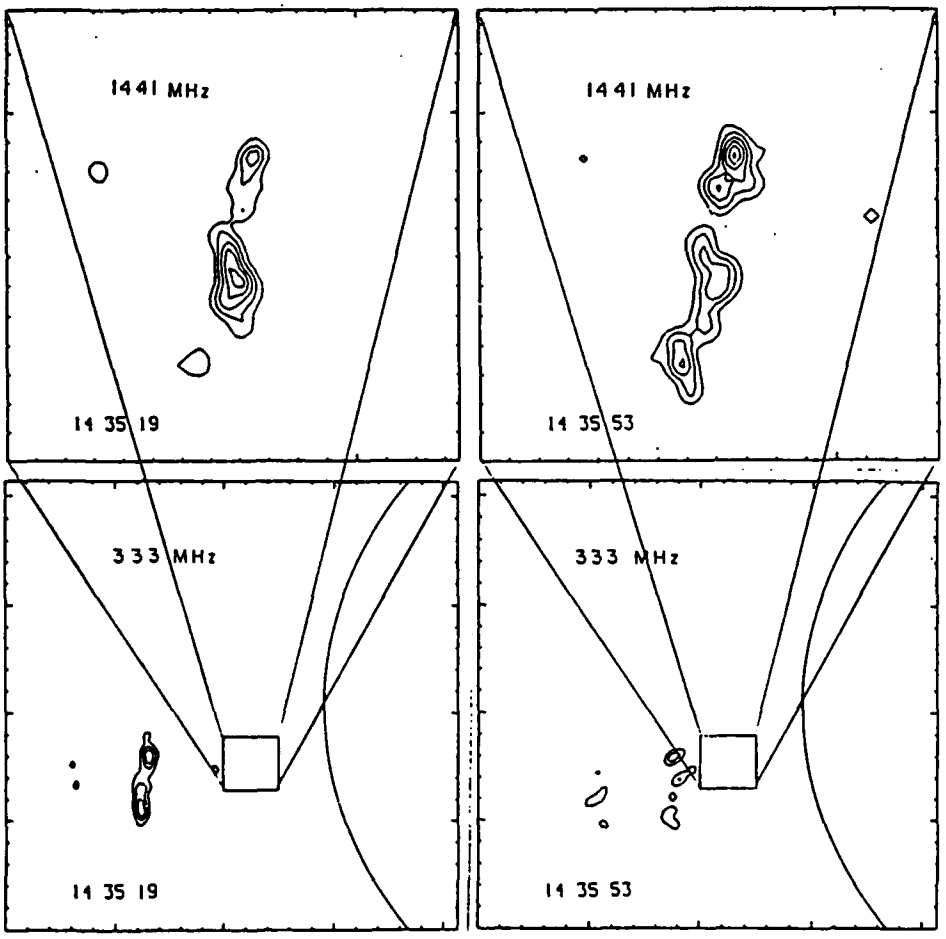

Fig. 2: *VLA snapshot maps with 3.3 s time resolution of total intensity at 1441 MHz (top) and 333 MHz (bottom) at the times indicated. The contours mark levels of equal brightness temperature, with an outermost contour and contour interval of T_b = 5.0 x 10^6 K at 1441 MHz and T_b = 8.4 x 10^6 K at 333 MHz. The fiducial marks are drawn at intervals of 10" for the 1441 MHz maps, and 60" for the 333 MHz maps. The boxes drawn on the 333 MHz maps denote the field of view of the 1441 MHz maps.*

3. PHOENIX observations

The frequency-agile PHOENIX broadband spectrometer of ETH Zurich (Switzerland) was operated in two frequency bands around the VLA frequencies 333 MHz and 1441 MHz: 20 frequencies with 3 MHz resolution in the 300-360 MHz range, and 60 frequencies with 10 MHz resolution in the 1150-1750 MHz band. The sweep spectrometer was operated with a time resolution of 40 ms. Both circular polarizations Stokes I and V are recorded, with a sensitivity of a few SFU at full time resolution. The PHOENIX spectrometer provides unique complementary information to VLA observations, such as high time resolution, broadband frequency spectra, and frequency-time drift rates.

The coregistered radio flux from VLA and PHOENIX is shown in Fig. 4 for the main flare phase, at the same frequency of 1441 MHz and with similar bandwidth (≈10 MHz) in both instruments. The RCP correlated flux of the shortest VLA baseline is compared with Stokes I of the full sun disk observation of PHOENIX. The broadband PHOENIX data reveal a considerable variety of radio bursts: **type III bursts** in the metric 0.30-0.35 GHz band; **type IIIdm, quasi-periodic pulsations**, and **intermediate drift bursts** in the decimetric 1.2-1.7 GHz band. Enlarged dynamic spectra of two episodes are displayed in Fig. 5.

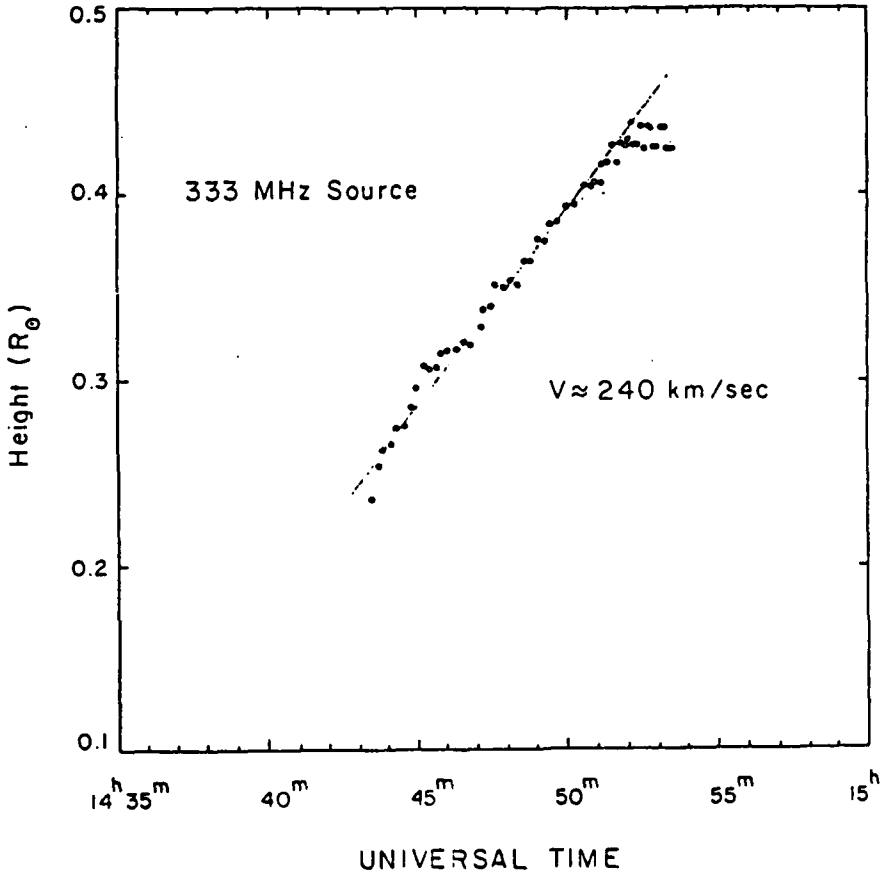

Fig. 3: *A plot of height versus time for the outwardly-moving 333 MHz source shown in Figure 2. The solid line represents a constant-speed fit to the data.*

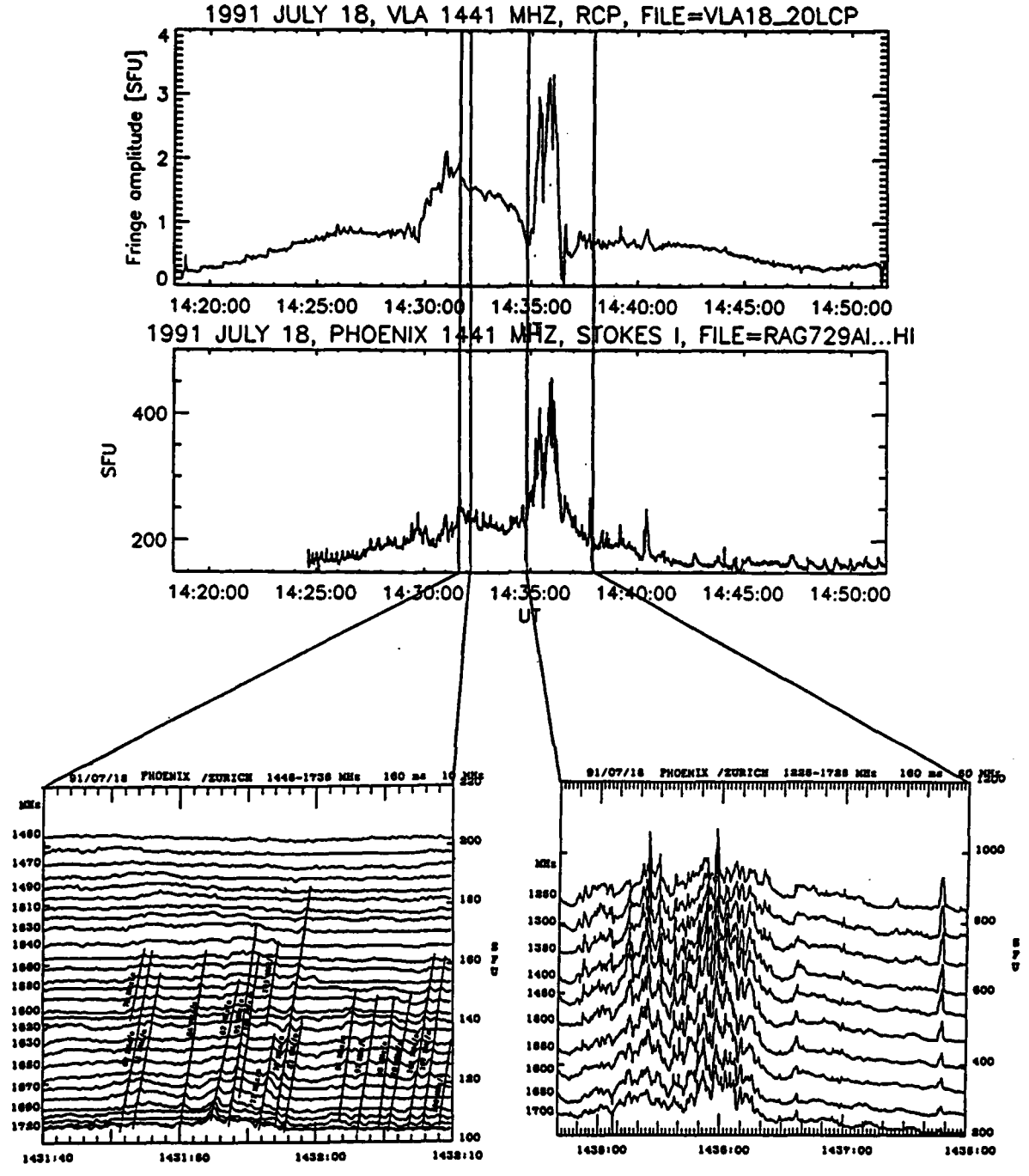

Fig. 4: *Comparison of VLA (top) and PHOENIX (middle) observations at 1441 MHz. The two enlargements (bottom) show broadband dynamic spectra of the "intermediate drift bursts" (bottom left) and of the "quasi-periodic pulsation" event (bottom right). The time resolution is 3.3 s (VLA, top), 0.04 s (PHOENIX, middle), and 0.16 s (PHOENIX, bottom). Note that the brightest radio emission during the flare is related to the quasi-periodic pulsation event.*

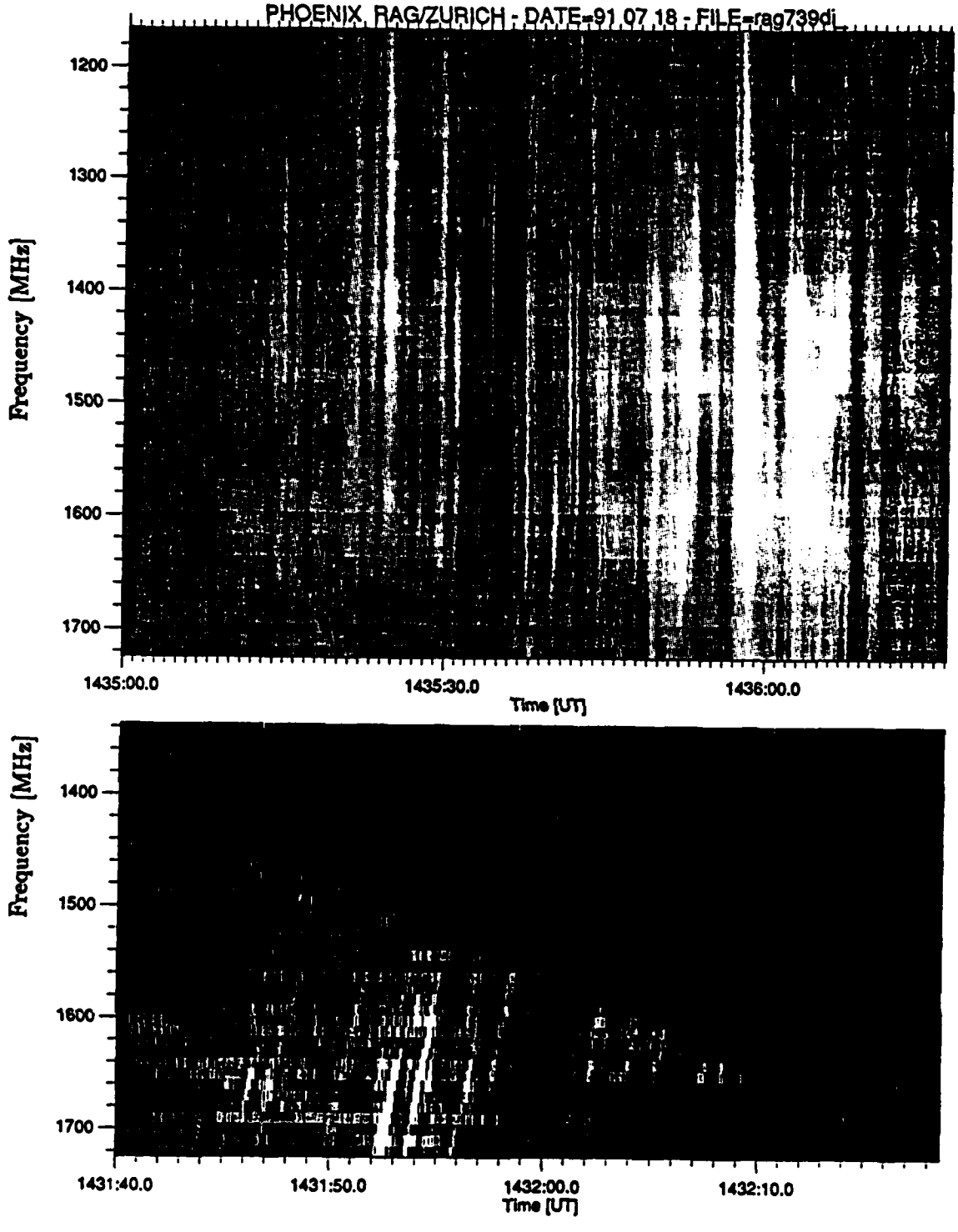

Fig. 5: *PHOENIX broadband observations at 1165-1725 MHz during the impulsive phase of the X1 flare. The white color in the grayscale indicates enhanced emission. The episode of "broadband quasi-periodic pulsations" at 1435-1437 UT is shown on top. Weak "intermediate drift bursts" are visible during 1431-1432 UT (bottom).*

3.1 Broadband, decimetric, quasi-periodic pulsations

The brightest radio emission at 20 cm occurs during 1435:00-1436:30 UT. While the VLA does not resolve many individual pulses, a total of about 80 pulses is identified in the PHOENIX record, with individual pulse durations of 1-2 s and frequency bandwidth of $\gtrsim 500$ MHz (Fig. 5). The frequency-time drift rate of these pulses has been measured with an automatic pattern recognition code, showing a symmetric distribution for positive and negative drift rates, where 80% of the pulses have a drift rate of $|d\nu/dt| \gtrsim 1000$ MHz/s. Monte-Carlo simulations of frequency-time drift rates with similar distributions have shown that the exciters of such radio emission originate in coronal structures with scale heights of $2 \cdot 10^3 - 2 \cdot 10^4$ km (Aschwanden and Benz, 1986). This is in good agreement with the spatial scale measured by the VLA, which is $\approx 7 \cdot 10^3$ km (10") for the half width of the 20 cm emission (Fig. 2, top) during the brightest pulses. This spatial scale probably corresponds to the transverse cross-section of large loops extending to heights of $\gtrsim 0.2 R_\odot$. Assuming plasma emission, the location of the 20 cm source corresponds to a density of $\gtrsim 10^{10}$ cm^{-3}. The time interval of the radio pulsation coincides roughly with the time of the steepest derivative in the soft X-ray time profile (Fig. 1), indicating the maximum heating rate during the flare, usually synchronized with the peak of hard X-ray emission. The characteristics of the pulsating radio time profile indicate the nonlinear dynamics of the underlying energy release mechanism (see review by Aschwanden, 1987); they cannot be explained by MHD eigen-modes which have much stricter periodicity.

3.2 Intermediate drift bursts

During the rise time of the impulsive flare phase we detected intermediate drift bursts with drift rates of ≈ -80 MHz/s (Fig 4,5). These bursts are detected for the first time in this high frequency range at 1.5-1.7 GHz. The normalized drift rate $(d\nu/dt)/\nu \approx 0.05$ is consistent with intermediate drift bursts found in the metric and decimetric range, also called "fibre" bursts. They represent a frequent fine structure of type IV bursts and can be used for diagnostics of the magnetic field. In current models they are interpreted in terms of Alfven wave solitons (Treumann et al. 1990) or whistler wave trains (Mann et al., 1987). 3D reconstruction of the magnetic field (using the Sakurai code) and the electron density (using the diagnostics from plasma emission of simultaneously localized type III bursts) should allow us for the first time to decide between the two theoretical models and to exploit their diagnostic potential.

Acknowledgements Solar radio and X-ray studies of the Sun at Tufts University are supported by NASA grant NAGW-2383 and by grant AFOSR-89-0147 with the Air Force Office of Scientific Research. The work at NASA/GSFC was performed under grant NAS5-30442 at USRA. The VLA is operated by Associated Universities, Inc., under contract with the National Science Foundation.

References

Aschwanden,M.J. 1987, Sol.Phys., 111, 113.
Aschwanden,M.J. and Benz, 1986, A&A, 158, 102.
Mann,G., Karlicky,M., and Motschmann,U. 1987, Sol.Phys., 110, 381.
Treumann,R.A., Güdel,M. and Benz,A.O. 1990, A&A, 236, 242.

V. CURRENT FUNDING AND FUTURE RESEARCH PLANS

a) Expenditure of Funds Through FY91

We have spent all of the funds awarded in Grant AFOSR-89-0147 to complete all of the proposed research. The total award amount has been $316,794 during the 3.5 year period 11/1/88 to 4/30/92. As mentioned previously, this has been an extremely cost-effective grant in view of the expensive telescopes and satellites used, as well as the research productivity and return in publications of important ideas.

b) Proposed Funding Beginning in FY93

The Tufts University Solar Radio Physics Group will submit an unsolicited three-year proposal to the AFOSR for support at the $100,000 per year level beginning in Fiscal Year (FY) 1993. Such support will continue proven experience in acquiring data, obtaining access to satellites and telescopes, and building-up and training one of the few solar radio astronomy groups in the United States. The proposed future funding will provide stability and continuity to a research program that has already provided substantial scientific returns to the AFOSR.

c) Analysis and Publication of Existing Data

We have obtained Very Large Array (VLA) observations of the Sun in July, 1991, December, 1991, and January, 1992, together with simultaneous solar observations at radio wavelengths (PHOENIX Digital Radio Spectrometer), X-ray wavelengths (Yohkoh Satellite) and γ-ray wavelengths (Gamma Ray Observatory satellite). These data can only be fully analyzed and published with continued AFOSR support in FY93. At least one of these papers is now in the referee stage with the *Astrophysical Journal.*

d) Extension of the Ongoing AFOSR Program

Our unsolicited proposal will request support for future novel observations of the Sun from the ground and space. The proposed observations will amplify and extend our recent findings, while also including new, detailed investigations of coronal structures and their relationship to solar flares and coronal mass ejections. They will build upon our long-wavelength VLA studies of active region coronal loops (20 cm) and large-scale coronal loops (90 cm) that connect active parts with more distant parts of the Sun. All of these results will be enhanced by simultaneous X-ray observations using the United States Soft X-ray Telescope aboard the Yohkoh satellite.

Further investigations of recent findings will include:

1. Multiple-wavelength observations of quiescent filaments in absorption and emission.
2. Observations of the triggering of solar flares by the interaction of coronal loops within active regions, or along large-scale magnetic loops that connect widely-separated ones.
3. Feedback mechanisms between high-lying coronal loops and lower ones that may cause coronal mass ejections, energetic flares or noise storms.

Proposed new investigations of coronal structures will include:

4. Investigations of the evolution of coronal loops within active regions will provide a better understanding of the physical processes that lead to the buildup and release of magnetic energy and ultimately to the production of flares and high energy particles that interfere with the terrestrial environment. This will involve simultaneous observations of active region coronal loops with the VLA and the Solar Maximum Mission (SMM) and Yohkoh satellites.
5. Studies of the long-term evolution of large-scale coronal loops using synoptic magnetic field, radio and X-ray observations in order to examine their stability, to confirm the existence of recurrent large-scale structures and to understand their relationship to coronal holes and coronal mass ejections. These investigations will include images of the photospheric magnetic field (Stanford Wilcox Solar Observatory), radio maps of coronal loops (Very Large Array) and full-disk X-ray images of the hot coronal plasma (Yohkoh satellite).

e) The Tufts University Radio Physics Group

The small research group at Tufts University carrys out research at the cutting edge of modern solar physics by using facilities funded by the NSF (the Very Large Array) and NASA (the Solar Maximum Mission and Yohkoh satellites) and which cost hundreds of millions of dollars to build and maintain. Our small group can thus be sustained with relatively modest funding for salaries, while still obtaining data from the most recent telescopes on the ground and in space. We additionally maximize the scientific return of our research by combining data at different regions of the electromagnetic spectrum, thereby enhancing the scientific return beyond that expected from one region alone.

We have now built up the critical mass required to continue this productive research. Personnel include Professor Ken Lang, whose academic duties permit only part-time research, Research Professor Robert Willson, who has devoted nearly a decade to rewarding, full-time investigations of the Sun, and graduate student James Kile, who has completed his course work and will now do a Ph.D dissertation in solar radio astronomy. In spite of its small size, the Tufts' group has built up a strong record of credibility that continues to result in requested observing time with the Very Large Array and ongoing publications in the best journals.

Future support by the AFOSR is required for the continuity and stability of the Tufts group. Such funding will not only build upon prior commitment and investment by the AFOSR, but it will also provide the foundation for substantial future results. Our past

track record indicates that such results will be forthcoming in a relatively cost-effective and low-risk manner.

f) Relevance of Our Research to the United States Air Force

One of the key findings of the Tufts' Solar Radio Astronomy group has been the discovery that the hot coronal plasma and the ubiquitous magnetic loops can be imaged at radio wavelengths used by the Very Large Array (VLA), and that full-disk radio images can examine the global interaction of such loops with high angular resolution. The radio-emitting coronal loops sometimes do not have detectable X-ray counterparts, particularly in the regions of intense magnetic fields above sunspots. Moreover, the VLA maps can provide unique information on the structure and strength of the magnetic field. The radio data are therefore required to provide complete information on the structure and evolution of the solar corona.

The proposed VLA research will complement and extend future X-ray observations from space and are of interest to the Air Force. For example, full-disk VLA observations of the Sun at 20, 91 and 400 cm can be used to study the structure and evolution of long-lived coronal holes that are believed to be the source of the high-speed solar wind and geomagnetic activity. Multiwavelength images will specify the three-dimensional structure of these holes, a factor that influences the propagation of high energy particles that emanate from them.

VLA observations might also be used to resolve uncertainties over the origin of coronal mass ejections in which loop-shaped, magnetically confined plasma rises and expands into the solar wind. These events will be detected by orbiting coronagraphs such as the Coronal Mass Ejection Imager (CMEI), currently being designed for the U.S. Air Force. Coronal mass ejections are probably initiated by erupting filaments, interacting loops or magnetic reconnection in the low corona, and our multiwavelength VLA observations would be used to detect these effects.

We will also continue our investigations of the prediction and triggering of energetic solar flares that travel to the earth, interfere with communications and high flying aircraft and effect the health of astronauts and pilots. For example, we have shown that these flares are triggered by the interaction of nearby, but spatially separate loops, and that extensive theoretical work which involves flare emission from simple isolated coronal loops is probably wrong. Our VLA images of coronal loops also indicate that monitoring of the photospheric magnetic field will never result in reliable flare forecasting if considered alone.